

**EVALUATION OF THE INLAY PROCESS AS A MITIGATION
STRATEGY FOR PRIMARY WATER STRESS CORROSION CRACKING
IN PRESSURIZED WATER REACTORS**

David L. Rudland
Office of Research
United States Nuclear Regulatory Commission

and

Frederick Brust, Tao Zhang, Do-Jun Shim and Gery Wilkowski
Engineering Mechanics Corporation of Columbus

April 2010

Table of Contents

Table of Contents	ii
Executive Summary	iii
1 Introduction	1
2 Inlay Description	1
3 Weld Residual Stress Modeling for Inlays	3
3.1 Overview of Weld Modeling	3
3.1.1 Weld modeling overview	4
3.1.2 Thermal models	6
3.1.3 Structural models	7
3.1.4 Other issues	8
3.1.5 Validations/verification	9
3.2 Modeling of Inlay	10
3.2.1 Inlay weld process	11
3.2.2 Temper bead welding	18
3.2.3 Cases studied and description	23
4 Weld Residual Stress Results	24
4.1 Model 1 Weld Residual Stress Results	24
4.1.1 Line plots of weld residual stresses for Model 1	30
4.2 Model 2 Weld Residual Stress Results	48
4.2.1 Model 2 line plots for structural integrity assessment	52
5 Crack Growth Efforts	62
5.1 Determination of Crack Growth Parameters	63
5.1.1 PWSCC growth model – MPR-115	63
5.1.2 Recent A52/152 PWSCC Data	63
5.2 Idealized Flaw Growth	65
5.2.1 Stress intensity solutions	65
5.2.2 Conditions for crack growth	66
5.2.3 Welding residual stress	67
5.2.4 Transition from surface crack to through-wall crack	68
5.3 Crack Stability	69
5.4 Idealized Flaw Growth Results	70
5.4.1 Effects of repair assumptions	71
5.4.2 Effects of crack growth rate	72
5.4.3 Effect of global bending stress	73
5.4.4 Effects of operating temperature	73
5.4.5 Effects of flaw orientation and size	74
5.4.6 Effects of embedded defects	75
5.5 Natural Flaw Growth	76
5.5.1 AFEA method description	78
5.5.2 Natural flaw growth results	83
5.6 Comparison of Idealized and Natural Flaw Growth Results	95
6 Summary and Conclusions	97
7 References	99
Appendix A Axis-symmetric and Three-dimensional Pipe Weld Models	A-1
Appendix B Material Data Used for Analysis	B-1
Appendix C Summary of additional Weld Residual Stressess for Hot Leg	C-1

Executive Summary

The commercial nuclear power industry has proposed several mitigation techniques to address safety concerns due to primary water stress corrosion cracking (PWSCC) in nickel-based dissimilar metal (DM) welds (specifically Alloy 82/182 welds) in pressurized water reactors (PWRs). Since many of these welds reside in primary piping systems that have been approved for Leak-Before-Break (LBB), the mitigation strategies chosen must ensure that these systems still satisfy the LBB criteria. Mechanical Stress Improvement Process (MSIP), Full and Optimized Structural Weld Overlay (FSWOL, OWOL), and Inlay and Onlay cladding are examples of the currently proposed mitigation methods. The industry claims that these methods provide either a reduction in the inner diameter residual stress field (MSIP and WOL), and/or apply a non-susceptible corrosion resistant barrier to stop or retard PWSCC crack growth from forming a through-wall leak path (WOL, Inlay, Onlay). This report focuses on an evaluation of the inlay process for the mitigation of PWSCC since it may be the technique of choice for the large-diameter reactor coolant nozzles. Currently the ASME Section XI code is developing Code Case N-766 'Nickel Alloy Reactor Coolant Inlay and Cladding for Repair or Mitigation of PWR Full Penetration Circumferential Nickel Alloy Welds in Class 1 Items.' This code case is documenting the procedures for applying inlay welds.

In this effort, confirmatory welding residual stress and flaw evaluation analyses were conducted to evaluate the inlay as a mitigation technique. Two large bore, reactor coolant nozzle geometries were considered. The first was an 872 mm (34.3 inch) diameter, 68.1 mm (2.68 mm) thick reactor coolant outlet nozzle taken from an Areva inlay submittal. The second was a 923 mm (36.3 inch) diameter, 83.8 (3.3 inch) thick reactor coolant nozzle used to develop welding residual stress results for probabilistic fracture mechanics calculations. For each of these geometries, detailed finite element simulations were conducted to predict the welding residual stress through the application of the inlay. The effects of temper bead welding and weld repairs were considered. The following repair sizes were considered:

- 50% deep ID pre-service repair (before stainless steel safe end)
- 50% deep ID PWSCC repair (after stainless steel safe end but before inlay)
- 75% deep ID pre-service repair
- 75% deep ID PWSCC repair
- 50% deep ID pre-service repair and a 75% deep ID PWSCC repair
- 12% deep ID pre-service repair
- 12% deep ID PWSCC repair
- 12% deep ID pre-service repair and a 12% deep ID PWSCC repair

For each case, a final inlay thickness of 3mm was considered since this corresponded to the minimum thickness required by Code Case N-766. In addition, a 6-mm deep inlay was considered for the 50% deep ID pre-service and 50% deep ID PWSCC repair cases.

The results from the welding residual stress analyses suggest that the regardless of the repair history, the ID stress state is driven by the inlay repair. In most cases, the ID axial stress due to the inlay was about 400 MPa (58 ksi), which is just above the yield strength for the DM weld material. Even the beneficial effect of the stainless steel safe end weld was eliminated by the thin layer of inlay material on the ID surface of the pipe. For all of the inlay cases with pre-service repairs, the high axial stress on the ID dropped to zero at about 15 percent of the wall

thickness for all repair depths. For the cases with PWSCC repairs, the axial stress dropped to zero between 40 and 50 percent of the wall thickness for repairs greater than 50 percent deep and it dropped to zero at about 20 percent of the wall thickness for the 12 percent deep repair.

The results from the welding residual stress analyses were used in PWSCC growth analyses using both idealized-shaped and natural-shaped cracks assuming simulated crack growth rates. The idealized flaw analyses followed the techniques documented in the ASME Section XI flaw evaluation guidelines. Sensitivity studies were conducted on crack growth rate, bending stress, operating temperature, initial flaw size and orientation, and inlay depth.

For the idealized flaw analyses, the ASME Section XI flaw evaluation guidelines were used in conducting PWSCC growth calculations. The effects of crack initiation were ignored and an initial surface breaking defect was assumed in all analyses. This assumption is consistent with the Code Case N-766 requirement that a postulated surface breaking planar flaw that is 1.5mm deep will not grow through thickness due to fatigue for the life of the inlay. Crack growth times through the inlay, to through-wall penetration and to rupture were calculated. The following significant conclusions were obtained:

- The time for the initial defect to grow through-wall was dominated by the time for the initial defect to grow through the inlay, i.e., a large portion of the crack growth time is spent in the first 3mm of wall thickness. The only exception to this case was for the small weld repair (12%). In this case, the flaw arrested after passing through the inlay.
- For the 3mm deep inlay, the time through the inlay was typically about 10 years. After that point, the time to leakage varied with repair size, ranging from an additional 5 years for a 50% deep repair to arrest for a 12% deep weld repair.
- For the 6-mm deep inlay, the time through the inlay was about 25 years, with the additional time to leakage the same as for the 3-mm cases.
- The crack growth times through the inlay are directly proportional to the crack growth rate used. More experimental data on Alloy 52 crack growth rates is needed to quantify the uncertainty in the crack growth rate.
- Bending stress did not have a large effect on the time for the crack to pass through the inlay, but had a large effect on time to leakage, i.e., the lower bending stresses caused the crack to slow considerably near the middle of the wall thickness.
- Temperature had a large effect on the crack growth behavior. The time through the inlay, time to leakage, and time to rupture were increased by about a factor of 6 by reducing the temperatures from hot leg (327C) to cold leg (288C) conditions. Even for the fastest crack growth considered, the time to leakage was over 50 years at the cold leg temperatures.
- Initial crack length did not have a large impact on the time through the inlay or to leakage.
- Axial cracks grew faster than circumferential cracks due to the larger hoop stresses in the inlayed welds.

For the natural flaw growth analyses, the PipeFracCAE code, which was used in the Wolf Creek analyses, was modified to handle the unusual crack growth that may occur in an inlayed DM weld. Due to the differences in the crack growth rates between the inlay material (Alloy 52) and the DM weld (Alloy 82/182), a discontinuous, “balloon” shaped crack forms. After modifications to the PipeFracCAE code were complete, several sample cases were run for

comparisons to the idealized flaw analyses. The intent of these natural flaw analyses were to verify that the unusual flaw shapes did not highly impact the time through the inlay and leakage calculated using the idealized flaw assumption. The results from these runs illustrated that in some cases, the natural crack analyses gave slightly longer times to leakage, while in other cases the times to leakage were slightly shorter. The differences stemmed from the effect of the natural crack shape on the crack driving force and the more accurate representation of the welding residual stress field in the natural flaw analyses. Overall, the natural crack shape analyses demonstrated that reasonable approximations of crack growth time through the inlay and to leakage can be made with idealized flaw analyses.

Overall, several general conclusion can be made regarding the effectiveness of inlays as a mitigation technique. First, the sensitivity studies conducted assuming a postulated initial defect indicate that for the hot leg locations, the time to leakage values are less than the inlay design life even with Alloy 52 PWSCC crack growth rate improvement factors of 30 – 100. For the case of a 3-mm inlay, the times to leakage from the postulated defect ranged from about 12 years to 30 years. This conclusion assumes that the effect of crack initiation in Alloy 52 inlay materials is neglected and can be considered an additional conservatism in the results.

Second, the results presented in this report are highly influenced by the Alloy 52 crack growth rates assumed. Due to the limited Alloy 52 crack growth data, additional crack growth data is needed for these materials to fully understand and quantify the uncertainty in the results.

Third, the times to leakage calculated in this effort do not support sample inspections for inlay mitigated hot leg temperature welds. However, the effect of temperature on the growth rates is dramatic and therefore the results from this study support sample inspection for inlay mitigated cold leg temperature welds.

Finally, the results from this study suggest that a large portion of the time to leakage is spent growing the postulated defect through the inlay. Since the inlay may only be about three to five percent of the total wall thickness, it is recommended that both volumetric and ID surface examination be performed to locate a defect that may be present in the inlay material.

1 Introduction

Primary water stress corrosion cracking (PWSCC) in nickel-based dissimilar metal (DM) welds (specifically Alloy 82/182 welds) in pressurized water reactors (PWRs) can cause a safety concern due to the high crack growth rate and irregular shaped flaws. Since many of these welds reside in primary piping systems that have been approved for Leak-Before-Break (LBB), the domestic commercial nuclear power industry has proposed a number of mitigation strategies for dealing with the issue and assuring LBB is still applicable. Some of these methods include Mechanical Stress Improvement Process (MSIP), Full and Optimized Structural Weld Overlay (FSWOL, OWOL), and Inlay and Onlay cladding. The industry claims that these methods provide either a reduction in the inner diameter residual stress field (MSIP and WOL), and/or apply a non-susceptible corrosion resistant barrier to stop or retard PWSCC crack growth from forming a through-wall leak path (WOL, Inlay, Onlay).

For the larger bore piping systems, i.e. hot leg outlet nozzle, the industry considers methods such as FSWOL unfeasible due to various constraints. Hence, inlay cladding welds are being proposed on the inside surface of the pipe. Currently, the ASME code is developing Code Case N-766 'Nickel Alloy Reactor Coolant Inlay and Cladding for Repair or Mitigation of PWR Full Penetration Circumferential Nickel Alloy Welds in Class 1 Items.' This code case is documenting the procedures for applying these inlay welds.

As part of a confirmatory analysis, the US NRC Office of Research and its contractor, Engineering Mechanics of Columbus, have conducted both welding residual stress (WRS) and flaw evaluation analyses to evaluate inlay welds as a mitigation technique. Using two large bore geometries, detailed welding simulation analyses were conducted following the procedures set forth in draft Code Case N-766. Effects of weld repairs and temper bead welding are included. Using these residual stress results, PWSCC growth analyses using both idealized-shaped and natural-shaped cracks were conducted using simulated crack growth rates. Sensitivity studies conducted on crack growth rate, bending stress, operating temperature, initial flaw size and orientation, and inlay depth shed light on an appropriate inspection schedule for DM welds with inlays.

2 Inlay Description

Code Case N-766 'Nickel Alloy Reactor Coolant Inlay and Cladding for Repair or Mitigation of PWR Full Penetration Circumferential Nickel Alloy Welds in Class 1 Items' is currently being developed by ASME Section XI to document the procedures for designing and applying a weld inlay. The code case defines an inlay as

A corrosion resistant barrier applied on the inside diameter surface of the pipe between the stress corrosion cracking (SCC) susceptible material and the reactor coolant, requiring excavation of some portion of the SCC susceptible material.

The geometry and material for an inlay is specifically defined in Code Case N-766 and has the following requirements:

- Weld filler metal for the inlay or cladding shall be nickel alloy with a minimum chromium content of at least 28%.
- The minimum thickness shall be 1/8 in. (3mm).
- The inlay or cladding shall consist of at least two (2) layers after final surface preparation and comply with the minimum thickness requirements. These two layers shall each contain a minimum of 24% chromium
- The minimum thickness shall extend over and beyond the DM weld fusion zones by at least twice the demonstrated accuracy of the locating technique or 1/4 in. (6 mm), whichever is greater.

In addition, the following structural requirements are given

- A inspection of the DM weld must be done prior to the application of the inlay
 - If a defect is found, it must be repaired or shown to be acceptable per ASME Section XI, IWB-3600.
 - If a repair is needed, a post repair inspection with liquid die penetrant or the eddy current method is required.
- To aid in the reduction of hot cracking in the inlay, a stainless steel buffer layer is acceptable over the stainless steel (SS) base materials. This thickness is not credited to the thickness of the inlay.
- A postulated flaw of 1/16 inch (1.5 mm) depth must be shown to be acceptable for the life of the inlay for both Service levels A and B loading. The code case only requires a fatigue evaluation for this flaw.

A schematic of the inlay geometry is shown in Figure 1.

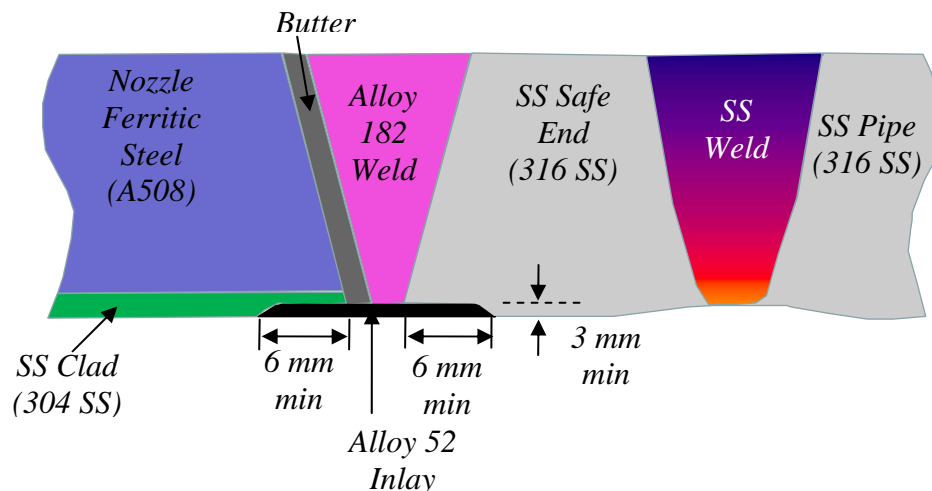


Figure 1 Inlay geometry schematic

3 Weld Residual Stress Modeling for Inlays

3.1 Overview of Weld Modeling

No attempt is made here to provide a complete overview of the development of weld process models over the years. However, many of the papers, and the publications cited therein, listed in this section can be viewed by the interested reader. Perhaps the first attempt to predict the residual stresses induced by the welding process was carried out by Rodgers and Fletcher [1] using an analytical approach. A number of other analytical approaches were developed from this time through the early 1970's to predict distortions and residual stresses (see for instance the survey paper by Masubuchi [2]). These approaches were quite novel and often provided reasonable predictions when compared with experimental measurements, but were often limited to single pass welds.

Such analytical approaches were replaced by numerical approaches in the early 1970's as the power of the finite element method was realized. The earliest published finite element models developed for predicting the residual stresses induced by the weld process were developed independently by Kamichika et al. in Japan [3] and Friedman [4] in the USA. Researchers (Barber et al. [5], McGuire [6], and Brust, Rybicki, and Kanninen et al. ([7], [8], [9] and references cited therein)) extended these models in the late 1970's and early 1980's to account for (among other features) multiple pass welds, material re-melting and annealing, phase changes and heat sinks. This work was also perhaps the first to use closed form analytical solutions to develop accurate high speed weld thermal analysis procedures for finite thickness (including thin) plates. These models were used extensively in studies for the nuclear power industry to develop weld procedures to mitigate heat affected zone inter-granular stress corrosion cracking in stainless piping systems in Boiling Water Reactors (BWR). Methods such as Heat Sink Welding (HSW – Barber [5]), Induction Heating for Stress Improvement (IHSI –McGuire et al. [6]), Backlay Welding (BW – Brust and Rybicki [7]) which were early forms of weld overlay repair procedures), were developed and optimized using these models. The methods are still used in many industries today. In fact, feasibility studies for the early forms of the mechanical stress improvement process (MSIP) were examined in these programs [9]. As such, this work probably represented the first industrial application of a weld process model to aid in solving a manufacturing fabrication problem.

Since 1990, weld process models have been extensively developed and are being used by many different organizations. Fricke, Keim, and Schmidt [10], Goldak et al. [11], Yang and Feng [12], and Buchmayr [13] summarize methods used by organizations in Germany, Canada, USA (Edison Welding Institute), and Austria, respectively, to model weld induced residual stresses and distortions. No attempt to summarize the methods used by these and other organizations is attempted here; rather the interested reader can consult these references and references cited therein and below for details. In the early to mid 1990's, the present authors began to greatly improve all of these weld analysis tools that were developed in the early 1980's. In particular, the high-speed thermal solution procedures and the structural procedures such as local annealing, melt element detection, etc., were extensively updated and improved for the nuclear industry, the aerospace industry, the Department of Energy, the automotive industry, among others. Zhang, Dong, and Brust [14] and Brust, Dong, and Zhang [15] and Zhang, Dong, Brust, Shack,

Mayfield, and McNeil [16] et al. describe these developments for thick plate nuclear applications. Further details can be found in all of these works.

Finally, the primary water stress corrosion cracking (PWSCC) issue in nozzle dissimilar metal welds, beginning circa 2001 to present, has led to the latest improvements in computational weld models. Rudland, Shim, Xu, and Wilkowski [17] performed a complete study of PWSCC and corresponding natural crack growth studies using the latest model developments and a similar study was performed by nuclear industry researchers (Broussard et al. [18]). A summary of numerous industrial applications of computational weld models along with mitigation methods for both weld residual stress and distortion control can be found in the book chapters by Chen, Brust, and Yang [19] and Brust and Kim [20]. In fact, the PWSCC issue has led to the development of weld residual stress and cracking sessions at the ASME pressure vessel and piping conferences from circa 2000 to the present 2010 [21]. The current methods used are completely documented in these references and those sited therein. It is seen that computational weld modeling has come a long way since the early analytically based models by Rogers and Fletcher in 1938[1]!

3.1.1 Weld modeling overview

Computational weld modeling is challenging because many of the processes of welding are highly nonlinear. Materials melt and re-solidify; very high transient thermal gradients are experienced; non-linear temperature dependent plastic straining and phase transformations can occur; these are among the multiple sources of nonlinearity that must be addressed in any weld modeling effort. Moreover, for weld modeling to have practical advantages in industrial production, computational solution times must be manageable since an optimum weld design of large, complex fabrications and nuclear piping systems requires numerous separate analyses. Figure 2 illustrates the three different types of advantages of computational weld modeling. On the first level, weld residual stresses can cause or lead to cracking. Both fatigue and stress corrosion crack growth can be affected by tensile weld residual stresses caused by welding. The second concern is distortions caused by welding (middle illustration in Figure 2). Distortion control can lead to fabrication cost savings, especially for large fabrications since rework to 'straighten' structures can be very expensive. Distortion control may lead to decreased fabrication costs in new nuclear plants for tolerance critical components. Finally, microstructure control (phases, hardness), as illustrated in the bottom illustration in Figure 3, is sometimes of concern.

Most computational weld models available commercially are mathematics and physics based models. ABAQUS and ANSYS are the main codes used in the nuclear industry for modeling the weld process, although other codes are used as well. The weld modeling procedure generally follows the outline shown in Figure 3. One first builds a finite element model (often from a CAD drawing). Next, the thermal solution is performed, either using a user written thermal flux routine (discussed in Section 3.1.2) or analytical solutions (often for three dimensional solutions to reduce solution time [19]). Next, the temperature time histories for each pass at each node point serve as input for the thermal elastic-plastic structural portion of the solution. This sometimes uses a user routine (UMAT in ABAQUS) or the constitutive laws in the finite element library. Finally, the distortions and weld residual stresses induced during weld metal shrinkage are calculated and post processed.

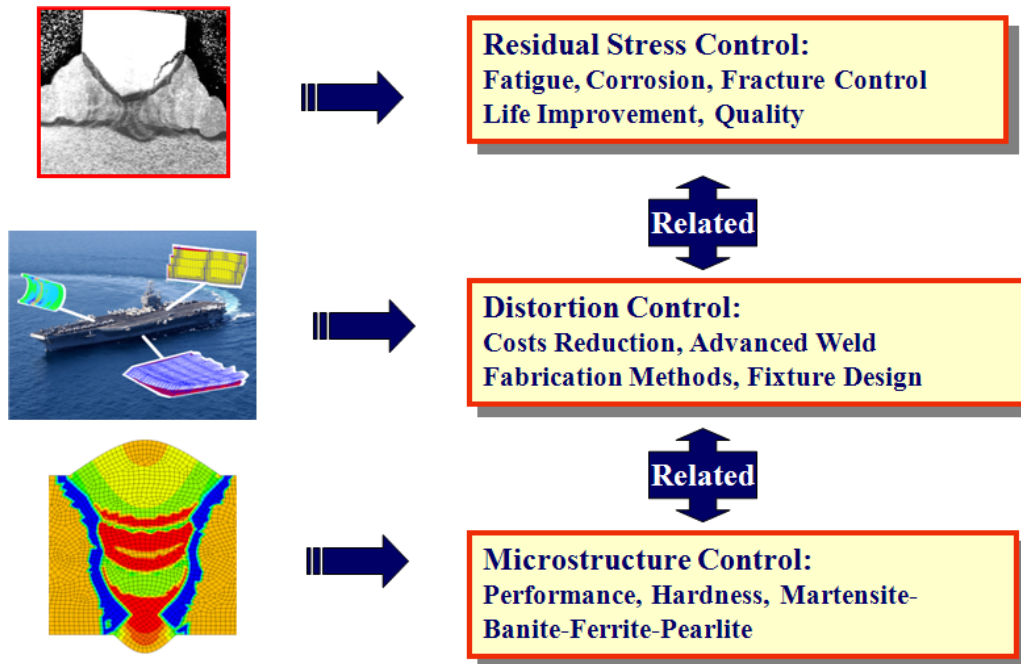


Figure 2 Purpose of computational weld models

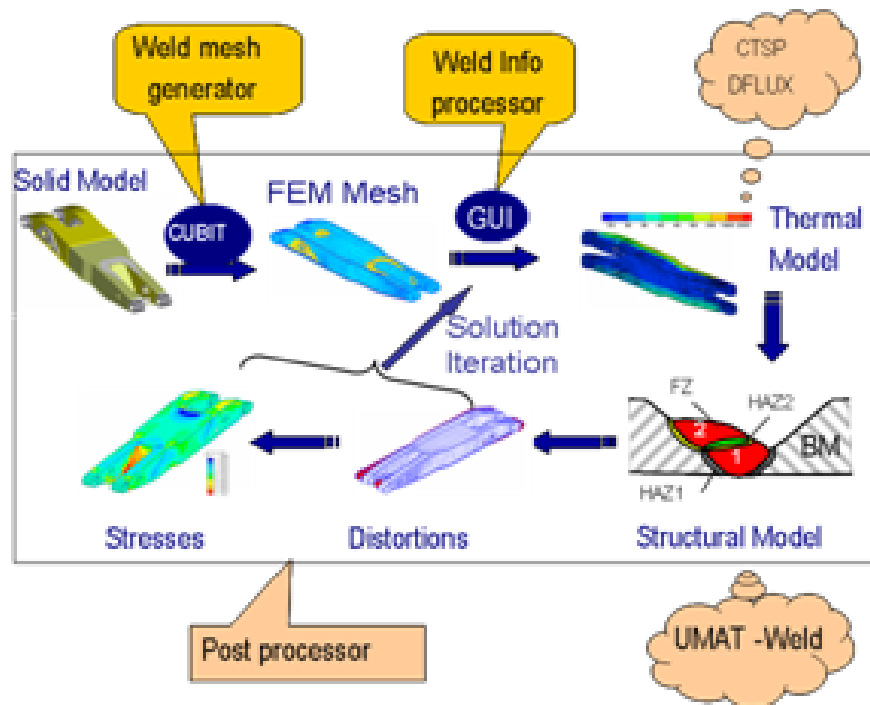


Figure 3 Typical computational weld model

3.1.2 Thermal models

An axis-symmetric model was used to obtain the temperatures that are used to calculate the residual stress field caused by the welding process in this study. Compared to three dimensional modeling, two-dimensional modeling of the thermal weld process is somewhat artificial and requires engineering judgment. Let us consider an axis-symmetric axial cross section in a pipe DM weld. In the actual pipe weld process, the weld beads approach the cross section, heat it up, and then the section cools. The cross section of interest does not ‘feel’ the heat from the weld bead until the heat source is very close to cross section (of course this depends on the torch speed). As the molten bead moves past the cross section the heat spreads out, especially in the directions normal to the weld bead direction as the molten metal cools. As the torch moves further along the circumference, material points on the cross section of interest cool down in an exponential fashion. Material points away from the weld bead reach their peak at a later time and then cool exponentially in time. By the time the weld torch completes a 360-degree revolution to complete the butt weld pass, the cross section of interest has cooled down.

When performing an axis-symmetric weld model analysis, the weld bead is assumed to be deposited at once, and cools at once. The thermal gradients and transients in the direction of the weld (both ahead of, and behind the weld torch) are ignored. Moreover, excessive constraint is introduced due to the ‘tourniquet’ effect of the complete cooling of the weld bead along the entire 360-degree region of the pipe weld. Appendix A, which compares two-dimensional and three dimensions welding simulation analyses, suggests that axis-symmetric analysis often produces stress predictions that are higher in absolute magnitude compared to the three dimensional solution. There are a number of different strategies for modeling the thermal weld process in a two dimensional solution, none of which is entirely satisfactory. There are a variety of thermal models to simulate the weld heat process for two dimensional problems ranging from a constant body flux over the weld bead, to analytical solutions, to the Goldak model where the weld power varies spatially within the weld bead as well as in the torch movement direction. Our results have shown that using a Goldak [22] double ellipsoidal with heat intensity varying throughout the weld bead, results in stresses that do not vary much from assuming a constant volumetric heat source. The procedure used here is discussed below.

The weld simulation process first requires application of sufficient heat to melt the weld metal (up to 1,700 K) and a small layer of the base metal. No two dimensional heat input model is purely predictive, the best approach is to adjust the heat input until there is a good agreement with measured temperatures, observed microstructure changes, and the size of the weld puddle. Here, the welding arc is treated as a volumetric moving heat source, taking the double-ellipsoidal distribution proposed by Goldak et al. [22]. However, such moving source analyses can be computationally intense because the heat intensity has to be calculated for all elements within the pass. Our experience when comparing the two methods is that the benefits for two dimensional or even three dimensional solutions are debatable. Therefore a uniform heat distribution was used across the weld bead cross-section. This approach, compared to other methods such as Goldak’s double-elliptical heat flux model, has been proven to be easier to implement and more robust for irregular shapes of weld metal. Experience in separate sensitivity studies suggests that the difference in the final distortion or residual stresses is insignificant between Goldak’s model and the current approach [23]. This axis-symmetric method effectively ignores the motion of the welding arc, allows for heat transfer radially away from the centerline of the weld path with no

heat transfer ahead or behind the weld bead, and “shortens” the welding time. To do this, a uniform energy density is added to the whole weld pass in an exponential function form:

$$q = \frac{\sqrt{3}Q}{\sqrt{\pi VT}} e^{-3(t-t_0)^2/T^2} \quad (1)$$

This is Goldak’s [22] model with constant flux within the weld bead itself. Where q is the energy density (W/mm³) from the weld arc, V is the total volume of the weld pass, t_0 is a starting time, T is the characteristic time of the traveling arc, and Q is the total heat input during the time of welding. Here t_0 is the time when the heat source attains its maximum value when it is at the axis-symmetric section. For this heat source model, every material point in the weld will experience the same heat source cycle and hence similar temperature histories. Therefore, at any time, there is no heat flux gradient and therefore minimum temperature gradients over the entire weld pass. This was implemented through ABAQUS subroutine DFLUX. Another subroutine UFIELD is used to track the peak temperature at each node so that the coefficients can be adjusted to ensure the entire weld region is properly molten.

The weld parameters for the DM weld and butter were not specified for each nozzle but rather ranges of proper procedures were specified in the weld specification sheets. Typical stainless steel weld parameters were used since specification sheets are not available.

3.1.3 Structural models

The approach used in the predictions of welding residual stresses and strains is based on extensive knowledge of the welding process and has been refined as the commercial finite element codes have been updated and improved. Thermo-elastic-plastic FE simulations were performed to simulate welding of the hot leg butt welds and corresponding inlay. The formation of the welding residual stress is a result of the thermo-mechanical deformation process during welding. The heat flow and mechanical deformation during welding were simulated using a sequentially coupled approach with the temperatures discussed above in Section 3.1.2. With this approach, the transient heat-transfer analysis was conducted to solve the temporal and spatial distribution of the temperature in the model, and then the computed thermal history was used as thermal loading input in the subsequent mechanical analysis calculating the residual stress field. Temperature-dependent mechanical properties were utilized and isotropic hardening was assumed here. Experience suggests that isotropic hardening tends to predict conservative (in absolute magnitude) stresses. The effects of melting, solidification, and annealing were simulated in the analysis. The welding heat flow was modeled as a heat-conduction problem. Temperature-dependent material properties, as summarized in Appendix B, were used here. The welding simulation was performed on a pass-by-pass basis. A weld pass was activated only when it was deposited.

The ABAQUS procedure for material annealing is used for elements adjacent to the weld metal that experience heating higher than the user defined temperature (which can range between the austenitic phase change temperature to melting, depending on material). This prevents unrealistic large plastic strains from developing in the material at very high temperatures where

the yield stress is very low. Note that isotropic hardening is frequently considered conservative to use, however, in certain cases where compressive residual stresses occur, it may be non-conservative to use. For instance, if the ID weld residual stresses were compressive, or for repair methods such as weld overlays where compressive stresses are used to prevent SCC from occurring, kinematic hardening may be considered more conservative for PWSCC growth. The effects of melting and re-solidification in metals subjected to high-temperature processes were treated by using the ‘anneal’ option in ABAQUS. When the temperature of a material point exceeds the annealing temperature, ABAQUS assumes that the material point loses its hardening memory. The effect of prior work hardening is removed by setting the equivalent plastic strain to zero. If the temperature of the material point falls below the annealing temperature at a subsequent point in time, the material point can work harden again. Depending on the temperature history, a material point may lose and accumulate memory several times, which in the context of modeling melting would correspond to repeated melting and re-solidification. The anneal temperatures for different materials are summarized in Appendix B. The boundary condition is constrained rigid body motion in normal direction at the end of nozzle end. This region is far away from the welding zone. While progressive annealing (used for instance in the VFT code [19]) may be physically more reasonable compared to the sudden approach in ABAQUS, the annealing feature does capture the appropriate effect.

3.1.4 Other issues

In many cases as with this study, computational weld models use the assumption of two-dimensional (2D) modeling because of the complexities of full moving-arc three-dimensional (3D) modeling. There are many cases where the 2D assumptions produce erroneous results. Numerous large-scale weld models have been analyzed in order to control weld distortions, residual stresses, and micro-structure. Appendix A and the references discusses many of these example problems and points out situations where full 3D solutions are desired compared with the 2D solutions often performed due to computational time constraints. Full 3D weld modeling is now possible and will become the rule rather than the exception in the future as computational resources continue to improve.

The constitutive laws used for all inlay analyses used classical plasticity theory with isotropic hardening. Isotropic hardening typically provides predictions that are larger in absolute magnitude compared with other hardening laws. Kinematic hardening tends to produce lower bound weld residual stress predictions. Mixed hardening within the Lemaitre-Chaboche framework [24], which is an option within ABAQUS, produces the most accurate predictions. However, for PWSCC crack growth assessment, it is possible that isotropic hardening may produce an over prediction (in absolute magnitude) of compressive residual stresses. This may reduce crack growth rates when the crack is growing through the compressive region and may possible result in arrest. Hence, there may be some cases where kinematic hardening may produce more accurate PWSCC growth.

Finally, phase transformation plasticity is a phenomenon which occurs in a number of ferritic steels, including A508. The thermal and thermal-mechanical processes associated with weld residual stress evolution during welding can be extremely complex. Rapid arc heating during welding produces a molten weld pool. The weld pool shape can be largely influenced by the

weld metal transfer mode and corresponding fluid-flow characteristics. On cooling, both rapid solidification within the weld pool and solid-state phase transformation in heat affected zones (HAZ) occur, depending on both peak temperature and cooling rate. The process becomes even more complicated in multi-pass welds. There are significant research activities on-going currently to address both the fundamental physics and numerical methods associated with these phenomena.

However, as far as WRS modeling is concerned, numerical procedures can be significantly simplified with adequate results. For residual stress predictions and distortion predictions, localized temperature distributions ranging from room temperature to above melting and structural restraint are of primary importance in determining the final residual stress state in a weldment. Considering an equivalent fusion profile in conduction-based heat flow solution techniques can ignore detailed weld pool phenomena. The material-melting behavior within the weld pool can be treated using phenomenological thermal-plasticity model within the continuum mechanics context (Brust et al, [25]). Here we briefly overview the numerical procedure for accounting for phase transformation effects within the framework of a computational weld model.

When the A508 nozzle steel adjacent to the weld is heated to a high enough temperature, which occurs near the weld/nozzle interface, the A508 reverts to austenite and becomes a face centered cubic (FCC) crystal. During cooling, at about 700C or so, the FCC changes phase to a body centered cubic (BCC), whereby the volume changes. Not only does the volume change, but there is an induced plasticity term associated with the expansion, cooling rate, and transformation kinetics. This can have a profound effect on the prediction of weld residual stresses. Reference [26] discusses applications of the Leblond model [27,28], which was developed to account for this phenomenon. For the inlay problem, this phenomenon would not be important unless one of the repairs were made near the interface, or partially within, the nozzle. The effect of phase transformation was not considered in this study.

3.1.5 Validations/verification

There is extensive validation of the computational weld models used for single material welds (see for instance [9,19,20]). However, for DM welds, there is little validation data at present. Figure 4 shows a comparison for the DM weld validation problem discussed in European NESC program [29]. This was a DM weld round robin problem where, after the entire weld was completed, it was post weld heat treated (PWHT). Therefore, modeling of the PWHT process was critical and proper creep constants for this are important. The measurements were made using neutron diffraction and it is seen that the predictions are reasonable, certainly given the uncertainty regarding the PWHT creep process modeling. There were also comparisons between predictions at other locations which were also satisfactory.

In addition, the computational weld models are beginning to be validated as part of joint NRC/EPRI mock-up program, but that validation data will not be finalized for some time. However, EMC2 does have a validation case for a DM weld safety nozzle performed for a European utility, which showed good comparison to measurements based on deep hole drilling.

However, that comparison is not yet available, but will be presented at the 2010 ASME PVP conference.

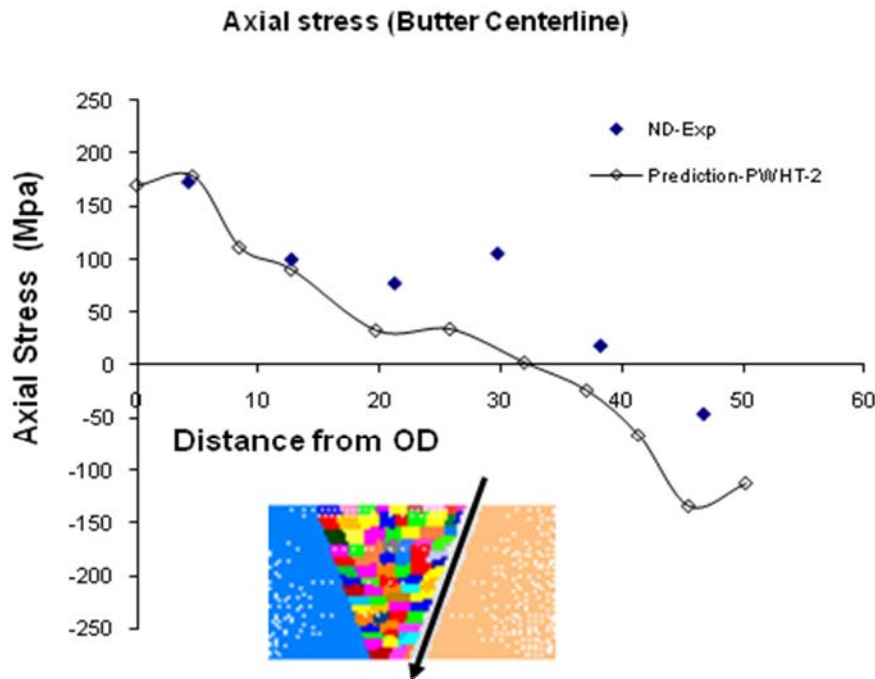


Figure 4 Axial residual stresses after welding, PWHT, and final machining is complete compared with neutron diffraction measurements (center of butter).

3.2 Modeling of Inlay

Figure 1 illustrates a typical inlay mitigation model that provides the current code case rules (which are being considered for approval). The ferritic nozzle steel, seen on the left in Figure 1, is usually an A516-70 or A508 type of steel, although other ferritic materials are used. This is clad with a stainless steel weld. Prior to the inlay application, the DM weld is made. Butter is applied to the nozzle steel, the Alloy 82/182 weld is deposited to the safe end, and then the safe end is welded to a section of stainless steel pipe in the field. The inlay PWSCC mitigation method consists of machining a section of the DM weld and material on each side of the weld, and Alloy 52 is deposited in the region that is machined. The Alloy 52 inlay is typically added for a distance of at least 1.5 mm below the pipe ID. This extra material is then machined to the actual pipe ID. At least two layers must be present after the final Alloy 52 machining step. The inlay itself must extend at least 6 mm beyond any of the Alloy 82/182 material in order to fully protect the susceptible material. The code case specifies temper bead deposition of the inlay to control micro-structure of the heat affected zone. The maximum heat input for the inlay temper bead deposition is currently specified to be 1.8 kJ/mm. Welding of the Alloy 52 material to the pipe is difficult. Large grains are produced which can migrate across different weld passes and micro-cracks can develop in the weld metal. The protective Alloy 52/152 layer, which has a higher chromium content compared to Alloy 82/182 (making it much less susceptible to PWSCC), must prevent fluid paths to the PWSCC susceptible Alloy 82/182 material. Hence,

micro-cracking in the inlay material is a potential concern that is dealt with by using careful temper bead welding.

3.2.1 Inlay weld process

This effort was designed to examine the effects of inlays for the purpose of mitigating PWSCC in DM welds in PWR nozzles. The first step in this analysis is to perform weld analyses of the inlay process for hot leg geometries. After this, flaw growth calculations will be made to ensure that the inlay is effective in mitigating PWSCC.

Two finite element models were developed for the inlay analyses. The geometries chosen and the inlay application are being developed to conform to inlay draft code case requirements (discussed above), including the temper bead procedure. Model 1 is identical to the case examined by AREVA in Document 81-9082202-000 (07-25-08), and Model 2 is a modification of the geometry used to produce the residual stresses that appear in the PRO-LOCA code [30]. Both are Type 3A DM weld hot leg geometries.

There are several key issues that make inlay modeling somewhat different from other DM weld models. First, the temper bead welding process for the inlays must be included. Second, the effect of phase transformation plasticity may need to be included (in later analyses) since the inlay only deposits a small layer of material along the length of the nozzle steel (this was neglected here). Finally, the three-dimensional nature of the weld is not considered.

3.2.1.1 Inlay weld model 1

Figure 5 illustrates the weld model for the case examined by industry in the code case support analyses. This geometry is referred to as Model 1. As seen, a rather long section of nozzle is included but this is not important since boundary conditions prescribed at different locations along this length result in minimal differences in residual stresses. As seen in Figure 5, A508 nozzle material (orange color) is clad with 304 stainless steel prior to the DM weld. The DM weld was deposited in 19 passes to a 316 stainless steel safe end. (The results presented here actually combined the first two passes, so there were 18 DM weld passes deposited). The deposition of the butter layer, followed by post weld heat treatment (PWHT) was not considered here since prior experience shows that it has little effect on the weld residual stresses in the DM weld region. The PWHT tends to remove most residual stresses induced by the butter process.

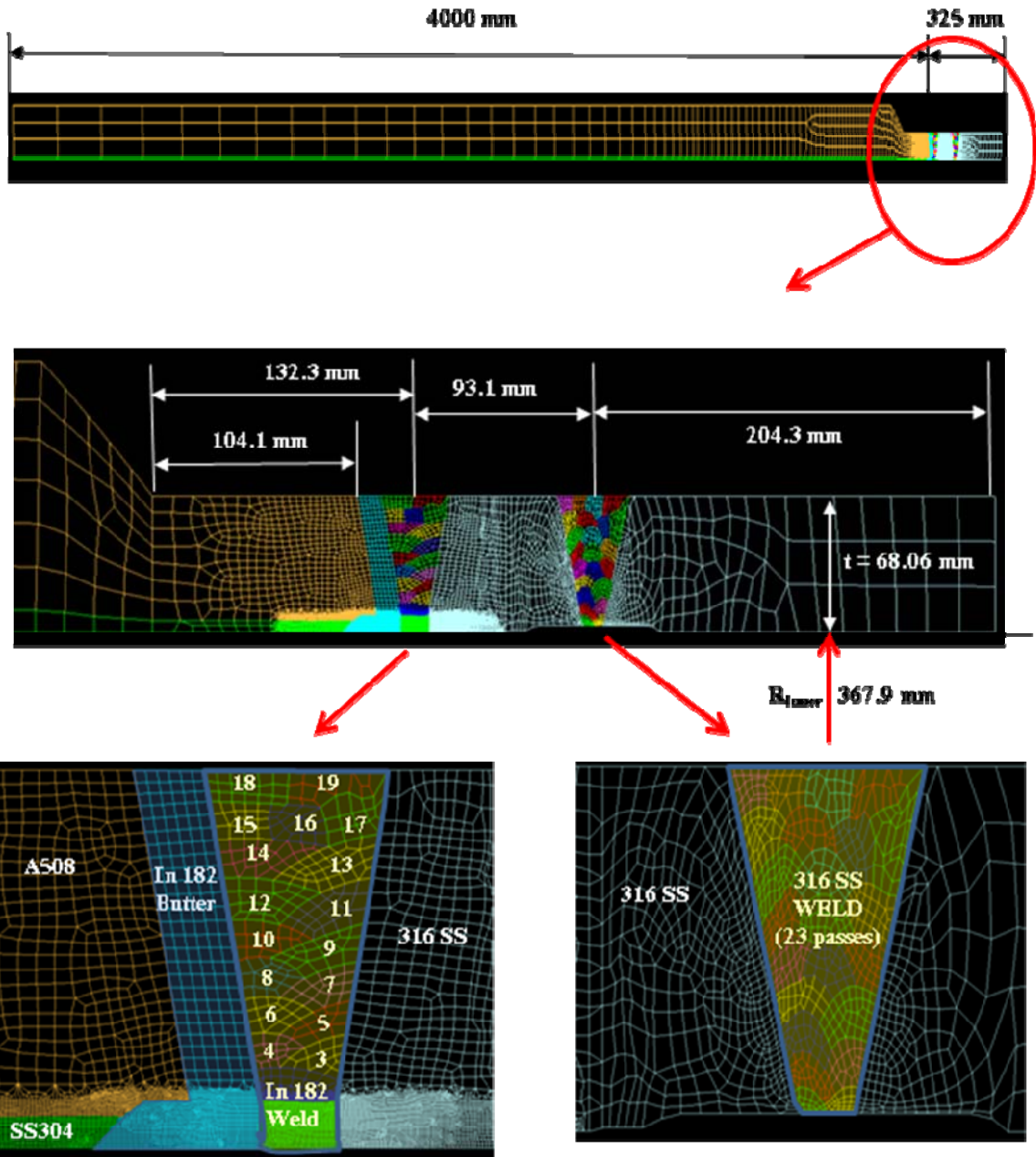


Figure 5 Weld model for the dissimilar metal weld (DMW) and stainless steel (SS) safe end welds. The weld passes are shown in different colors.

Figure 6 illustrates one of the weld repairs modeled for this case. A 50% region of material was removed from both the Alloy 82/182 butter and weld as seen in the top of Figure 6. Such a deep repair produces considerable tensile weld residual stresses along the pipe ID. Such a deep repair

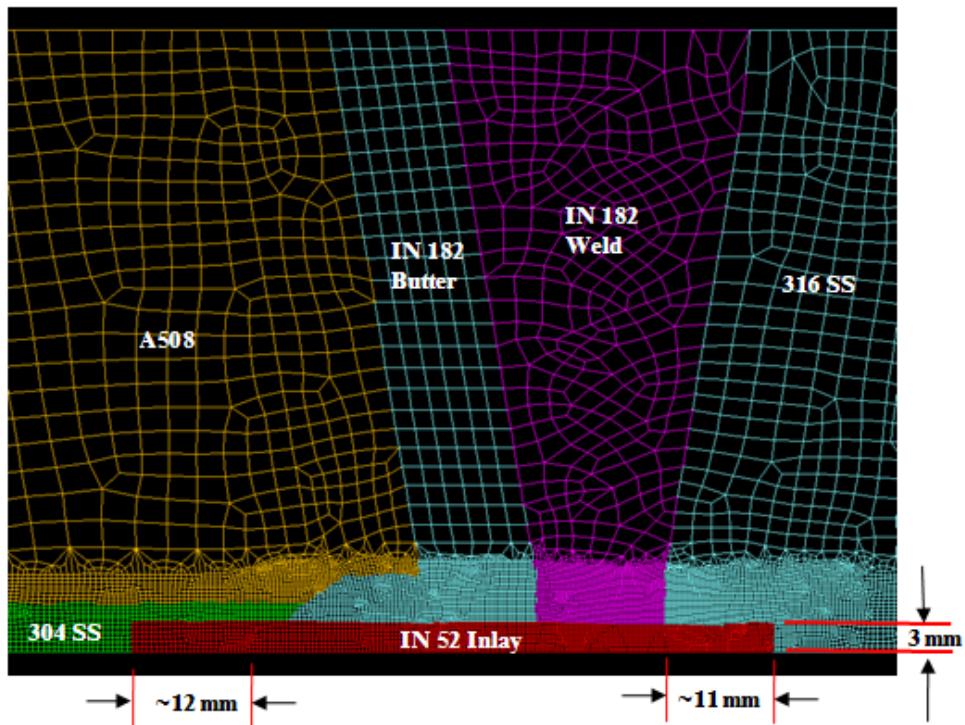
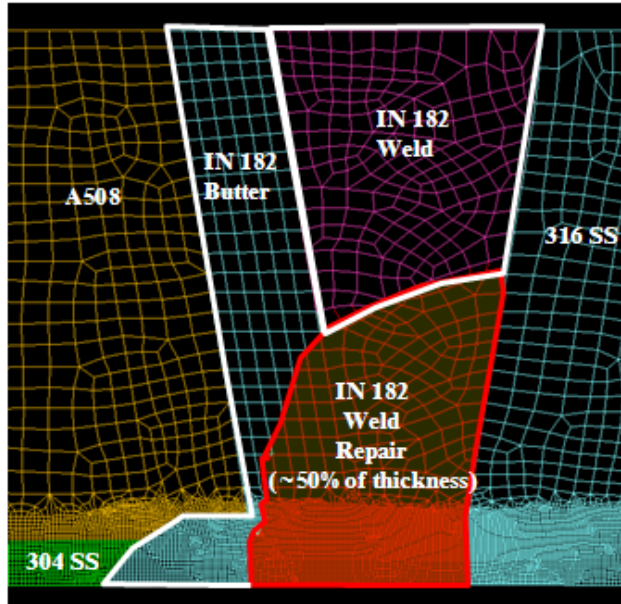


Figure 6 Weld repair model definition (top) which consisted of removing material to about 50% of the thickness and re-depositing in 12 passes. The bottom Figure shows the inlay mesh and model along with dimensions after final machining.

is considered to produce a conservative (highly tensile) weld residual stress state prior to the SS weld. The repair shape, which is a little irregular, does not matter much in defining the final residual stress state. It is also noted that repairs may occur entirely in the weld and butter,

partially in the weld and nozzle steel, or partially in the weld and the stainless steel. Here the repair was entirely in the weld and butter. Sensitivity studies performed recently, some of which are presented in Appendix C for repairs in the weld and butter alone, suggest that the repair depth is most important. The effect of repairs being made partially in the nozzle or stainless steel safe-end should be looked at in the future.

Next, the stainless steel weld is deposited in 23 passes (Figure 5) to a section of 316 stainless steel pipe. It is interesting to note that this stainless steel weld provides an important beneficial effect on the axial and hoop weld residual stresses that develop in the vicinity of the DM weld along the pipe ID. The radial shrinkage of the stainless steel weld acts in a similar manner as the mechanical stress improvement process (MSIP) if the weld is close enough to the DM weld. Here (Figure 5), the centerline to centerline distances between the DM and SS welds is about 93 mm, which is well within the beneficial range. It is noted that the VC Summer plant did not have this stainless steel safe end weld which may have contributed to the cracking in the hot leg pipe. Finally, as seen in the bottom of Figure 6, the inlay region is machined out and the Alloy 52 inlay material is deposited in three layers. After deposition of the three layers, the inlay material extends 1.5 mm below the original pipe ID. The final step consists of machining this 1.5 mm layer.

The inlay modeling procedure is fully described in Figure 7 and Figure 8 with a series of eight steps for Model 1. Example stresses are shown here, but are described in more detail later. In Step 1 of Figure 7, the original DM weld is made. The effect of modeling the butter and post weld heat treat (PWHT) prior to the deposition of this DM weld was omitted here. Step 1 shows the DM weld area in red, which is the weld fusion zone from the weld model. Step 2 shows the removal of the weld repair material in gray. The repair weld was deposited in 12 passes.

Step 3 shows the axial weld residual stresses after completion of the weld repair. The stress contours are shown in MPa in the scale in Figure 7. Tensile axial residual stresses appear on the pipe ID at the location of the DM weld. These high stresses are driven by the weld repair. Step 4 shows the effect of the hydro-test application to the safe end. A pressure equivalent to 1.25 times the operating pressure of 15.5 MPa is applied and released. From Figure 7, it is seen that the hydro-test application slightly reduces the axial weld residual stresses.

Step 5 in Figure 7 shows the axial weld residual stresses after application of the stainless steel safe end to pipe weld. The weld lines are drawn in the Step 5 figure for both DM and SS welds. It is seen that the stainless steel weld reduces the axial stresses in the region of the DM weld.

Figure 8 (Step 6) shows the axial weld residual stresses after deposition of the three inlay layers. These three layers were deposited using 137 passes. The final layer, which extends 1.5 mm below the pipe ID, is evident here. Note that a rather significant length of tensile weld residual stresses occur along the entire inlay region for a distance above the inlay along much of the pipe ID and at the DM weld location. It is seen from Figure 5 that a very fine mesh was required in this region to capture the weld residual stress pattern correctly. Clearly, while the inlay material is resistant to PWSCC compared to the Alloy 82 material, the weld residual stresses produced are tensile. This will have an important impact on inlay effectiveness.

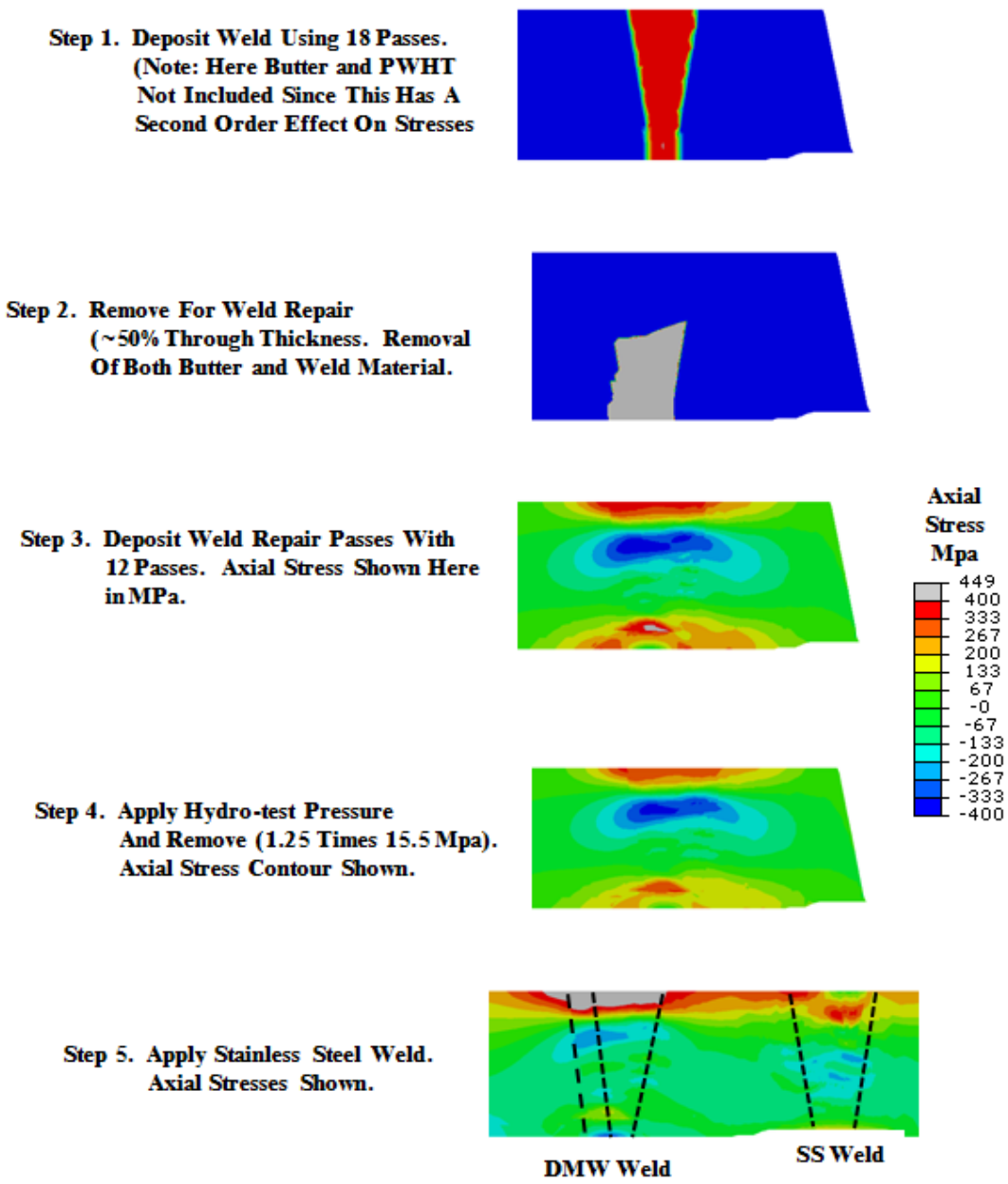


Figure 7 Weld modeling steps for inlay. Steps through deposition of the SS weld. This is for Case 1 of Table 1, which had a 50% pre-service repair (see Section 3.2.3).

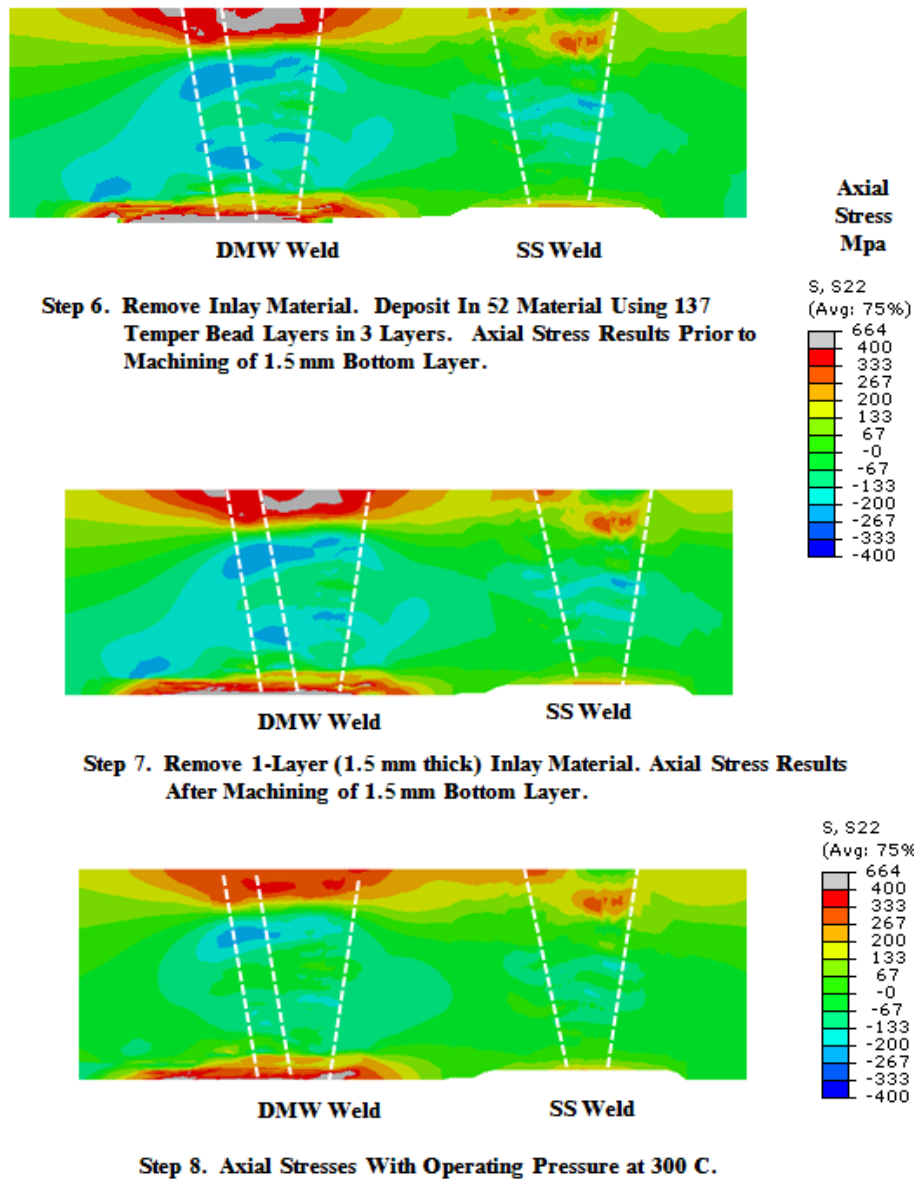


Figure 8 Inlay modeling steps 6 to 8 and some axial stress results. This is for Case 1 of Table 1, which had a 50% pre-service repair (see Section 3.2.3).

Finally, Steps 7 and 8 of Figure 8 show the axial weld residual stress pattern after removal of a 1.5 mm region of the inlay, and at operating pressure and temperature (300 C) conditions.

3.2.1.2 Inlay weld model 2

The second model chosen for inlay analysis is for a hot leg geometry that was used to produce the weld residual stress distributions that appear in the PRO-LOCA code in Reference [30]. This geometry is quite a bit thicker than the model analyzed above (~86 mm versus 68 mm). The original PRO-LOCA hot leg model is shown at the top of Figure 9. The original model used A516-70 material for the nozzle and a machined region under the Alloy 82/182 DM weld.

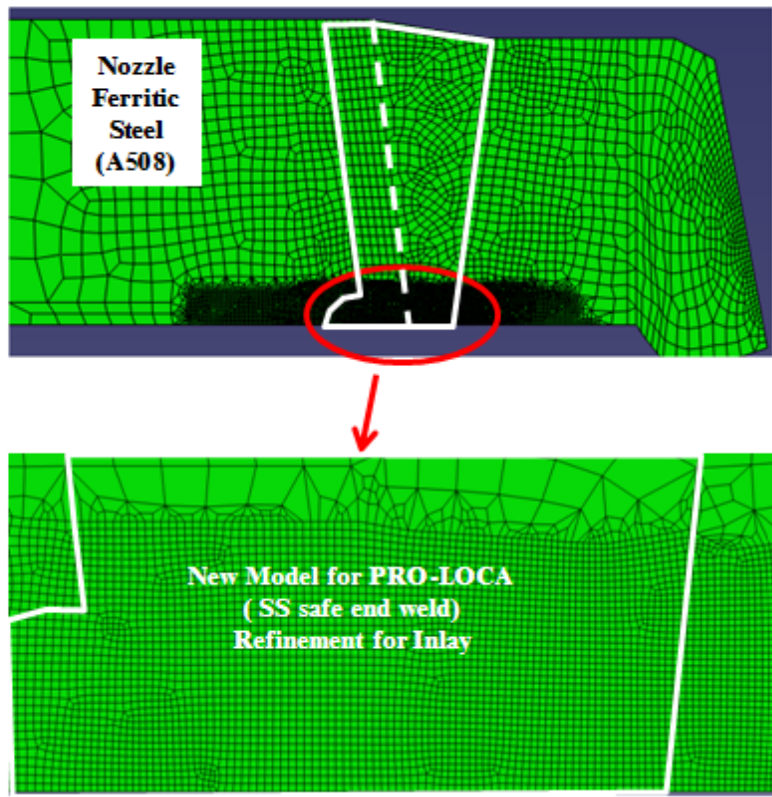
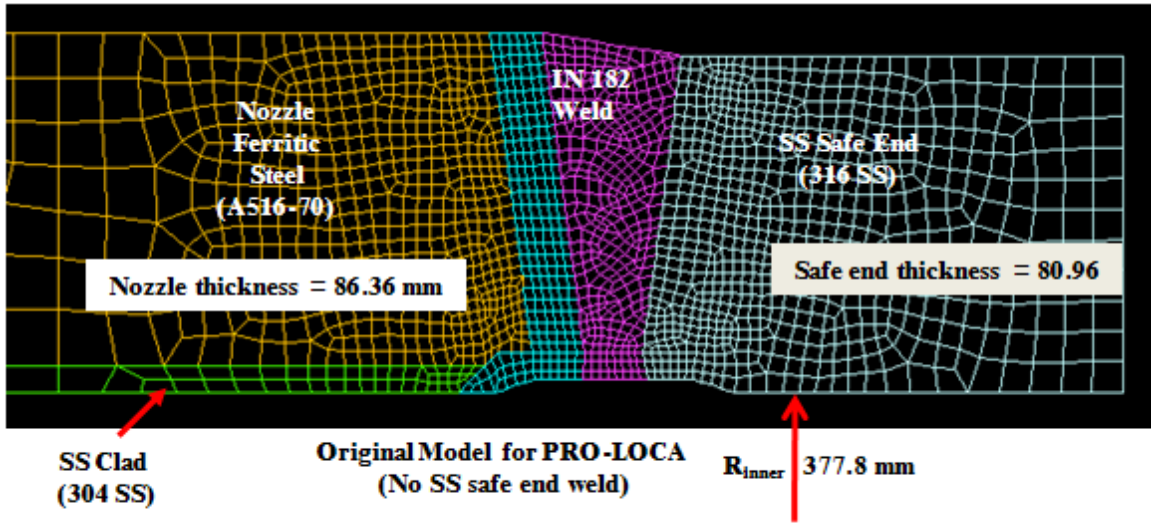


Figure 9 Model and dimensions for second inlay analysis. This model is identical to the geometry used to produce the PRO-LOCA residual stress distribution for the hot leg.

The hot leg Model 2 considered in this report is shown in Figure 9. The inlay model considered here also included a safe end weld. Other inlay models will be analyzed using this same

geometry, but will not include the safe end weld. The full inlay model is seen in Figure 10. It has the slight offset between the nozzle and the stainless steel pipe as often seen in practice. However, we have observed that this offset has little effect on the DM weld residual stresses.

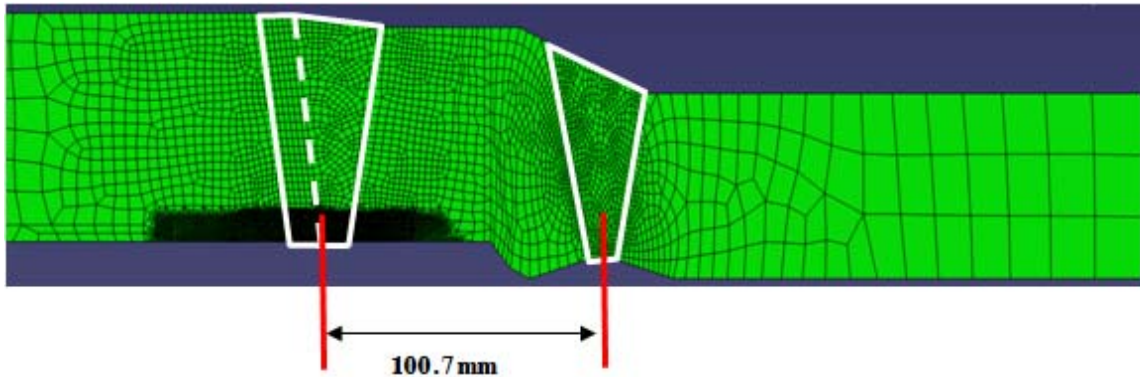


Figure 10 Full hot leg model for inlay model number 2.

Before presenting the inlay results for Model 2 (Section 4.2) it is useful to compare the weld residual stresses predicted here with those produced several years ago for this model [30]. These are nearly identical models except the nozzle materials were different (A516-70 for the original model and A508 for Model 2). The material property differences between A516 and A508 are small. Figure 11 compares the axial weld residual stresses after the DM weld is completed between the original model and Model 2 (before application of the inlay). This is after the hydro-test and release, at room temperature. This figure illustrates that despite a large difference in mesh refinement, the final results are quite close. Note also that the new analysis, which used an extremely fine mesh in the area where the inlay will be subsequently deposited, did not alter the results significantly. Therefore, the mesh refinement used in the past is adequate for weld analyses.

3.2.2 Temper bead welding

Figure 12 illustrates the temper bead weld process. Because Alloy 52 weld material is difficult to weld, the temper bead process is used, as specified in the code case. As the weld bead is deposited and cools, there are several temperature ranges that the base metal and prior weld metal (for passes which are deposited on or near previously deposited passes) experience. The material closest to the molten weld bead, which experiences temperatures to about 1050 C, tends to lead to a coarse grain heat affected zone (HAZ) structure. Beyond this, to about 900 C, a fine grained HAZ structure develops. Figure 12 also shows the inter-critical and sub-critical zones as well. The sizes of these zones depend on weld heat input and the corresponding cooling rates.

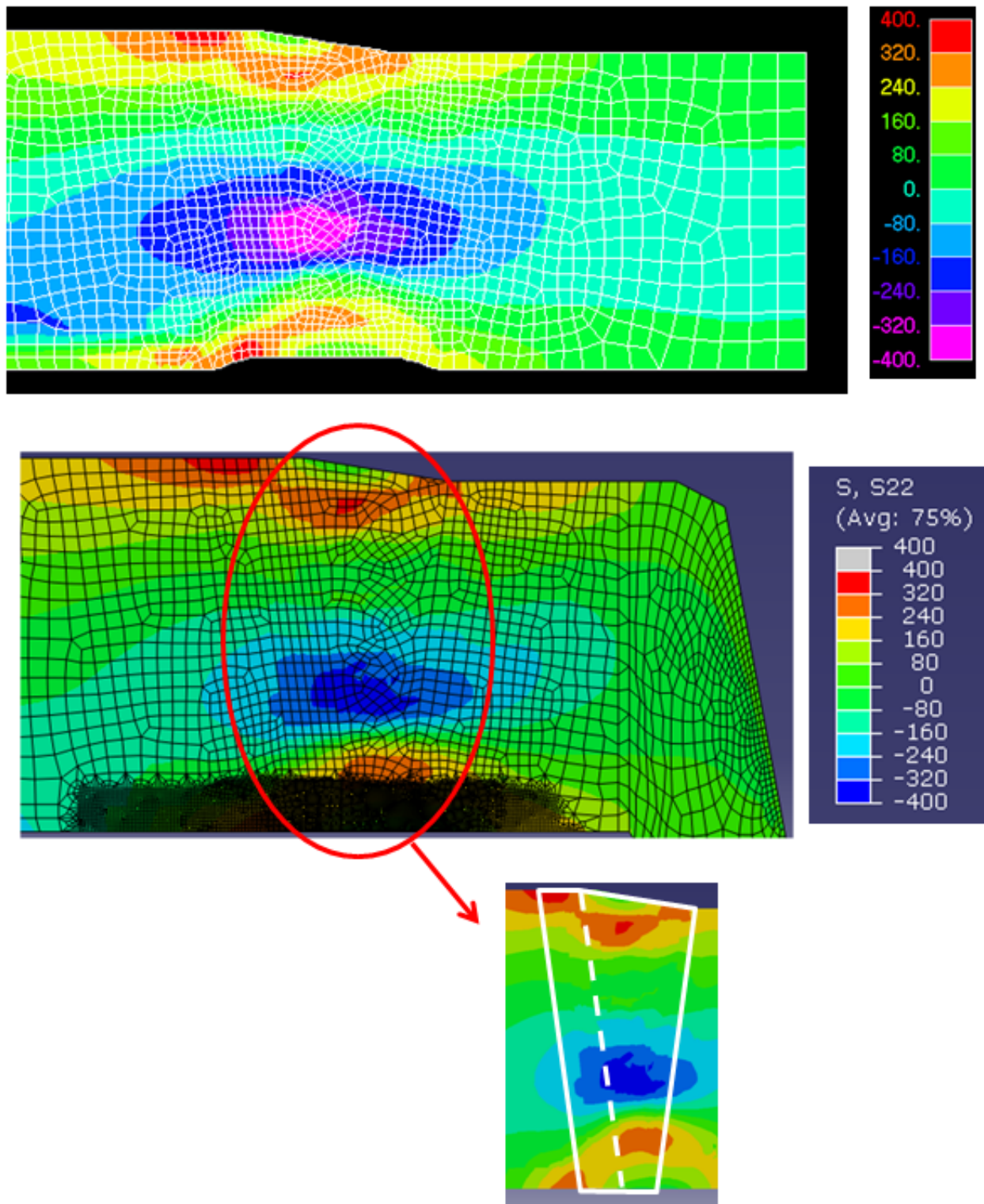


Figure 11 Comparison of axial weld residual stresses from original model [30] and the new Model 2. These results are after repair weld of 12% of the thickness with no stainless steel weld or inlay applied. Top model is the original model.

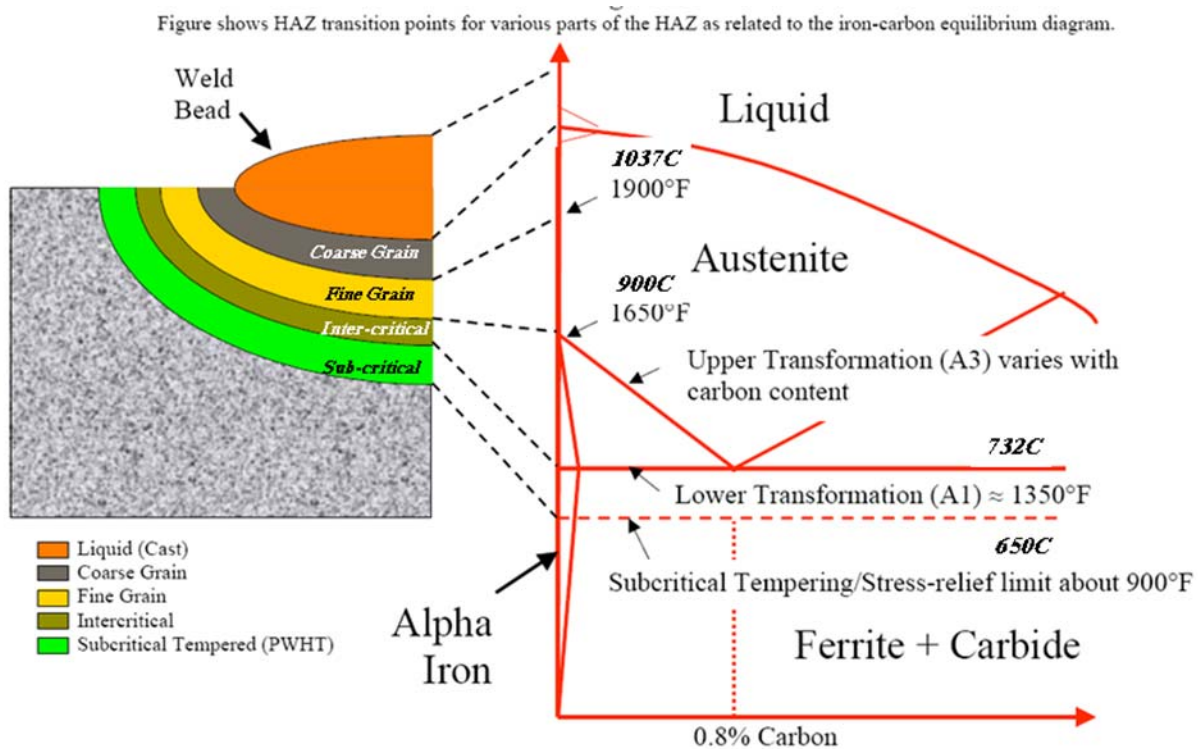


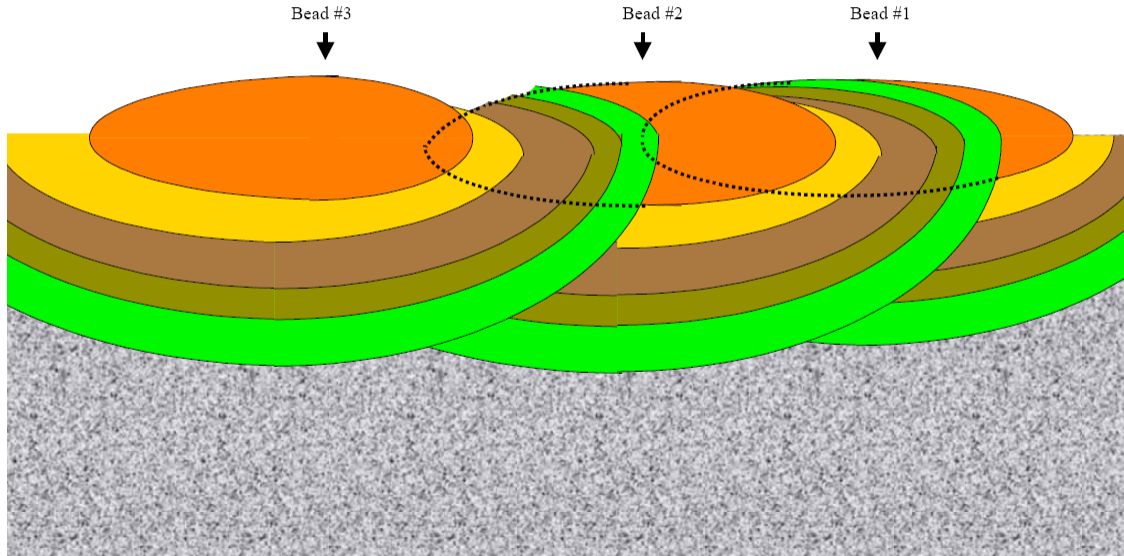
Figure 12 Temper bead weld metallurgy

Figure 13 illustrates how additional weld beads ‘temper’, or can be used to control the microstructure of the HAZ regions for the base and weld materials. One can see that the coarse and fine grained HAZ regions can be controlled by the temper bead process. In general the temper bead process utilizes small weld passes and low heat input. Modeling this effect in a three dimensional weld model poses no difficulties since the heat inputs (amps, volts, torch speed) are simply input. However, modeling this in a two dimensional model is more of a challenge since two dimensional effects are somewhat artificial. Here we attempted to keep the weld melt zone about 5 to 10% (maximum) beyond the molten deposited metal. Also, two heat input ranges for the temper bead welding were considered. For Model 1, the effect of heat input on the weld residual stresses after cool down (room temperature) are compared in Figure 14.

This figure presents line plots of weld residual stresses through the pipe thickness at the weld centerline and along the butter – weld interface for different heat inputs. It is clearly seen that the higher the heat input used for the inlay temper bead weld process, the lower the magnitude of weld stresses produced. However, the spatial distribution is very similar. The weld residual stresses are mainly affected in and near the inlay region. The weld residual stresses are very similar except that the lower heat input case produces stresses that are lower in magnitude. Also shown in Figure 14 are line plots of weld residual stresses predicted independently by another organization for code case support. The code case analysis used kinematic hardening but the actual heat input used is not known. The comparison of the solutions indicates the results between the analyses are similar. Note that isotropic hardening, used here, tends to predict the pass to pass stress fluctuations more so than kinematic hardening. Also, kinematic hardening tends to produce lower bound results.

This figure shows the effect of overlap of subsequent beads on the extent of the heat affected zone of the previously deposited bead. The dotted lines show the previous weld bead locations

Note that the middle bead overlaps the right-hand bead by about 50% of the bead width, and that the remaining heat-affected zone of the first bead is much smaller than the remaining heat-affected zone of the middle bead. The left-hand bead overlaps the middle bead by about 10%, resulting in very little effect on the heat-affected zone of the middle bead.



Effect of the second layer of weld metal on the weld metal and heat-affected zone of the first layer. The dashed oval shows the location of the first bead. Note the untempered heat-affected zone at the arrow. The technique for tempering of this zone is shown below.

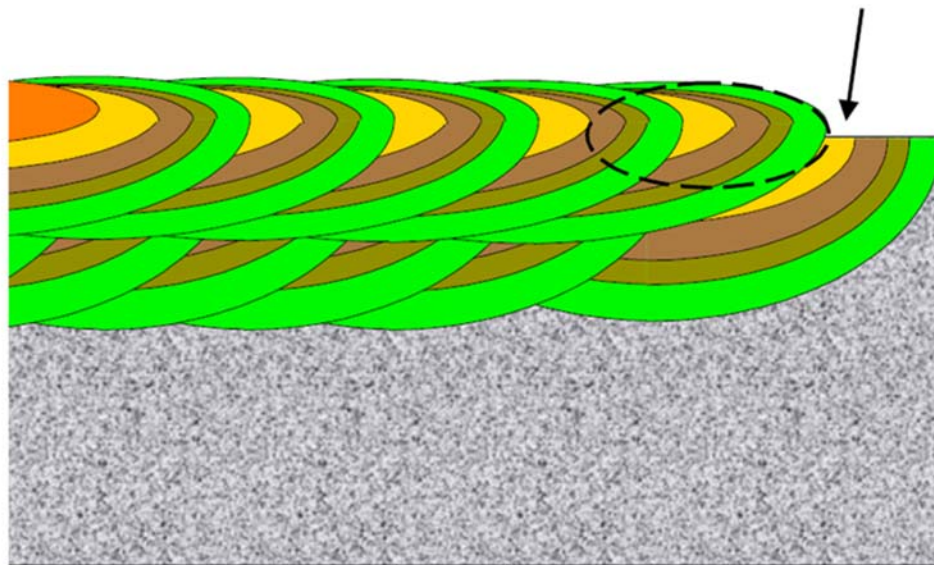


Figure 13 Overlapping weld beads and tempering.

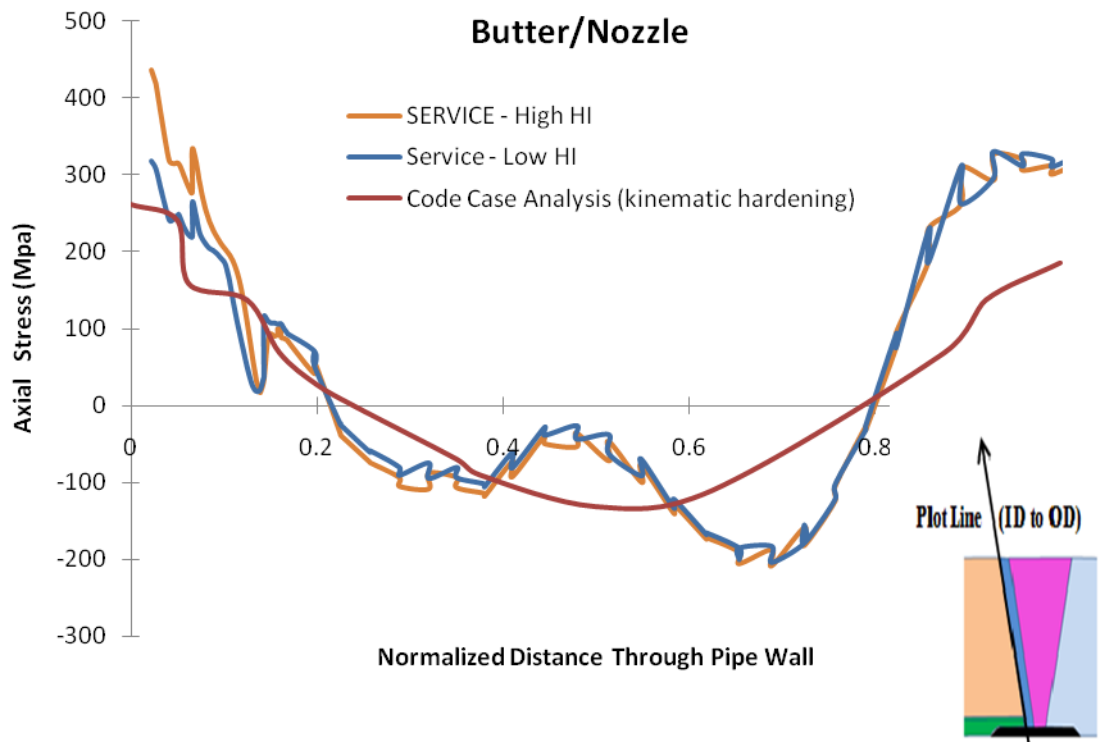
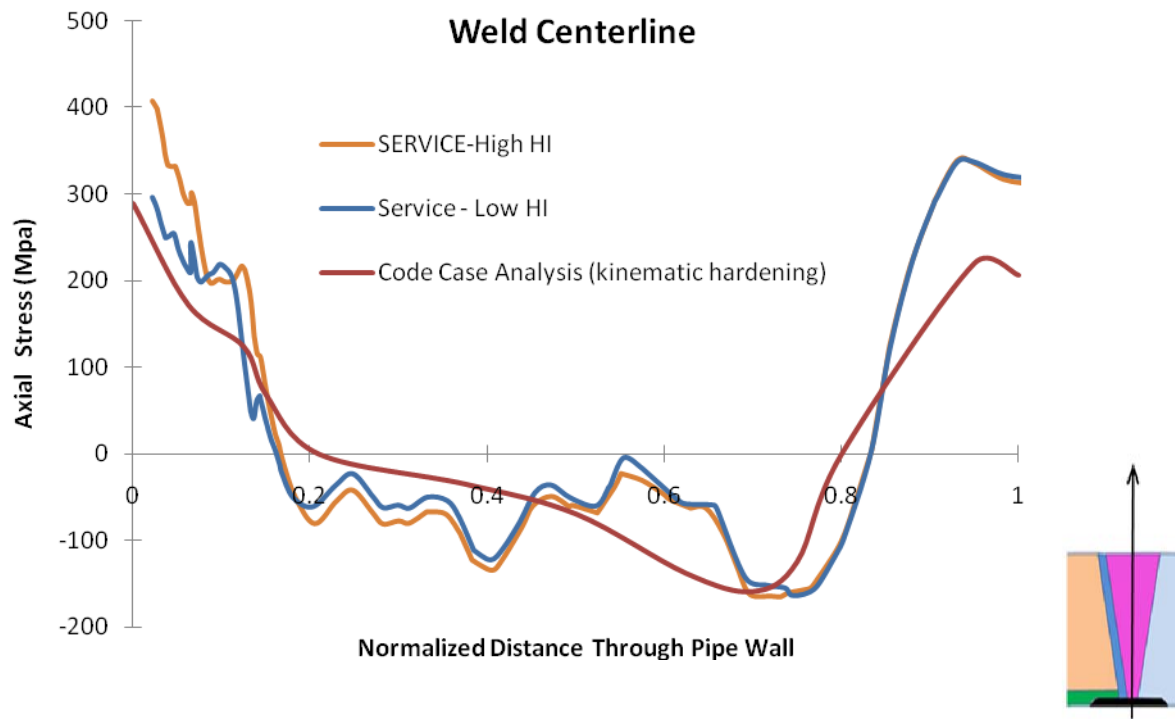


Figure 14 Weld residual stresses for inlay temper bead welds – heat input effect.

3.2.3 Cases studied and description

There were a number of weld analysis cases considered for each hot leg geometry in this study. Moreover, using these weld residual stress analyses results different crack growth analyses were performed, which will be discussed later. A complete listing and description of the welding residual stress results are given in Appendix C.

Table 1 Weld Residual Stress Analysis Cases Considered for Model 1

WRS Case #	WRS case	Inlay depth	Comments
1	50% pre-service repair	3mm	DMW-50% Repair-SS Weld- Inlay
2	50% PWSCC repair	3mm	DMW-SS Weld-50% Repair-Inlay
3	75% (2-inch) pre-service repair	3mm	DMW-75% Repair-SS Weld- Inlay
4	75% (2-inch) PWSCC repair	3mm	DMW-SS Weld-75% Repair-Inlay
5	50% preservice-75%PWSCC repair	3mm	DMW-50% Repair-SS Weld- 75% Repair- Inlay
6	50% pre-service repair	6mm	DMW-50% Repair-SS Weld- Inlay
7	50% PWSCC repair	6mm	DMW-SS Weld-50% Repair-Inlay
8	50% pre-service repair – No SS Weld	None	DMW-50% Repair*
9	50% pre-service repair –SS Weld	None	DMW-50% Repair-SS Weld*
10	Pre-existing flaw cases	3mm	Deep embedded OD flaw and embedded flaw near ID*
11	50% pre-service repair	3mm	DMW-50% Repair-SS Weld- Inlay* Cast Stainless Steel Properties

*Results only in Appendix C

Two general weld analysis cases were considered here with two distinct types of repairs. The first is called a *pre-service repair*. This type of repair considers the original DM weld, a repair, followed by the stainless steel weld, and then the inlay application. The second type of repair is called a *PWSCC repair*. This is defined as a repair that occurs after the stainless steel weld, but prior to the inlay application. For Model 1 (Figure 5), the different inlay weld analysis cases are listed in Table 1. The weld residual stress analyses performed for Model 2 (Figure 10) are shown in Table 2.

Table 2 Weld Residual Stress Analysis Cases for Model 2.

WRS Case #	WRS case	Inlay depth	Comments
1	12% pre-service repair	3mm	DMW-12% Repair-SS Weld- Inlay
2	12% preservice-12%PWSCC repair	3mm	DMW-12% Repair-SS Weld-12% Repair-Inlay
3	12% PWSCC repair	3mm	DMW-SS-12% Repair-Inlay
4	50% pre-service repair	3mm	DMW-50% Repair-SS-Inlay
5	50% PWSCC repair	3mm	DMW-SS-50% Repair-Inlay
6	25% pre-service repair	3mm	DMW-25% Repair-SS-Inlay
7	25% PWSCC repair	3mm	DMW-SS-25% Repair-Inlay
8	12% repair – No SS weld	None	DMW-12% repair – No SS weld*
9	25% repair – No SS weld	None	DMW-25% repair – No SS weld*
10	50% repair – No SS weld	None	DMW-50% repair – No SS weld*
11	12% repair –SS weld	None	DMW-12% repair – SS weld*
12	25% repair – SS weld	None	DMW-25% repair – SS weld*
13	50% repair – SS weld	None	DMW-50% repair – SS weld*

*Results only in Appendix C

4 Weld Residual Stress Results

The inlay weld residual stresses for both Model 1 and Model 2 for the cases listed in Table 1 and Table 2, respectively, are presented in this section. Only the cases relevant to the flaw evaluations are summarized here. For completeness, all welding residual stress results are summarized in Appendix C.

4.1 Model 1 Weld Residual Stress Results

The first case considered is Case 1 in Table 1 which is a 50% pre-service repair with the inlay applied. This case will be presented in some detail while only key results of some of the other similar cases will be presented. The axial weld residual stresses after deposition of the full three inlay layers are shown in Figure 15. The top illustration shows the stresses for a large region of the DM weld and the stainless steel weld. It is seen that the stresses in the DM weld region go from a high value of tension at the region of the inlay, through a compression zone in the middle of the DM weld, to tension at the ID. The axial weld residual stress zone in the inlay region extends over nearly the entire inlay region. The lower illustration in Figure 15 shows details of the axial weld residual stresses after deposition of all three inlay layers. The white lines illustrate the boundaries of the nozzle material, the Alloy 82/182 butter and weld material, the stainless steel safe end, and the Alloy 52 inlay material (outlined with dash lines separating the first two layers from the third layer.) The butter near the left side of the lower illustration is seen to undercut the nozzle material as is typical in DM welds. The required mesh refinement is evident. The inlay was deposited with 137 passes to properly model the effect of the temper bead weld procedure.

The hoop weld residual stresses after deposition of the full three inlay layers are shown in Figure 16. Again, the top illustration shows the stresses for a large region of the DM weld and the

stainless steel weld. It is seen that the hoop stresses in the DM weld region are quite high at the region of the inlay. As with axial weld residual stresses, the hoop weld residual stress zone in the inlay region extends over nearly the entire inlay region. The lower illustration in Figure 16 shows details of the hoop weld residual stresses after deposition of all three inlay layers.

The axial weld residual stresses prior to, and after machining the third inlay layer are compared in Figure 17 (room temperature). It is seen that the axial stress transfer after machining actually increases the stress very near the ID of the pipe. The large axial tensile stresses in the inlay could help initiate and grow micro-cracks in the Alloy 52 inlay. This effect will be studied Section 5 where PWSCC is modeled.

Finally, weld residual stress contour plots are presented in Figure 18 and Figure 19 for the inlay at service conditions (15.5 MPa pressure, temperature = 300C). Figure 18 presents axial stresses and Figure 19 presents hoop stresses. It is important to emphasize that proper prediction of weld residual stresses for inlay PWSCC mitigation cannot be made without a very fine mesh. For these predictions isotropic hardening and axis-symmetry assumptions were used. The Alloy 52 material was modeled using Alloy 82/182 properties since material properties Alloy 52 material were not available at the time. However, it is now known that the stress-strain curves for Alloy 182/82 and Alloy 152/52 are very similar and only differ slightly at room temperature. The comparison is shown in Appendix B.

Finally, it is noted that ABAQUS was used for these predictions. Since the Alloy 182/82 material and Alloy 52/152 material are different, the modeling approach required careful attention to when the different materials were deposited, removed, and re-deposited. Since one cannot change material definitions within ABAQUS, it was necessary to define two sets of elements (over lapping) with the identical nodes. Each element set was assigned a different set of properties and removed/activated when necessary.

The contour plots of weld residual stresses for the other cases considered in Table 1 will not be shown here since only the line plots are important for the PWSCC assessment.

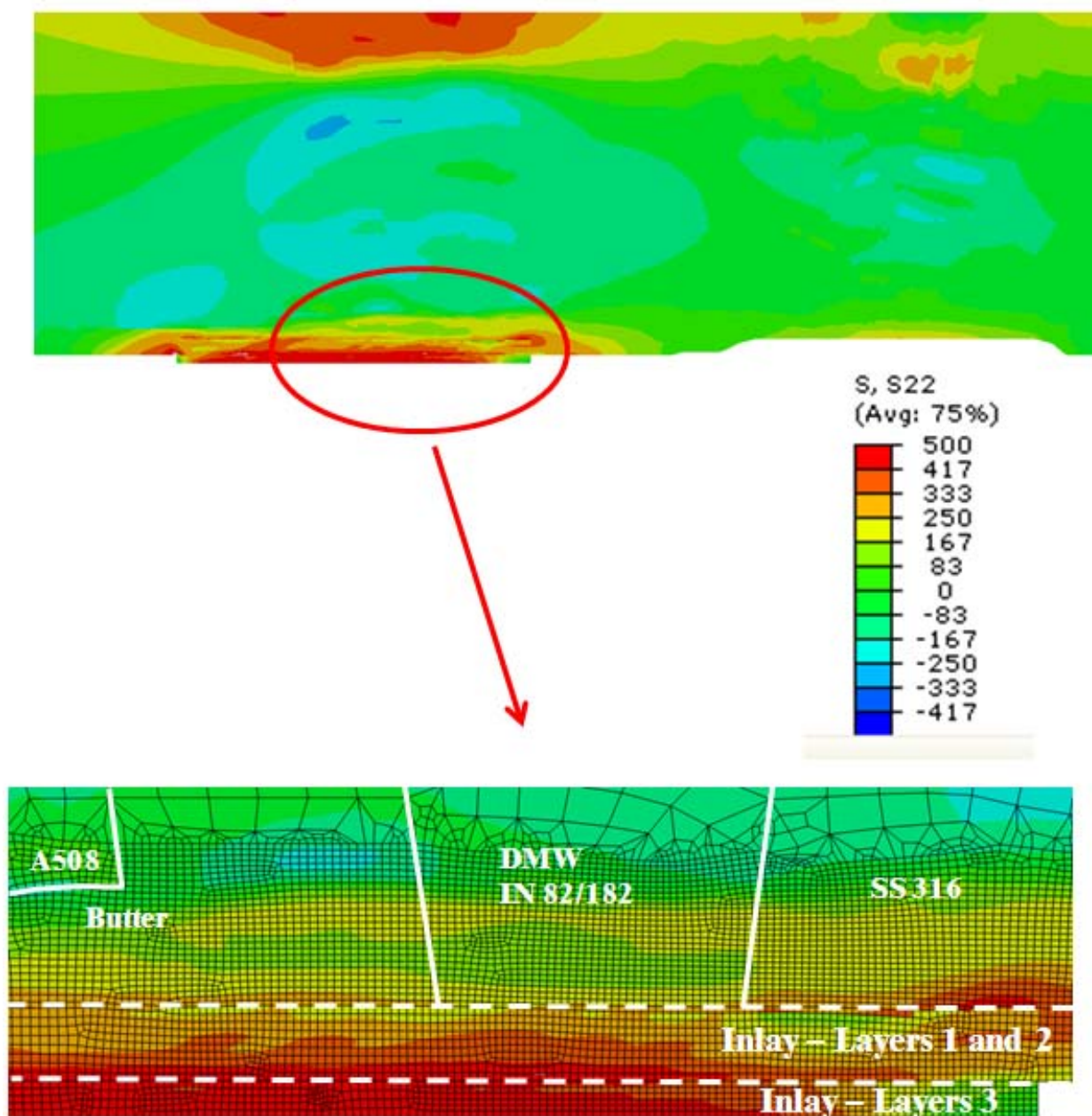


Figure 15 Axial weld residual stresses after deposition of the Alloy 52/152 inlay but prior to machining Layer 3 of the inlay. The top illustration shows a global view of the stress pattern at the DM and SS weld regions. The bottom illustration shows the stresses with the mesh refinement shown near the DMW weld.

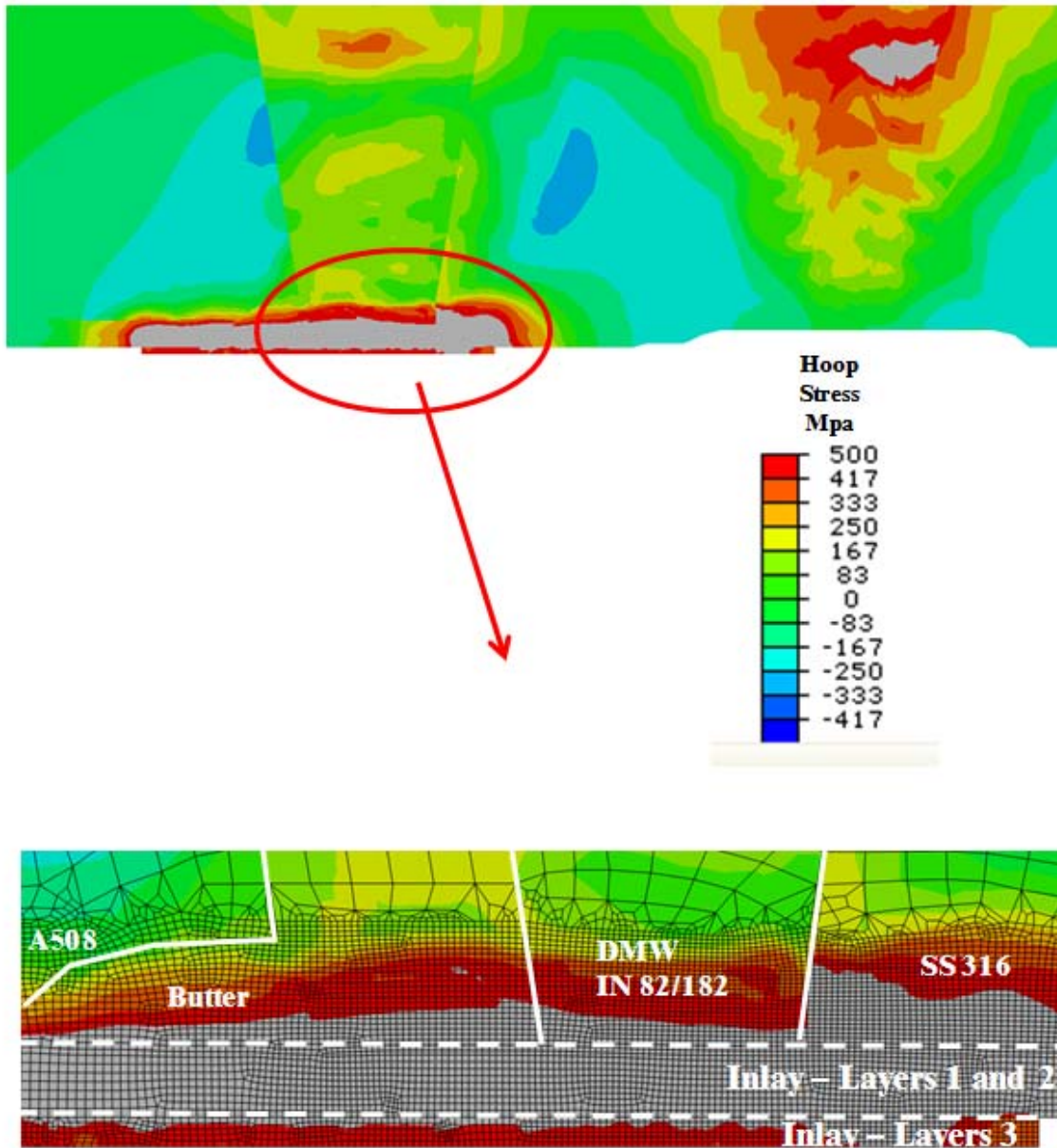


Figure 16 Hoop weld residual stresses after deposition of the Alloy 52/152 inlay but prior to machining Layer 3 of the inlay. The top illustration shows a global view of the stress pattern at the DM and SS weld regions. The bottom illustration shows the stresses with the mesh refinement shown near the DM weld.

(a) Prior to Machining

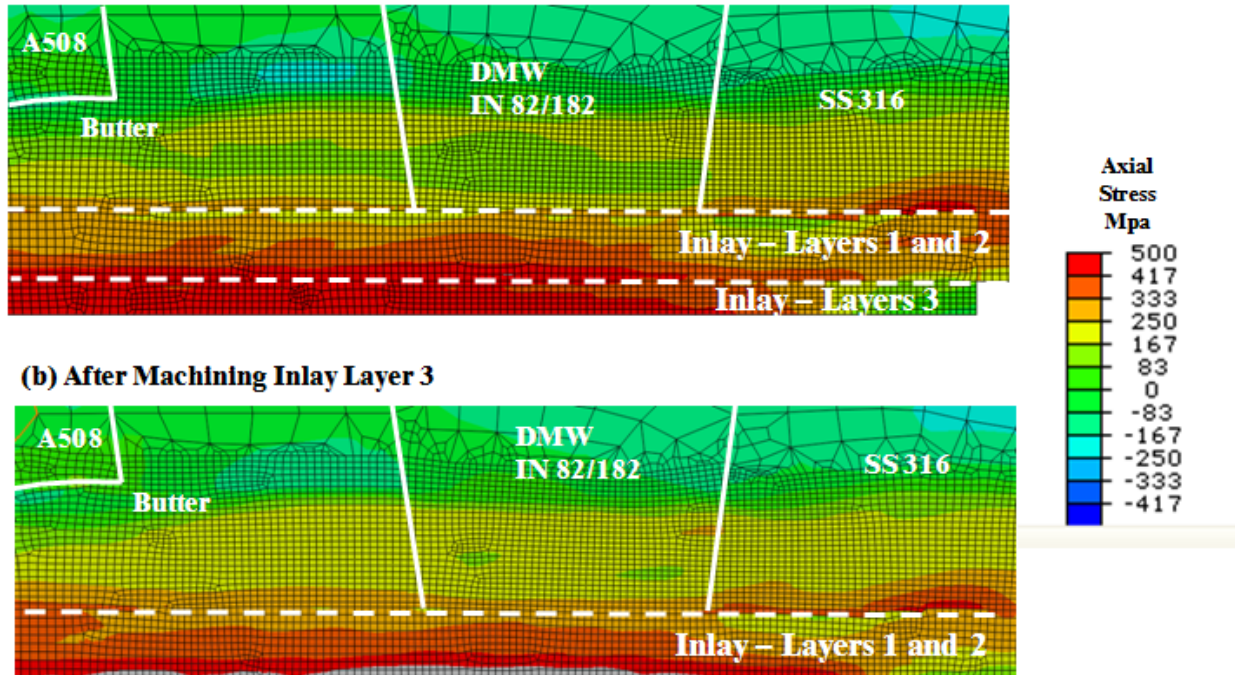


Figure 17 Comparison of axial weld residual stresses before and after machining of inlay layer number 3.

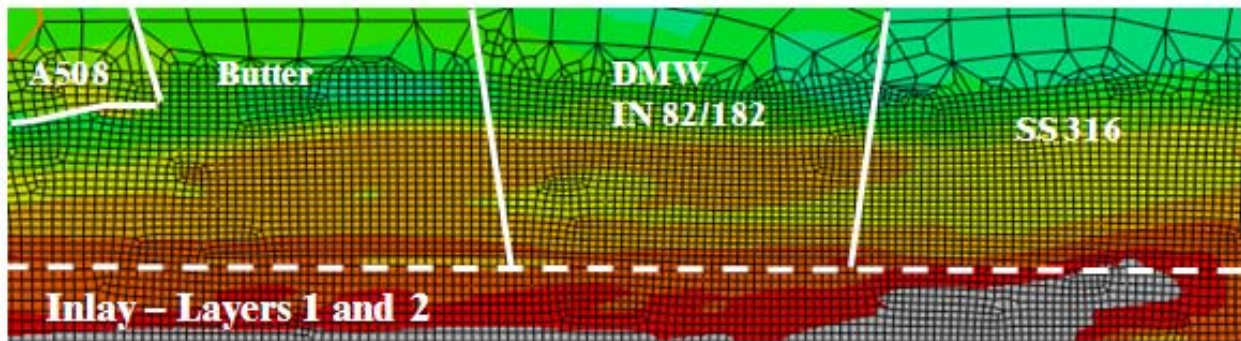
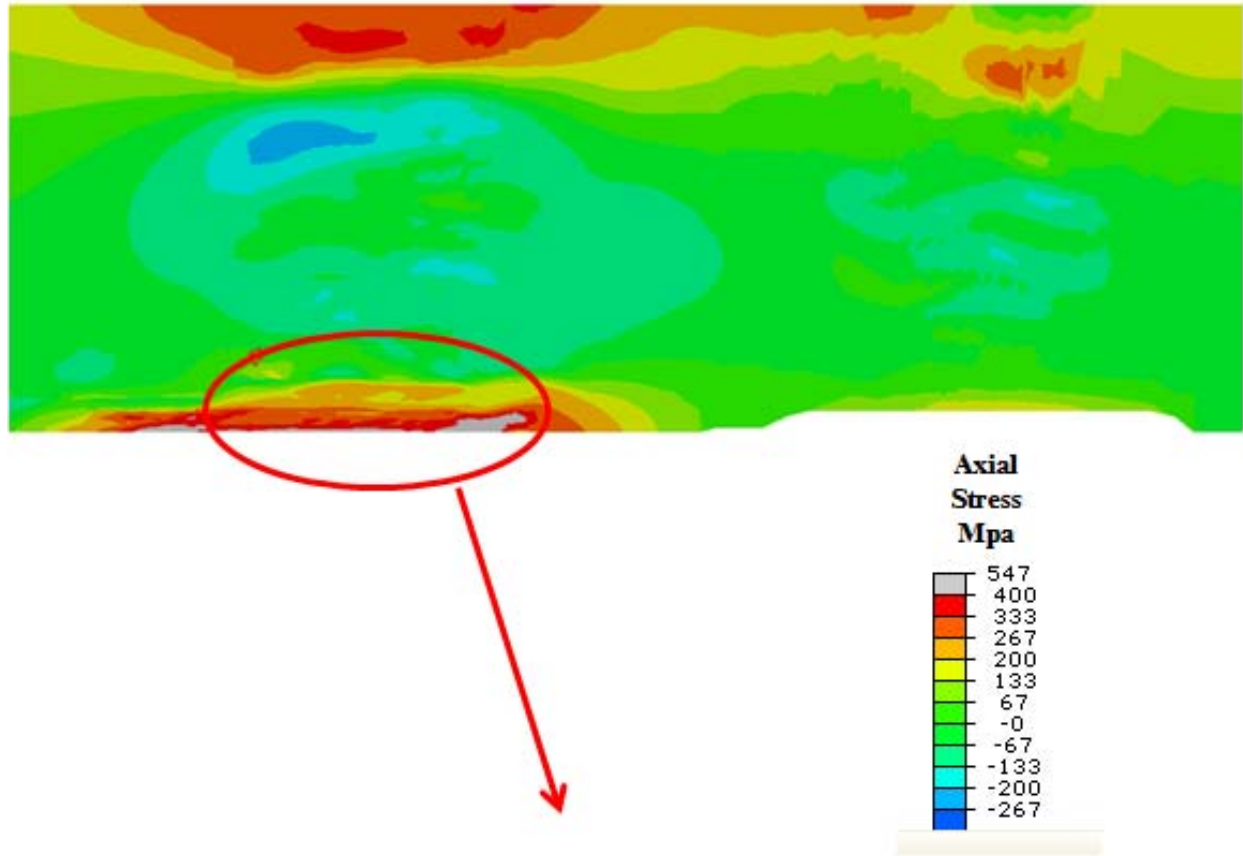


Figure 18 Axial weld residual stress in inlay repair at service conditions (15.5 MPa pressure and 300C).

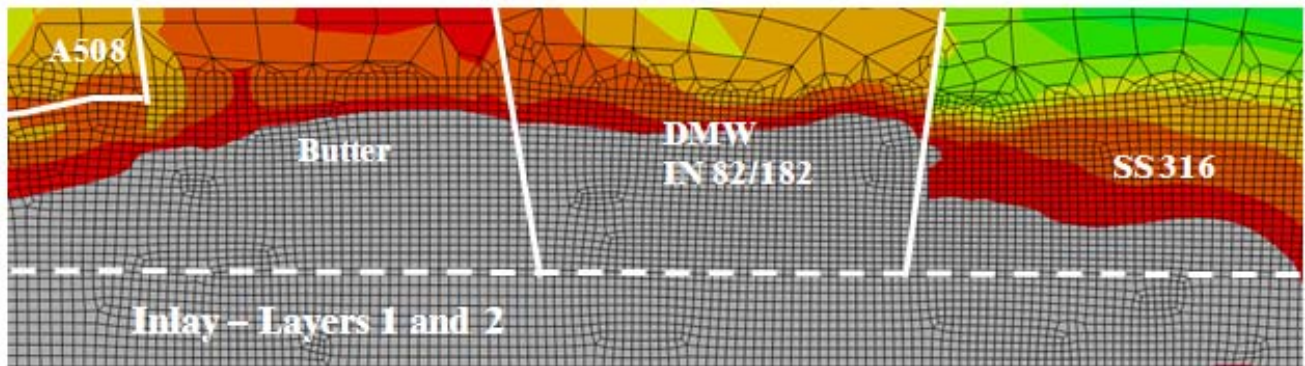
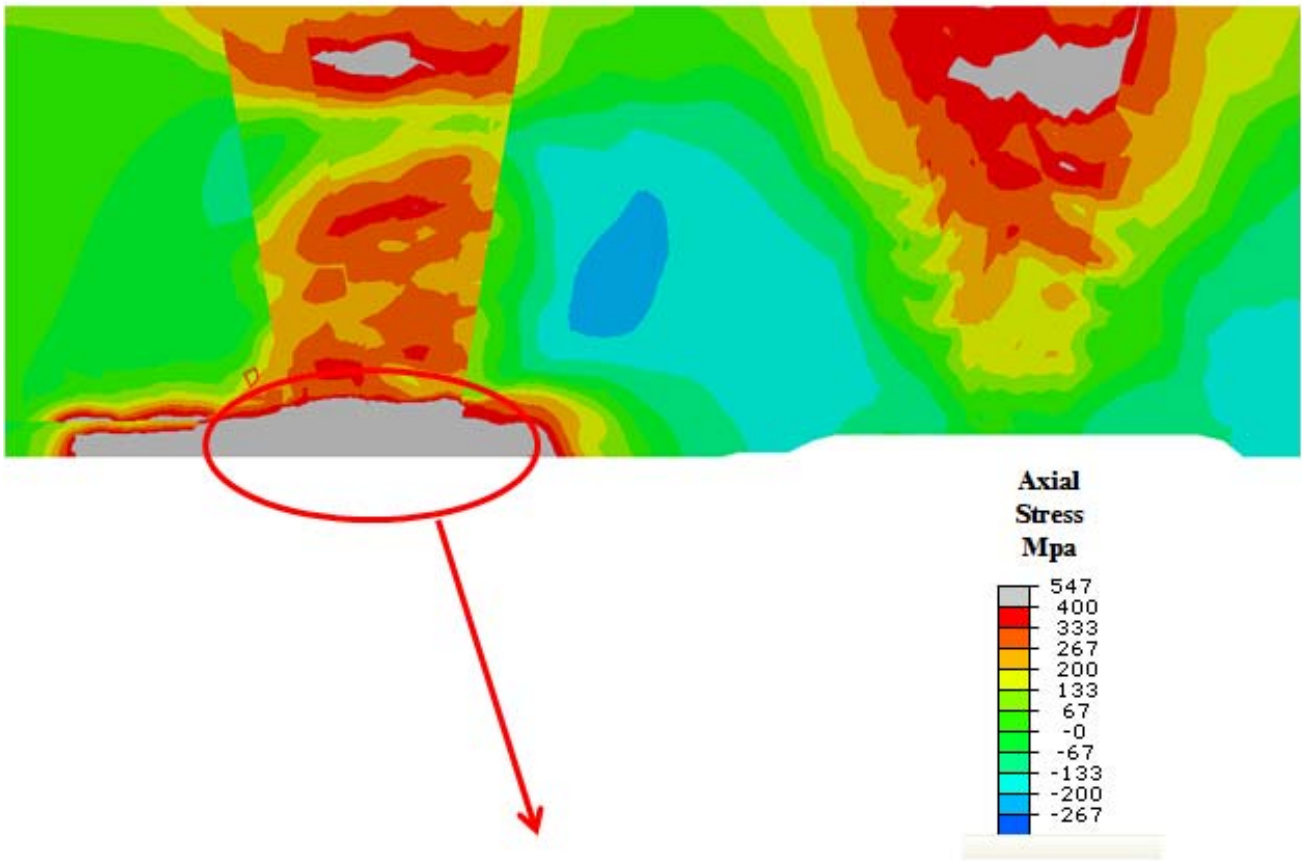


Figure 19 Hoop weld residual stress in inlay repair at service conditions (15.5 MPa pressure and 300C).

4.1.1 Line plots of weld residual stresses for Model 1

Line plots of the weld residual stresses at several locations are shown for many of the cases listed in Table 1. These line plots are used for the PWSCC crack growth analyses conducted in Section 5.

4.1.1.1 Case 1 (50% Pre-service repair)

Structural integrity assessments will be made for all inlay models considered. This will consist of PWSCC analyses of cracks growing through the Alloy 52 inlay layer and through the Alloy 82/182 DM weld. Both idealized and natural crack growth is considered in Section 5. For this purpose, line plots of stresses through the thickness at several critical locations will be presented.

The weld residual stress distribution that develops along the inner surface of the DM inlay weld is presented prior to showing the through thickness stresses. Figure 20 and Figure 21 show both axial and hoop weld residual stresses (respectively) along the inner surface of the pipe at the different stages of welding (after the 50% pre-service weld repair is complete). The pre- and post- hydro test results represent the axial stresses that develop in the safe-end prior to introducing the stainless steel weld. The pre-hydro test results are before introducing the hydro-test load (1.25 time operation pressure). These plots also show the butter weld line and both sides of the Alloy 82/182 weld on the ID of the pipe for reference. The centerline of the stainless steel weld is also shown. The hydro-test has a minimal effect on the weld residual stresses within the butter and weld, reducing both axial and hoop stresses slightly along the right half of the weld at the pipe ID. It is seen that the introduction of the stainless steel safe-end to pipe weld has an important effect of significantly lowering both axial and hoop weld residual stresses in the Alloy 82/182 region of the DM welded pipe. This effect is well known and suggests that pipe systems without this weld may develop PWSCC (as was seen in VC Summer). The ‘inlay complete’ and ‘inlay-machine’ in Figure 20 and Figure 21 represent the stresses after completing the inlay and after machining the bottom layer, respectively. The inlay significantly raises both axial and hoop weld residual stresses along the ID. Although not shown here, the constraint (measured as the one third the trace of the stress tensor) is quite large in this region as well. High constraint is known to reduce fracture toughness. Finally, the service stresses are shown in these figures and are reduced mainly due to the elastic modulus decrease as the temperature rises from room temperature to 300C. However, the thermal expansion mismatch between the materials, where the stainless steel expands more as it is heated, plays a role in service stresses as well.

The weld residual stresses through the thickness of the DM weld tend to drive the PWSCC growth rates. These stresses are shown at several different times during the weld and inlay fabrication process in the following plots. Figure 22 shows the axial weld residual stresses along the weld/safe-end line. The inset in Figure 22 illustrates this location. The normalized distance is measured from the bottom of the pipe at the location of the inlay prior to machining (hence the values in Figure 22 start at a normalized distance of about $1.5/68 = 0.02$) since these results are all presented after machining. These stresses would then drive a circumferential crack through the pipe wall along this interface. The stresses along this line have not been smoothed. However, because this location is at a junction between different materials, and the hoop stresses can be discontinuous (see for instance Figure 19), such local fluctuations are possible. However, the ABAQUS plotting routine contributes to this effect and the results will be smoothed before structural integrity assessments are made. From Figure 22, the inlay markedly increases the weld residual stresses for a significant distance through the pipe wall thickness. The normalized length of the inlay thickness is about $0.07t$ and it is seen that the stresses go from tensile to compressive at about $0.14t$. This shows that the inlay increases the tensile stress zone for a distance of about twice the total inlay thickness (before machining).

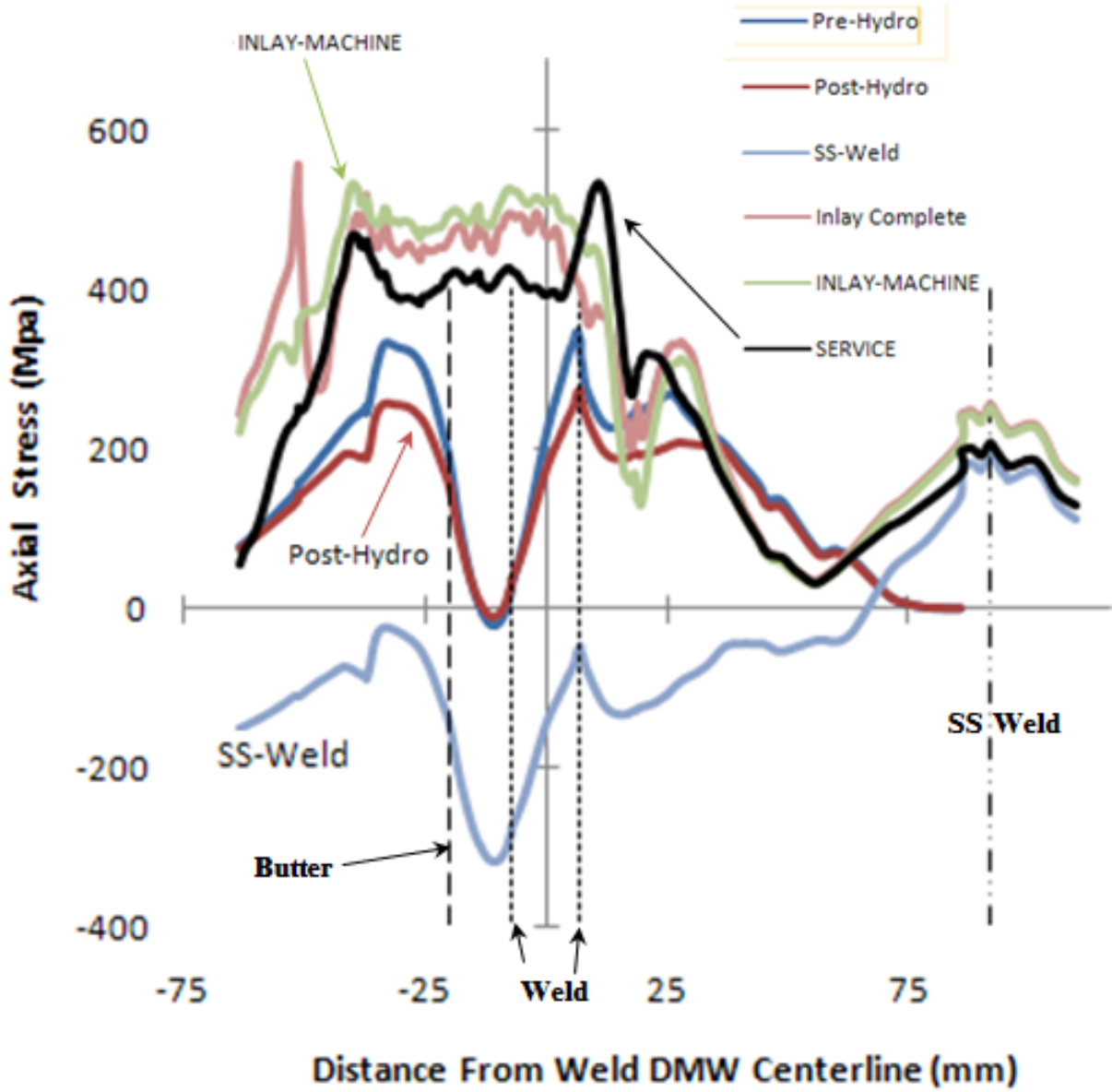


Figure 20 Axial weld residual stress line plots along the inner surface of the DM weld at different stages of the analysis.

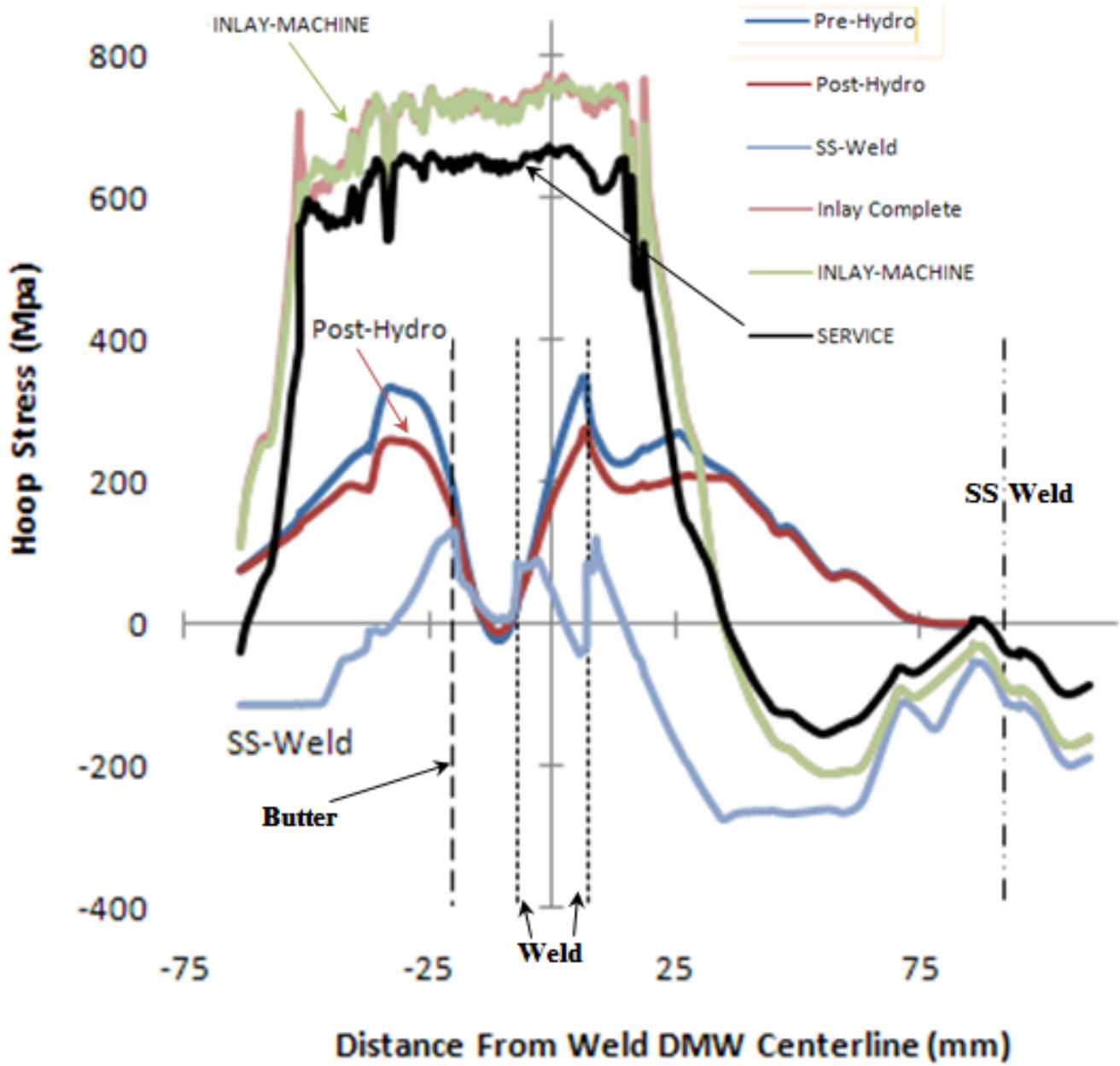


Figure 21 Hoop weld residual stress line plots along the inner surface of the DM weld at different stages of the analysis.

Figure 23 through Figure 25 illustrate through-wall residual stresses at the center of the DM weld, the butter/weld fusion line, and the butter/nozzle fusion line, respectively. In all cases, the axial stresses increase from the compressive stress state that existed after deposition of the safe end weld to tensile after deposition of the inlay.

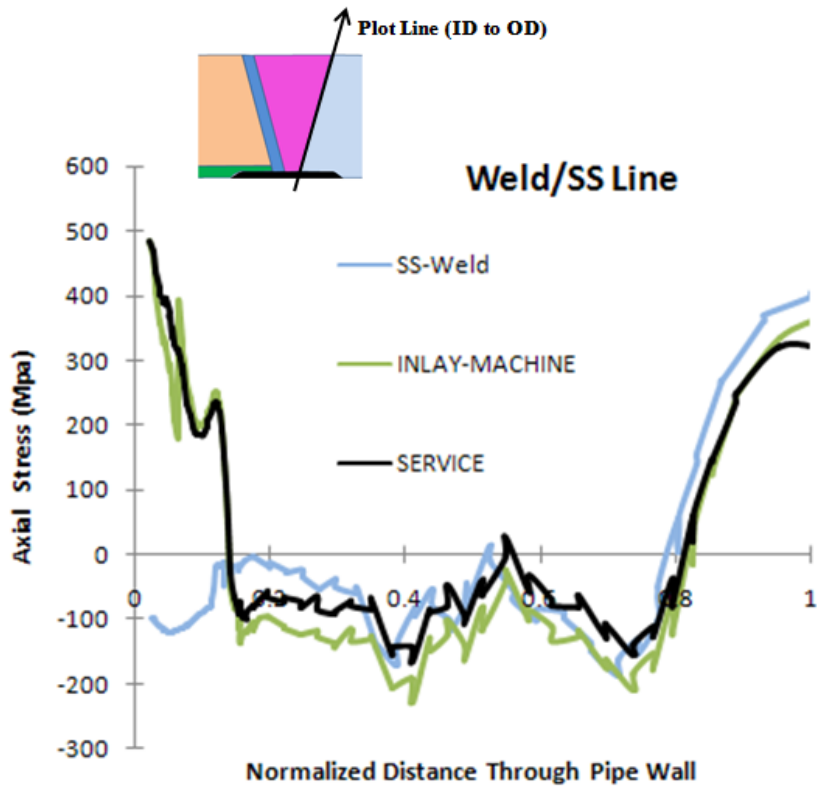
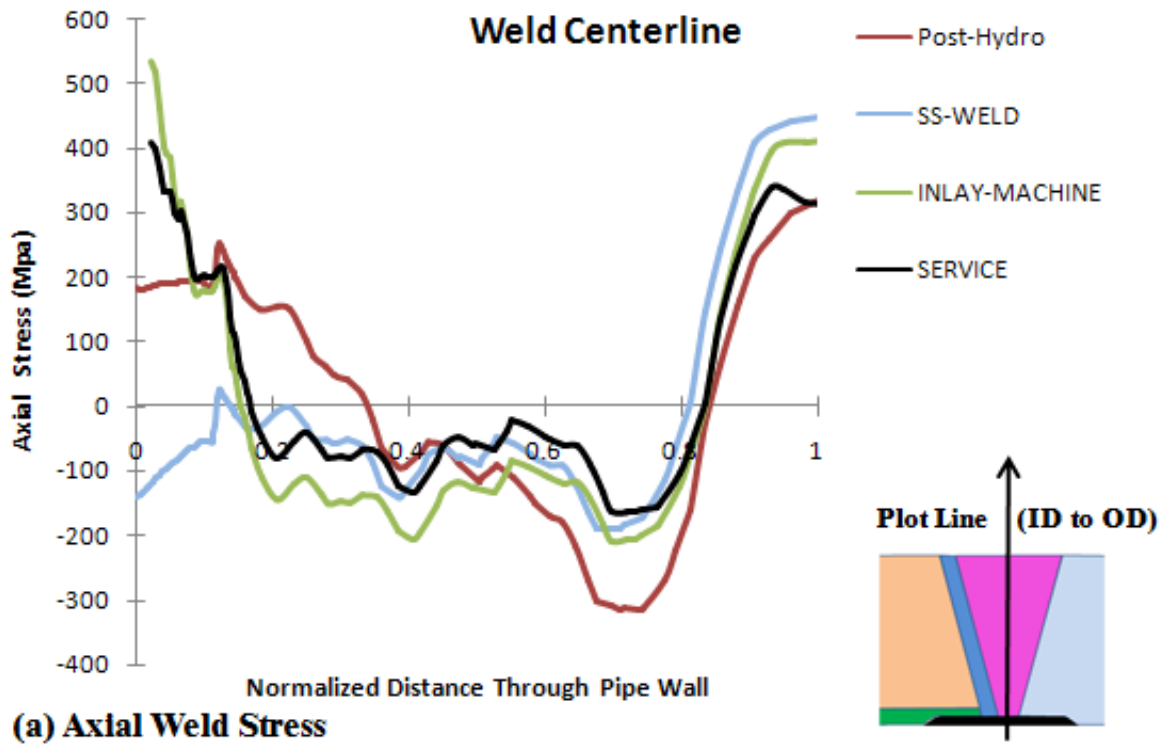
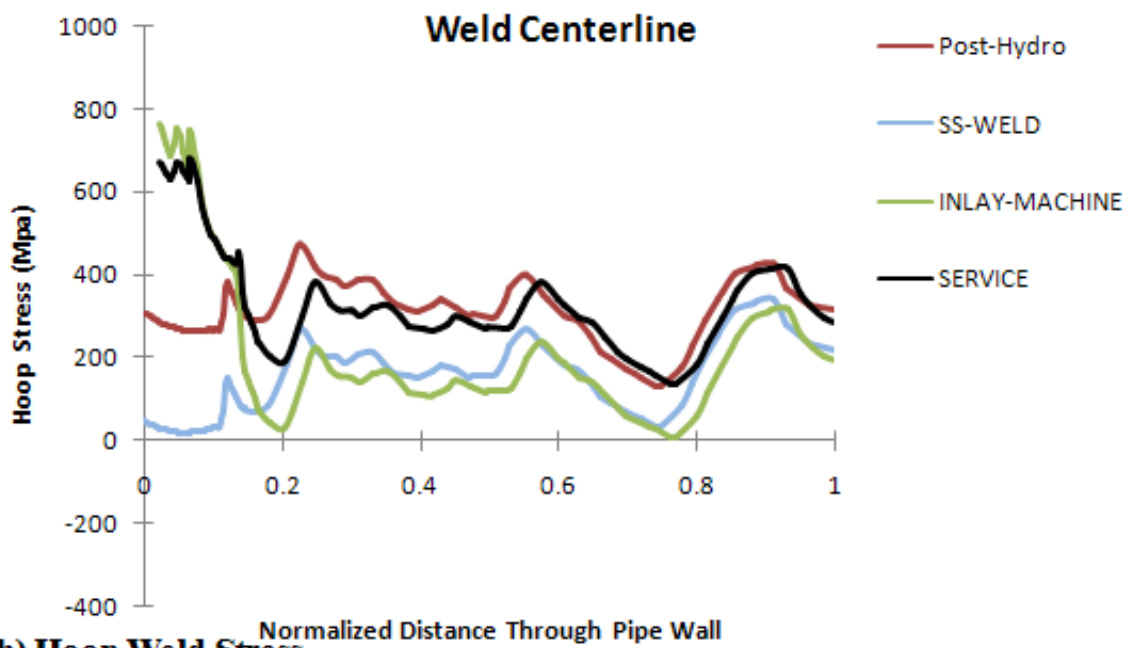


Figure 22 Axial weld residual stress line plots along the DM weld and 316 SS safe end at different stages of the analysis.



(a) Axial Weld Stress



(b) Hoop Weld Stress

Figure 23 Axial and hoop weld residual stress line plots along the centerline of the DM weld at different stages of the analysis.

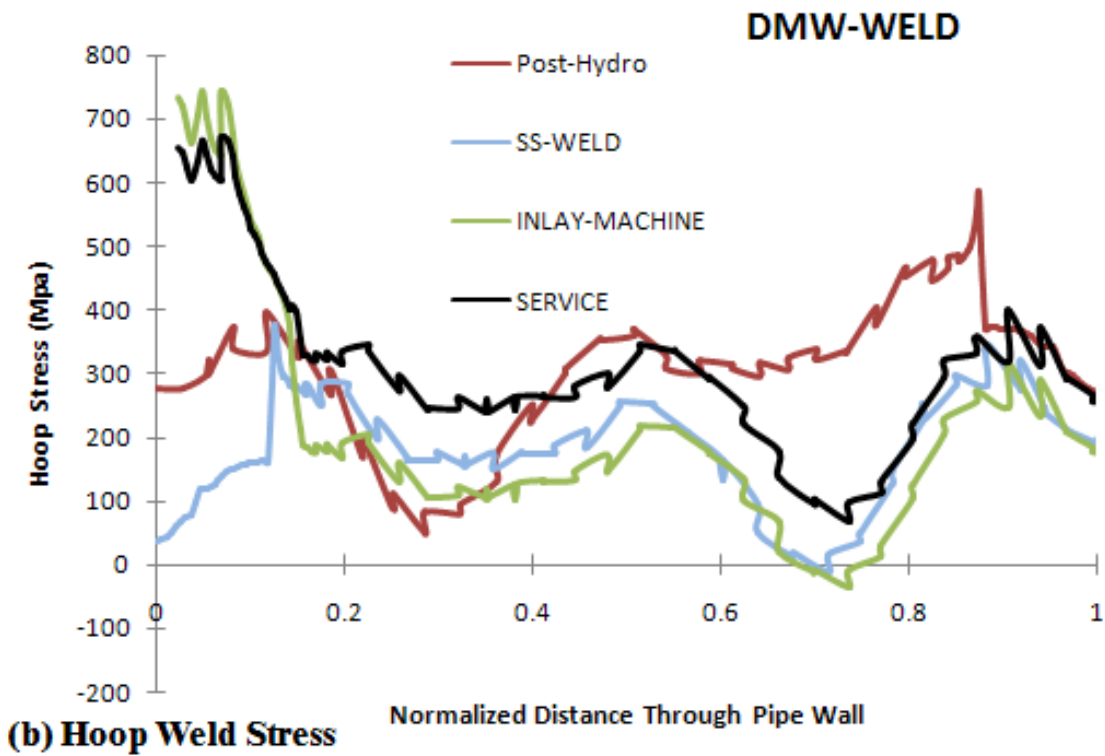
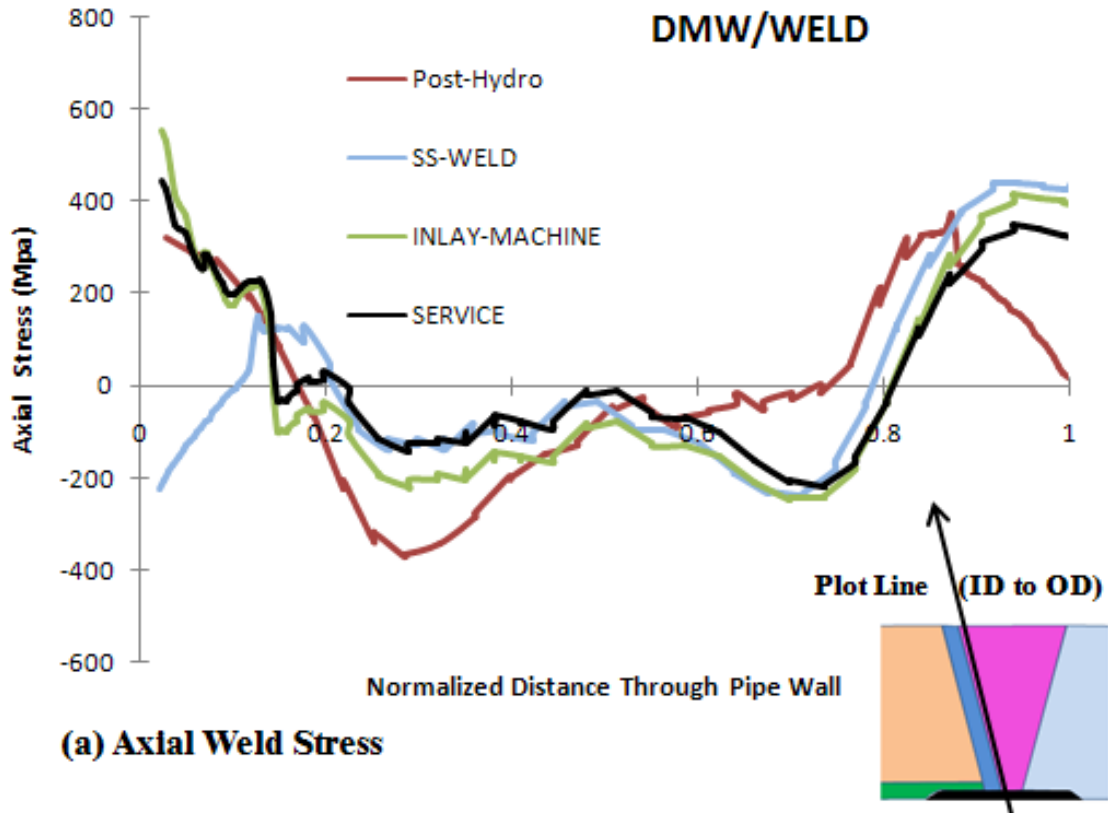


Figure 24 Axial and hoop weld residual stress line plots along the Butter/DM Weld at different stages of the analysis.

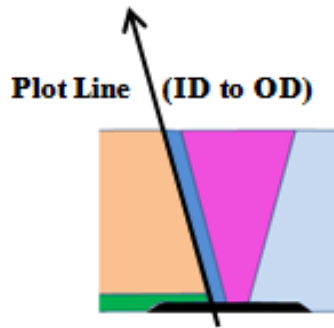
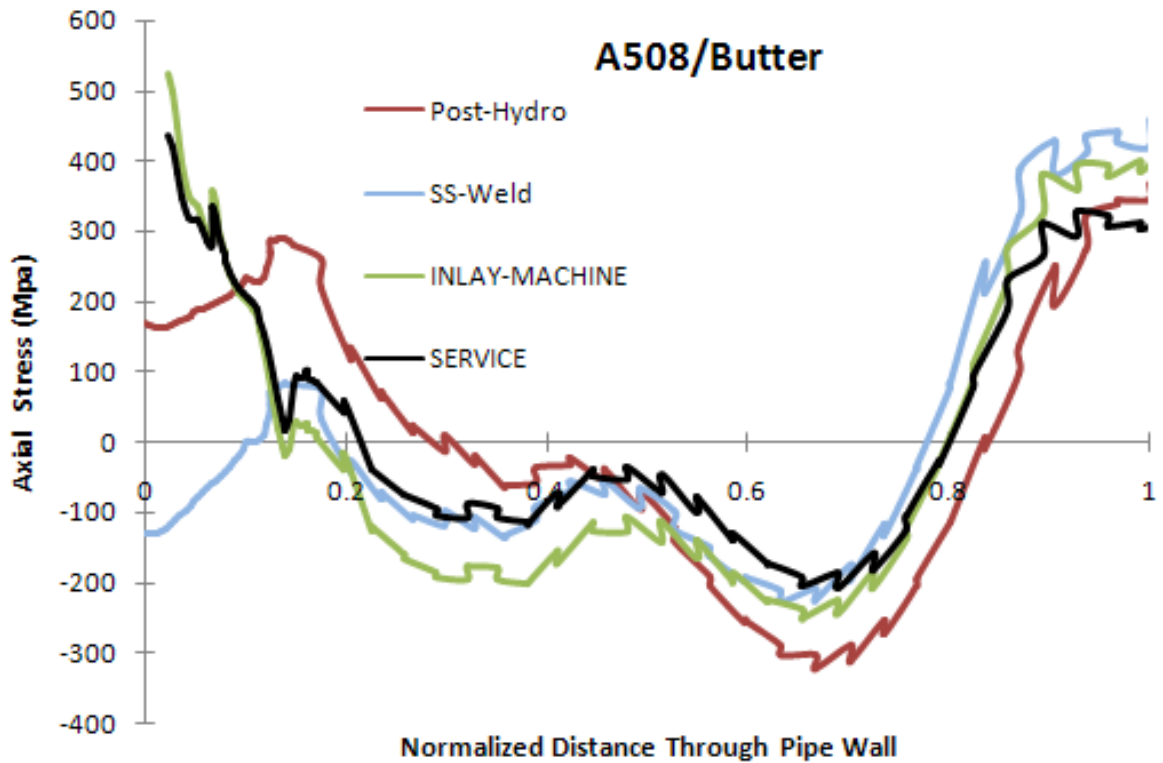


Figure 25 Axial weld residual stress line plot along the A508/Butter weld line at different stages of the analysis.

4.1.1.2 Cases 2 (50% PWSCC Repair), Case 3 (75% pre-service repair), and Case 4 (75% PWSCC repair)

Results are presented for Cases 2 through 4 from Table 1 in the form of line plots. The analysis procedures were quite similar to that shown in detail for Case 1. The line plots will be presented for different locations through the DM weld.

Figure 26 shows the weld residual stresses plotted through the weld centerline. The result for the 50% pre-service repair (Case 1 of Table 1) is represented by the red curve (this result was also shown in Section 4.1.1.1). The black line represents the case of a 50 % PWSCC repair (Case 2). It is seen that the magnitude of the axial weld residual stresses remains about the same. However, for the PWSCC repair, the axial stresses reverse from tension to compression at about 25% of the wall thickness compared with about 15% for the case of the pre-service repair. This will result in PWSCC crack growth rates that are different from the baseline case of the repair before the stainless steel weld, with growth rates likely to be higher.

As seen also in Figure 26 for the weld centerline case, the 75% deep pre-service repair (Case 3 in Table 1) does not significantly affect the stress state as compared with the 50% repair. Apparently, the repair depth effect is obliterated by the inlay weld. In addition, the 75% deep PWSCC repair (Case 4 in Table 1) does not significantly affect the stress state as compared with the 50% PWSCC repair. In essence, when inlay is involved, the depth of the repair (50% or 75%) has less of an effect on the through-wall residual stress distribution compared with whether the repair occurs before or after the stainless steel weld. The beneficial effects of the stainless steel weld are eliminated when the repair is made after the stainless steel weld is deposited.

The stress results along the DMW/SS line is shown at the bottom of Figure 26. The trends are similar to the results from the weld centerline, but the values differ slightly.

Results of Cases 1 through 4 from Table 1 are also shown in Figure 27 for the DMW/Butter line in (top) and Butter/Nozzle line (bottom). Again, the trends shown in Figure 27 are similar to that from the weld centerline results. The effect of the weld repair depth is not as important as whether the repair is made before or after the stainless steel weld.

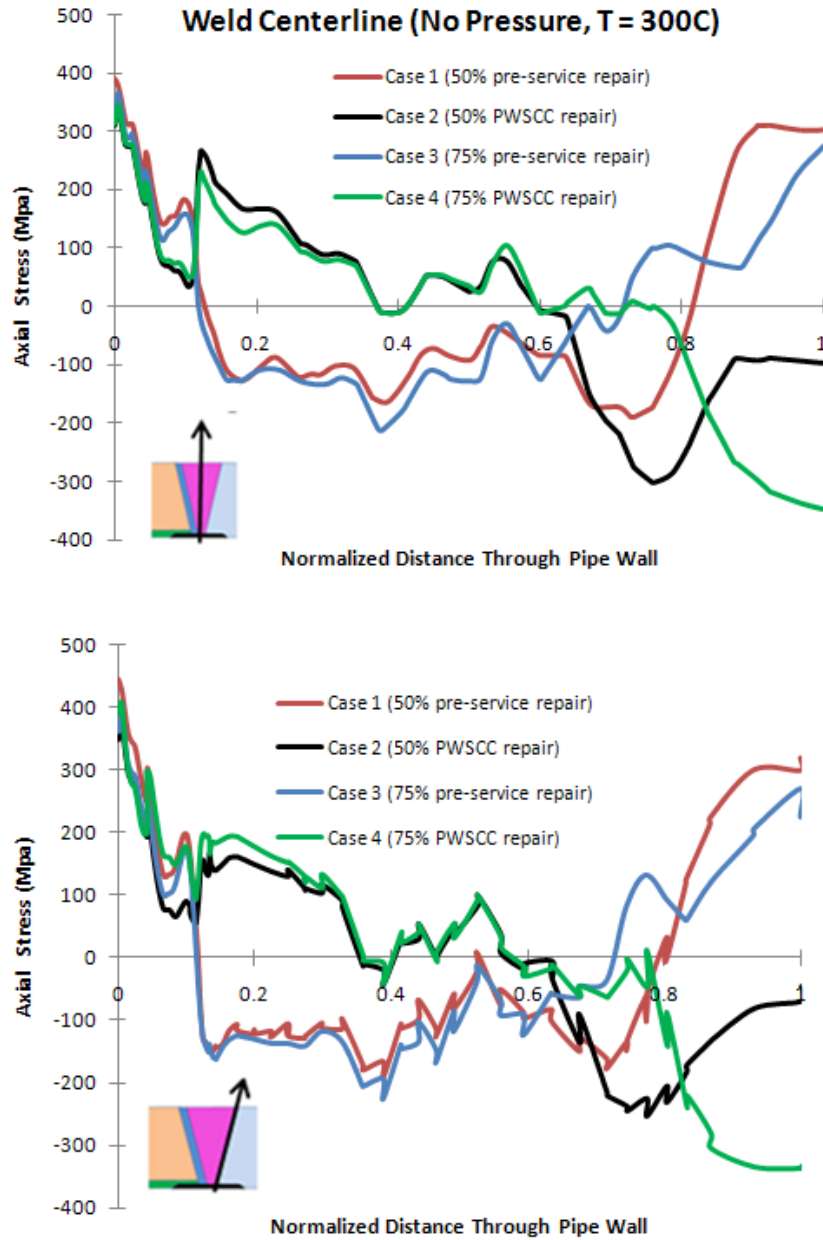


Figure 26 Through thickness stresses at operating temperature (300C), no pressure, for different analysis cases. (top) weld centerline (bottom) DMW/SS line.

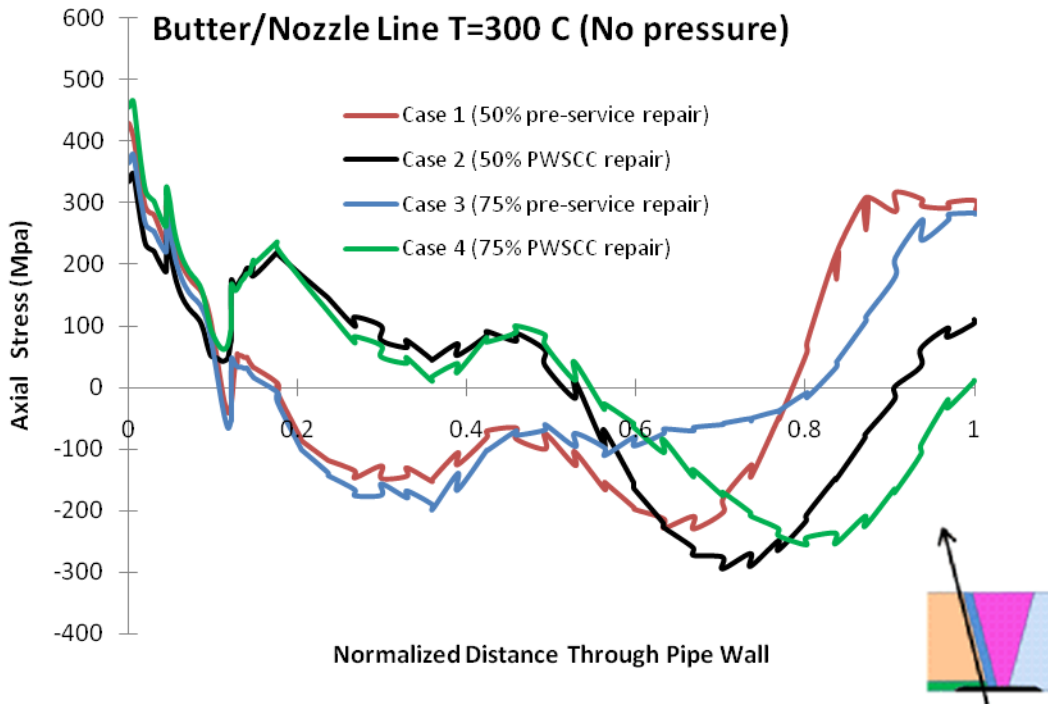
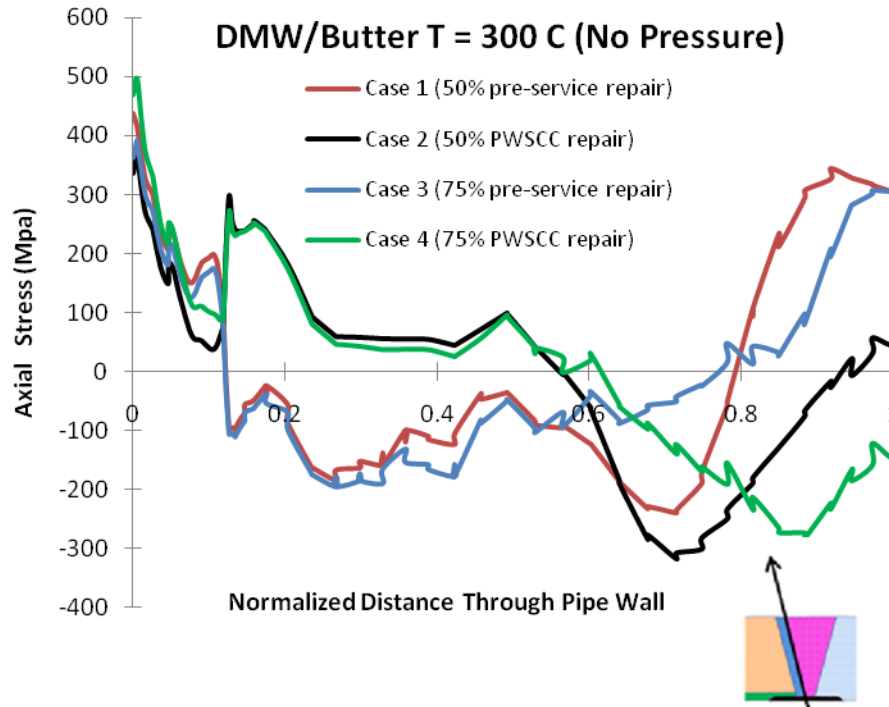


Figure 27 Through thickness stresses at operating temperature (300C), no pressure, for different analysis cases. (top) DMW/Butter (bottom) Butter/Nozzle.

4.1.1.3 Case 5 (50% pre-service repair and 75% PWSCC repair)

From Table 1, Case 5 is a combination repair case and consists of a 50% pre-service repair and a 75% PWSCC repair that is applied prior to the inlay application. Figure 28 shows the weld residual stresses through the nozzle weld centerline for Case 5 (black line with black markers). It is seen that Case 5 is the worst possible repair scenario, although it appears to be unlikely. The weld residual stresses are tensile for more than 60% of the wall thickness. For all of the PWSCC repair examples (Cases 2, 4, and 5), the stress does not cross from tension to compression until nearly 60% of the wall thickness and the stress at the OD remains compressive. For all of the pre-service repair examples (Cases 1 and 3) the weld residual stresses are tensile at the pipe OD. However, it is clear that the inlay causes tensile weld residual stresses at the nozzle ID of between 300 and 400 MPa for all repair cases.

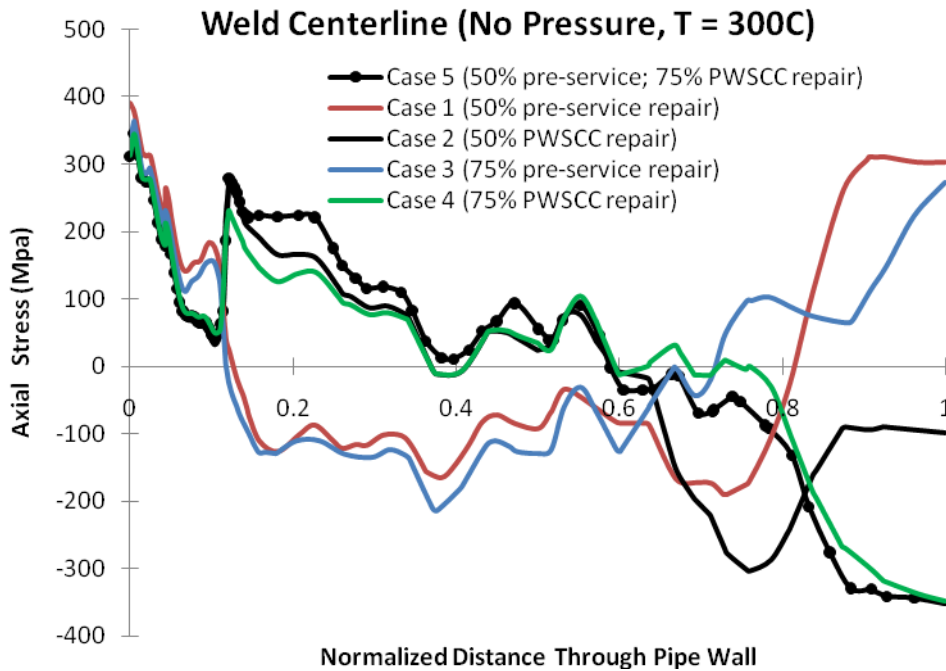


Figure 28 Axial through-wall stresses at weld center-line for Cases 1 to 5.

The results for other locations for Case 5 are shown in Figure 29 for the DMW/SS line location, Figure 30 for the DMW/butter line, and Figure 31 for the nozzle/butter line. The results for Case 4, which was a 75% PWSCC repair, are shown as well for comparison purposes. Case 4 is the worst location in terms of weld residual stresses for driving a PWSCC crack.

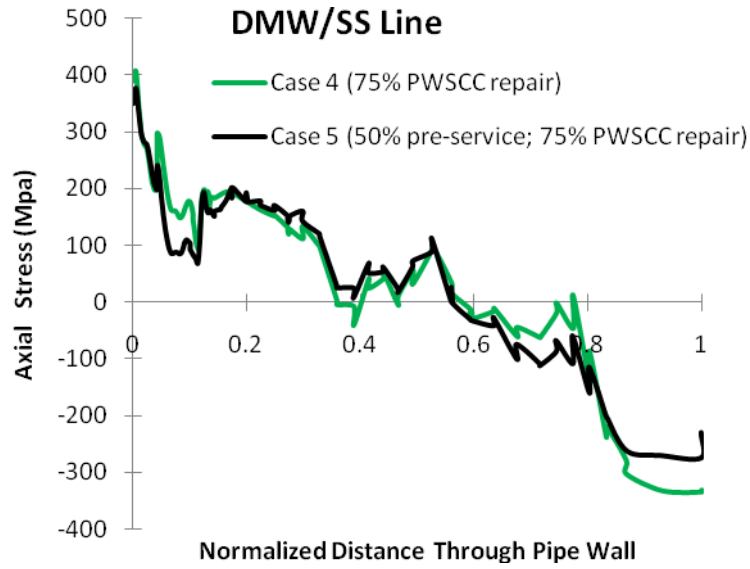


Figure 29 Axial through-wall stresses at DMW/SS line for Case 5.

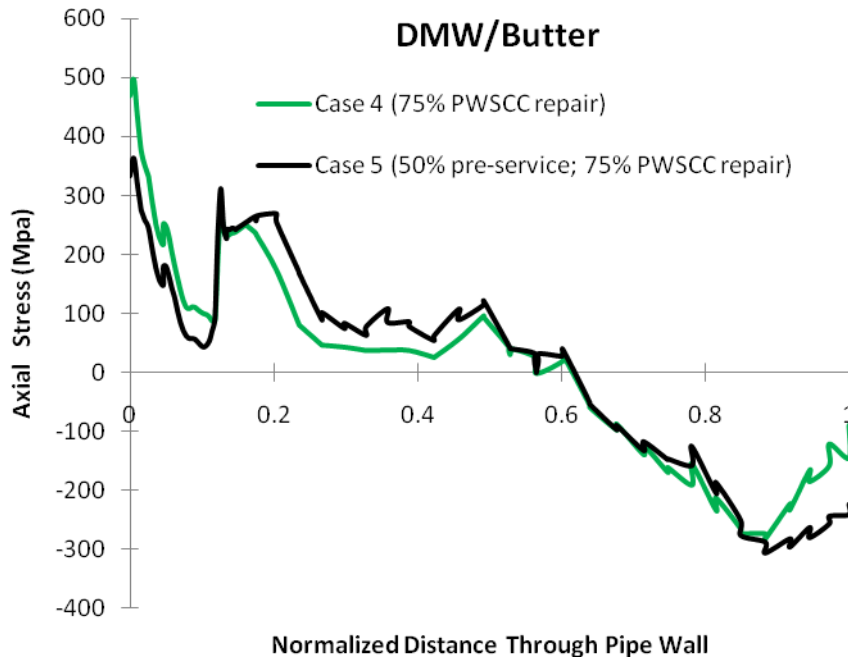


Figure 30 Axial through-wall stresses at DMW/Butter line for Case 5.

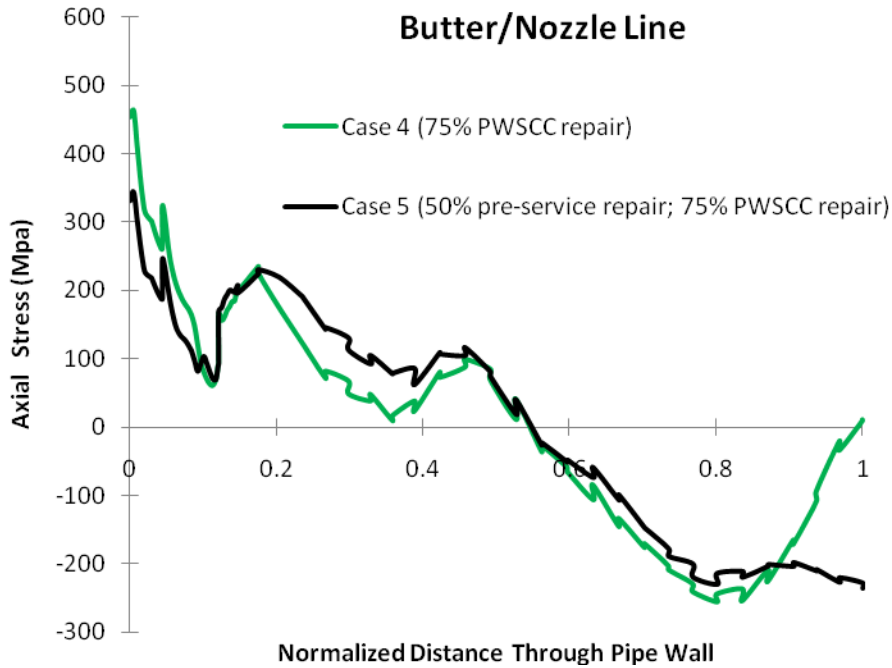


Figure 31 Axial through-wall stresses at Nozzle/Butter line for Case 5.

4.1.1.4 Cases 6 and 7 inlay 6-mm thick (50% pre-service repair and 75% PWSCC repair)

The crack growth assessments discussed later in Section 5 show that crack growth through the inlay and into the underlying Alloy 182/82 weld metal may be rather fast for some of the severe weld cases. In this section, a thicker inlay was investigated. While it can be anticipated that a thicker inlay may have a residual stress field similar to the 3-mm inlay, the additional time it takes to grow through the thicker material would provide more margin. Here the weld residual stresses for Cases 6 and 7, a 6-mm thick inlay, are presented.

The weld residual stresses for Case 6, which is a 50% pre-service repair, followed by the stainless steel weld and the application of the 6-mm inlay are shown in Figure 32 (at the weld centerline and along the DM weld and stainless steel line and in Figure 33 along the DMW/butter and nozzle/butter lines). It is seen for both these pre-service repair cases that the maximum magnitude of the axial weld residual stresses at the ID are almost identical between the two inlay cases. Moreover, the distance where the stresses cross from tension to compression is deeper through the thickness for the 6-mm inlay as compared with the 3-mm inlay. The level of compressive stress is also slightly larger in magnitude for the thicker inlay. This will lead to slightly faster PWSCC growth within the 6-mm inlay due to the higher weld residual stresses. However, as will be seen in Section 5, the time growth within the inlay is much greater.

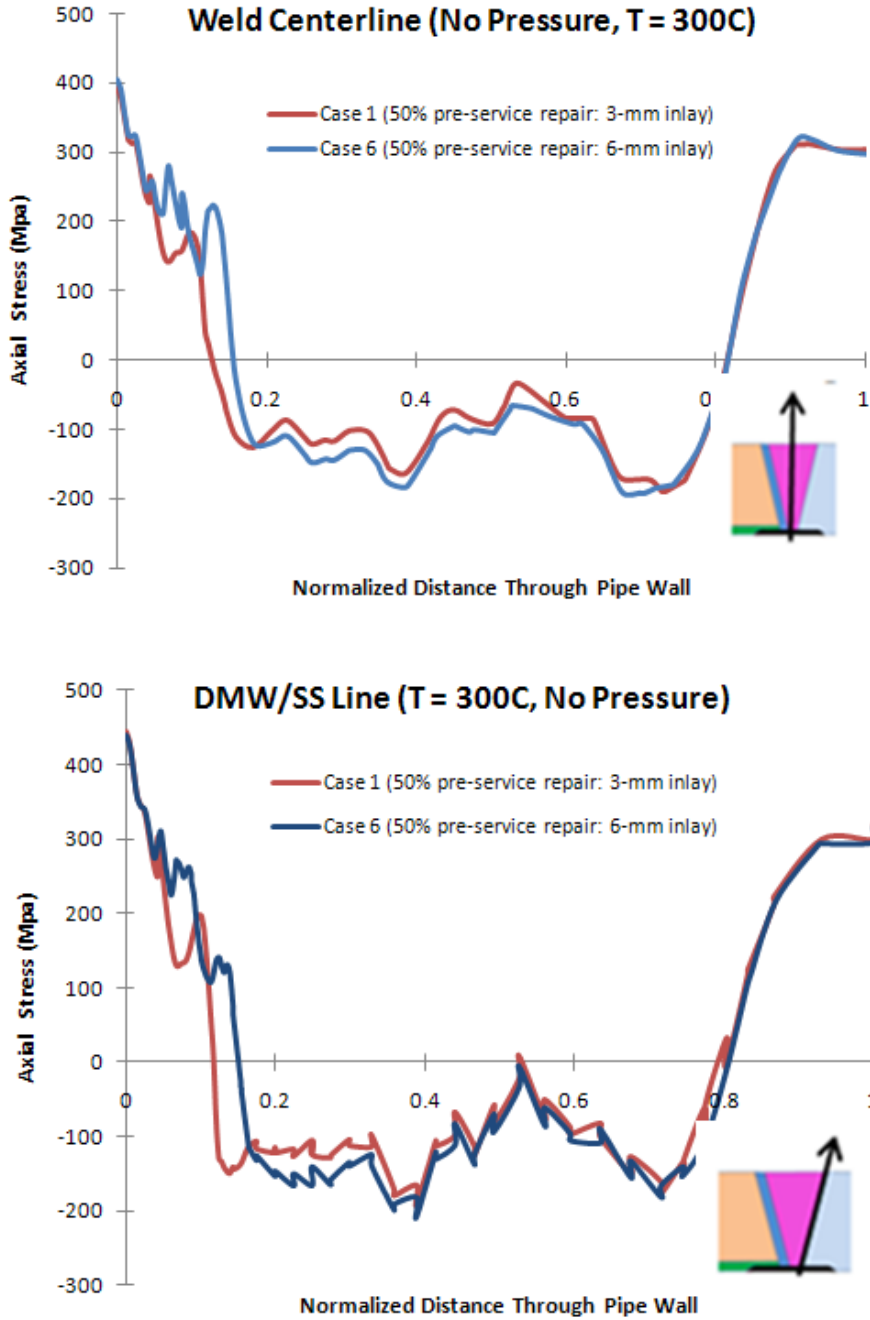


Figure 32 Axial weld residual stresses for 6-mm inlay for Case 6 compared with the Case 1 result. These are both pre-service repairs with different inlay thickness.

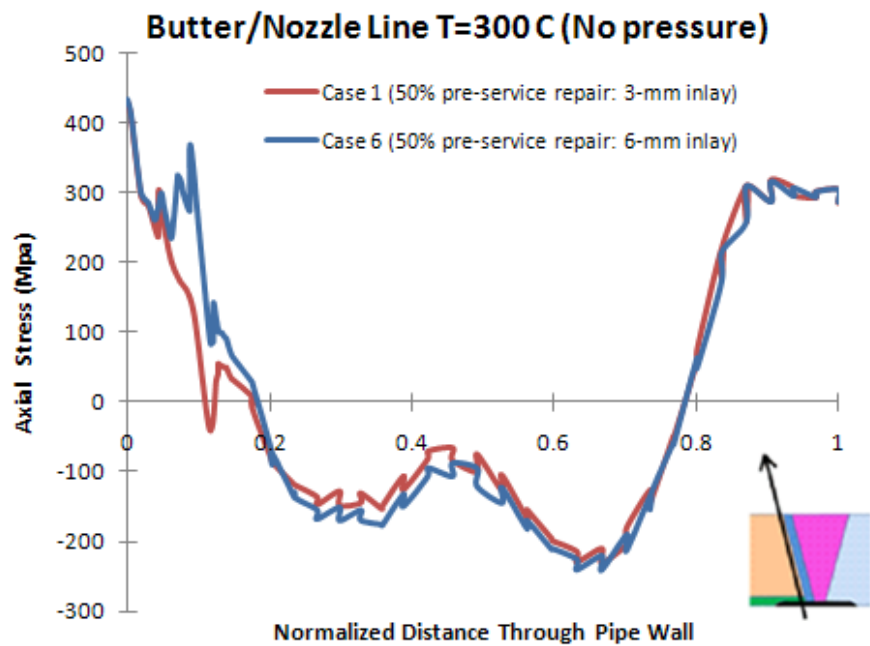
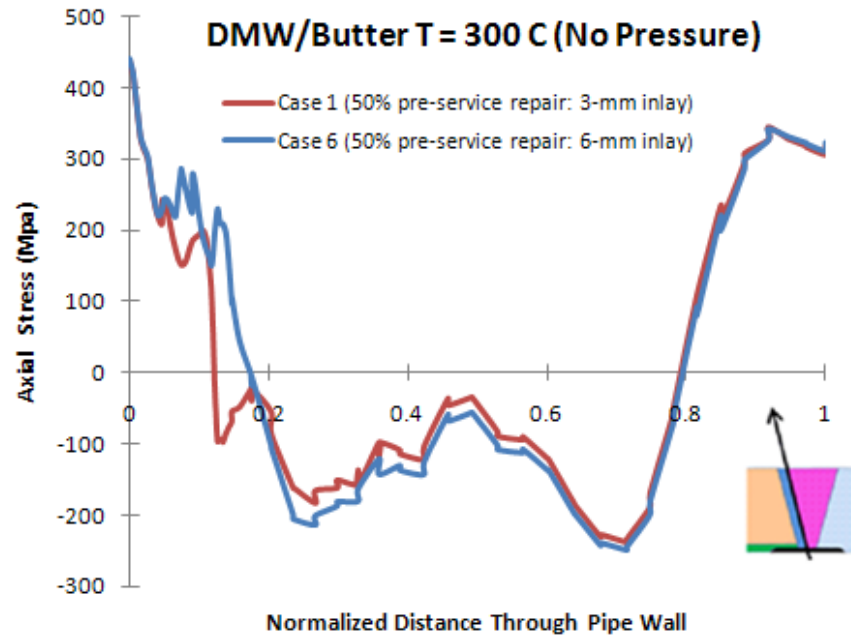


Figure 33 Axial weld residual stresses for 6-mm inlay for Case 6 compared with the Case 1 result. These are both pre-service repairs with different inlay thickness.

The weld residual stresses for the 6-mm and 3-mm inlay with a 50% PWSCC repair are compared in Figure 34 and Figure 35. Again, the 6-mm inlay case has slightly higher weld residual stresses.

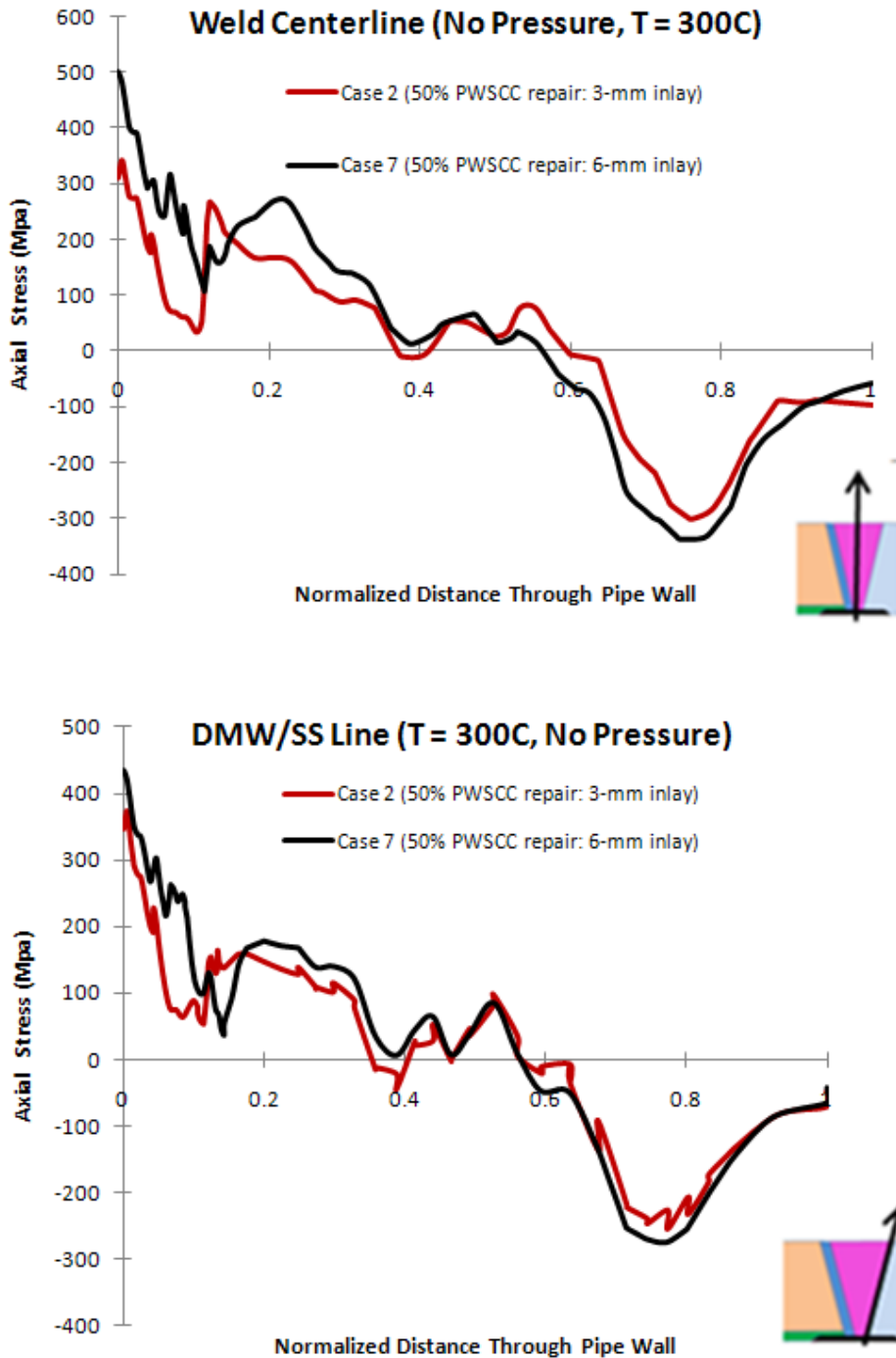


Figure 34 Comparison of weld residual stresses between Case 2 (3-mm inlay) and Case 7 (6-mm inlay) at the weld centerline and along the DMW/SS line.

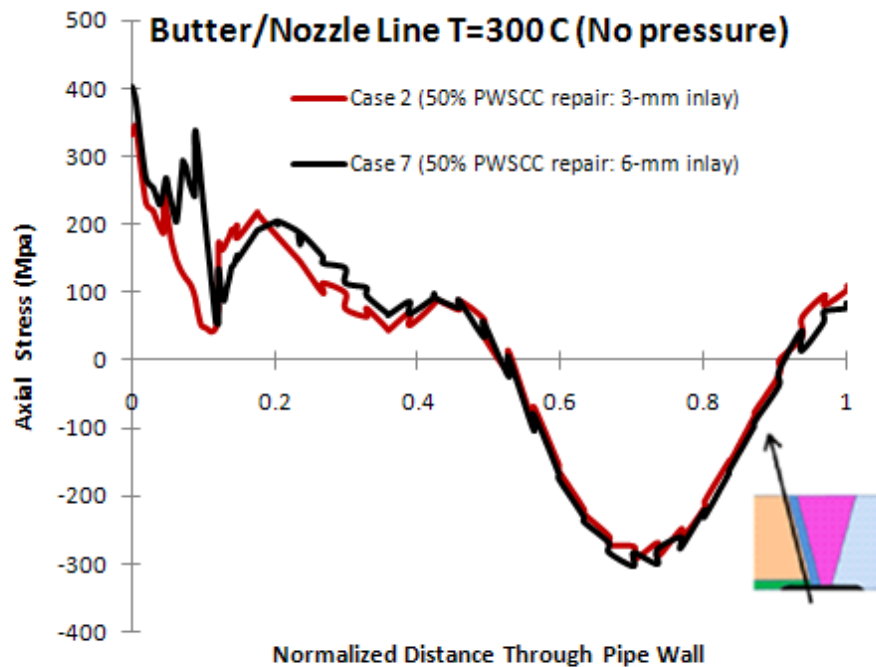
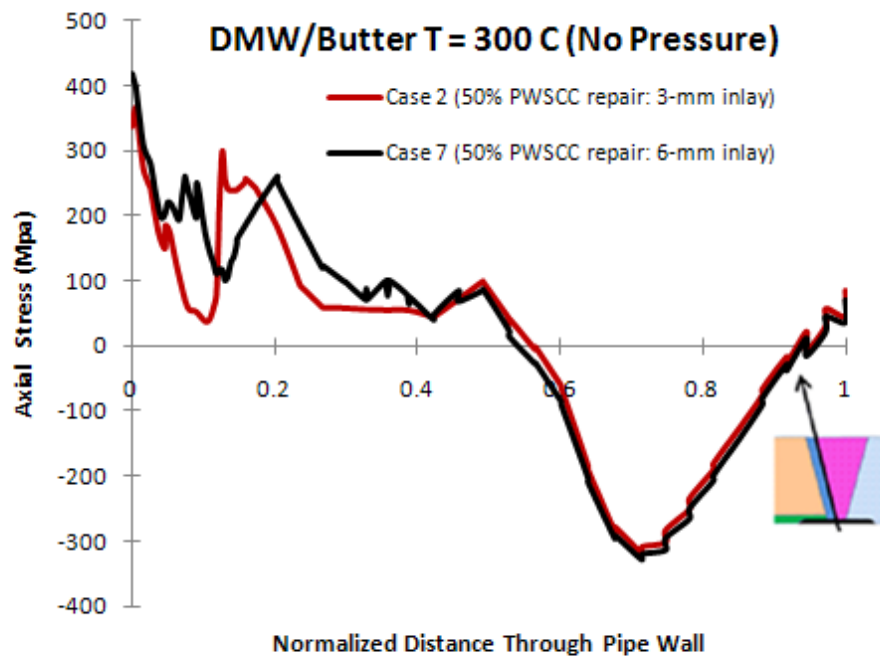


Figure 35 Comparison of weld residual stresses between Case 2 (3-mm inlay) and Case 7 (6-mm inlay) along the DMW/butter line and along the nozzle DM weld line.

Finally, a comparison between the 50% pre-service and PWSCC repair cases with different thickness inlays are shown in Figure 36. The PWSCC repair case has higher weld residual stresses at the ID and cross into compression deeper through the pipe wall. Also, the 6-mm inlay produces a slightly more tensile WRS field as compared with the thinner inlay.

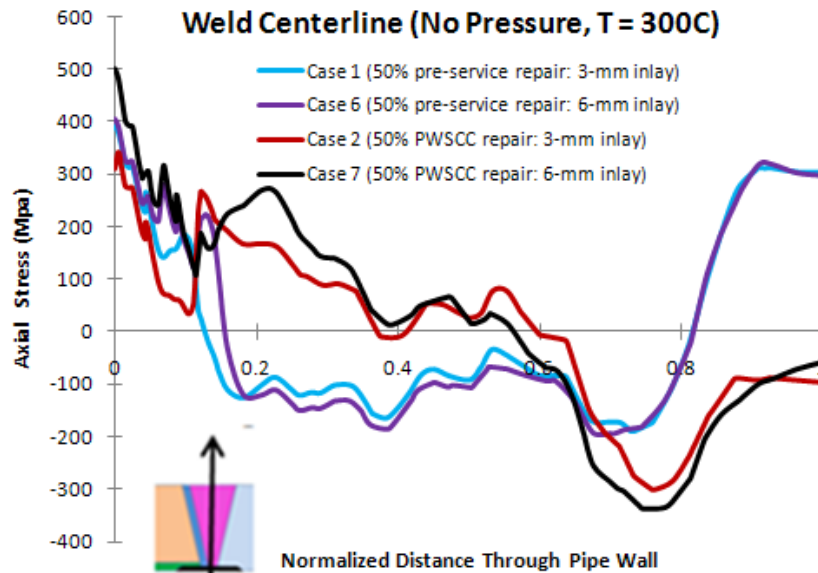


Figure 36 Residual stress comparisons for the 50% repair cases.

Additional weld residual stress analyses (Cases 8-11 in Table 1) were performed for the Model 1 case and are presented in Appendix C. Cases 8 and 9 provide baseline analysis results with no inlay. Case 10 examines a pre-existing flaw in the DM weld prior to applying the inlay. Finally, Case 11 examines the effect of assuming cast stainless steel material properties for the safe end.

4.2 Model 2 Weld Residual Stress Results

The details of the Model 2 geometry were presented in Section 3.2.1.2. Here, only the results for Case 1 of Table 2 are presented so that a direct comparison of the full field weld residual stresses for Models 1 and 2 can be made. Figure 37 illustrates the axial weld residual stresses after completion of the inlay, but prior to machining of the third inlay layer. Comparing to Figure 15, the residual stress pattern from Model 2 differs from the Model 1 results. In particular, the compressive residual stresses are higher in magnitude for this model (Model 2). Recall that the repair for Model 1 was 50% through the thickness while the repair depth for Model 2 was 12%. Figure 38 shows the effect of machining on the axial stress state. The response is similar to Model 1 where overall the axial stresses slightly decreased, but the stresses at the pipe ID increased. Finally, Figure 39 and Figure 40 illustrate the axial and hoop residual stresses for the Model 2 case at operation temperature and pressure, respectively. In general, the weld residual stresses for Model 1 are lower in absolute magnitude than those for Model 2.

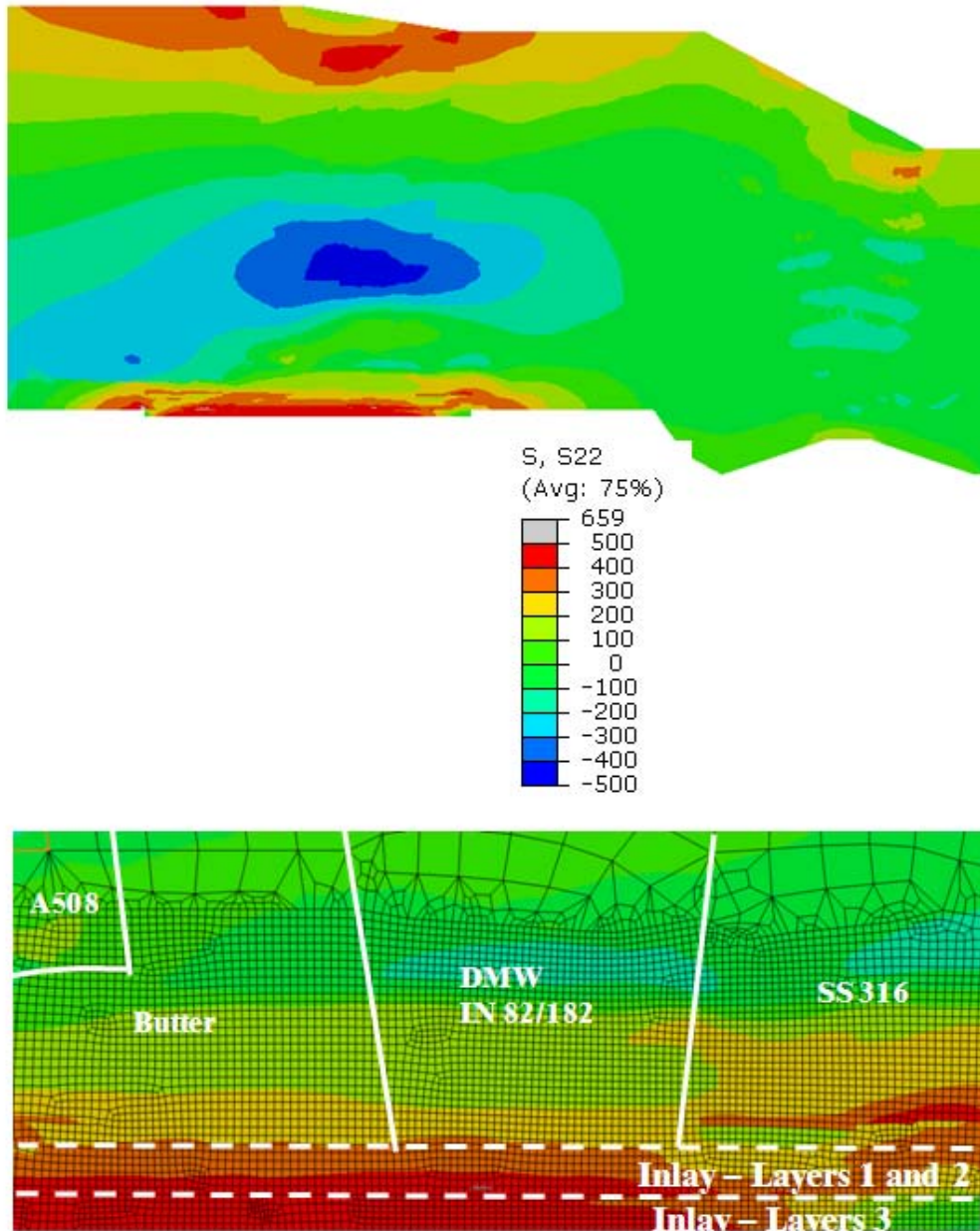


Figure 37 Axial weld residual stresses after deposition of the Alloy 52/152 inlay but prior to machining the third inlay layer. The top illustration shows a global view of the stress pattern at the DM and SS weld regions. The bottom illustration shows the stresses with the mesh refinement shown near the DM weld.

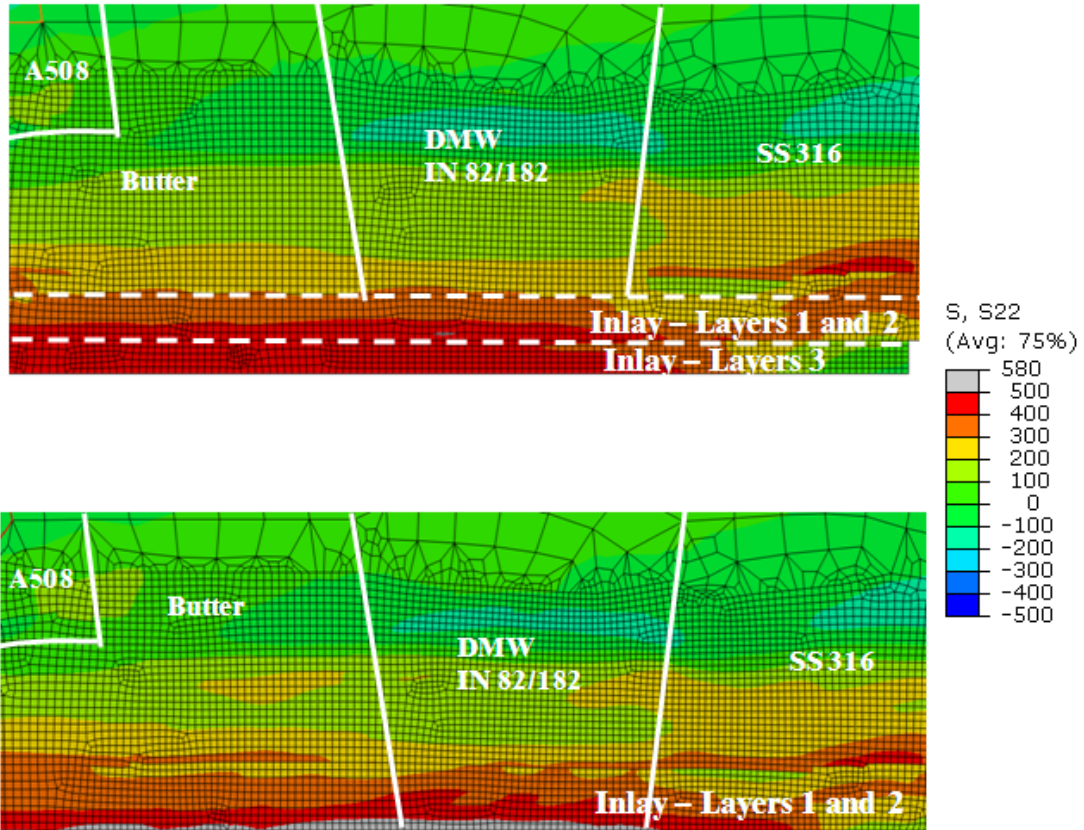


Figure 38 Comparison of axial weld residual stresses before and after machining inlay layer number 3 for Model 2

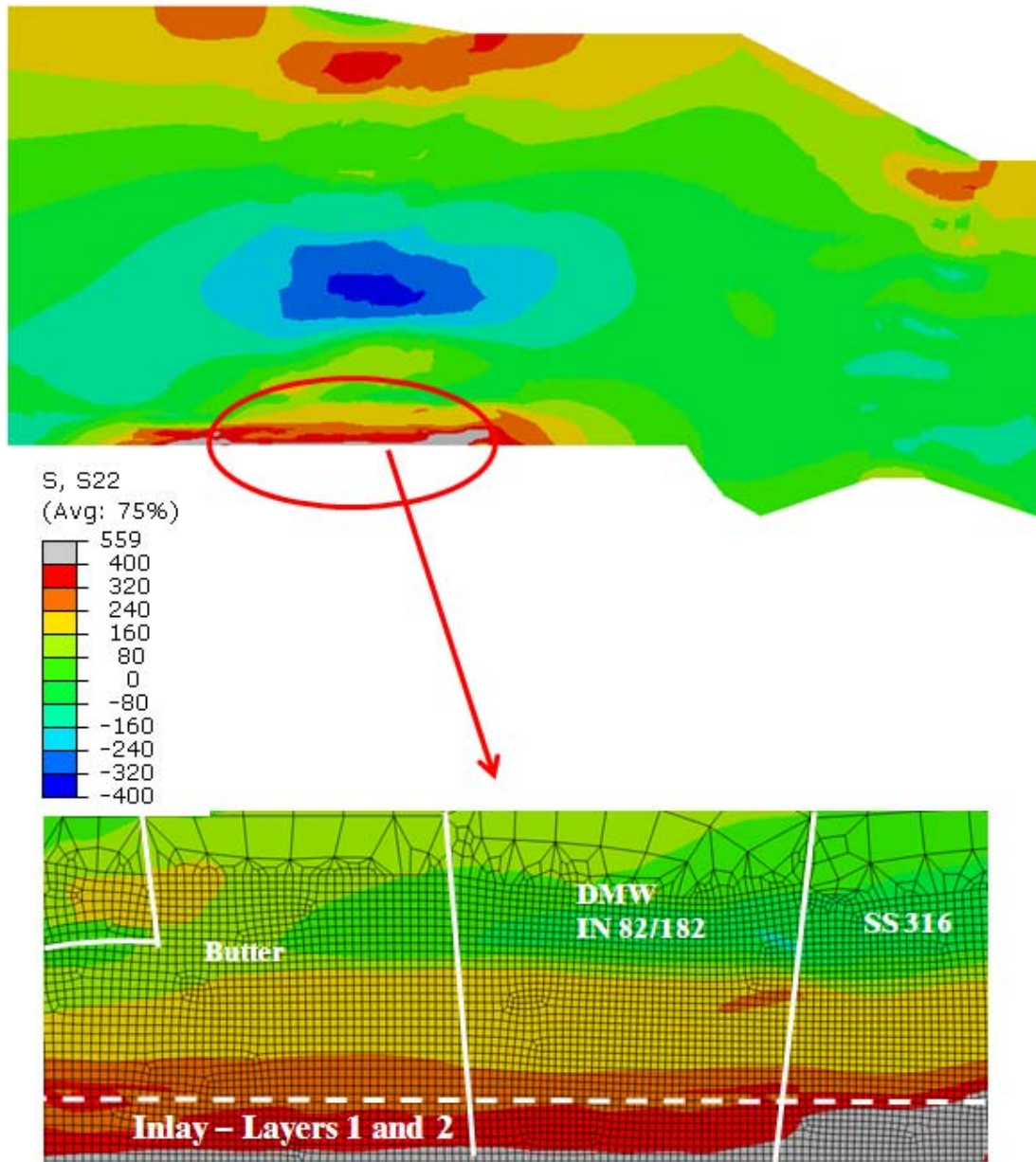


Figure 39 Axial weld residual stress in inlay repair at service conditions (15.5 MPa pressure and 300C) for Model 2.

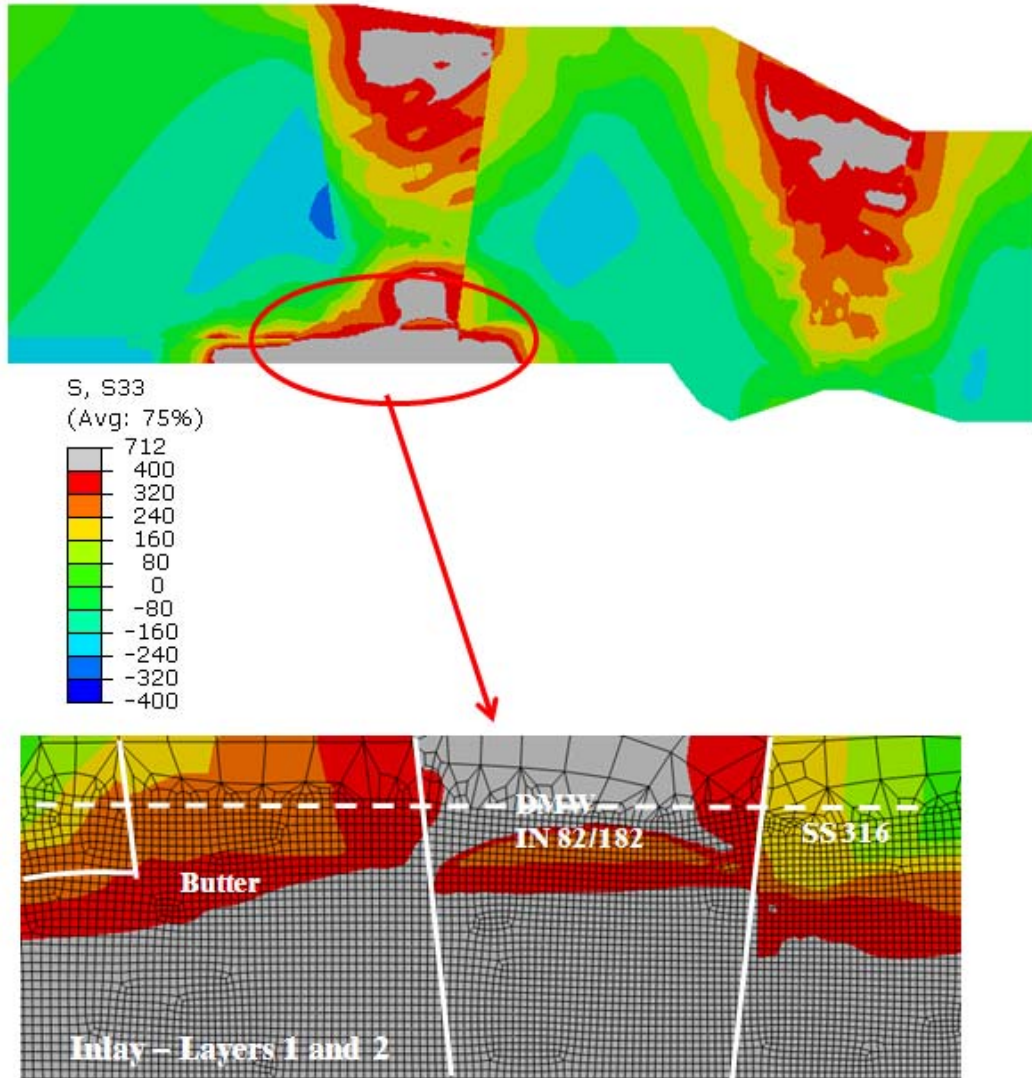


Figure 40 Hoop weld residual stress in inlay at service conditions (15.5 MPa pressure and 300C) for Model 2

4.2.1 Model 2 line plots for structural integrity assessment

Finally, line plots of residual stresses are presented for Model 2. These are the stresses that are used for structural integrity assessments. As with the line plots for Model 1, some of these line plots have a jagged appearance. This is due to the ABAQUS plotting routines and occurs along different material interfaces.

4.2.1.1 Case 1 (12% pre-service repair) for Model 2

Figure 41 and Figure 42 illustrate line plots along the pipe inner diameter (ID) at different stages of the analysis, for axial and hoop components, respectively. The post hydro-test plot line

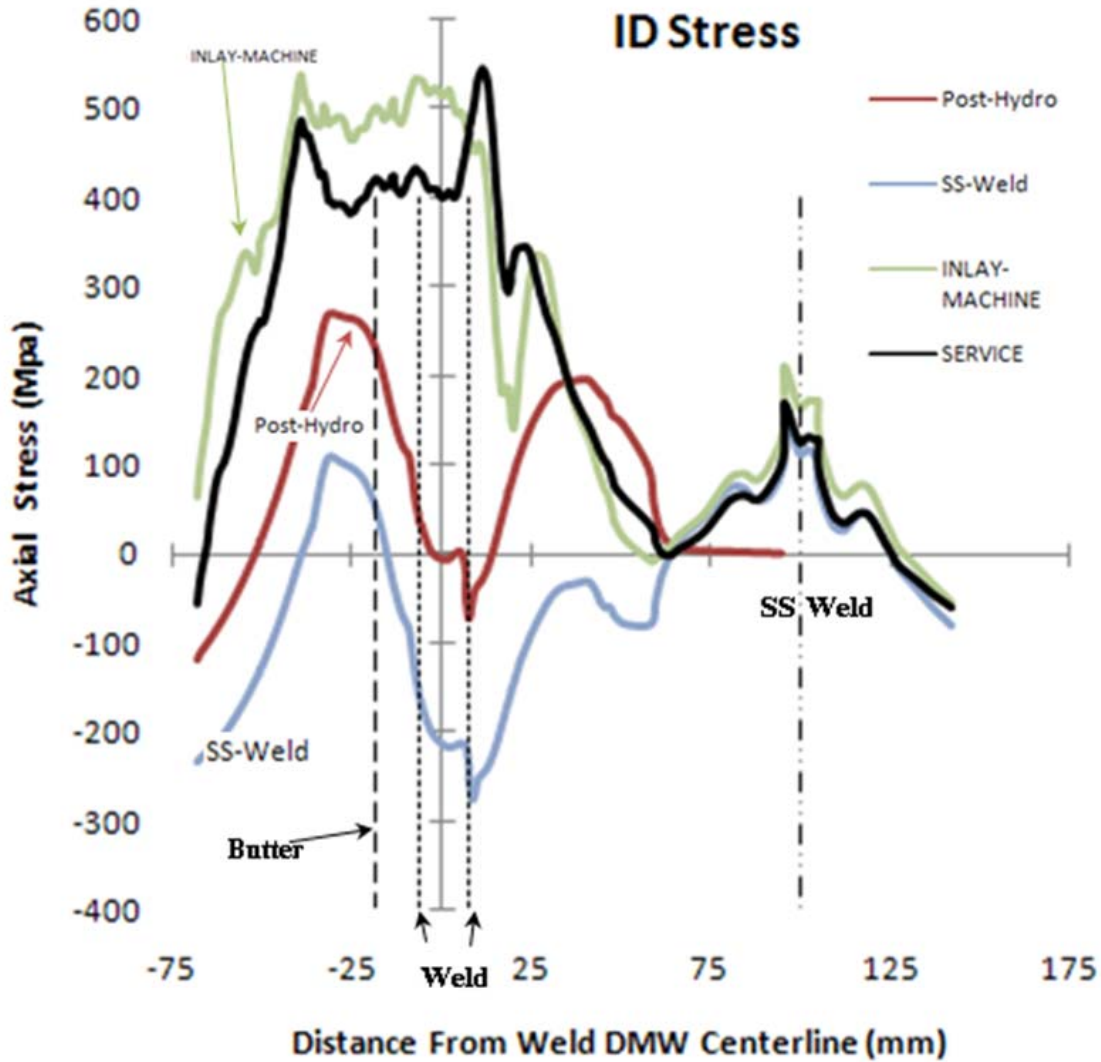


Figure 41 Axial weld residual stress line plots along the inner surface of the DM weld at different stages of the analysis for Model 2

shows tensile weld residual stresses in the butter region and low-level tensile stresses in the weld. For Model 1 (Figure 20), the same general pattern is observed but the axial stresses are more tensile in the weld for this model. Recall that Model 1 had a 50% repair while Model 2 had a 12% repair. The hoop stresses likewise show a similar shape between Model 1 (Figure 21) and Model 2 (Figure 42). However, the post hydro-test hoop stresses remain tensile along the ID for Model 2.

After the stainless steel weld, the axial stresses reduce, but remain tensile near the edge of the butter region (Figure 41). By contrast, the axial stresses remain tensile for Model 1 (Figure 20) after the SS weld is completed. This is because the DM and SS welds are farther apart for this model (~12 mm closer centerline to centerline) compared with the Model 1.

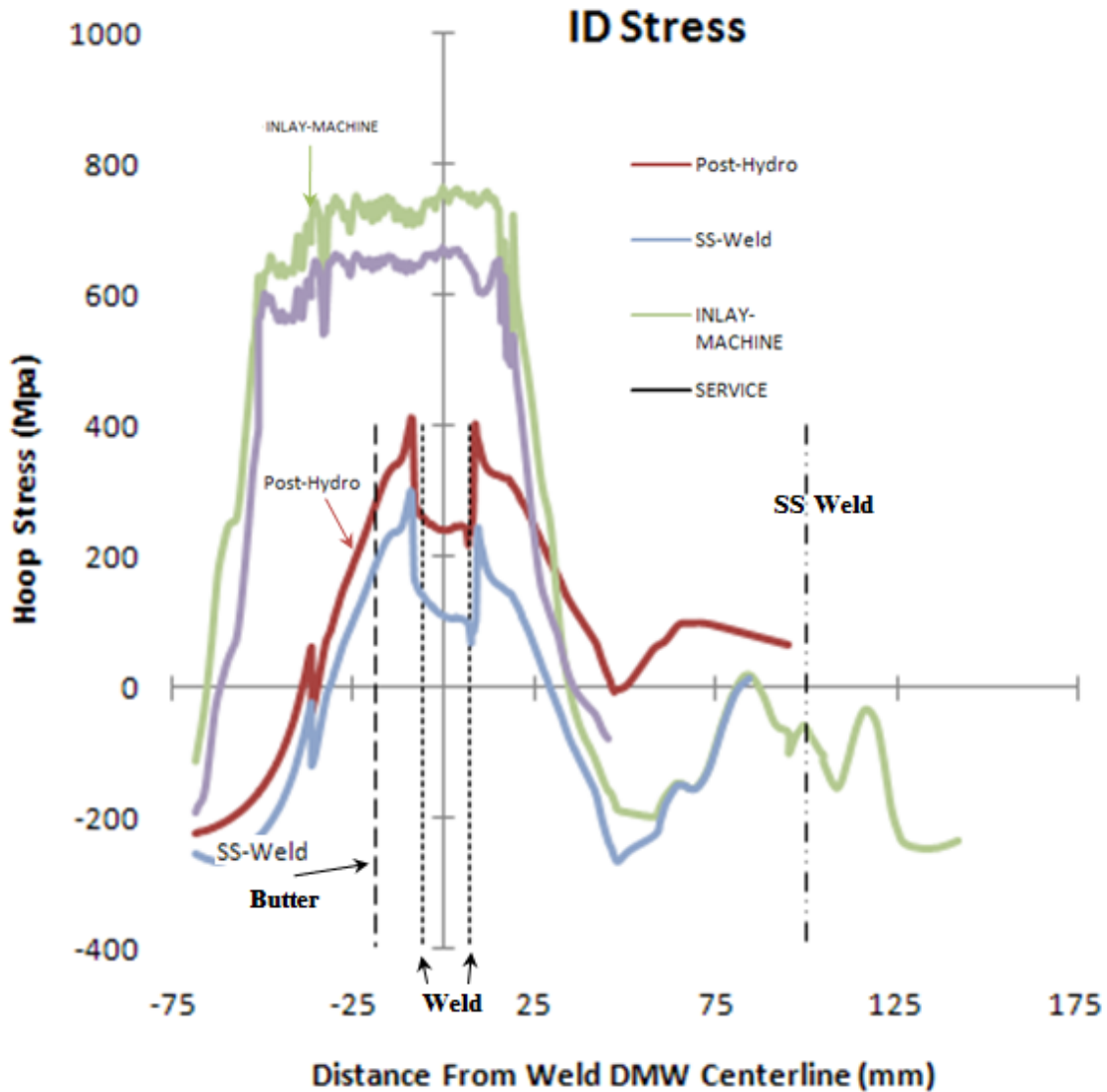


Figure 42 Hoop weld residual stress line plots along the inner surface of the DM weld at different stages of the analysis for Model 2

If the stainless steel safe end to pipe weld is too far from the DM weld the benefit of the SS weld is not realized. If a repair occurs after the SS weld, it will likely remove all benefit of the SS weld. Such situations should be carefully examined in nuclear plant repair procedures since these pipes are more likely to experience PWSCC.

Figure 41 and Figure 42 also show the effect of the inlay on the axial and hoop weld residual stresses. Both stress components are quite high.

Figure 43 shows axial weld residual stress line plots through the pipe wall at the weld centerline and compares the stress to those from Model 1. The centerline plot is at a temperature of 300C only while the bottom plot at the DMW/SS line include pressure loads. These plots are normalized by the thickness (recall that Model 1 is 68mm thick and Model 2 is 86 mm thick).

Very high levels of tensile axial weld residual stress develop near the pipe ID. The Model 2 stresses remain tensile for a distance of almost 30% through the pipe wall along the DMW/SS interface. This is significant since tensile stresses exist for a large distance into the Alloy 182/82 material for Model 2. ***Since the inlay thickness (after machining) is 3mm, this represents only 3.4% of the wall thickness for Model 2!*** The compressive stresses for Model 2 are larger in magnitude compared with Model 1 along both interfaces (Figure 43). Figure 44 illustrates the axial weld residual stresses in the DMW/Butter for both Models 1 and 2. The axial stresses for Model 2 extend to nearly 30% of the pipe wall.

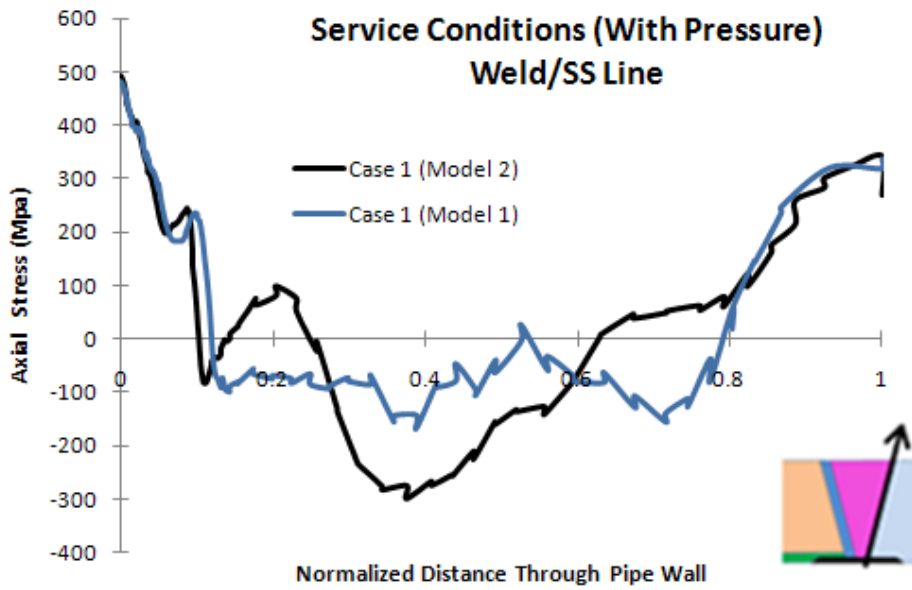
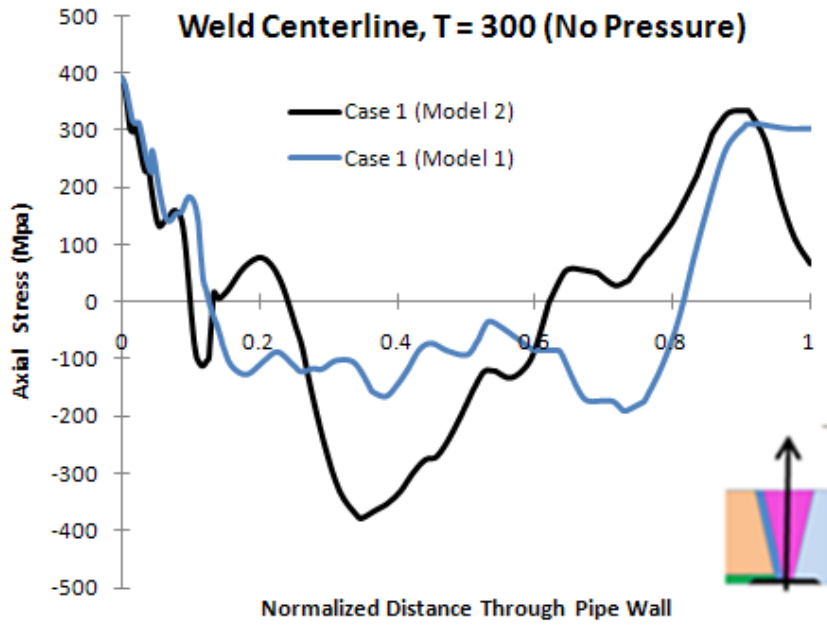


Figure 43 Axial stresses at the DM weld centerline for Models 1 and 2.

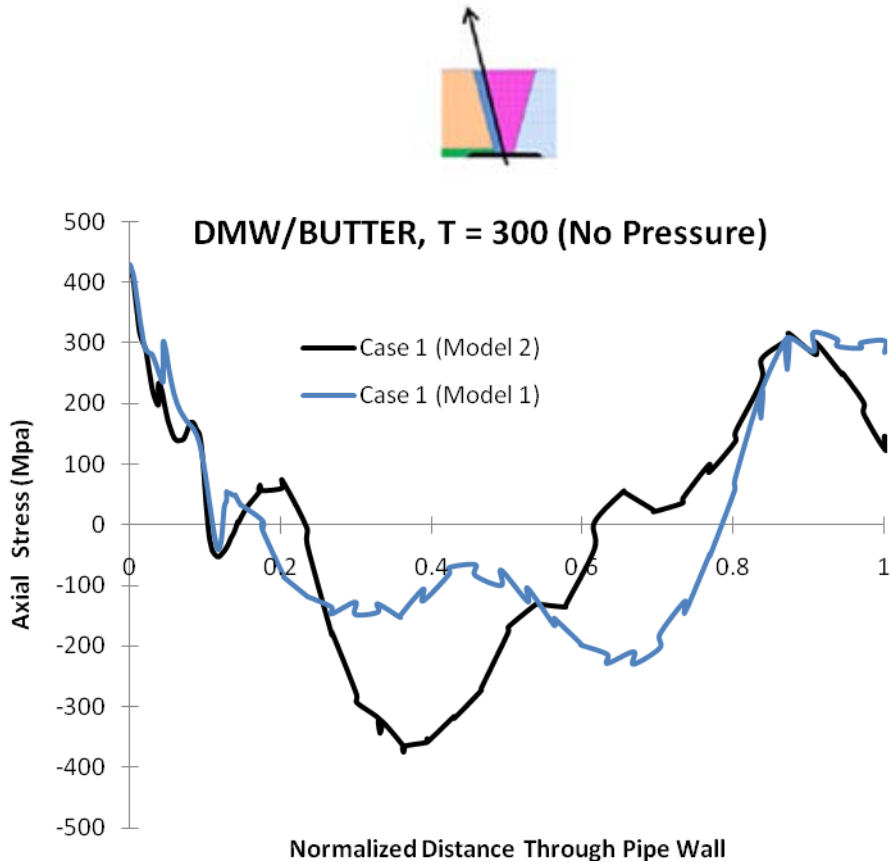


Figure 44 Axial stresses at the DM weld interfaces for Models 1 and 2

4.2.1.2 Cases 2 and 3 for Model 2

From Table 2, Case 2 represents a 12% pre-service/12% PWSCC repair and Case 3 represents a 12% PWSCC repair only. This repair depth is small compared with the repair depth considered with Model 1. Figure 45 illustrates the through-wall thickness weld residual stresses (axial) at the weld centerline (top) and the DMW/SS line (bottom). It is seen that the stresses are quite similar between Cases 1 to 3. Case 2, a 12% pre-service/12%PWSCC repair, is the worse case since the stresses rise sharply to about 200 MPa just after crossing the zero stress line. However, the differences between the 12% deep repair cases are relatively small. Figure 46 shows a comparison of stresses at the DMW/butter and the nozzle/butter line. There are some differences, especially along the nozzle/butter line. However, the PWSCC crack growth should not differ significantly between the cases.

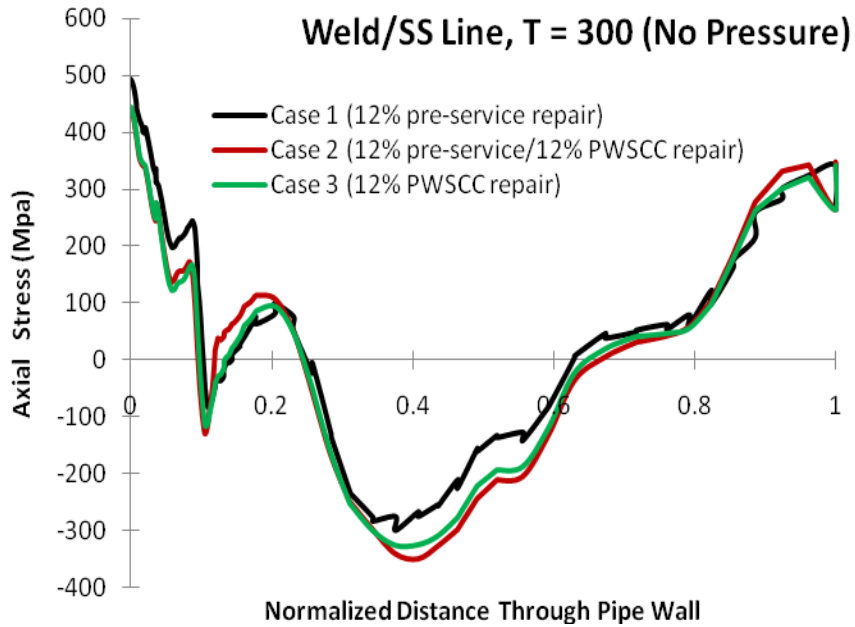
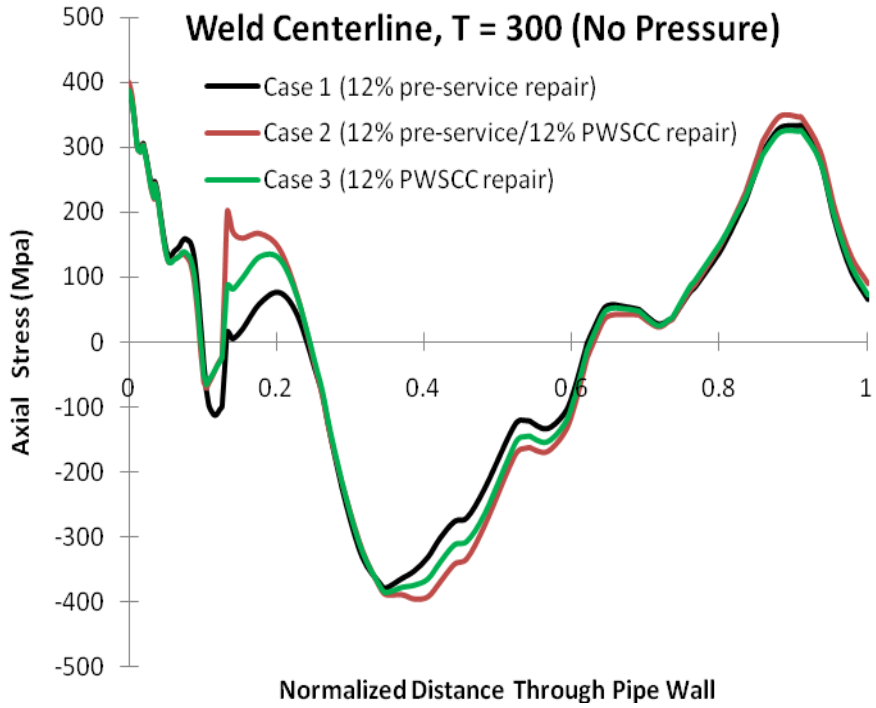


Figure 45 Weld residual stresses for Model 2, Cases 1 to 3 (center line and DMW/SS line).

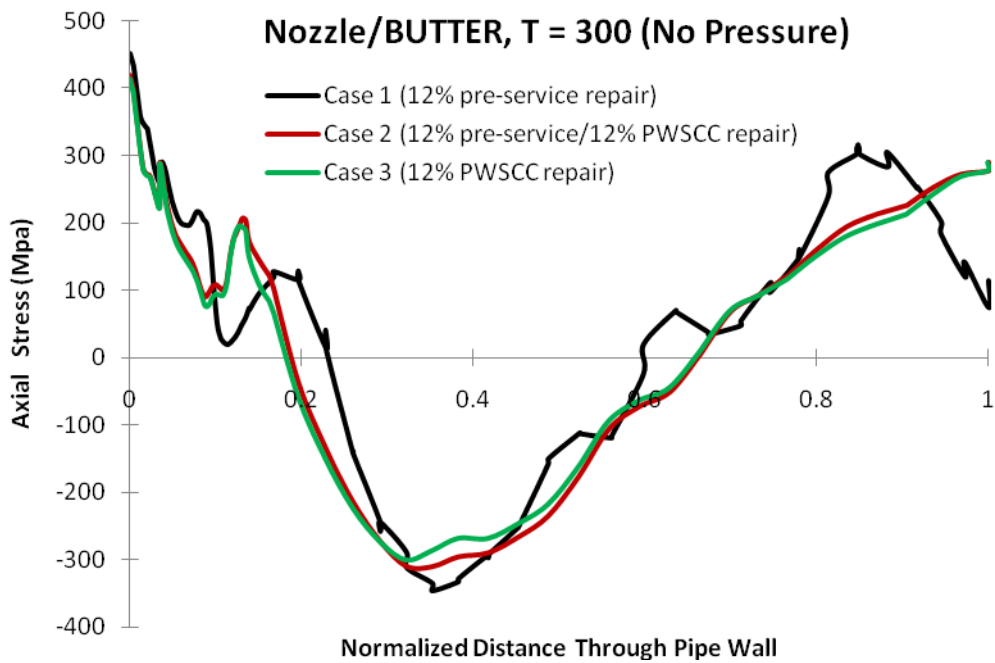
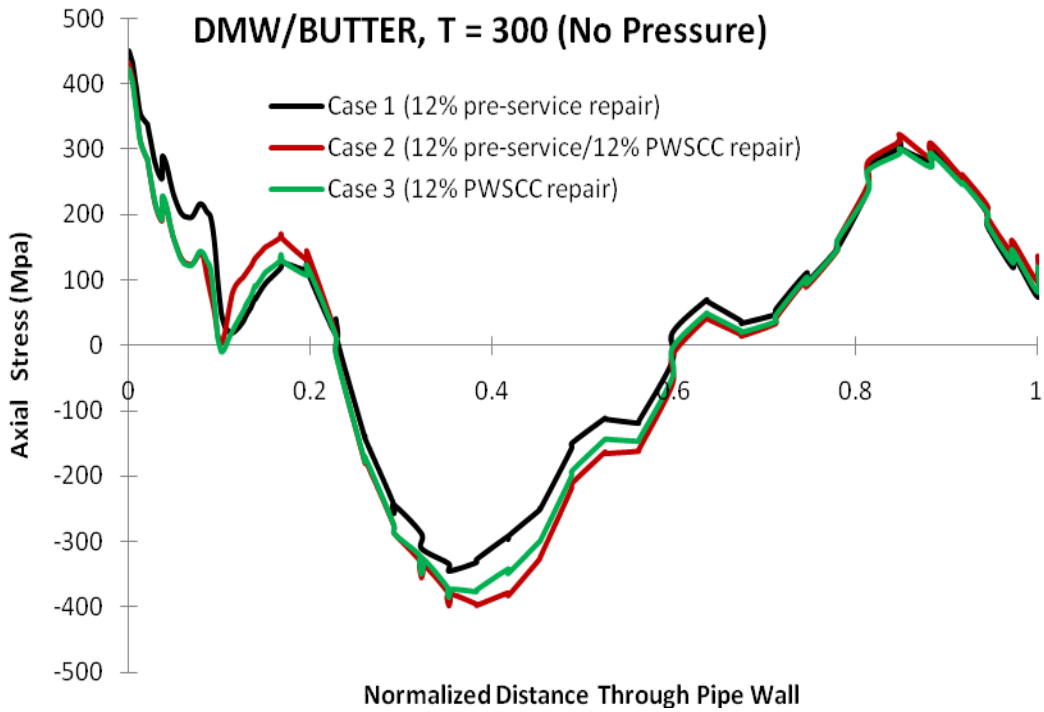


Figure 46 Weld residual stresses for Model 2, Cases 1 to 3 (DMW/butter and nozzle/butter).

4.2.1.3 Cases 4 and 5 for Model 2

To complete the weld residual stress distributions for Cases 4 to 7 are presented here, with emphasis on the 50% repair cases (see Table 2). More details of the 25% repair cases (Cases 6 and 7) along with WRS with no inlay are included in Appendix C for reference. Figure 47 shows the axial WRS distribution for the Model 2, PWSCC repair cases considered here. These are at 300C, with no pressure applied. It is clear that the deeper PWSCC repair cases will result in the more rapid through-wall circumferential crack growth at all locations. In particular, the 50% PWSCC repair has the lowest magnitude of compressive stresses (which will slow down crack growth as the crack transgresses this compressive field), and the longest depth through the nozzle wall where tension prevails. Note also by comparison to Figure 34 and Figure 35 (model 1 50% PWSCC results) that Model 1 has a similar WRS field except that the axial stresses on the OD remain compressive for Model 1. This means that the circumferential length of the crack for Case 1 will be longest for the 50% PWSCC cracks.

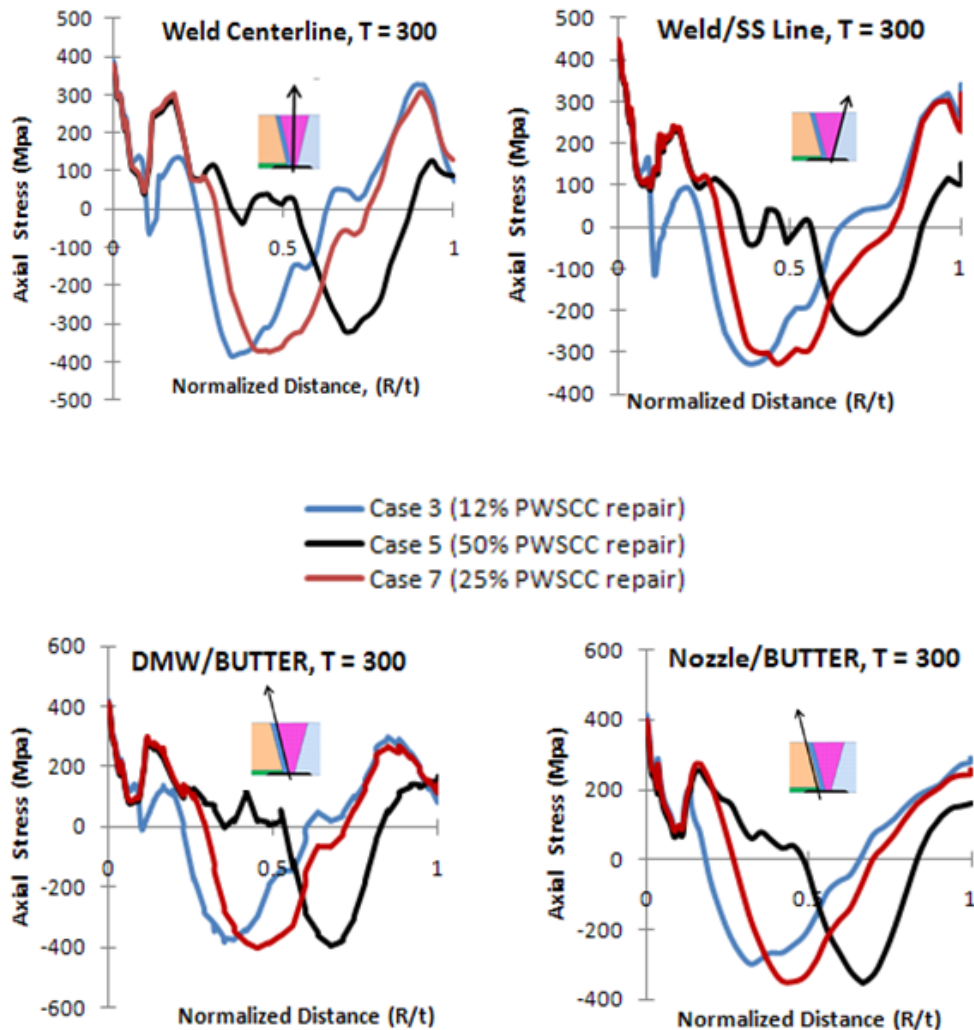


Figure 47 Axial through-wall WRS for PWSCC repairs for Model 2.

Figure 48 shows the pre-service repair through thickness axial WRS at the weld centerline and along the dissimilar metal weld/butter line (the other locations at the nozzle/DMW and DMW/SS lines are similar). The 50% pre-service repair case showed slightly higher compressive stress mid-wall, which will increase the crack growth rate as compared to the other cases.

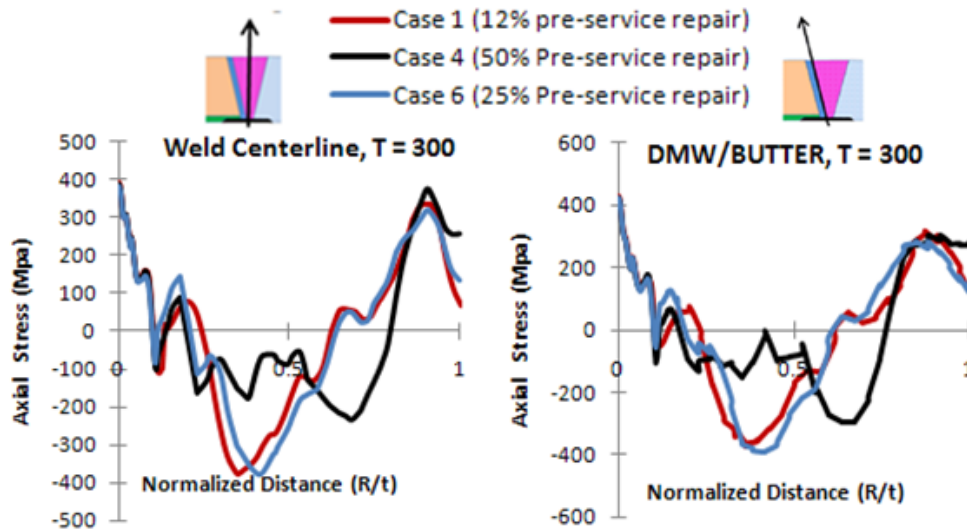


Figure 48 Axial through-wall WRS for Pre-service repairs for Model 2.

Finally, Figure 49 compares weld residual stresses for two of the different types of repairs considered here (50% pre-service and 50% PWSCC) for Model 2. These represent Cases 4 and 5 from Table 2. The PWSCC repair eliminates the stress benefit of the stainless steel safe-end weld. Because the inlay is applied after all other processes are completed, the stresses in the inlay itself, for both Models 1 and 2, are very similar over the inlay and slightly beyond it (about 10% of nozzle wall on average). The inlay produces tensile axial WRS in this region. The effect of the repair depth is only important if the depth is considerably deeper than the inlay depth. Here, for the three repair depths considered (12%, 25%, and 50%), only repairs greater than 25% had an important effect on the final inlay stresses. This is because the inlay dominates the WRS for depths less than about 10% of the nozzle wall for 3 mm deep inlays.

Appendix C provides WRS results for some of the other cases listed in Table 1 and Table 2 that were not presented in this section. In particular, the WRS field for these model geometries with and without the stainless steel weld (with no inlay are presented) for both model geometries for cases of different repair depths. These can be used as references values for PWSCC analyses performed in the future.

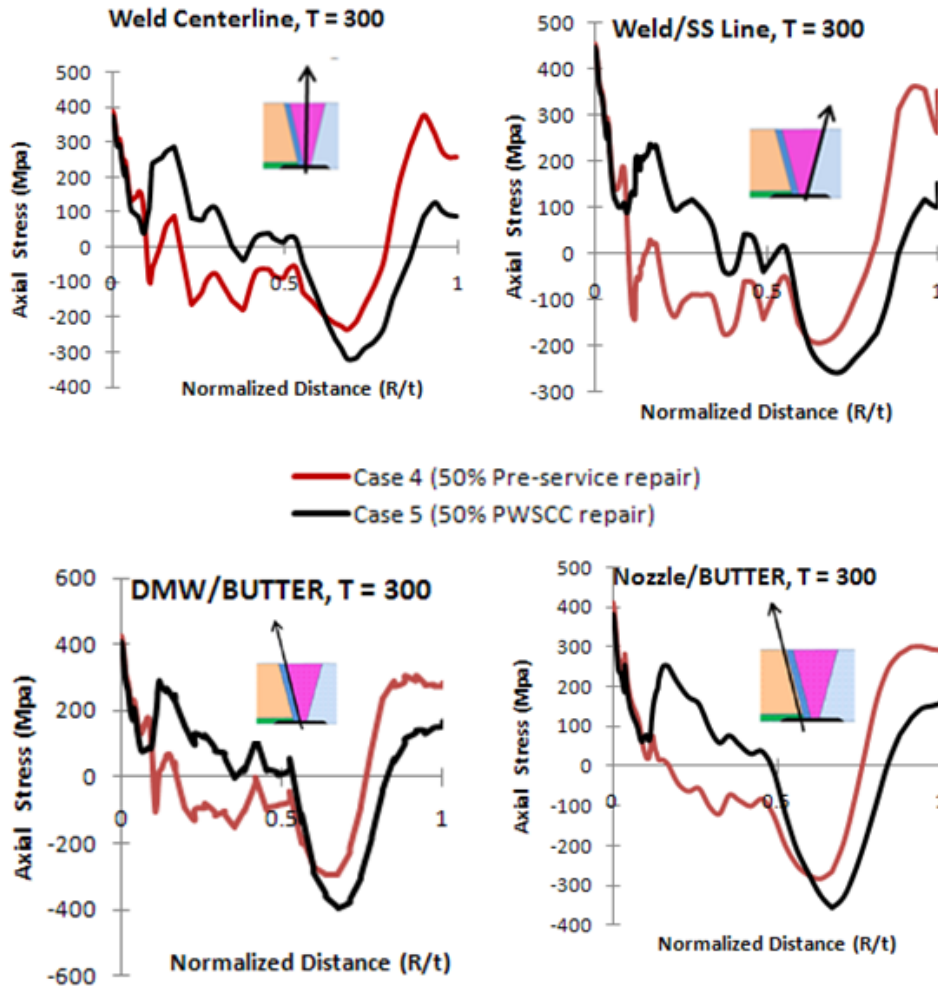


Figure 49 Comparison of the 50% pre-service and PWSCC repair cases for Model 2.

5 Crack Growth Efforts

ASME Section XI Draft Code Case N-776, “Nickel Alloy Reactor Coolant Inlay and Onlay for Mitigation of PWR Full Penetration Circumferential Nickel Alloy Welds in Class 1 Items,” states that it is required to demonstrate that a postulated surface breaking planar flaw that is 1.5mm deep will not grow through thickness due to fatigue for the life of the inlay. Only fatigue is required because the Alloy 52 material used for the inlay is assumed to be non-susceptible to PWSCC. In this section of the report, using current PWSCC growth rate data on Alloy 52/152, PWSCC growth analyses are conducted for a similar postulated surface breaking flaw in the inlay. These analyses will add insight into the in-service inspection intervals required for welds mitigated with inlays.

5.1 Determination of Crack Growth Parameters

5.1.1 PWSCC growth model – MPR-115

PWSCC of the inlay and main DM weld is the only subcritical cracking mechanism that is considered in this study. For many of the applications where inlays may be used, the fatigue usage factor is small and therefore can be neglected. Over the recent years, researchers have conducted laboratory experiments to measure the growth rate of PWSCC in Alloy 82/182 DM welds. The collective experimental data used in this effort have been gathered and analyzed by EPRI in MRP-115 [31]. In this effort, a distribution of crack growth rates as a function of temperature, alloy, and crack orientation were developed. These data were fit to the following functional form:

$$\dot{a} = \exp\left[-\frac{Q_g}{R}\left(\frac{1}{T} - \frac{1}{T_{ref}}\right)\right] \alpha f_{weld} f_{alloy} f_{orient} K^\beta \quad (2)$$

where

- \dot{a} = crack growth rate at temperature T in m/s
- Q_g = thermal activation energy for crack growth = 130 kJ/mole
- R = universal gas constant = 8.314×10^{-3} kJ/mole-K
- T = absolute operating temperature at the crack location in K
- T_{ref} = absolute reference temperature to normalize data = 598.15K
- α = power law constant = 9.83×10^{-13}
- f_{alloy} = 1.0 for Alloy 182
- f_{orient} = 1.0 for growth parallel to dendrite solidification direction
- f_{weld} = 1.49 for 75th percentile of data
- K = crack stress intensity factor, MPa-m^{0.5}
- β = exponent = 1.6

The uncertainty in the crack growth rate was characterized by f_{weld} . In [31], the MRP disposition curve for Alloy 182 was defined as the 75th percentile of the distribution of the crack growth data. This curve was used as a baseline in this investigation.

5.1.2 Recent A52/152 PWSCC Data

Alloy 52/152 weld metal is known to be less susceptible to PWSCC than the lower Chromium content Alloy 82/182. However, even though the material is labeled as being less susceptible to stress corrosion cracking, it is not resistant to cracking. Current research is being conducted by both the US NRC and the nuclear industry on the cracking behavior of Alloy 52/152 in PWR environments. Many issues such as heat treatment, cold work, and hold time are currently under investigation. The results from these efforts are suggesting that even though the crack growth behavior is scattered, it is on average lower than the crack growth rate measured in the Alloy 82/182 material. In a recent [32] presentation given by Pacific Northwest National Laboratory (PNNL), the collection of current Alloy 52/152 crack growth rate data at operating pressure and temperature were presented. This data is reproduced in Figure 50. Also included with this figure is the Alloy 182 disposition curve from MRP-115 [31], and offsets of that in multiples of 10, i.e., 10, 100, 1000.

The data in this figure represents compact tension PWSCC growth experiments conducted at PWR operating conditions. Three laboratories conducted these experiments as part of this data set, i.e., Pacific Northwest National Laboratory (PNNL), Argonne National Laboratory (ANL) and General Electric (GE). Due to the difficult nature of conducting these experiments and the complicated procedures to initiate and sustain PWSCC growth in these materials, different hold times at constant load were employed. In between these regions of constant load, high R-ratio (minimum over maximum stress) fatigue was used to re-initiate the crack growth, which was then transitioned back to PWSCC. The labels in the figure document the hold time at constant load for each data point. A label of “constant” represents a hold time over 100 hours.

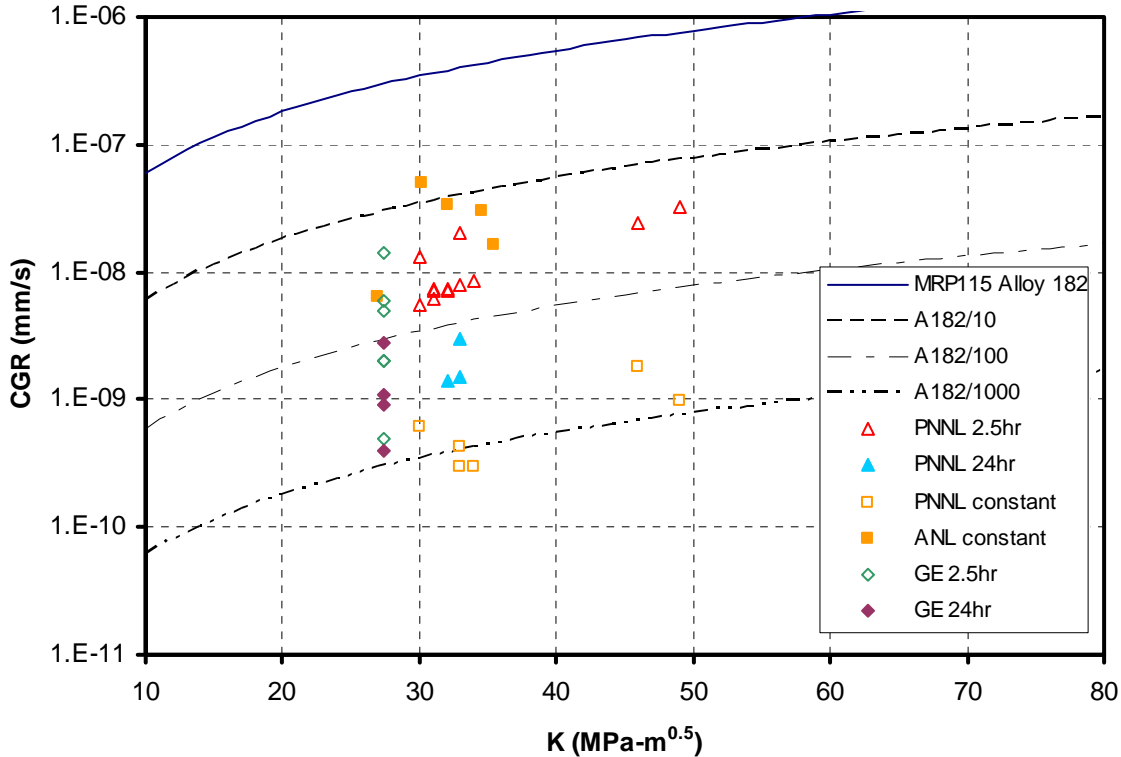


Figure 50 Comparison of Alloy 52/152 PWSCC growth test data to MRP-115 disposition curve

As shown in Figure 50, the data generated by PNNL suggests that as the hold time during these experiments was increased, the crack growth rate decreased by two orders of magnitude. For the same hold time, the ANL data was higher than the PNNL data by two orders of magnitude. Similarly, the GE data showed a decrease in crack growth rate by one order of magnitude as the hold time increased by a factor of 10. Clearly, this data suggests that the hold time is affecting the crack growth rate; however, the discrepancy between the ANL and PNNL data at constant load also illustrates the effects of different material heats and testing capabilities. Therefore, in conducting flaw growth analyses using this data, the uncertainty in the crack growth rate must be investigated. For the analyses conducted in this effort, the MRP-115 Alloy 182 data with a factor of 100 offset (A182/100) will be used as the baseline case. Changes to the crack growth rate will be investigated in the sensitivity study.

5.2 Idealized Flaw Growth

Following the ASME Section XI flaw evaluation guidelines, crack growth calculations were conducted to assess the effectiveness of the inlay as a PWSCC mitigation technique. In this section, idealized flaw analyses, i.e., surface flaws with a semi-elliptical crack front and through-wall flaws with a radial crack front, were conducted. For these analyses, it was assumed that the geometric shape of the initial flaw, i.e., semi-elliptical for surface flaws, did not change as the crack grew. As indicated in the previous section, it is assumed that the crack tip stress intensity factor controls the driving force for these flaws. A description of the stress intensity solution is provided in the next section.

5.2.1 Stress intensity solutions

For a cracked structure under remote or local loads, the stress intensity factor (K) is a measure of the stress field ahead of the crack. In elastic fracture mechanics, when the applied value of the stress intensity exceeds the materials critical value, crack advance occurs. For subcritical cracking, the process of crack advance is linked to the applied values of the stress intensity through curve fits with extensive experimental data, see Figure 50. The stress intensity is not only a function of the loading, but also the global component geometry and local crack shape. Over the years, many researchers have developed K-solutions for circumferential and axial surface and through-wall cracks in cylindrical vessels based on finite element parametric analyses. In all cases, the K-solutions were developed using the principle of superposition. The principle of superposition states that the solution for a multiple load case is equal to the sum of the results from the individual load cases. These individual cases can then be combined to describe a more complicated loading history.

For the idealized crack growth analyses conducted in this investigation, K-solutions for both surface and through-wall cracks in cylinders from API-579 were used. The K-solutions for a circumferential surface crack on the inside pipe diameter are given in [33]. Per [33], given that a through-wall stress distribution in an uncracked cylinder can be represented by a polynomial of the form

$$\sigma(x) = \sigma_0 + \sigma_1 \left[\frac{x}{t} \right] + \sigma_2 \left[\frac{x}{t} \right]^2 + \sigma_3 \left[\frac{x}{t} \right]^3 + \sigma_4 \left[\frac{x}{t} \right]^4 \quad (3)$$

when a crack is introduced into this stress field, the stress intensity can be calculated as

$$K_I = \left(\sigma_0 G_0 + \sigma_1 G_1 \left[\frac{a}{t} \right] + \sigma_2 G_2 \left[\frac{a}{t} \right]^2 + \sigma_3 G_3 \left[\frac{a}{t} \right]^3 + \sigma_4 G_4 \left[\frac{a}{t} \right]^4 + \sigma_5 G_5 \right) \sqrt{\frac{\pi a}{Q}} \quad (4)$$

where Q is the surface-crack shape parameter and G_i are the influence functions¹, which are non-dimensional representations of K.

The solutions from [33] were generated for R/t values from 3 to 100, c/a values from 1 to 32 and a/t values from 0.2 to 0.8. Influence functions G_0 and G_1 , and G_5 (global in-plane bending) were

¹ Note that σ_5 is the global in-plane bending stress, and G_5 is the influence function for this stress.

generated using parametric finite element techniques. The influence function G_2 , G_3 , and G_4 are inferred from the weight function formulas given in [34]. For the case of a circumferential semi-elliptical surface crack, the crack growth at both the deepest (90 degrees) and surface (0 degrees) locations are calculated and applied to the initial crack sizes. The finite length surface crack is always assumed to remain semi-elliptical.

There are several shortcomings to these solutions. First, the influence functions were only generated for a/t values from 0.2 to 0.8. This becomes a problem when trying to predict crack behavior from initiation to failure. Therefore, several assumptions are made. First, it is assumed that the influence functions can be extrapolated from $a/t=0.8$ to $a/t=1.0$. Secondly, a solution by Chapuliot [34] is used for a/t approaching 0. Linear interpolation is used between these values and Anderson's results at $a/t = 0.2$.

In addition to the elliptical surface crack results, K solutions for $a/c = 0$ (infinitely long surface crack) were also used from [33]. Since long surface crack K-solutions are currently not available, it is assumed that for surface cracks with c/a greater than 32, the K solution at the free surface is equal to the K-solution at $c/a = 32$. At the deepest point, the K-solutions equals that of the K-solution for $a/c = 0$. This assumption is conservative in the length direction, because as the crack length gets longer, the influence functions (hence the K-solution) at the free surface tend toward zero. By using the K-solution at the free surface equal to $c/a = 32$, slightly larger crack growth will occur, producing conservative time to leakage probabilities.

The K-solutions for a circumferential through-wall crack in a pipe are given in [35]. These solutions were generated for R/t values from 1 to 100 and to crack lengths of about 66 percent of the circumference. The solutions were generated for both the inside and outside surface of the through-wall crack, however; only the G_0 , G_1 and G_5 influence functions are available. In [35], the through-wall crack K solutions were curve fit and the coefficients were presented for R/t values of 1, 3, 5, 10, 20, 60, and 100. These coefficients are used in this study and linear interpolation was used to predict the coefficients for other R/t values. The influence function on both the inside and outside surface of the through-wall crack are calculated, and then averaged to get the K-solution for through-wall-crack growth.

5.2.2 Conditions for crack growth

Since only PWSCC was considered in this study, the loads defined for crack growth will be limited to this mechanism. Since PWSCC grows under static load conditions, only the loads present during normal operation will be considered for subcritical crack growth. Therefore, the loads (membrane and global bending) considered include:

- Temperature
- Pressure
- Dead weight
- Thermal expansion
- Welding residual stress

For the analyses conducted in this study, the axial loads and the pressure were held constant, while the bending stress, weld residual stress and temperature were varied in a sensitivity study. The baseline loads used in these analyses are:

- Bending stress = 96.5 MPa (14 ksi) - varied in sensitivity analysis
- Axial stress = 38.6 MPa (5.6 ksi) - includes pressure loading = 15.5 MPa (2250 psi)
- Temp = 326 C (620F) - varied in sensitivity study

Using this list and the definitions from the previous section, the total stress used for crack growth is given as

$$\sigma_{CG} = (\sigma_{0A} + \sigma_{0CFP} + \sigma_{0WRS}) + \sigma_{1WRS} \left[\frac{x}{t} \right] + \sigma_{2WRS} \left[\frac{x}{t} \right]^2 + \sigma_{3WRS} \left[\frac{x}{t} \right]^3 + \sigma_{4WRS} \left[\frac{x}{t} \right]^4 + \sigma_B \quad (5)$$

where

σ_{0A}	=	Axial stress
σ_{0CFP}	=	Crack face pressure
σ_{nWRS}	=	Weld residual stress curve fit coefficients
σ_B	=	Bending stress
t	=	Wall thickness
x	=	Distance from pipe inner diameter

The welding residual stress (WRS) terms used in these analyses are described in the next section.

5.2.3 Welding residual stress

Welding residual stress is one of the major drivers to stress corrosion cracking and must be included for proper predictions of subcritical crack growth. Issues such as weld repairs, grinding, etc., will all impact the calculated crack growth rates. For these analyses, the welding residual stresses described in Section 4 were used. These through-thickness stress profiles were fit to a 4th order polynomial using the standard Microsoft Excel routine. A 4th order fit was used to be compatible with the influence functions described earlier in this report. An example of the fit relative to the finite element results is shown in Figure 51.

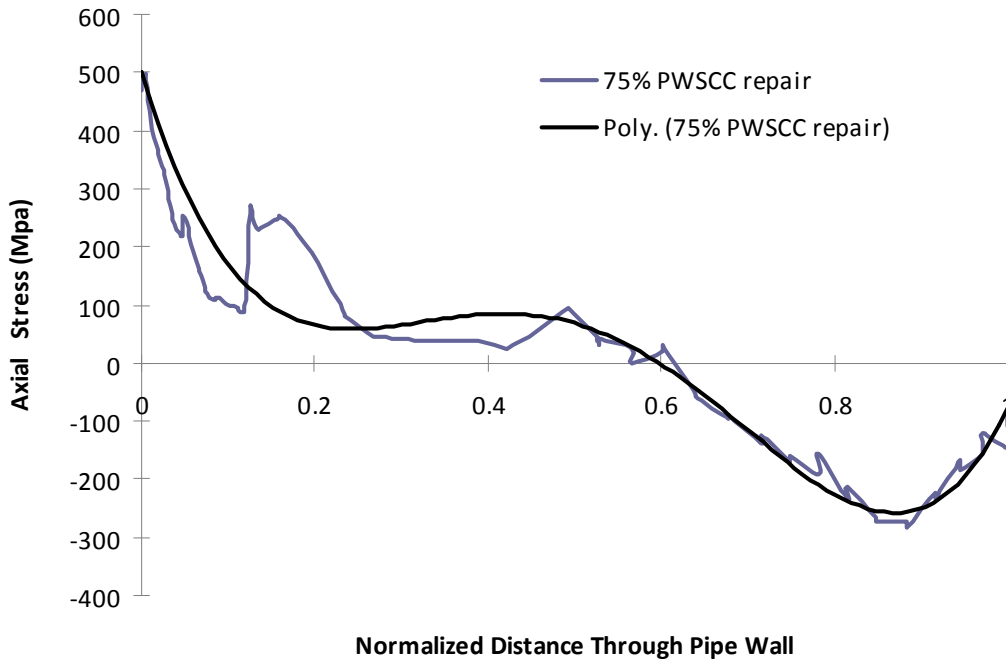


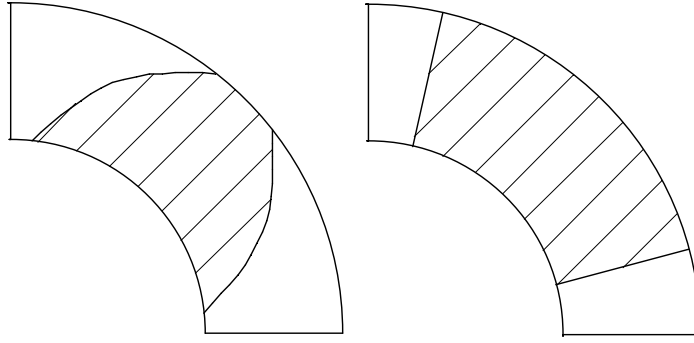
Figure 51 Weld residual stress curve fit

A couple of points to be made about making this curve fit approximation:

- A 4th order fit to the FE results does not always produce an ideal representation of the stress. In these cases, uncertainty is added to the crack growth results. As described in Section 5.5, the analyses used for natural growth of the cracks do a much better job of approximating the through-thickness stress distribution. As those results illustrate, the difference due to this uncertainty is small.
- In some cases, the curve fit was forced to match the behavior near the ID surface. While this did not drastically change the coefficient of determination (R^2) for the fit, it did provide a more accurate representation of the stress field on the inner 25 percent of the wall thickness.

5.2.4 Transition from surface crack to through-wall crack

As an internal surface crack begins to penetrate the wall thickness, only a small breach of the pressure boundary is first observed. For an internal surface crack that becomes a leaking crack, the crack length on the OD is much smaller than that on the ID due to the previous crack growth. In idealized through-wall behavior, the crack front runs radially, and the actual OD crack length is longer than that on the ID, see Figure 52.



(a) Penetrating crack (b) Idealized through-wall crack

Figure 52 Illustration of penetrating cracks and idealized through-wall crack

For the crack shapes in Figure 52a, general stress intensity solutions do not exist. There are flat plate solutions in the WinPraise manual [36], and cylinder solutions for $R/t=8$ that were developed through the NURBIM program [37], but the accuracy of those solutions relative to the low R/t values for primary piping is unknown. Therefore, for this study, it will be assumed that, as the surface crack penetrates the wall thickness, an idealized through-wall crack with the same crack area will be formed. The assumption is conservative from a crack growth/stability standpoint, but may be non-conservative from a leakage perspective.

5.3 Crack Stability

The behavior of through-wall cracks and surface cracks in nuclear grade piping has been the subject of many experimental programs conducted by the NRC. Many reports have been written with the majority of the past research summarized in [38]. This report deals with flaw stability in base metals and similar metal welds. Although limited research has been performed on flaw stability for DM welds, the NRC published a technical note [39] that recommends several methodologies for handling cracks in DM welds.

In cases of elastic-plastic fracture, which will be prevalent for DM welds, the operating stresses used to calculate critical flaw size are independent of the local welding residual stress. The plasticity that forms during the deformation process eliminates the influence of the local weld residual stresses. Therefore, for elastic-plastic crack stability, the total stress used in making critical crack determinations is given as

$$\sigma_{CS} = (\sigma_{0A} + \sigma_{0CFP}) + \sigma_B \quad (6)$$

The Section XI IWB-3640 and Appendix C equations account for EPFM fracture behavior in a very simplified, but effective manner. The approach is to use a correction factor on the limit-load solution, where that correction factor is a function of the toughness of the cracked material, as well as the pipe diameter. This approach was first developed by Zahoor and Gamble for the EPRI as the technical basis for the stainless steel SAW crack evaluations [40], and later for ferritic pipe flaw evaluations [41]. This EPFM correction factor is called a Z-factor, which is simply the thin-shell Net-Section-Collapse [42] predicted maximum load divided by the

maximum load determined from the GE/EPRI J-estimation scheme for circumferential through-wall cracks in pipes [43]. *The base-metal strength was used in the GE/EPRI scheme for Z-factors for welds.* Although the ratio of limit load/EPFM varies with crack length for the through-wall-crack GE analysis, the Z-factor was conservatively taken as the maximum value. This Z-factor changes with pipe diameter, i.e., a Z-factor equation exists as a function of pipe diameter for each material. Even though the Z-factor was developed from a through-wall-crack analysis, it is applied to surface-cracked pipes. From the prior discussion on constraint differences between surface and through-wall-cracked pipes, this is a conservative approach. However, to date a Z-factor for cracks in Alloy 82/182 welds has not been incorporated into the Code.

The Z-factor used in this study [44] was taken from a series of analyses conducted using the LBB.ENG2 [45] J-estimation scheme and limit-load analyses using the stainless steel base metal strength. The J-R curve used for the Alloy 182 weld metal came from a CE cold-leg DM weld [46]. The flow strength of the stainless steel base metal was assumed to be 314 MPa.

5.4 Idealized Flaw Growth Results

For the idealized flaw analyses, the calculations were conducted using the parameters in Section 5.2.2. An example of the crack growth results for Model 1 with a 50% PWSCC repair before the 3mm inlay (Case 2) is shown in Figure 53. In this figure, the solid diamonds are the crack depth results and the solid squares are the crack length results. The large change in slope for the crack depth results at about 11 years represents the crack tip as it crosses the inlay-DM weld boundary. At this point, the crack growth rate increases until the crack penetrates the wall in about 16 years. The through-wall crack continues to grow until rupture at 25 years. Credit for leakage detection was not considered in these analyses.

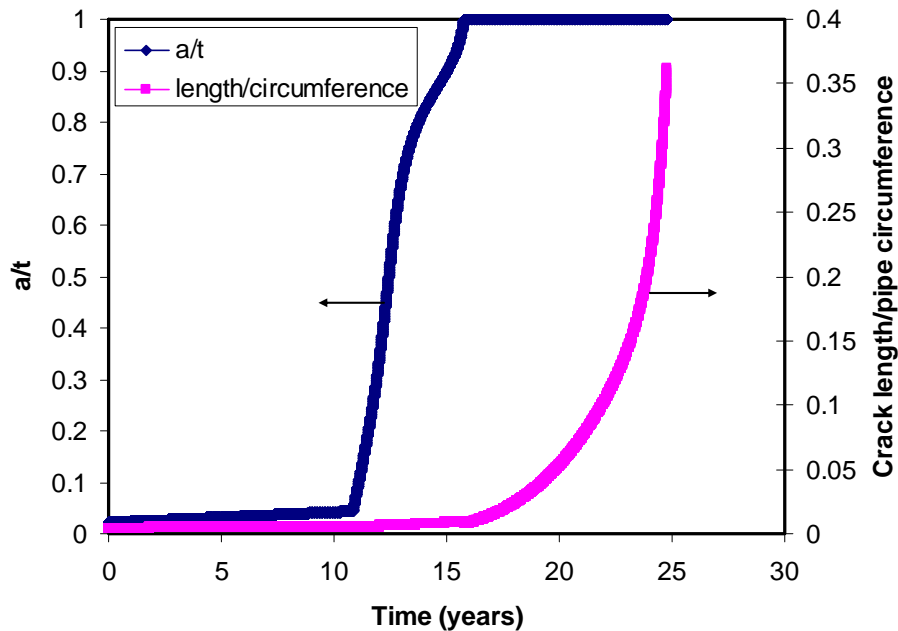


Figure 53 Crack growth results for PWSCC repair with inlay

5.4.1 Effects of repair assumptions

In the first set of analyses, the weld repair and inlay assumption were varied. For each of the cases, the following variables were held constant:

- Bending stress = 96.5 MPa (14 ksi)
- Axial stress = 38.6 MPa (5.6 ksi) - includes pressure loading = 15.5 MPa (2250 psi)
- Temp = 326 C (620F)
- Crack growth rate = A182/100
- Initial crack size: 1.5 mm deep and 10 mm long.

The inlay and repair cases used are fully described in Section 4, but are summarized here for convenience.

1. The first case is Model 1 with a 50% deep pre-service repair. This repair occurs before the stainless steel safe end weld. The 3-mm inlay is placed after the stainless steel safe end weld.
2. The second case is Model 1 with a 50% deep PWSCC repair. This repair occurs after the stainless steel safe end weld but before the 3-mm inlay weld.
3. The third case is Model 1 with a 75% deep pre-service repair. This large repair was chosen to match that of a recent inlay submittal. The repair occurs before the stainless steel safe end weld. The 3-mm inlay is placed after the stainless steel safe end weld.
4. The fourth case is Model 1 with a 75% deep PWSCC repair. The repair occurs after the stainless steel safe end weld but before the 3-mm inlay weld.
5. The fifth case is Model 1 with a 50% deep pre-service, which occurs before the stainless steel safe end weld and a 75% deep PWSCC repair, which occurs after the safe end weld but before the 3 mm inlay weld.
6. The sixth case is the same case Case 1, but contains a 6-mm inlay weld.
7. The seventh case is the same as Case 2, but contains a 6-mm inlay weld
8. The eighth case is Model 2 with a 12% back-chip and re-weld repair before the stainless steel safe end weld. The 3-mm inlay occurs after the safe end weld.
9. The ninth case is Model 2 with a 50% deep PWSCC repair after the stainless steel safe end weld, but before the 3-mm inlay weld.

The results from the idealized flaw analyses for these cases are given in Table 3. Comparing the first five cases illustrate that there is not a large difference in the time it takes for the crack to cross from the inlay into the original Alloy 182 weld. This similarity is due welding residual stress behavior from the inlay controlling the through-thickness stresses in the first 3mm of the wall thickness. The most severe case is the 75% deep PWSCC weld repair, which had a time through the inlay of only 7.5 years. Realistically, a 75% deep weld repair is not practical since much of the base metal on both sides would have to be removed to accommodate such a deep repair. The other four cases gave a time through the inlay of about 10 years. Also, the time to through wall leakage is much greater for the 50% deep pre-service then for the 50% deep PWSCC repair. This difference is due to the location where the welding residual stress crosses through zero. As shown in Section 4, for the PWSCC repair, the welding residual stress remains tensile until about 50% of the wall thickness, which the pre-service repair becomes compressive at about 15% of the wall thickness. For these cases, the effect of the stainless steel safe end weld counteracts the effects of the pre-service weld repair and reduces the through-wall stress. The high ID stress in these cases is due to the inlay.

Table 3 Idealized flaw analysis results for a variety of repair and inlay configurations

Flaw Analysis Case #	WRS case and # from Table 1 or Table 2	Model #	Inlay depth	Time, years		
				Inlay	Through-wall	Rupture
1	50% pre-service repair, Case 1	1	3mm	9.7	25.1	33.7
2	50% PWSCC repair, Case 2	1	3mm	10.9	15.9	24.8
3	75% pre-service repair, Case 3	1	3mm	10.1	31.0	39.7
4	75%PWSCC repair, Case 4	1	3mm	7.5	12.1	23.3
5	50%preservice-75%PWSCC repair, Case 5	1	3mm	10.3	15.1	24.0
6	50% pre-service repair, Case 6	1	6mm	23.6	38.8	46.0
7	50% PWSCC repair, Case 7	1	6mm	28.5	33.4	40.6
8	12% pre-service repair, Case 1	2	3mm	10.0	>100	>100
9	50% PWSCC repair, Case 5	2	3mm	10.3	16.1	23.7

The effects of the inlay depth are illustrated in Cases 6 and 7 in Table 3. As mentioned earlier, the initial flaw depth is the same for these cases, but the inlay depth is doubled. As expected for the 6mm inlay, the time from the start of the analysis to the time when the crack passes out of the inlay into the Alloy 182 material is about double that of the 3-mm inlay. In addition, the time between leakage and the time the crack passes through the inlay is the same for both the 3mm and 6mm deep inlay. This is to be expected since the welding residual stresses in the weld away from the inlay are the same for both inlay depths.

A smaller weld repair with Model 2 in investigated in Case 8. The effect of the 12% deep weld repair on the time until the crack passes through the inlay is minimal, i.e., the welding residual stresses from the inlay control the behavior. However, the time until leakage is greatly increased for the shallow repair case. In fact, for the case analyzed, the time to leakage was greater than 100 years. As discussed in Section 4, for this case, without the influence of the deep weld repair, the welding residual stress dips deeply into compression at about 40% of the wall thickness. As the crack tip approaches this point, the growth slows down tremendously until it passes through this compression region. Clearly, the depth of the weld repair has a significant influence on the time to leakage results for inlayed DM welds.

The crack arrest behavior demonstrated in Case 8 was further investigated in Case 9, which increased the weld repair to 50% deep and placed it after the stainless steel safe end weld. In this case, the times through the inlay, to leakage and to rupture are nearly identical to those of Case 2, which was the same repair case but on Model 1 geometry. This result suggests that the geometry had little effect on the result, and size of the weld repair drove the time through wall. In addition, the weld repair size had no effect on the time through the inlay since Cases 2, 8 and 9 had about the same time through the inlay.

5.4.2 Effects of crack growth rate

In order to investigate the effects of the crack growth rate uncertainty on the time to leakage and rupture, Case 2 from Table 3 was revisited with different crack growth rates. Using the trends shown in Section 5.1.2, the crack growth results were generated and are shown in Table 4. A quick statistical analysis of the data from Section 5.1.2 confirmed that the A182/1000 represented about the 5th percentile, while A182/30 represented the 95th percentile of the data

presented. Therefore for these analyses, these growth rates were chosen. As expected the crack growth rate has a large influence on the time to leakage and rupture. In addition, the time for the crack to travel through the inlay is also highly dependent on the crack growth rate.

Table 4 Idealized flaw analysis results for a variety of crack growth rates

Flaw Analysis Case #	WRS case	Growth Rate	Time, years		
			Inlay	Through-wall	Rupture
2	50% PWSCC repair	A52=1/100(A182)	10.9	15.9	24.8
		A52=1/30(A182)	3.4	8.4	16.0
		A52=1/1000(A182)	108.5	114.9	123.2

The crack growth times through the inlay are directly proportional to the crack growth rate factor applied to the MPR-115 crack growth rate. For instance, the time through the inlay for the A182/1000 is 100 times longer than the time for the A182/10 case. This difference again illustrates the importance of the crack growth rate assumption in predicting leakage times for inlayed DM welds.

5.4.3 Effect of global bending stress

Another variable that will impact the leakage times is the level of global bending stress. For the cases presented in Table 3, the global bending stress was held constant at 96.5 MPa (14ksi). For the cases presented in Table 5, the global bending stress was varied between 48 MPa and 129 MPa. These values were chosen to bracket typical global stress values for the reactor coolant inlet/outlet nozzles. As illustrated, when the bending stress was halved, the time through the inlay was only decreased by about 15 percent, but the time to leakage was increased dramatically. For the inlay welding residual stress cases chosen in Table 5, the additional bending stress in the 96.5 MPa case was enough to increase the total through thickness stress to a level to drive the crack through-thickness. For the 48MPa bending stress, this was not the case, and the low crack driving force mid-thickness caused the crack to slow down considerably. This behavior is similar to that of the 12% deep weld repair case shown in Table 3.

Table 5 Idealized flaw analysis results for a variety of global bending stresses

Flaw Analysis Case #	WRS case	Bending	Time, years		
			Inlay	Through-wall	Rupture
4	75%(2-inch) PWSCC repair	96.5 MPa (14ksi)	7.5	12.1	23.3
		48.0 MPa (7ksi)	8.6	61.7	84.2
		129.0 MPa (18.7 ksi)	6.9	10.2	17.5

5.4.4 Effects of operating temperature

As illustrated in Equation 1, the PWSCC growth rate behavior is corrected for temperature by using an Arrhenius relationship, which has been verified by comparison with experiments in MRP-115 [31]. Since the inlay procedure may be used on both hot and cold leg components, these temperatures were investigated in the analyses. The results from the analyses are given in

Table 6. For the average (A182/100) and the 5th percentile (A182/30) crack growth rates, the operating temperatures of 327C (620F) and 288C (550 F) were considered. As expected, the effects of this temperature difference are dramatic. The time through the inlay, time to leakage, and time to rupture were increased by about a factor of 6. Even for the fastest crack growth considered, the time to leakage was over 50 years at the cold leg temperatures.

Table 6 Idealized flaw analysis results for a variety of operating temperatures

Flaw Analysis Case #	WRS case	Growth Rate	Temperature	Time, years		
				Inlay	Through-wall	Rupture
4	50% PWSCC repair	A52=1/100(A182)	327C (620F)	10.9	15.9	24.8
			288C (550F)	68.6	99.3	145.4
		A52=1/30(A182)	327C (620F)	3.4	8.4	16.0
			288C (550F)	21.0	51.7	91.4

5.4.5 Effects of flaw orientation and size

The effects of flaw orientation and flaw size on the time to leakage are given in Table 7 and Table 8, respectively. For the analyses in Table 7, the same input was used, but the flaw was orientated in the axial direction instead of the circumferential direction. The axial crack influence functions in [33] were used to predict the stress intensity factors. Hoop welding residual stress was used for the axial crack analyses. The results from these analyses suggest that the time to leakage is slightly shorter for the axial flaw as compared to the circumferential flaw. However, the time between when the flaw crosses the inlay boundary to the time to leakage is much shorter for the axial case as compared to the circumferential. This is mainly due to the hoop stress through-thickness profile. As is typical in these analyses, the hoop welding residual stress is tensile throughout the wall thickness, while the axial stress crosses into compression and back into tension. The high through-thickness hoop tensile stresses push the axial crack much faster through wall after the inlay. The differences in the time through the inlay are represented by the differences in the ID stress for the hoop and axial direction.

Table 7 Idealized flaw analysis results for different flaw orientations

Flaw Analysis Case #	WRS case	Flaw orientation	Time, years	
			Inlay	Through-wall
4	75%(2-inch) PWSCC repair	Circumferential	7.5	12.1
		Axial	10.1	10.6

In order to investigate the effects of flaw size on the results, the initial flaw length was increased while keeping the initial flaw depth constant. All other inputs were kept constant. The results of the analyses are given in Table 8. As illustrated in Table 8, the effects of increasing the initial flaw length were minimal on the time to leakage. An approximate 18 percent decrease in time to leakage was observed as the initial crack length was increased by a factor of 3. As the initial crack length is increased further, it is expected that the difference in the time to leakage would decrease significantly, since the influence functions at the crack free surface do not change greatly for long surface cracks.

Table 8 Idealized flaw analysis results for a variety of initial crack lengths

Flaw Analysis Case #	WRS case	Flaw size	Time, years		
			Inlay	Through-wall	Rupture
4	75%(2-inch) PWSCC repair	Circ 1.5x10mm	7.5	12.1	23.3
		Circ 1.5x15mm	6.6	11.1	22.0
		Circ 1.5x30mm	5.4	10.0	19.9

5.4.6 Effects of embedded defects

One of the scenarios from Code Case N-766 is that embedded flaws may be left in place after repair and inlay applications. Specifically, the code case states, “Surface indications with major dimensions greater than 1/16 in. (1.5 mm) shall be removed, **reduced in size**, or weld repaired in accordance with the following requirements.” Therefore, an existing flaw may be reduced in size by the repair and/or the inlay and placed back into service. Once the flaw is partially repaired, an embedded defect is present, and may be in line with an initiating PWSCC flaw in the inlay. Even though this scenario is unlikely, the effects on the time to leakage were investigated. Two cases were considered. First, for Case 4, the 75% deep PWSCC repair, it was assumed that a 90% deep surface connecting flaw was present before the 75% deep repair was conducted. This repair left 15% of the wall thickness cracked. Second, for Case 1, a 50% deep flaw was assumed before the inlay, leaving about 45% of the wall thickness cracked. As illustrated in Section 4, the welding residual stress analyses with embedded defects were not different in the weld away from the embedded defect. However, near the defect, the stress were redistributed and concentrated near the tip of the defect. For these analyses, it was assumed that the residual stress was not modified, but the flaw in the inlay was inline with the embedded defect. This alignment caused a jump in the crack behavior as the inlay flaw interacted with the embedded defect. The change in the leakage times are illustrated in Table 9. As expected, the time through the inlay was not affected by the presence of the embedded defect. However, the time to leakage was decreased by the presence of the embedded defect. The time to leakage estimates are very conservative since it is unlikely that the flaws would be in perfect alignment with each other.

Table 9 Idealized flaw analysis results for embedded flaws

Flaw Analysis Case #	WRS case	Embedded flaw	Time, years		
			Inlay	Through-wall	Rupture
4	75%(2-inch) PWSCC repair	none	7.5	12.1	23.3
		a/t=90% before PWSCC repair	7.5	9.5	21.6
1	50% preservice repair	none	9.7	25.1	33.7
		a/t=50% before inlay	9.7	17.2	25.3

5.5 Natural Flaw Growth

The idealized PWSCC flaw growth analyses can be performed rather quickly and it will be seen that these provide a good estimate of growth through the wall compared to the natural flaw growth analyses presented in this section. Figure 54 illustrates natural crack growth in a pipe with an inlay. The top left illustration in Figure 54 shows Model 1 with the pipe dimensions. The right side illustration shows the idealized crack growth assumptions discussed in Section 5.4. As seen, the crack growth rate in the Alloy 82 is determined by the PWSCC equation for Alloy 82 while for the inlay the Alloy 52 growth law, which is much slower than Alloy 82, is used. When the crack becomes a through-wall crack, a thickness weighted average PWSCC growth law is used in the idealized analysis. The illustration at the bottom of Figure 54 shows the anticipated 'balloon' shaped crack expected. When the surface crack meets the Alloy 82 material under the inlay, the growth increases dramatically, leading to the crack shape shown at the bottom of Figure 54.

With the advanced finite element analysis (AFEA) approach, the crack growth is controlled by the local stress intensity factors along the crack front. Ideally, AFEA automatically grows the crack an increment, then automatically re-meshes the new crack size, calculates K again, etc. However, for the balloon growth in the inlay, this automatic growth procedure was challenging as discussed in the next section. Due to the complexity of the problem, automated natural crack growth was possible for portions of the growth and manual growth was required for other portions of the growth.

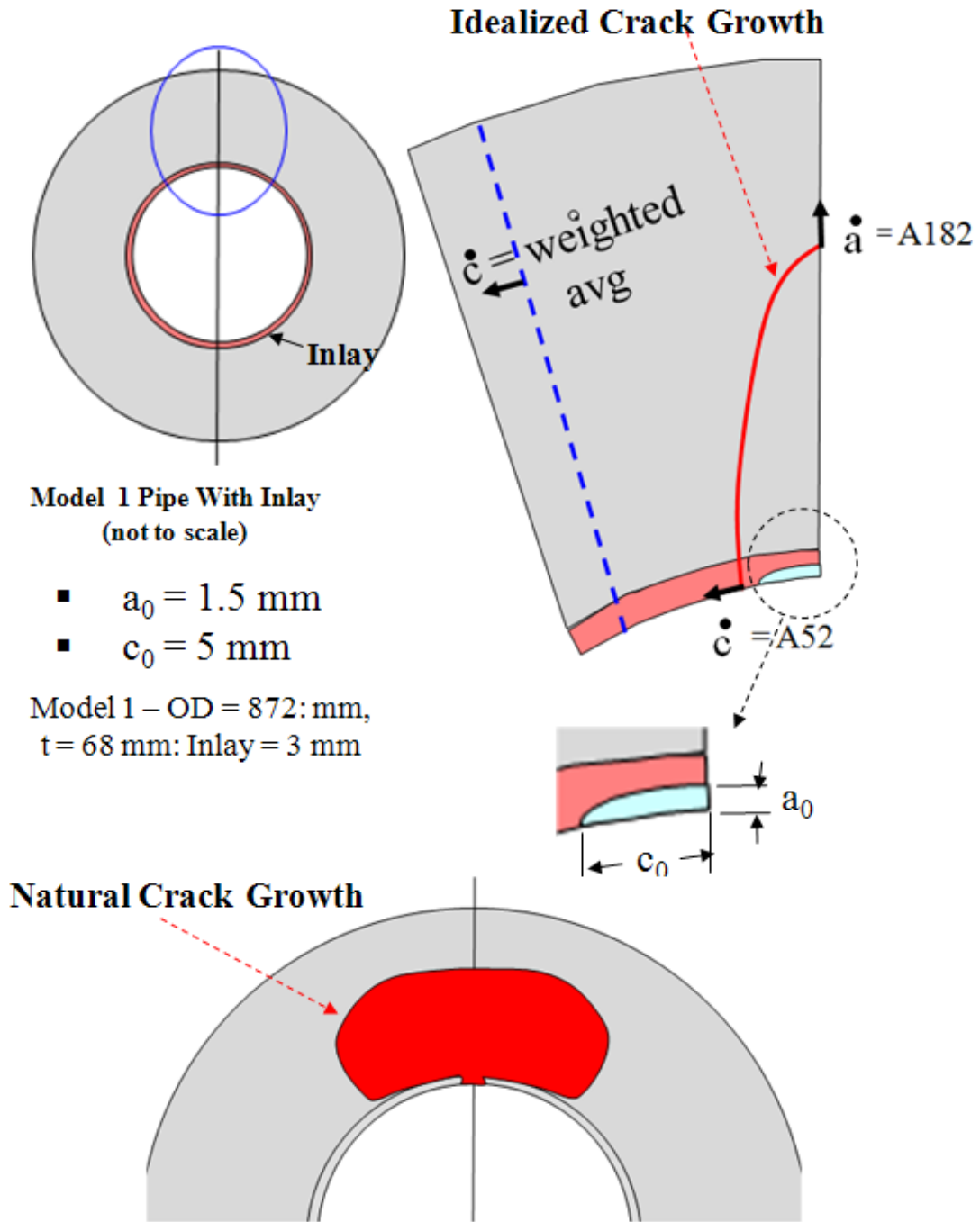
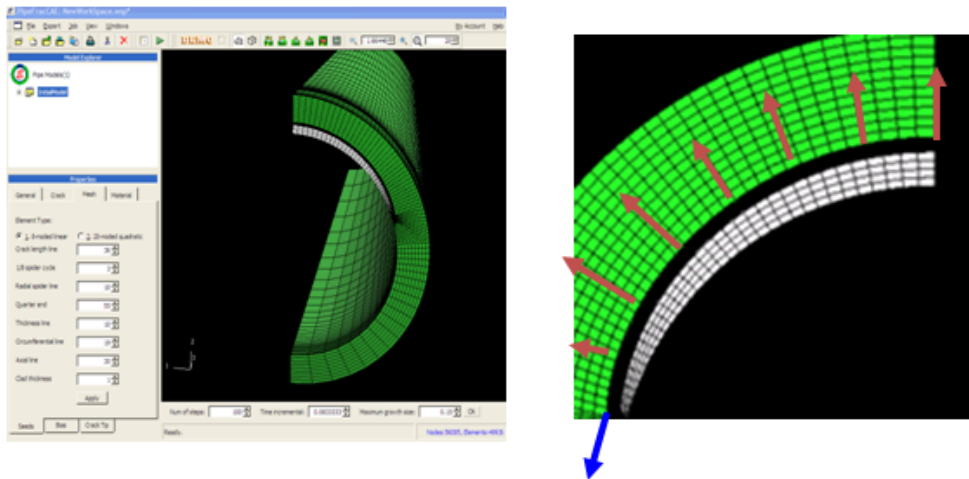


Figure 54 Illustration of idealized and natural crack growth for PWSCC in Model 1

5.5.1 AFEA method description

The AFEA method for use in PWSCC calculations was mainly developed and used for the Wolf Creek crack growth analyses [17]. Figure 55 illustrates the approach. The PWSCC crack growth law is a relation based on the stress intensity factor, K , as seen in the box at the top of Figure 55, where the loads consisting of weld residual stress, temperature gradients, internal pressure (with end cap forces), and bending moment during operation are considered. The PipeFracCAE code is used for the analyses. As seen at the bottom, a mesh is automatically developed with an initial flaw with all loads applied. The stress intensity factors at points along

- **Pipe with crack in Weld Developed**
- **Initial Crack Size Defined**
- **Loads: Residual Stress, Temp, Pres, Moment**
- **PWSCC (or Fatigue) $\frac{da}{dt} = A(K_I)^p$**



ANALYSIS PROCEDURE:

1. **ABAQUS Analysis – Extract Stress Intensity Factor (K)**
2. **Crack Growth for all crack tip points**
 - ◆ **'Natural' PWSCC Crack Growth**
3. **Automatic Re-Mesh**
4. **Automatic ABAQUS Model Produced**
5. **LBB Assessment Made**
 - ◆ **NRC Procedure (Leak Rate, Fracture)**

Figure 55 Advanced finite element analysis (AFEA) crack growth procedure

the crack front are determined from an ABAQUS analysis. Based on the stress intensity factors, the equation in the box at the top of Figure 55 is used to increment the crack over some prescribed time increment. The arrows in the right hand illustration of Figure 55 show the crack growth direction, which are assumed to be perpendicular to the current crack front. The crack size is then incremented, a new crack mesh is developed with PipeFracCAE, and an input file

with all loads, boundary conditions, etc., is developed. A python scripting procedure is used to submit the job as an ABAQUS analysis. ABAQUS calculates the stress intensity factors, and the crack is incremented through another time step, and so on. The procedure for the Wolf Creek analyses was automated so that the crack grew through the nozzle wall, became a through wall crack (TWC), and then grew around the circumference. The time at which a leaking crack occurs and the resulting through-wall crack becomes unstable is recorded.

5.5.1.1 Inlay enhancements to AFEA

The crack growth shape for growth through inlays, discussed in Section 5.5 and seen in Figure 54, was quite different from the cracks grown without an inlay using PipeFracCAE. The challenges were mainly caused by the unique crack shapes that developed when an inlay is considered. This process was semi-automated, but could not be made fully automatic. Next, a description of the process used to grow the cracks into a balloon shape is given.

The initial flaw shape ($a_0 = 1.5$ mm, $c_0 = 5$ mm) is shown as the 'blue' half ellipse in the upper part of Figure 56 for Case 4. The vertical axis represents the symmetry plane. The three millimeter deep inlay depth is shown shaded red and the plot is in plane view (curved pipe not shown). After about 6.525 years, the crack hits the Alloy 82 weld metal and begins to grow much quicker. In the meantime, the growth in the circumferential direction in the Alloy 52 material remains slow, resulting in a bubble shaped crack. After 7.11 years, the crack is growing quite fast in the Alloy 182/82 material and has the shape represented with the red line shown in Figure 56. At this point, the automated PipeFracCAE meshing scheme begins to break down because of the 'kink' in the crack shape labeled as 'B' in Figure 56. Essentially, the crack growth profiles cross each other since growth is assumed to be normal to the current crack shape, leading to overlapping meshes. Crack instability occurs and the crack becomes balloon shaped. Due to the numerical difficulties, a spread sheet calculation is performed that uses the stress intensity factors at each point along the crack front to estimate the balloon shape. The crack is grown normal to the crack front for a time increment (0.1 year). This is shown with the triangle marked line in Figure 56. The crack growth in the Alloy 52 inlay during this time is quite slow due to the growth law assumption used ($A_{52}=A_{82}/100$ in this case). Note in the bottom illustration in Figure 56, K is very large near the crack 'kink' point at 'B'. This is rather typical for fracture analysis as stress intensity factors at crack front discontinuities reach large values. The automated crack growth procedure within PipeFracCAE estimates the balloon shape and an updated procedure is used to grow the crack from the balloon shape. A key assumption made here is that point 'B' grows very rapidly to the balloon shape. Another assumption with this approach is that when the crack front discontinuity (kink) forms (7.11 year curve shape in Figure 56), only growth in the depth direction is permitted since meshing difficulties occur. This general procedure was used for all natural crack growth analyses.

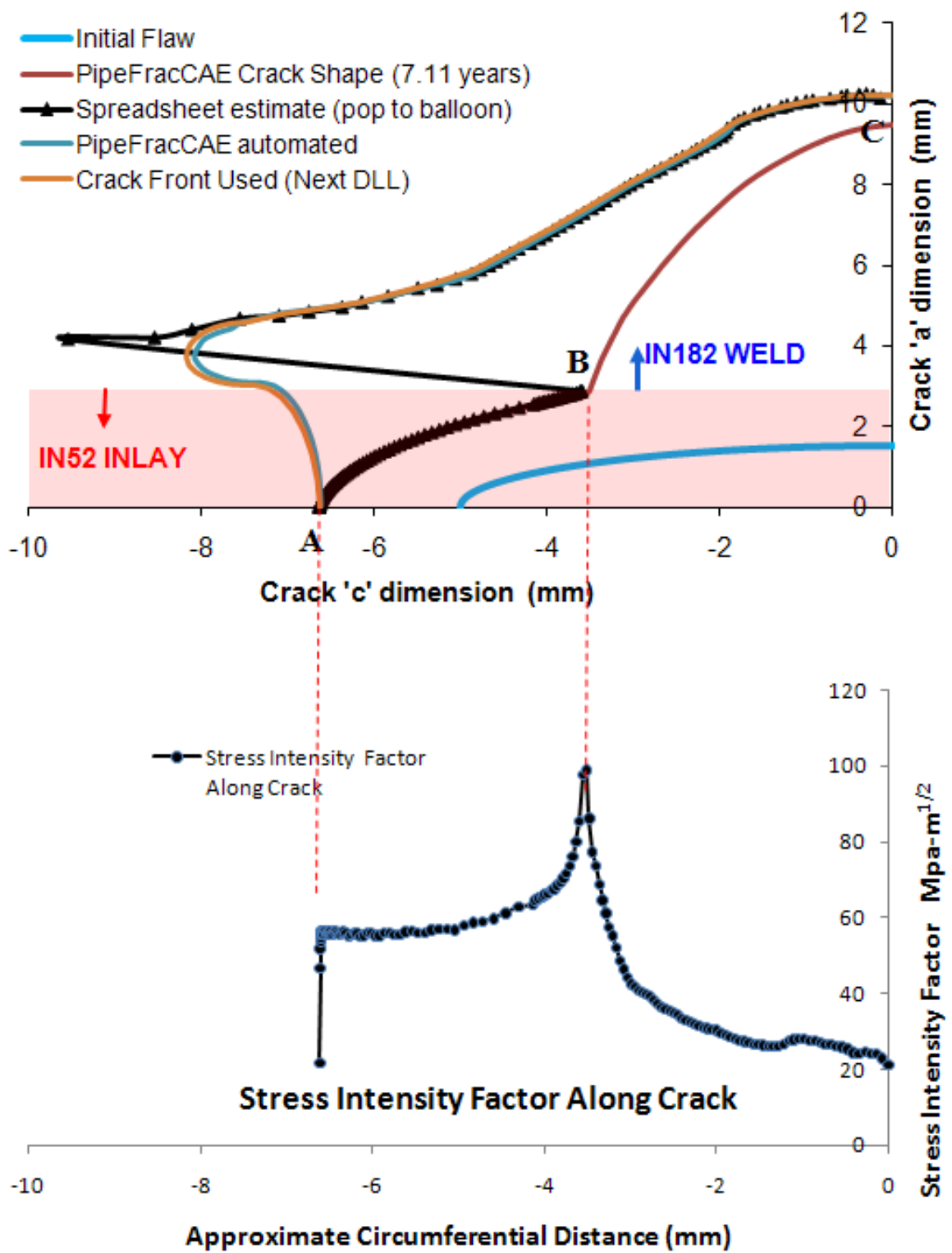


Figure 56 Crack growth procedure for growth to 'balloon' shaped crack (Case 4)

To further illustrate the PipeFracCAE improvements and challenges required to model inlay growth, a series of mesh snap shots is given in Figure 57 as the crack grows through the wall for the Case 4 residual stress fields. The initial crack shape and the shape just after the inlay is breached (depth location) are shown in this figure. The crack then grows rapidly in the Alloy 182/82 material as seen after 7.125 years. As discussed above, during the period prior to the balloon shape, the crack in the Alloy 182 only grows in the depth direction because otherwise crack mesh instability occurs. After a short period of time, the first balloon shape is shown at 7.255 years. Note that the weld residual stress distributions (Figure 27) are tensile throughout a large portion of the wall thickness and becomes compressive at the nozzle OD. The crack will tend to grow for a long distance in the Alloy 182/82 material into a large balloon shape. It will be seen that for other cases (eg. Case 1) this type of growth is not as severe. The next crack shape shown in Figure 57 is at 7.775 years and then 8.65 years. Due to the welding residual stress distribution, the crack growth through the pipe thickness slows down considerably as the crack reaches the compressive field and is only driven by the service loads which produce a low level of tension at the crack tip. As such, by 9.6 years, there is a very large balloon shaped crack.

The meshing scheme to automatically grow this shape required extensive modifications to the PipeFracCAE code. It required the building of mesh development 'blocks' to manage the mesh at different portions along the crack. Moreover, at times, due to the unique crack growth patterns which developed, meshing errors would occur. When this happened, the analysis was stopped, a corrected mesh was developed by hand which overcame these local shape difficulties, and the analysis was continued. As seen at the bottom of Figure 57, the automatic growth process for the balloon shaped cracks required very large meshes (on the order of 175,000 to 200,000 elements for each time step).

When the crack was ready to penetrate the wall thickness (bottom left, Figure 57), a spread sheet growth analysis was performed to develop the first through-wall crack (TWC). The automated procedure for going from a large balloon shaped surface crack to a TWC could not be automated due to meshing issues. During the TWC portion of growth, partial automation and partial spread sheet growth was required since, from time to time, the TWC mesh would become unstable.

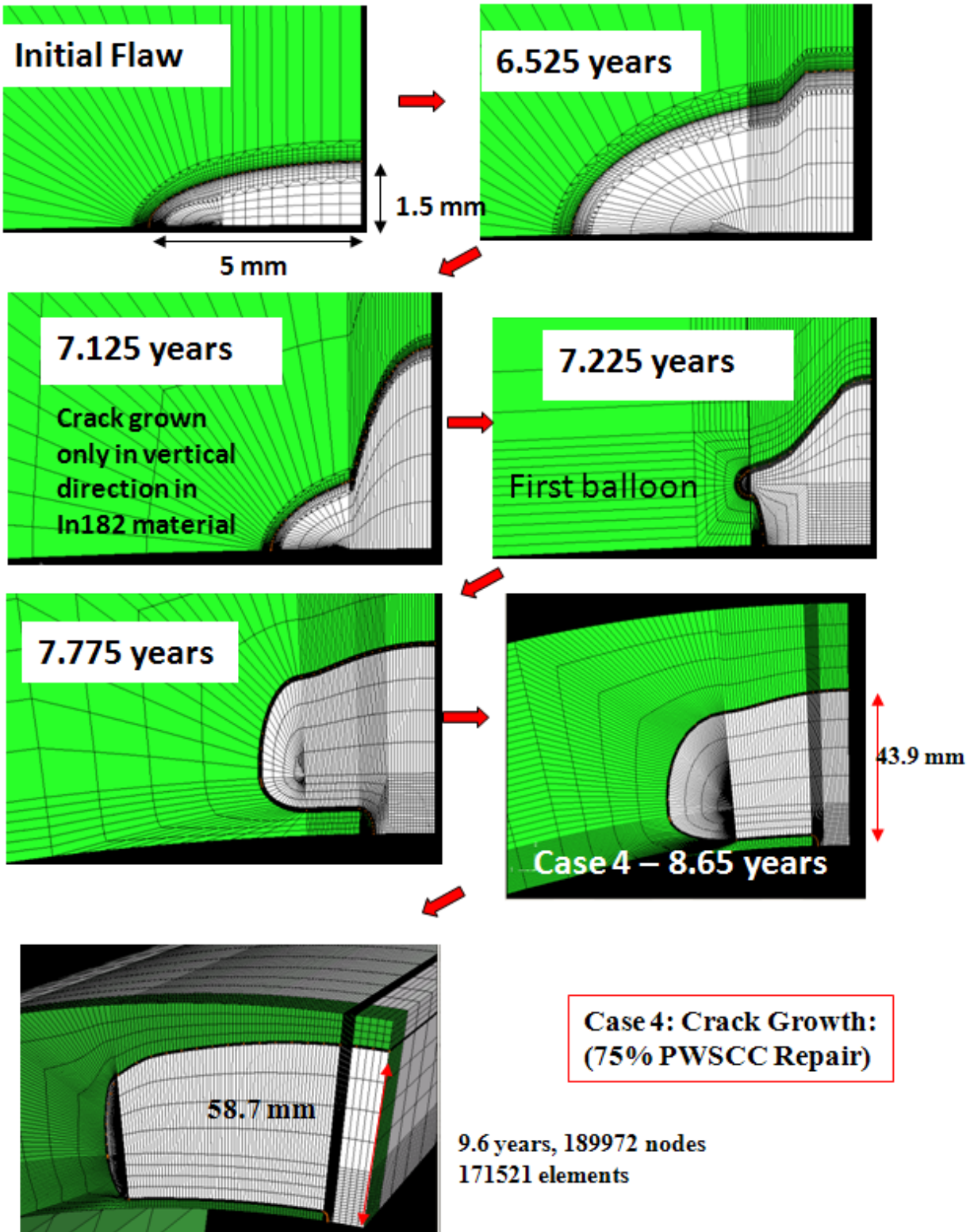


Figure 57 Crack growth progression through wall for Case 4

5.5.2 Natural flaw growth results

Natural flaw growth analysis results are presented here and compared to the idealized growth results. Only select analyses for the cases listed in Table 3 were conducted. The results from these analyses are used to verify the reasonableness of the idealized flaw growth predictions presented in Section 5.4.

5.5.2.1 Case 1 50% Pre-service Repair

Case 1 from Table 3 is the baseline case of a 50% deep repair made before the stainless steel safe-end and inlay welds. Figure 58 shows the crack mesh just before leakage. The weld residual stress distribution is shown in Figure 26 and also repeated in the inset in Figure 58. The WRS are tensile near the ID, cross to compression at $a/t = 0.12$ and back to tension at $a/t = 0.81$. This suggests that the crack will grow quickly at the beginning, slow down, and then grow quickly again when it reaches the OD. The size of the balloon shaped crack for this WRS distribution is also much smaller than that for the PWSCC repair cases (discussed later) because of this distribution. The top illustration shows an axial stress contour plot with the outline of the crack shape just before leakage at 31.5 years. A blow-up of the crack mesh, also shown with axial stress contour plots, is shown in the middle illustration. The crack mesh regions are also shown near the top and bottom illustrating the ‘spider web’ features necessary to produce accurate K values. The crack in the inlay is subject to high tensile stresses and corresponding high K-values (greater than $100 \text{ MPa}\cdot\text{m}^{1/2}$). However, since the PWSCC growth rate in the Alloy 52 inlay is much lower (100 times less) than the Alloy 182/82 growth rate, the crack remains slow. On the other hand, the K-values on the crack tip near the nozzle OD are on the order of $60 \text{ MPa}\cdot\text{m}^{1/2}$ (since the crack now resides in the high tensile weld residual stress field along with the tensile service loads) and the crack is growing rapidly. In fact, the crack breaks through the wall in 0.15 years from this point.

As the surface crack progressed through wall thickness, there was a question of whether the inlay would tear due to the service loads. At several times during the analysis, a separate elastic-plastic analysis was performed using the service loads and the weld residual stresses. For crack instability predictions, it has been assumed in the past that weld residual stress distributions are eliminated by the large amount of plasticity that occurs near a crack tip. However, since the loads are relatively low (in this case), the weld residual stresses may play a more important role. The effects of the WRS were included, and the service loads were applied for the elastic-plastic analysis. The WRS increase the values of the J-integral at the inlay region slightly, and were thus included. For the crack shape just before leakage (Figure 58 and Figure 59), the maximum value of the J-integral calculated in the inlay at the nozzle ID was 52 kJ/m^2 . This is much lower than the tearing value for Alloy 52 material (which is proprietary). Hence, the conclusion is that tearing of the inlay ligament during PWSCC caused by the service loads is not expected for Case 1. As will be seen shortly, this is not always the case.

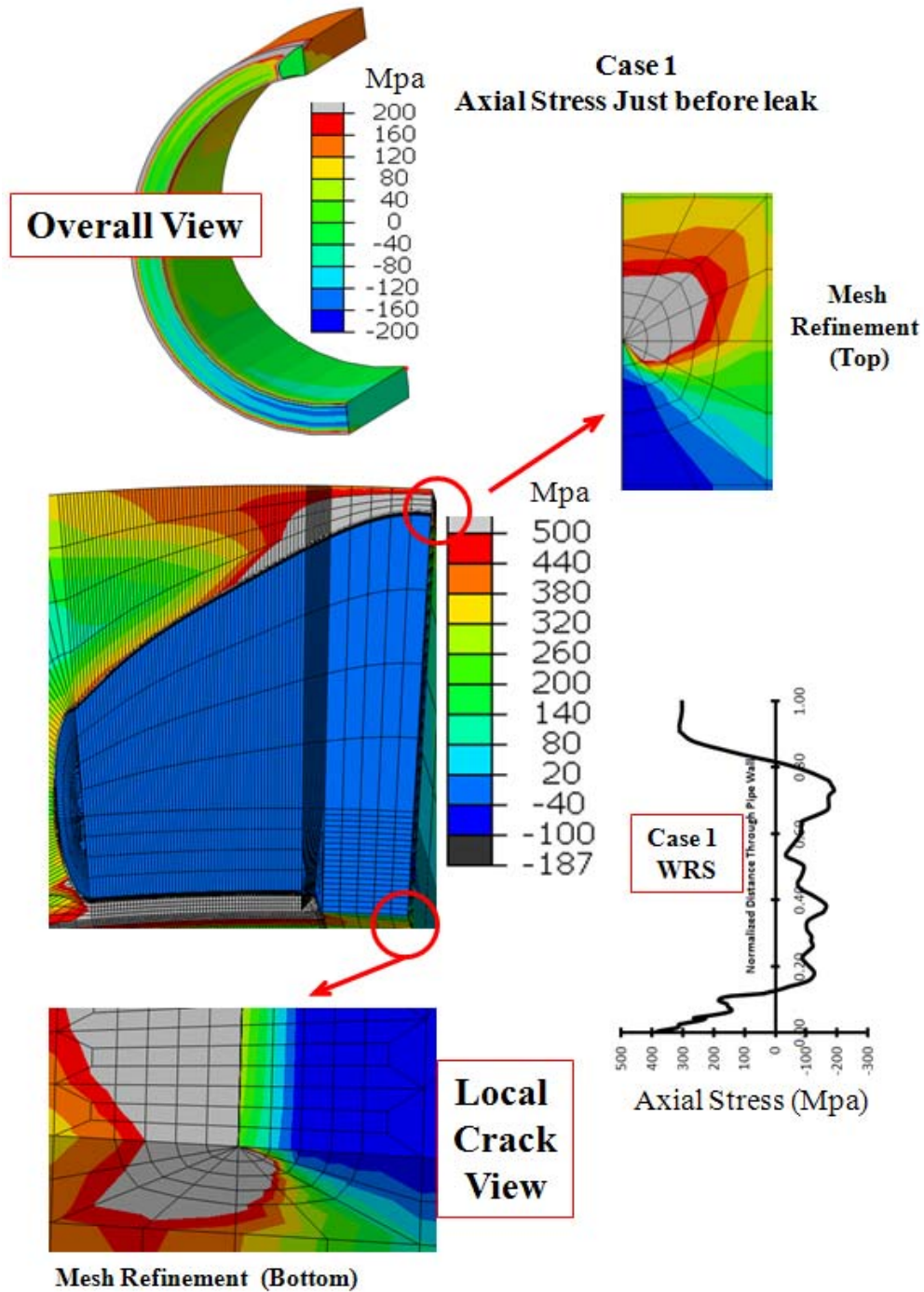


Figure 58 PWSCC growth crack shapes (along with axial stress) for Case 1 of Table 3 after 31.4 years of growth (just before leakage)

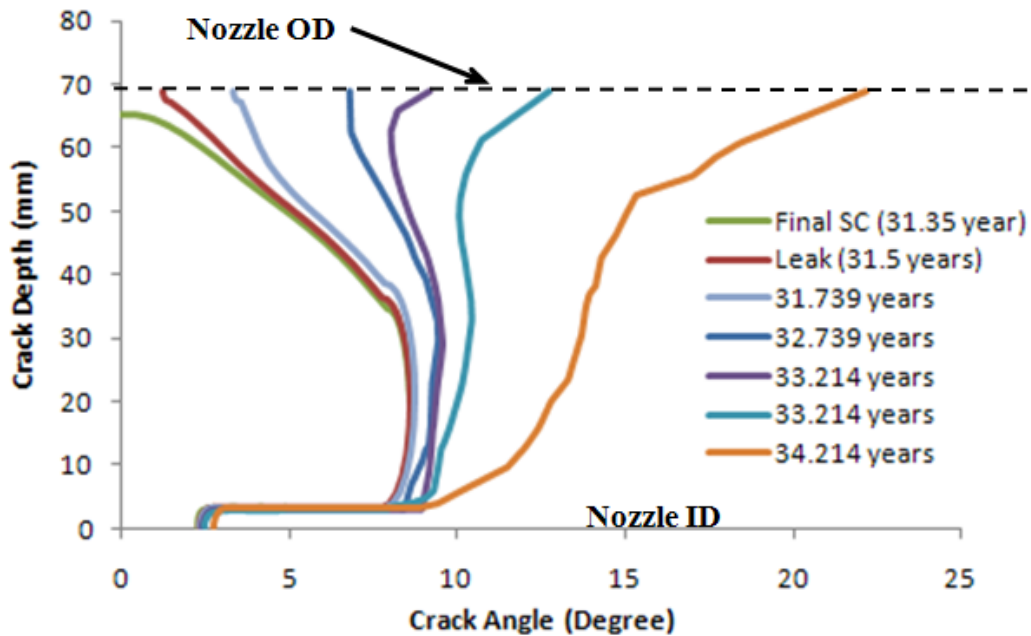


Figure 59 Crack profile shapes for Case 1 of Table 3.

The progression of crack growth from the just before leakage to through-wall crack growth is shown in Figure 59. This is plotted in plate view coordinates and the crack shape shown is the actual shape that was predicted with AFEA analysis. The final surface crack shape, shown in green, occurs at 31.35 years of growth and first leakage is at 31.5 years. After first leak, the crack continues to grow, especially along the ID where the high tensile residual stress field exists. At mid thickness, the crack grows slower due to the compressive WRS. Note that this figure presents only half of the crack front with the crack symmetry plane at the 0-degree line.

For the through wall crack shape at 34.214 years, it is assumed that tearing of the inlay ligament occurs to increase the size of the crack at the inlay. The J-Resistance curve for Alloy 52 is lower than that of Alloy 82/182 material. Figure 60 (reference [46]) summarizes some J-resistance data collected for Alloy 182 material. It is seen that the lowest value for the fusion line has an initiation value of about 308 kJ/m^2 . The proprietary J-resistance curve for Alloy 52, which cannot be published here, is lower than this. Moreover, the slope of the curve is lower than that of Alloy 182, suggesting less resistance to tearing instability is expected for Alloy 52. For the crack shape shown Figure 59 at 34.214 years, an elastic plastic analysis was performed to calculate J. The value of J at the inlay ligament region is 315 kJ/m^2 . This is higher than the fusion line J-initiation value for A182 and much higher than the proprietary Alloy 52 value. This suggests that the crack will tear at the inlay ligament at this time (and possibly before this time). A true tearing instability analysis would require continued calculation of J while growing the crack at the inlay location and following the J-resistance curve until instability occurs. This cannot be done easily and was not performed in this study.

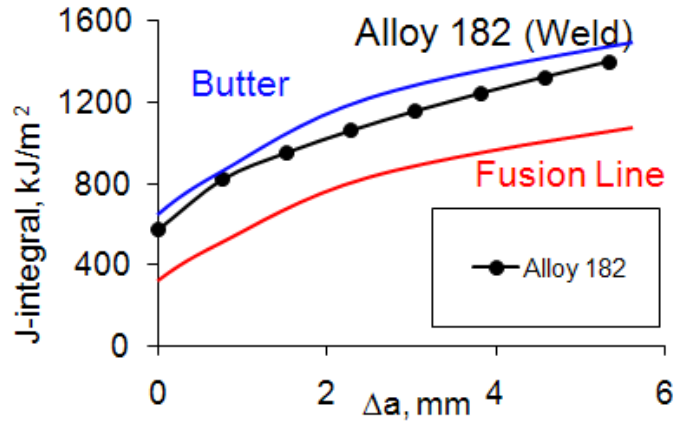


Figure 60 J-Resistance Curves for A182/82 material [46].

Moreover, recall that crack growth in the Alloy 52 inlay in the negative radial direction (ie., toward the ID) is not included in the PipeFracCAE calculations since the meshing of the growing crack is not possible. If crack growth were permitted in the inlay, the effective inlay thickness would be less than 3 mm at the crack location and as this dimension becomes smaller, meshing becomes more and more difficult. In reality, it is likely that the crack will grow there, effectively reducing the ligament thickness along the inlay crack region. This will have the effect of increasing J (and K if it were included for the PWSCC calculations). Therefore, it is reasonable to assume that, at time of 34.214 years, the inlay crack tears, and a new crack shape evolves. This is certainly conservative from an instability standpoint, although it may not be from a leak rate calculation.

Figure 61 shows the crack shape after this local tearing to TWC instability. The crack shape prior to inlay crack tearing at 34.214 years is shown in this figure (it is also included as the last shape in Figure 59). After inlay tearing, the growth through the entire weld is based on the Alloy 182/82 crack growth law. The slow inlay growth for the TWC will tend to retard the overall growth. However, the elastic-plastic J-integral calculations for the through-wall crack show that the inlay will further tear. This procedure was followed for all crack growth cases. From Figure 61, it is interesting to note that the TWC is slightly larger at the OD and ID (where the tensile WRS reside) and approaches a slight 'C' shape. TWC instability for this case occurs at an average crack angle of about 63-degrees.

Crack growth through the inlay is predicted in 11.9 years, time to leakage is 31.5 years, and crack instability is predicted after 37.4 years.

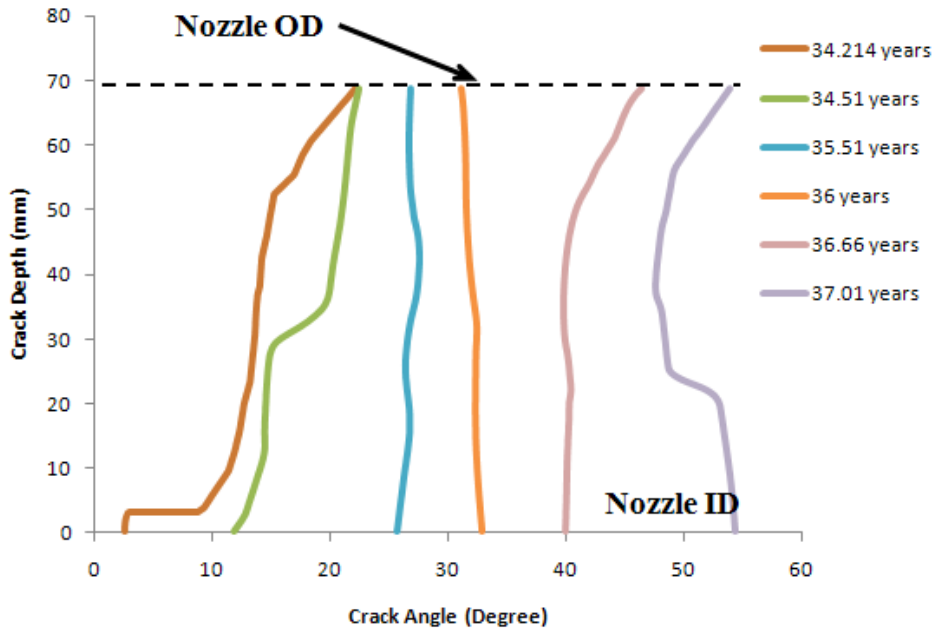


Figure 61 Case 1 through-wall crack shapes after 34.214 years.

5.5.2.2 Case 2 50% PWSCC Repair

Case 2 represents a 50% PWSCC repair from Table 3. Figure 26 shows the axial WRS distribution used for the PWSCC calculations. This WRS distribution starts with tensile values at the ID, then, due to the repair being performed after the stainless steel weld, the tensile stresses rise again and do not cross into compression until an a/t value of 0.6. The WRS then go to compression and stay in compression at the nozzle OD. As one may expect, this results in a drastically different balloon shaped crack. The crack grows for a long distance along mid-thickness just above the inlay because the through thickness growth slows down as the depth of the crack reaches the compressive zone. This case is shown in some detail to illustrate the issues.

The evolution of the crack shape up to just before the time of surface crack penetration is shown in Figure 62. The bottom illustration presents crack initiation ($a_0 = 1.5$ mm, $c_0 = 5$ mm) through a time of 11.625 years. The red shape shows that after the crack leaves the inlay and begins growing faster in the Alloy 182 material, the crack front is discontinuous at the inlay interface. As discussed earlier, this is where the PipeFracCAE meshing routine breaks down because mesh points begin to overlap. The growth to the green shape is performed in a spreadsheet and the bubble shaped crack is determined from the procedure discussed in Figure 54.

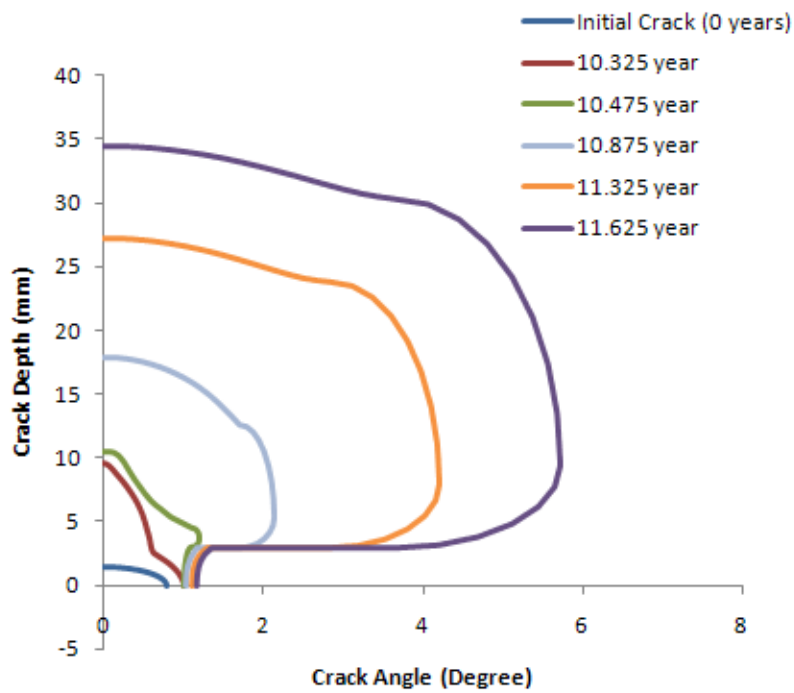
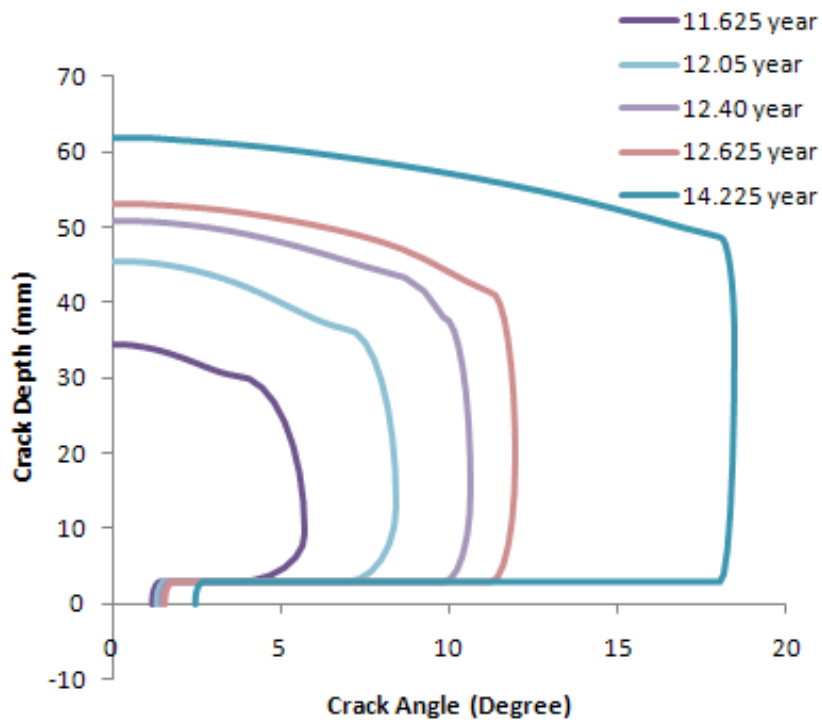


Figure 62 Evolution of crack shape for Case 2 up to leakage.

After the bubble shaped crack forms, another routine is used to automatically grow the crack within the PipeFracCAE framework up to a time of 11.625 years. This shape is represented by the purple crack shape in the top illustration in Figure 62. Note the slow crack growth at the inlay on the ID due to the PWSCC growth rate in Alloy 52.

After reaching 11.625 years of growth (for Case 2) meshing issues occur due to the small inlay crack size and the large balloon shaped crack. The top illustration in Figure 62 shows the evolution of crack growth from the time of 11.625 years to leakage. During this time, the growth is automatically controlled within the PipeFracCAE framework. Finally, the crack is grown to leakage using a spreadsheet calculation. The through-wall crack growth is controlled by using a combination of spreadsheet growth increments and PipeFracCAE.

It is also interesting to observe the crack shape formation within the framework of meshing. Figure 63 shows the axial stress distribution close to the crack just before and just after bubble shape forms, and after 11.625 years of growth. The fine meshes required to model these unique shapes are shown. Note that the axial stresses shown in Figure 63 are elastic for PWSCC growth, and are large.

For the Case 1 description discussed in Section 5.5.2.1, the possibility of ductile tearing due to the service loading was considered. It was found that the Case 1 crack shape is not expected to tear at the inlay. The crack shape shown in Figure 64 is the actual shape just prior to leakage. Because of the nature of the WRS, which is compressive along the nozzle OD for Case 2, the crack growth slows in the depth direction. While this occurs, the PWSCC balloon shaped growth in the Alloy 182 material is quite rapid leading to this crack shape. For this crack shape, an elastic-plastic finite element analysis was performed for the service loads and the J-integral was calculated along the crack. The weld residual stresses were included in this analysis. This is shown in Figure 64 where J is calculated along the crack front. The points 'A to F' are illustrated on the crack and also on the J plot for easy reference. It is seen that J at the inlay location (A-B) is about 310 kJ/m^2 , which is quite a bit higher than the initiation value for Alloy 52. This suggests that the inlay crack will tear.

For this example, the inlay crack length, c , is about 16 mm (the half crack angle from the nozzle centerline is 2.44-degrees). The crack may tear a small amount and stop. Identical elastic-plastic finite element analyses were performed for inlay crack lengths of 32, 48, 64, 79, 95, and 111 mm. The plot of the average J-integral along line A-B (in Figure 64) is plotted in Figure 65. It is seen that J is still about 250 kJ/m^2 even for an inlay opening of nearing 120 mm, which is nearly complete tearing of the inlay ligament. This value is high and suggests that complete tearing will occur. It also clearly shows that J at the deepest point of the crack is quite low ($\sim 28 \text{ kJ/m}^2$) and is also nearly independent of inlay tearing length.

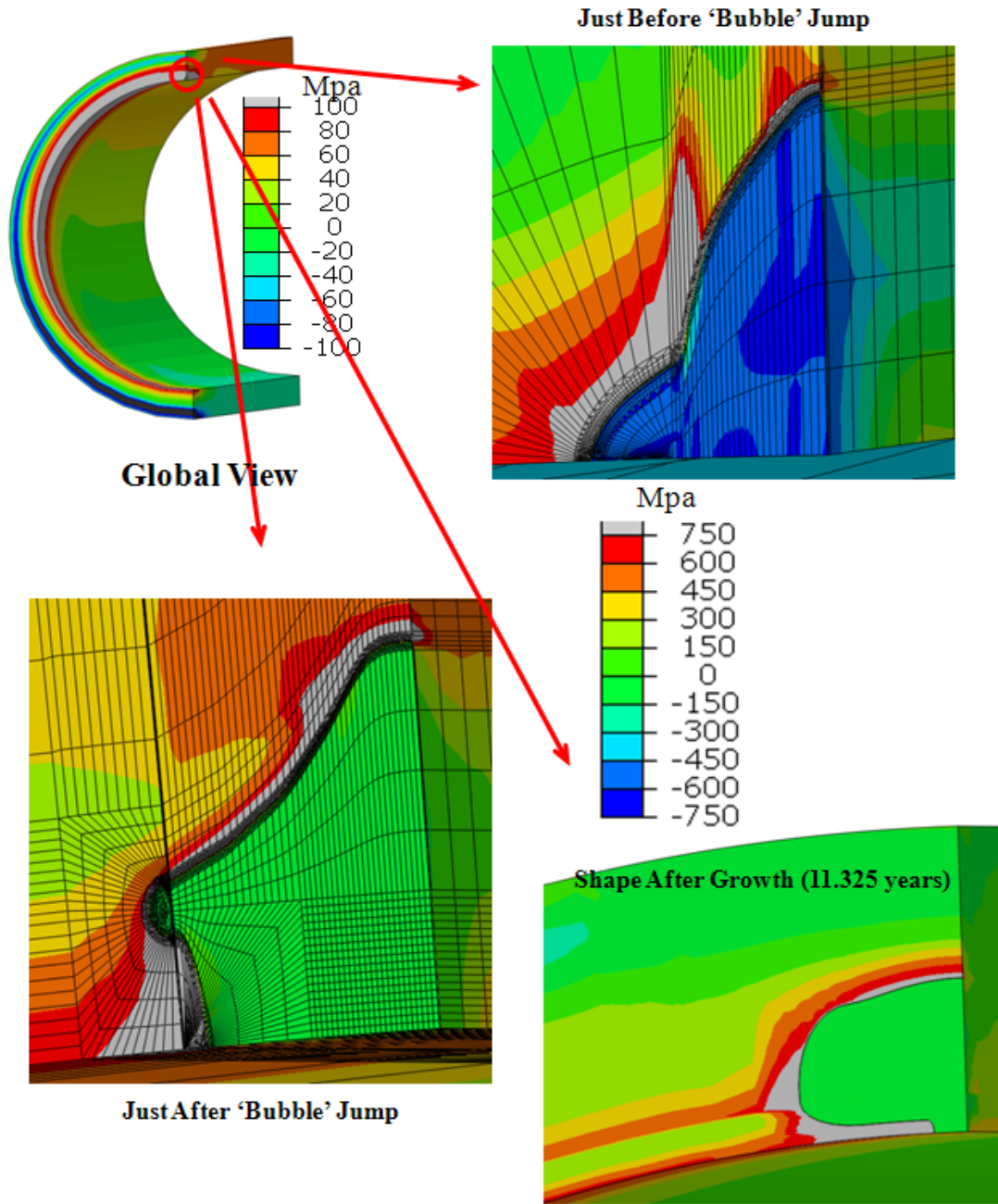


Figure 63 Axial stress distribution in Case 2 as the crack growth transitions into the bubble shaped crack until 11.325 years

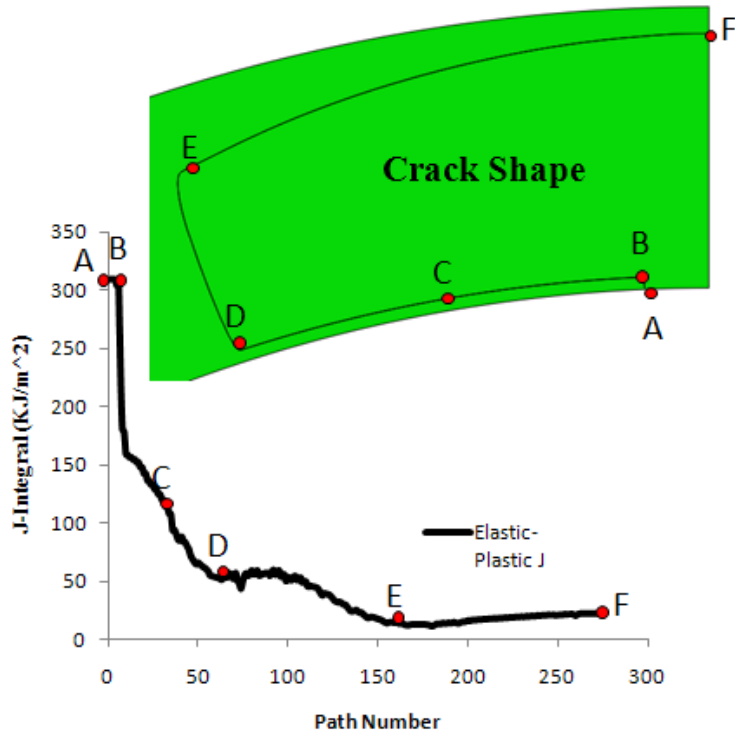


Figure 64 Crack shape and J-calculation for Case 2 crack just prior to leakage.

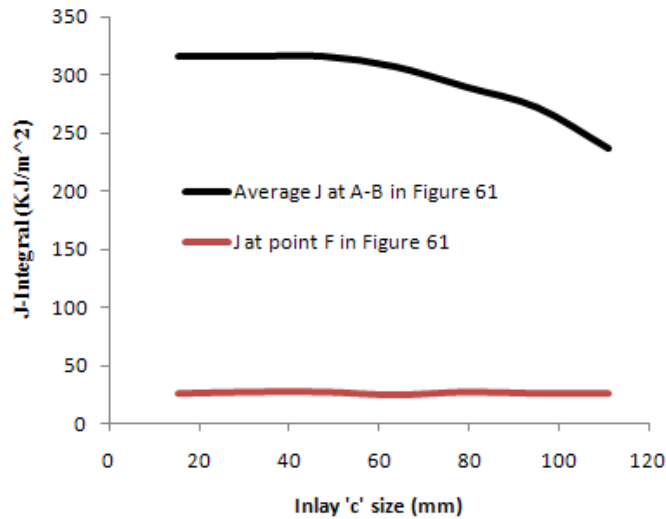


Figure 65 Calculations of J versus inlay crack length ('c') just prior to leak.

For a correct tearing analysis one would have to grow the crack following the J-resistance curve since resistance increases as a function of crack length. Hence comparing the driving force J to the J_{Ic} value to determine how much crack tearing along the inlay occurs is not strictly valid. However a full tearing analysis of the inlay crack caused by service loads is beyond the scope of this program. Since crack growth underneath the inlay (along B-C-D downward in Figure 64) is not permitted here it is likely that the inlay ligament will actually be smaller than the inlay depth

of 3 mm. This smaller depth will increase J significantly along A-B since the ligament is even smaller. Therefore, it is a reasonable conclusion to expect tearing of the ligament for Case 2 when leakage occurs.

The crack growth for the through-wall crack portion of the analysis was made assuming that tearing of the inlay ligament occurred from time to time. Crack growth through the inlay is predicted in 8.5 years, time to leakage is 15.1 years, and crack instability is predicted after 19.3 years.

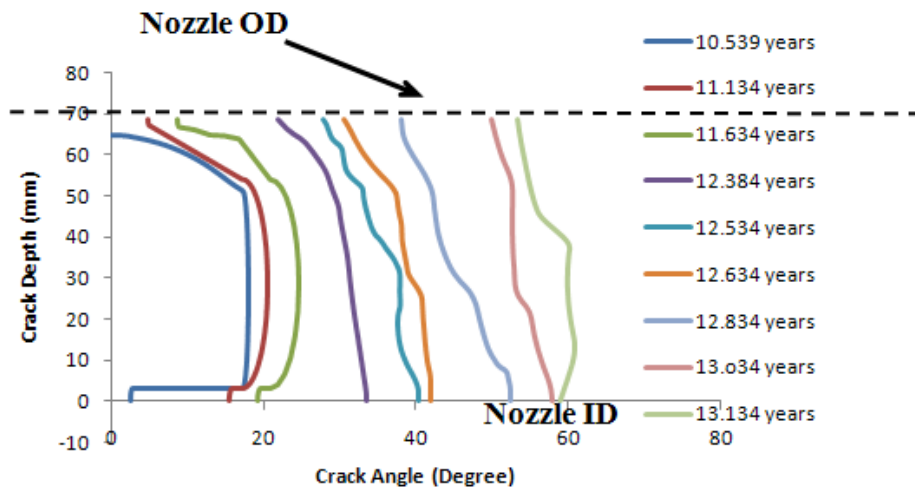
5.5.2.3 Case 4 75% PWSCC Repair

The weld residual stresses for Case 4 of Table 1 (75% PWSCC repair) at the four different locations considered here (weld centerline, DMW/SS line, DMW/Butter line, and Nozzle/Butter line) can be compared to those of Case 2 (50% PWSCC repair) in Figure 26 and Figure 27. The axial WRS are very similar between Case 2 and Case 4 over about 60% of the wall thickness. Beyond 60% of wall thickness, the distributions between the two differ significantly. Case 4 has a large compressive stress at the OD. Case 2 also has compression at the OD, but is much lower in magnitude. Therefore, for Case 4 it is to be expected that large circumferential crack growth will occur in the Alloy 82/182 weld metal while the crack grows through the pipe wall. Moreover, due to the large compression for Case 4, PWSCC will slow down as the crack approaches the OD, and grow further circumferentially at the mid-wall thickness.

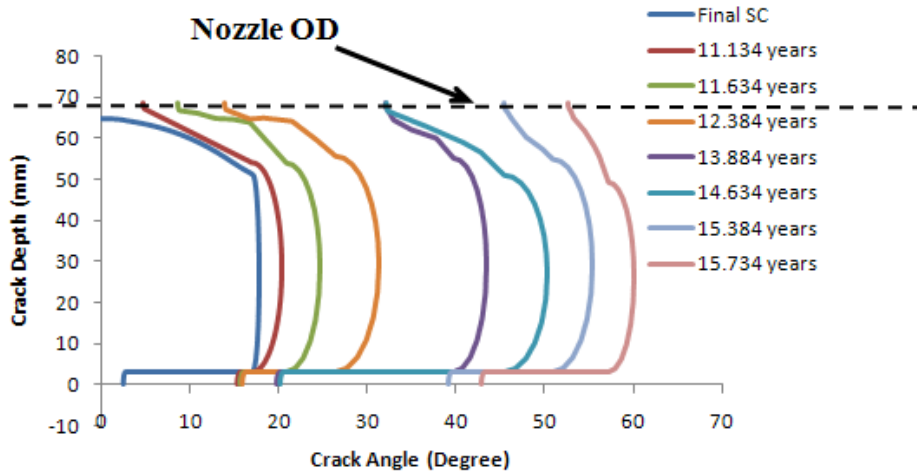
The evolution of the crack shapes for Case 4 (surface crack portion) were already discussed in Section 5.5.1.1 with regard to the AFEA enhancements required to model inlay crack growth. Figure 57 provided the evolution of the crack shapes during PWSCC growth. As was the case for Case 2, it is seen that large growth in the DM weld occurs while the growth on the ID is rather small.

Figure 66 shows the through-wall crack growth profiles. The top illustration shows the shapes as a function of time when it is assumed that tearing of the inlay crack continuously occurs. Note that the crack begins leaking at about 11.1 years of growth. A J-integral analysis for this case clearly shows that tearing will occur at the inlay – especially when the crack is leaking. The lack of ligament near the inlay causes the J-integral to be large. The J-value is larger at this region for the through-wall crack case as compared to the corresponding surface crack since there is no ligament along the OD to carry the stress. Assuming tearing occurs continuously during the through-wall crack growth is certainly conservative. For this growth assumption, the crack grows from leakage to rupture in 2 years.

The lower illustration in Figure 66 shows the crack profiles as a function of time when the assumption of intermittent tearing of the ID inlay ligament occurs. The inlay crack location can be seen at each time at the ID. For this case, the ID crack is not permitted to grow for some period of time until the J-integral value is clearly large enough to guarantee an increment of tearing. For this case, the time from leakage to rupture is 4.25 years. Note that the crack shape is not ‘smoothed’ during the growth process. This leads to some irregular crack shapes that correct themselves as the growth proceeds.



Assume Tearing Occurs During Growth



Assume Intermittent Tearing Occurs During Growth

Figure 66 Case 4 TWC growth: top (assume ID tearing as crack grows, and bottom (assume intermittent tearing occurs)

Crack growth through the inlay is predicted in 6.5 years, time to leakage is 11.1 years, and crack instability is predicted after 13.2 or 15.8 years depending on the tearing assumptions used. For all other cases the more conservative ‘continuous tearing’ assumption is reported for the time between leakage and rupture.

5.5.2.4 Case 11 Modified 50% PWSCC Repair (Alloy 52 growth law = A182/30)

Case 11 has a residual stress distribution identical to that for Case 4, which is for a 75% PWSCC repair. The residual stress distribution for this case (75% PWSCC repair) is shown in the upper

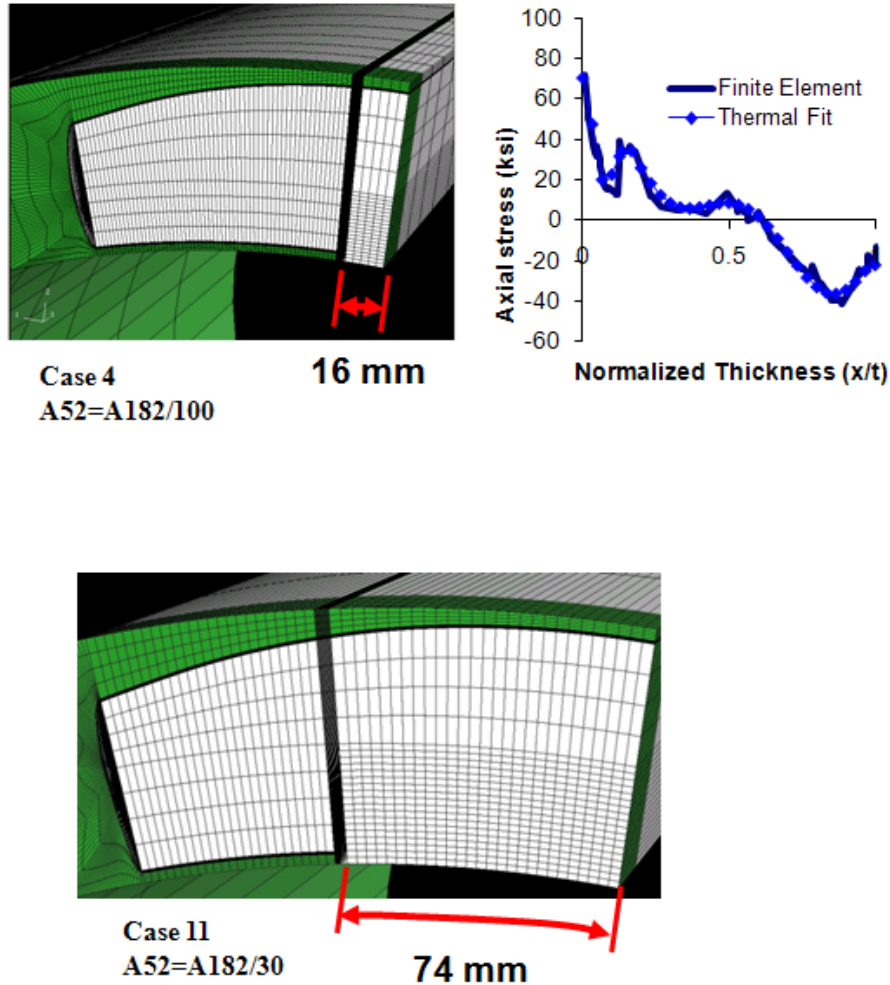


Figure 67 Crack profiles for Case 11 and Case 4 just before leak.

right in Figure 67. As discussed in Section 5.5.1, the residual stress field is fit with a thermal distribution through the nozzle wall thickness to mimic the weld residual stress field. WRS are similar to a displacement controlled thermal stress field since the stress state can decrease as the crack grows². Because the WRS field can actually be fit with separate thermal distributions to through the thickness, the actual shape can be fit rather well, as seen in the comparison in Figure

² Recent developments in AFEA permit the use of the weld residual fields directly. They are transferred from the mesh used to predict the weld residual stresses to the crack growth mesh and used to drive the PWSCC crack. This has the advantage of permitting the entire WRS field, including spatial variations within the weld, to be accounted for correctly. This is especially necessary for axial PWSCC crack growth. The thermal field was used here. In addition, future plans are to permit tearing to occur automatically based on local J-integral analysis and following the J-R curve.

67. Note that the use of a polynomial fit (Figure 51) cannot capture the distribution as well as a multi-thermal fit.

Also seen in Figure 67 are the crack shapes for Case 4 and Case 11 just prior to leakage. These two shapes are similar except that the inlay circumferential length is almost five times larger for Case 11 (74 mm for Case 11 compared with 16 mm for Case 4). Of course, this is due to the much higher inlay growth rate used (Alloy 52 growth = A182/30). Finally, Figure 68 shows a J-integral calculation for the crack shape just prior to leakage. It is clear that tearing of the surface crack is expected since the J values are higher the resistance at the inlay (A-B, see also Figure 60).

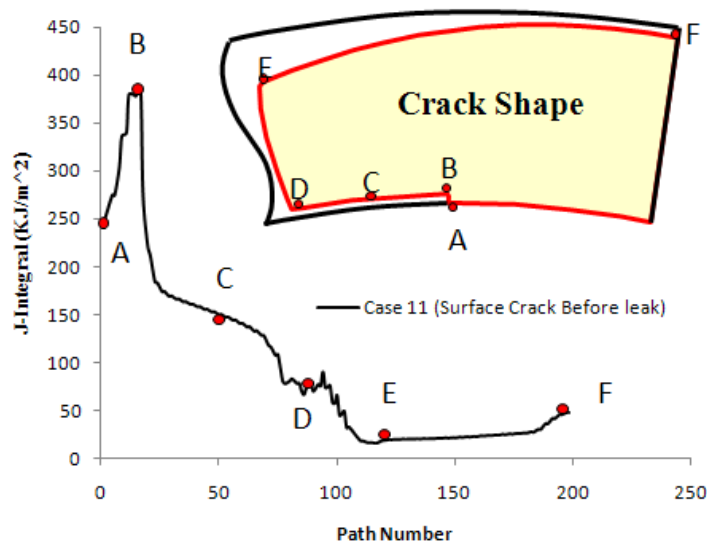


Figure 68 Elastic-plastic J for Case 11 just before leak

Crack growth through the inlay is predicted in 1.65 years, time to leakage is 5.2 years, and crack instability is predicted after 6.8 years. This is due to the rapid growth through the inlay compared with the lower Alloy 52 inlay growth rates used for the other analyses.

5.5.2.5 Case 16 Modified 75% PWSCC Repair (Large bending moment)

Case 16 is identical to Case 4 (75% PWSCC WRS distribution) except the larger bending moment is applied (129 MPa (18.7 ksi) for case 16 versus 96.5 MPa (14 ksi) for Case 4). Crack growth through the inlay is predicted in 6 years, time to leakage is 9.5 years, and crack instability is predicted after 11.5 years. The crack growth shapes for this case is quite similar to Case 4, except faster.

5.6 Comparison of Idealized and Natural Flaw Growth Results

Comparison of the idealized and natural crack growth results for PWSCC through the inlay are presented in Table 10. Considering the differences in crack shape which evolve with the two different crack growth methods, surprisingly good comparisons are seen in Table 10. The idealized PWSCC growth analysis procedure is much faster and easier to perform since natural

crack growth analyses, which result in balloon shaped cracks, are a challenge to automate, as discussed in Section 5.5.1. The idealized crack procedure summarized above in Section 5.2 and illustrated in Figure 54 is seen to be quite adequate here. As such, the PWSCC predictions used for the cases which were not analyzed with the natural growth procedure should be considered reasonable. Note that Cases 1, 2, and 4 are the same as in Table 3. The last two entries in Table 10 come from Table 6 and Table 5 respectively.

Table 10 Comparison of idealized and natural flaw growth results for selected cases.

Case #	WRS case	Total time, years (Idealized Growth)			Total time, years (Natural Growth)		
		Inlay	TWC	Rupture	Inlay	TWC	Rupture
1	Case 1 50% pre-service repair	9.7	25.1	33.7	11.9	31.5	37.4
2	Case 2 50% PWSCC repair	10.9	15.9	24.8	8.5	15.1	19.3
4	Case 4 75% PWSCC repair	7.5	12.1	23.3	6.5	11.1	15.8 ⁺ 13.2 [*]
4	Case 4 Modified 75% PWSCC repair (A52=1/30(A182))	3.4	8.4	16	1.7	5.2	6.8
4	Case 4 Modified 75% PWSCC repair (Larger Bending Moment)	6.9	10.2	17.5	6.0	9.5	11.5

⁺Assuming Intermittent Tearing of Inlay

^{*}Assuming full tearing of inlay at each growth step

In Table 10, it is seen that five cases were considered for the natural flaw analyses. For Case 1, the 50% pre-service repair, the time of growth for all three stages (inlay, through-wall crack (TWC), and rupture) were slightly under-predicted using the idealized growth assumptions. For the rupture life prediction with this case, it is assumed that tearing occurs locally at the inlay for each time step of the natural growth procedure. This means that, essentially, the Alloy 82 growth law was used for the TWC growth predictions, which is conservative. For Case 2, the 50% PWSCC repair, the growth through the inlay and the time from through-wall crack to rupture is predicted to occur faster with the natural crack growth procedure. However, the time to a TWC is very close between the two approaches.

For Case 4, the 75% PWSCC repair, the natural crack growth was slightly faster compared with the idealized growth. This may be due to the fact that the idealized growth WRS fit (Figure 51) misses the ‘hump’ in stress caused by the deep repair prior to application of the inlay near a normalized depth of about 0.2. Even so, the comparison is quite good. For Cases 11 and 16 (Table 10) the natural growth predictions are slightly faster perhaps for this same reason.

In summary, the idealized crack growth predictions compare quite well with the natural growth predictions. This is very convenient since idealized growth is much simpler and faster compared with the natural growth procedure. As discussed above in Section 5.5 natural crack growth in the inlay is quite a challenge because of the odd crack shapes predicted. The automated crack growth procedure becomes unstable and increments of growth using a spread sheet is required to go from one crack shape type to the next. Moreover, when the crack is long in the Alloy 82/182 weld metal, and short at the inlay, and tearing is likely to occur at the inlay. As such, a combination of PWSCC and tearing can occur which cannot be modeled automatically.

The predictions using idealized growth are considered to be quite reasonable for the other cases that were not modeled with AFEA since the comparison for the cases analyzed using both methods were reasonable.

6 Summary and Conclusions

In this report, the effectiveness of inlays as a mitigation technique was assessed by conducting confirmatory welding residual stress and flaw evaluation analyses. Using two large bore geometries, detailed welding simulation analyses were conducted following the procedures set forth in draft Code Case N-766. Within the welding residual stress analyses, the following inlay and repair sizes were considered:

- 50% deep ID pre-service repair (before stainless steel safe end)
- 50% deep ID PWSCC repair (after stainless steel safe end but before inlay)
- 75% deep ID pre-service repair
- 75% deep ID PWSCC repair
- 50% deep ID pre-service repair and a 75% deep PWSCC repair
- 12% deep ID pre-service repair
- 12% deep ID PWSCC repair
- 12% deep pre-service repair and a 12% deep PWSCC repair
- 3mm deep inlay in all cases
- 6mm deep inlay for the 50% deep ID pre-service and 50% deep ID PWSCC repair cases.

The results from the welding residual stress analyses suggest that the regardless of the repair history, the ID stress state is driven by the inlay repair. In most cases, the ID stress due to the inlay was about 400 MPa (58 ksi), which is just above the yield strength for the DM weld material. Even the beneficial effect of the stainless steel safe end weld was eliminated by the thin layer of inlay material on the ID surface of the pipe. For all of the inlay cases with pre-service repairs, the high axial stress on the ID dropped to zero at about 15 percent of the wall thickness for all repair depths. For the inlay cases with PWSCC repairs, the axial stress dropped to zero between 40 and 50 percent of the wall thickness for repairs greater than 50 percent deep and it dropped to zero at about 20 percent of the wall thickness for the 12 percent deep repair.

Using these residual stress results, PWSCC growth analyses using both idealized-shaped and natural-shaped cracks were conducted using simulated crack growth rates. Sensitivity studies

were conducted on crack growth rate, bending stress, operating temperature, initial flaw size and orientation, and inlay. Conclusions from these analyses include:

- The time for the initial defect to grow through-wall was dominated by the time for the initial defect to grow through the inlay, i.e., a large portion of the crack growth time is spent in the first 3mm of wall thickness. The only exception to this case was for the small weld repair (12%). In this case, the flaw arrested after passing through the inlay.
- The 75% deep, PWSCC repair case had the lowest time to leakage. However, this size repair is not practical and was only used in these analyses since a licensee used it for an inlay relief request.
- For the 3mm deep inlay, the time through the inlay was typically about 10 years. After that point, the time to leakage varied with repair size, ranging from an additional 5 years for a 50% deep repair to arrest for a 12% deep weld repair.
- For the 6mm deep inlay, the time through the inlay was about 25 years, with the additional time to leakage the same as for the 3mm cases.
- The crack growth times through the inlay are directly proportional to the crack growth rate factor applied to the MPR-115 crack growth rate. For instance, the time through the inlay for the A182/1000 case was 100 times longer than the time for the A182/10 case.
- Bending stress did not have a large effect on the time for the crack to pass through the inlay, but had a large effect on time to leakage, i.e., the lower bending stresses caused the crack to slow considerably near the middle of the wall thickness.
- Temperature had a large effect on the crack growth behavior. The time through the inlay, time to leakage, and time to rupture were increased by about a factor of 6 by reducing the temperatures from hot leg (327C) to cold leg (288C) conditions. Even for the fastest crack growth considered, the time to leakage was over 50 years at the cold leg temperatures.
- Initial crack length did not have a large impact on the time through the inlay or to leakage.
- Axial cracks grew faster than circumferential cracks due to the larger hoop stresses in the inlayed welds.
- The time through the inlay was not affected by the presence of an embedded defect. However, the time to leakage was decreased by the presence of the embedded defect. The time to leakage estimates are very conservative since it is unlikely that the flaws would be in perfect alignment with each other.

Natural flaw growth analyses were conducted to verify that the unusual flaw shapes did not highly impact the time through the inlay and leakage calculated using the idealized flaw assumption. The results from these runs illustrated that in some cases, the natural crack analyses gave slightly longer times to leakage, while in other cases, the times to leakage were slightly shorter. The differences stemmed from the effect of the natural crack shape on the crack driving force and the more accurate representation of the welding residual stress field in the natural flaw analyses. Overall, the natural crack shape analyses demonstrated that reasonable approximations of crack growth time through the inlay and to leakage can be made with idealized flaw analyses.

Overall, several general conclusion can be made regarding the effectiveness of inlays as a mitigation technique.

- The sensitivity studies conducted assuming a postulated initial defect indicate time to leakage values less than the inlay design life even with Alloy 52 PWSCC crack growth rate improvement factors of 30 – 100.
- The effect of crack initiation in Alloy 52 inlay materials is neglected here and can be considered an additional conservatism in the results.
- Due to the results using the currently available Alloy 52 crack growth data, additional crack growth data is needed for these materials to fully understand and quantify the uncertainty in the results.
- The results from this study do not support sample inspections for inlay mitigated hot leg temperature welds.
- The results from this study support sample inspection for inlay mitigated cold leg temperature welds.
- The results from this study demonstrate a need for both volumetric and ID surface examination due to the rapid growth that may occur after a growing flaw passes out of the inlay into the original DM weld material.

7 References

- 1 Rodgers, D. E. and Fletcher, P. R., 1938, “The Determination of Internal Stresses from the Temperature History of a Butt Welded Pipe,” *Welding Journal Research Supplement*, pp. 4-7.
- 2 Masubuchi, K., 1970, “Control of Distortion and Shrinkage in Welding,” *Welding Research Council Bulletin No. 149*, Apr. 1970.
- 3 Kamichika, R., Yada, T., and Okamoto, A., 1974, “Internal Stresses in Thick Plates Weld-Overlaid with Austenitic Stainless Steel (Report 2),” *Transactions of the Japan Welding Society*, Vol. 5, No. 1, Apr.
- 4 Friedman, E., 1975, “Thermomechanical Analysis of the Welding Process Using the Finite Element Method,” *Trans. Journal of Pressure Vessel Technology*, Vol. 97, Aug., pp. 206-213.
- 5 T. E. Barber, F. W. Brust, H. W. Mishler, and M. F. Kanninen, 1981, “Controlling Residual Stresses by Heat Sink Welding”, *EPRI Report NP-2159-LD*, December.
- 6 P. A. McGuire and J. J. Groom, 1979, “Computational Analysis and Experimental Evaluation for Residual Stresses From Induction Heating”, final Report to *EPRI (RP1394-4)*, Battelle Memorial Institute, Dec. 28.
- 7 F. W. Brust and E. F. Rybicki, 1981, “Computational Model of Backlay Welding for Controlling Residual Stresses in Welded Pipes”, in *Journal of Pressure Vessel Technology*, Trans. ASME, Vol. 103, August, pp. 294-299.
- 8 F. W. Brust and M. F. Kanninen, 1981, “Analysis of Residual Stresses in Girth Welded Type 304-Stainless Pipes”, *ASME Journal of Materials in Energy Systems*, Vol. 3, No. 3.
- 9 F. W. Brust and R. B. Stonesifer, 1981, “Effects of Weld Parameters on Residual Stresses in BWR Piping Systems”, *EPRI Final Report, NP-1743*, March.
- 10 Fricke, S., Keim, E., and Schmidt, J., 1998, “Numeric Determination of Residual Weld Stresses”, presented at and appeared in *Proceedings of ICES’98*, October 7 - 9, Atlanta.
- 11 Goldak, J, et. al., 1998, “Progress and Pacing Trends in Computational Weld

- Mechanics”, presented at and appeared in *Proceedings of ICES’98*, October 7 - 9, Atlanta, Ed. Atluri.
- 12 Yang, Y. Y., and Feng, Z., 1997, “Analysis of Welding Processes”, *Proceedings of McNU ’97*, June 29-July 2, Northwestern University.
- 13 Buchmayr, B., 1993, “PC-Based Software in Welding Technology”, In: *Mathematical Modeling of Weld Phenomena*, Ed. H. Cerjak and K. E. Easterling, The Institute of Materials.
- 14 Zhang, J., Dong, P., and Brust, F.W., 1997, “A 3-D Composite Shell Element Model for Residual Stress Analysis of Multi-Pass Welds,” Transactions of the 14th International Conference on Structural Mechanics in Reactor Technology (SMiRT 14), Lyon, France, Vol. 1, pp. 335-344.
- 15 F. W. Brust, P. Dong, J. Zhang,, 1997d, *Crack Growth Behavior in Residual Stress Fields of a Core Shroud Girth Weld*. Fracture and Fatigue, H. S. Mehta, Ed., PVP-Vol. 350, pp. 391-406.
- 16 Zhang, J., Dong, P., Brust, F. W., William J. Shack, Michael E. Mayfield, Michael McNeil, 2000. “Modeling Weld Residual Stresses in Core Shroud Structures”, Nuclear Engineering and Design, 195, pp. 171-187.
- 17 Rudland, D., Shim, D. J., Xu, H., and Wilkowski, G. M., “Evaluation of Circumferential Indications in Pressurizer Nozzle Dissimilar Metal Welds at the Wolf Creek Power Plant,” Final Report to NRC, April, 2007, Report number ML071560398.
- 18 Materials Reliability Program: Advanced FEA Evaluation of Growth of Postulated Circumferential PWSCC Flaws in Pressurizer Nozzle Dissimilar Metal Welds (MRP-216, Rev. 1) EPRI, Palo Alto, CA: 2007. 1015383.MRP-216, Rev. 1.
- 19 Brust, F. W., Chen, X. L., Yang, Z., “Modeling Distortion and Residual Stress During Welding,” Chapter 7 in *Processes and Mechanisms of Welding Residual Stress and Distortion*, Woodhead Publishing, July 2005, pp. 225 – 263.
- 20 Brust, F. W., and Kim, D., “Mitigating Welding Residual Stress and Distortion,” Chapter 8 in *Processes and Mechanisms of Welding Residual Stress and Distortion*, pp. 264 – 294, Woodhead Publishing, July 2005.
- 21 ASME Pressure Vessel and Piping (PVP) conferences, “Welding and Residual Stress Sessions,” Materials and Fabrication (M&F) Committee, 2000 to 2008.
- 22 J. Goldak, A. Chakravarti, and M. Bibby, “A New Finite Element Model for Welding Heat Sources,” *Metall. Trans.*, Vol. 15B, 299-305, 1984.
- 23 Engineering Mechanics Corporation of Columbus, Technical Progress Monthly Report to US NRC, Phase II – Alloy 600 Cracking, June, 2006.
- 24 Lemaitre., J. L., and Chaboche, L
- 25 Brust, F. W., Dong, P., and Zhang, J., “A constitutive model for welding process simulation using finite element methods,” *Advances in Computational Engineering Science*. Eds. S.N. Atluri, and G. Yagawa, pp. 51-56.
- 26 Oh, J. and Brust, F. W., “Phase Transformation Effects on Weld Distortion and Residual Stress Predictions”, PVP2005-71631, proceedings of ASME PVP conference (2005), Denver Co.

- 27 Leblond, J. B., Devaux, J., and Devaux, J. C., "Mathematical Modelling of Transformation Plasticity in Steels I: Case of Ideal-Plastic Phases", *International Journal of Plasticity*, vol. 5, pp. 551-572, 1989
- 28 Leblond, J. B., "Mathematical Modelling of Transformation Plasticity in Steels II: Coupling with Strain Hardening Phenomena", *International Journal of Plasticity*, vol. 5, pp. 573-591, 1989
- 29 Katsareas, D. E., "NEST III Project – TG6 (Simplified) Computational Round Robin", NESCDOC TG6 (02) 03, May, 2002.
- 30 Rudland, D., Xu, H., Wilkowski, G., Scott, P. Ghadiali, N., and Brust, F., "Evaluation of Loss-of-Coolant Accident (LOCA) Frequencies using the PRO-LOCA Code," draft report for the US NRC, December 2005
- 31 G.A. White, N.S., Nordmann, J. Hinkling, and C.D. Harrington, "Development of Crack Growth Rate Disposition Curves for Primary Water Stress Corrosion Cracking (PWSCC) of Alloy 82, 182 and 132 weldments," *TMS (The Minerals, Metals and Materials Society)*, Proceedings of the 12th International Conference on Environmental Degradation of Nuclear Power Systems – Water Reactors, (2005)
- 32 M. Toloczko, M. Olszta, and S. Bruemmer, "SCC Crack Growth Testing and Characterization of Alloy 690 and its Weld Metals at PNNL, Alloys 690/52/152 PWSCC Research Collaboration Meeting, ADAMS Accession ML092250707, August 6-7, 2009, Rockville, MD.
- 33 Anderson, T.L., Thorwald, G., Revelle, D.A., and Lanaud, C., "Stress Intensity Solutions for Surface Cracks and Buried Cracks in Cylinders, Spheres, and Flat Plates," Structural Reliability Technology final report to The Materials Property Council, Inc., March 14, 2000.
- 34 Chapuliot, S., Lacire, M.H and Le Delliou P., "Stress Intensity Factors for Internal Circumferential Cracks in Tubes Over a Wide Range of Radius over Thickness Ratios," PVP-Vol. 365, Fatigue, Fracture and High Temperature Design Methods in Pressure Vessels and Piping, American Society of Mechanical Engineering, 1998.
- 35 Anderson, T.L., "Stress Intensity and Crack Opening Area Solutions for Through-wall Cracks in Cylinders, and Spheres," Structural Reliability Technology final report to The Materials Property Council, Inc., January 29, 2003.
- 36 Harris, D. O., and Dedhia, D., "WinPRAISE: PRAISE Code in Windows," Engineering Mechanics Technology, Inc. Technical Report TR-98-4-1, 1998.
- 37 Brickstad, B., Chapman, O.J., Schimpfke, T, Schulz, H., and Muhammed, A., "Review and Benchmarking of SRM and Associated Software," NURBIM Final Report D4, Contract FIKS-CT-2001-00172, DNV, Stockholm, 2004.
- 38 Wilkowski, G.M., Olson, R.J., and Scott, P.M., "State-of the-Art Report on Piping Fracture Mechanics," U.S. Nuclear Regulatory Commission report NUREG/CR-6540, BMI-2196, February 1998.
- 39 G. Wilkowski, D. Rudland, D.-J. Shim, and H. Xu , "Technical Note on Critical Crack Size Evaluations for Circumferential Cracks in Dissimilar Metal Welds," May 2007, ADAMS Accession number ML071560385.

- 40 “Evaluation of Flaws in Austenitic Steel Piping,” (Technical basis document for ASME
IWB-3640 analysis procedure), prepared by Section XI Task Group for Piping Flaw
Evaluation, EPRI Report NP-4690-SR, April 1986.
- 41 Zahoor, A. and Gamble, R., “Evaluation of Flaws in Ferritic Piping,” EPRI Report NP-
6045, prepared by Novetech Corporation, October 1988.
- 42 Rahman, S.; "Net-Section-Collapse Analysis of Circumferentially Cracked Cylinders -
Part II: Idealized Cracks and Closed-Form Equations"; Engineering Fracture Mechanics;
Vol. 61; 1998; pp. 213-230.
- 43 Kumar, V., and German M. D., “Elastic-Plastic Fracture Analysis of Through-Wall and
Surface Flaws in Cylinders,” EPRI Report NP 5596, January 1988.
- 44 Wilkowski, G., Rudland, D.L., Chen, Y., and Zhang, T., “Determination of the Elastic-
Plastic Fracture Mechanics Z-factor for Alloy 82/182 Weld Metal Flaws for Use in the
ASME Section XI Appendix C Flaw Evaluation Procedures,” PVP2007-26733,
Proceedings of ASME-PVP 2007:, 2007 ASME Pressure Vessels and Piping Division
Conference, July 22-26, 2007, San Antonio, TX, USA
- 45 Gilles, P., and Brust, F. W., “Approximate Methods for Fracture Analysis of Tubular
Members Subjected to Combined Tension and Bending Loads,” Proceedings of the 8th
OMAE Conference, Hague, The Netherlands, 1989.
- 46 C. Williams, F. Brust, P. Scott, D. Rudland, G. Wilkowski, R. Tregoning, and C. Santos,
“The Impact of Fracture Toughness and Weld Residual Stresses of Inconel 82/182
Bimetal Welds on Leak-Before-Break Behavior,” 2004 ASME PVP Conference.

Appendix A

Axis-symmetric and Three-dimensional Pipe Weld Models

The three-dimensional aspect of weld modeling is a topic of interest in the computational weld community at present. In this appendix, we briefly discuss the effects of three-dimensional modeling on predicted weld residual stress. More details on three-dimensional modeling can be found in References [1, 2, 3]. In general, it can be said with confidence that an axis-symmetric pipe weld model will produce conservative weld residual stress results compared with a full three-dimensional solution as long as the axis-symmetric solution is considered away from any weld start/stop locations.

Early computational work used the axis-symmetry assumption because 3D pipe modeling was not possible. The conservative predictions came about mainly by comparing predictions to measurements [4,5], and observing that the measurements were usually lower in absolute magnitude compared to predictions.

Consider the safe-end weld shown in Figure A-1. A safe-end is a controlled shop weld intended to provide a transition between a carbon steel nuclear containment vessel nozzle (A508 or A516 in Figure A-1) and a stainless steel pipe (304 or 316 stainless). The weld is made with an Inconel alloy (A82 in Figure A-1). In Figure A-1, Passes 1 to 9 represent what is called 'butter' welds that are made directly over the carbon steel. The assemblage with the butter weld is then post-weld heat treated (PWHT) by heating to 593C and holding at this temperature for about 1 hour for every 25 mm of pipe thickness. This is modeled by permitting secondary creep to occur during the PWHT process causing the stresses to reduce due to creep relaxation. Weld Passes 10 through 20 then are applied (Figure A-1). The geometry used for the surge nozzle analysis has an inner radius of 128 mm (5.03 inches), an outer radius of 170 mm (6.68 inches) with a wall thickness of 42 mm (1.65 inches). The mean radius-to-thickness ratio (R_m/t) for the surge nozzle is 3.5.

The temperature-dependent material properties used for all three materials in the dissimilar metal (DM) weld can be found in References [3] and [6] (including Appendix B), including creep properties. The weld parameters, thermal physical properties, and all other modeling parameters required to model the welds can be found in Reference [3] and the references cited therein. For the three-dimensional analysis, full moving-arc solutions were performed since 'lump pass' solutions produce similar results to axis-symmetric solutions.

In most cases, the DM welds in the larger diameter pipe were completed, the inner diameter (ID) region was ground out (~10 to 15% of the wall thickness here), and a weld bead re-deposited over the full 360-degree pipe. It turns out that this grind and re-deposit process typically increases the tensile residual stresses in the repair region. This effect is especially detrimental in thick pipe such as in the pressurizer surge nozzle.

Axial stresses in the butter region for the pressurizer surge nozzle weld are shown in Figure A-2. This figure illustrates the residual stresses using an axis-symmetric solution and a full three-dimensional solution. The three-dimensional results are at a location 180 degrees from the start/stop location of the welds. The weld geometry for the surge line is shown in Figure A-1. The assumption of axis-symmetry is acceptable for locations away from start/stop locations but is drastically different near these locations. Figure A-2 further supports the commonly held belief that axis-symmetric solutions produce conservative predictions (higher in absolute magnitude) compared with the 3D solution. It is seen that the axis-symmetric results do differ more for this case near the outer diameter (OD) of the pipe compared with the 3D results. In fact, the axial stresses on the pipe OD in the butter region are quite a bit higher in the axis-symmetric analysis. Note from Figure A-2 (lower 3D plot) that the pipe inner diameter (ID) is shown (white line) since the ID is not entirely distinguishable. Keep in mind that the three-dimensional axial residual stresses self-equilibrate around the circumference and not through-thickness as required in the axis-symmetric solutions.

Figure A-3 shows the corresponding hoop weld residual stresses for both cases. In general, the hoop residual stresses are larger in the axis-symmetric solution. However, the higher hoop stresses appear to spread further into the carbon steel (left side) in the three-dimensional analysis. This is somewhat surprising since this same effect is not seen for axial stresses (Figure A-2).

Notice that the mesh refinement for both the axis-symmetric and 3D solutions is identical so that differences cannot be attributed to mesh size differences. Also, note that these stresses are at maximum operating stress temperature of 324C rather than room temperature but the differences are quite similar at room temperature.

During construction of piping systems in nuclear power plants, repair welds were necessary if a weld defect was found. This was typically performed by grinding out the damaged region of weld and re-depositing the weld metal. Figure A-4 illustrates this procedure. Here, after deposition of the nine butter passes (see bottom of Figure A-1), and eleven weld passes, the 360-degree grinding operation is modeled (about 15% of the thickness is removed) and two repair passes are deposited. After this, the 90-degree repair is modeled as seen in Figure A-4. A 26 percent through-thickness repair is deposited in four new weld passes. The repair was designed such that the center of the 90-degree repair coincided with 180 degrees from the original start/stop location of the pipe weld as seen in Figure A-1 (upper right). The effect of the repair is dramatic. The three-dimensional solution had 55,000 elements and took four days to run on a two processor machine using ABAQUS in 2005. In 2009, this analysis would only take 1 day on a four-processor machine.

Figure A-5 shows the corresponding axial weld residual stresses in the pipe at a section at the center of the 90-degree repair. The white outline indicates the butter and weld boundaries. Also for the 3D solution, the pipe ID location is marked with white boundaries to illustrate the bevel geometry. It is clear that the weld residual stresses are strongly affected by the repair. Note that these results are at the 324C operating temperature.

Figure A-6 illustrates the residual stress distribution in the butter (through-thickness) for the axis-symmetric and 3D solutions without the 90-degree repair, and the 3D solution with the 90-degree

repair. The repair increases the depth of the tensile residual stresses but the magnitude is not increased significantly. The 15% grinding and re-deposition of these weld passes was the dominant weld feature here which imposed high weld residual stresses on the pipe ID. If this grinding step was not included here, there would have been a significant effect on the weld repair.

Figure A-7 provides a view of the pipe ID centered over the weld repair. These are axial stresses. The two 'red' regions represent the 400 MPa contour levels and the 'green' regions in between these two levels are the stresses in the welds (compare with Figure A-5, top illustration). For this case, circumferential primary water stress corrosion cracking (PWSCC) in DM welds may occur in the repair region. It is clear that partial weld repairs must be analyzed using 3D solutions. One can see that the effect of the start-stop weld repair location is to dramatically alter the weld residual stress state at this location, actually reversing the sign of the stresses at some locations near the start and stop locations of the repair. This is due to the shrinkage of the weld material in the repair region, which causes tension, pulls the un-repaired region into compression just beyond the end of the repair. Figure A-8 shows a plot of axial stress in the weld repair center as a function of normalized distance around the circumference (starting at the 90- and ending at the 270-degree locations). The effect of the repair is present for only a short distance beyond the stop location but extends for quite a distance before the start of the repair. Note that these stresses are along the center of the repair.

Summary – Pipe and Vessel Type 3D Solutions. The following comments summarize the three-dimensional effect of pipe weld analysis for DM welds. Similar comments hold true for single material welded pipe also.

- Axis-symmetric solutions tend to produce higher weld residual stress predictions compared with a more physically correct full moving arc three-dimensional solution. Hence, axis-symmetric solutions are more conservative in general.
- Axis-symmetric solutions model the application of the girth weld passes in one step. In effect, the weld is modeled as being deposited around the 360-degree weld simultaneously and cooled in a similar manner. For a 360-degree weld, especially for a large-diameter pipe, the deposited weld material has cooled by the time the weld returns to the start position. The axis-symmetric solution essentially models the radial shrinkage of the weld bead simultaneously around the 360-degree circumference. This over predicts the radial shrinkage compared with a 3D solution, which leads to the over prediction of both axial and hoop weld residual stresses.
- The three-dimensional axial stress solutions do not self-equilibrate through the pipe wall thickness as they do in the axis-symmetric solutions. This is important near start/stop weld locations or in repair weld regions. Therefore, the through-wall axial residual stresses may be tensile through-thickness in some regions, although this is considered unlikely for thick pipe.
- The axis-symmetric solutions here differed somewhat from the full three-dimensional results near the pipe OD.
- Predicted 3D stresses near the start/stop locations in pipe are significantly different from the axis-symmetric solutions.

- Lump pass solutions, where the entire weld bead is deposited simultaneously, produce conservative predictions (larger in absolute magnitude) of weld residual stresses.
- Lumping several passes into a larger pass also tends to produce conservative weld residual stresses.
- Full three-dimensional solutions are preferred and will replace the simple axis-symmetric analysis procedures in coming years.

Please see References [1, 2, 3] for many more details regarding three-dimensional solutions.

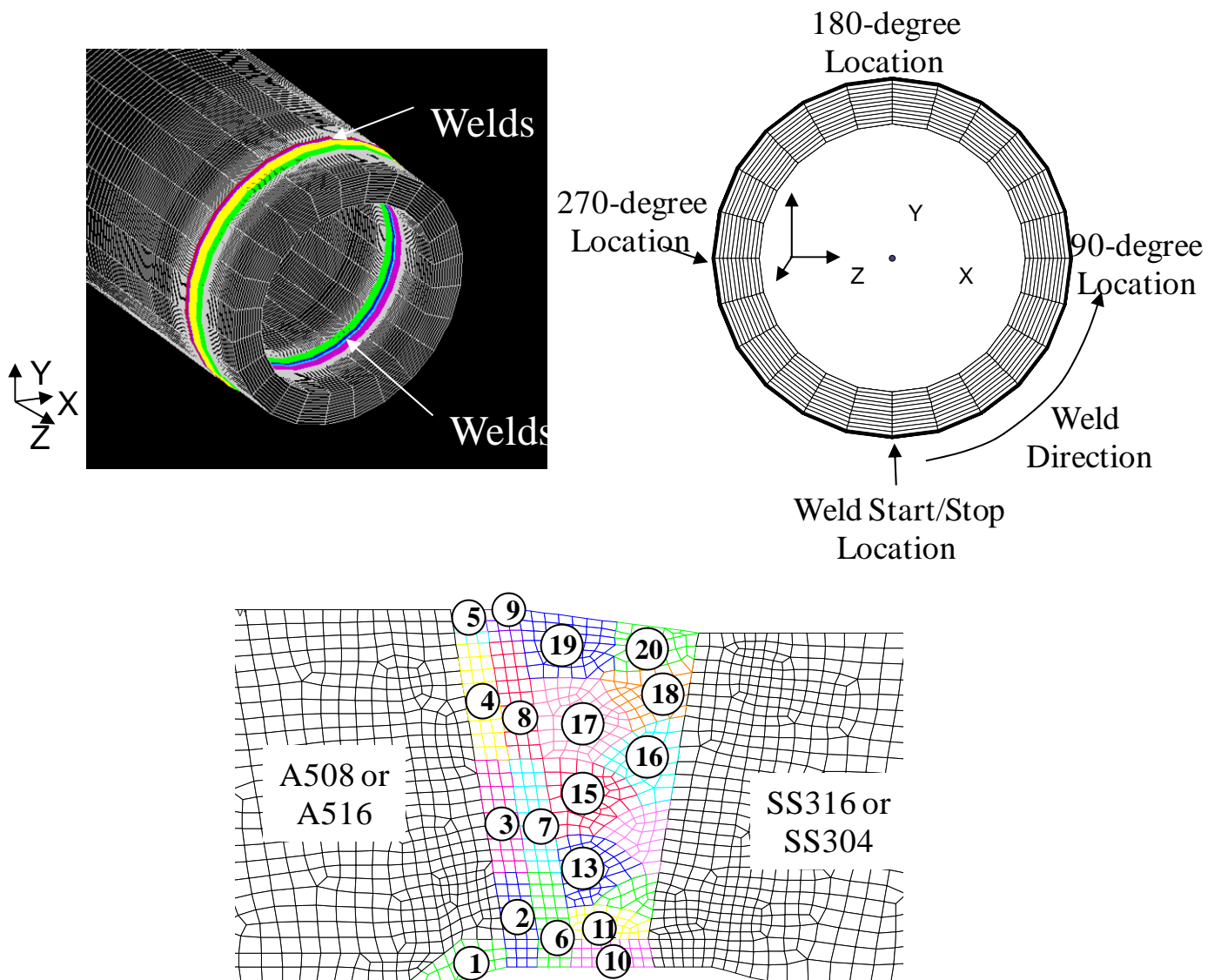


Figure A-1 Schematic description and mesh for surge nozzle weld

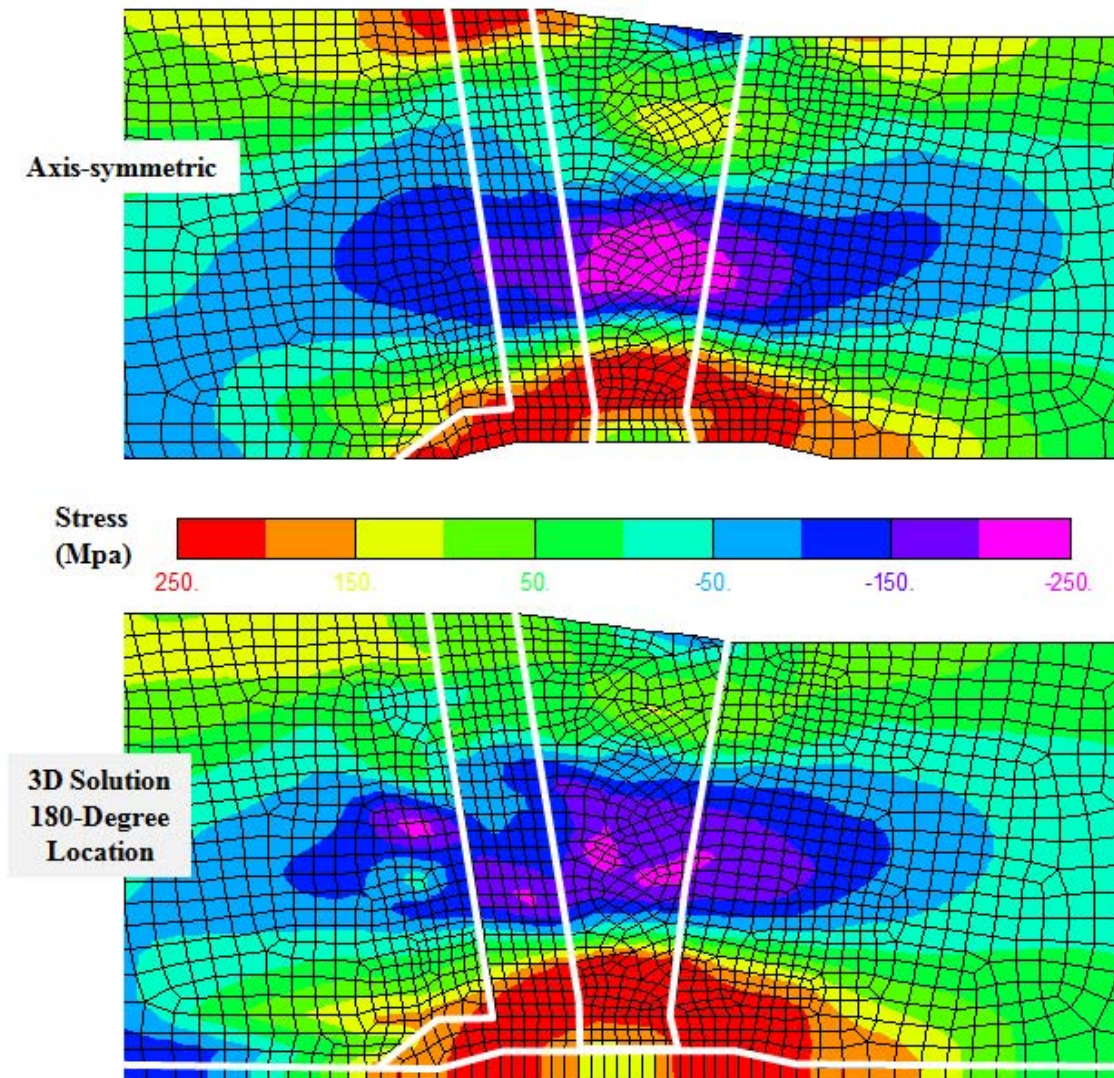


Figure A-2 Axis-symmetric (top) and three-dimensional (bottom) axial weld residual stresses for surge nozzle DM weld. These stresses are at operating temperature of 324C.

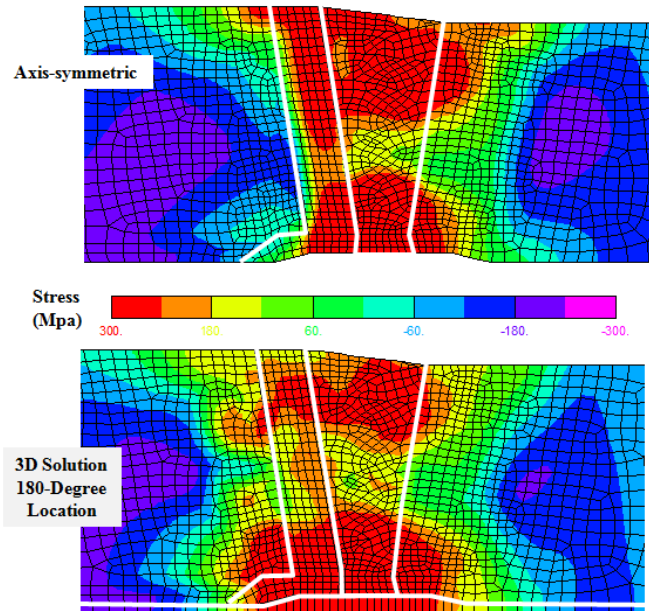


Figure A-3 Axis-symmetric (top) and three-dimensional (bottom) hoop weld residual stresses for surge nozzle DM weld. These stresses are at the operating temperature of 324 C.

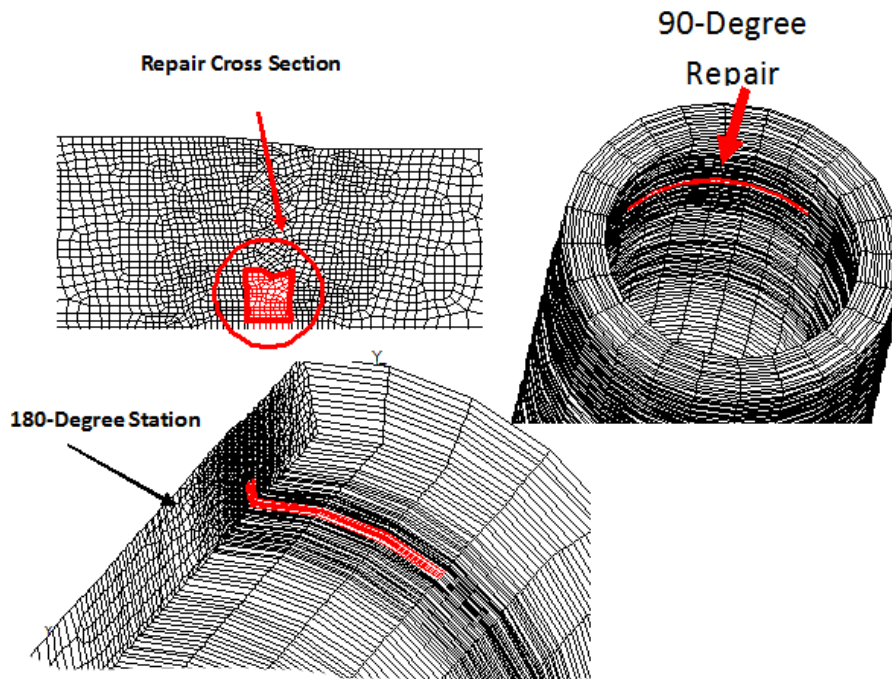


Figure A-4 Weld repair of surge nozzle weld

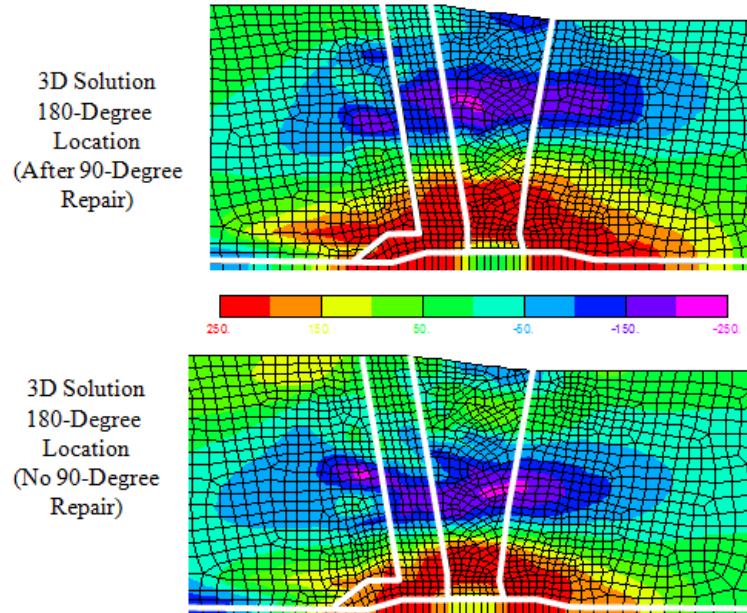


Figure A-5 Surge nozzle weld residual stresses

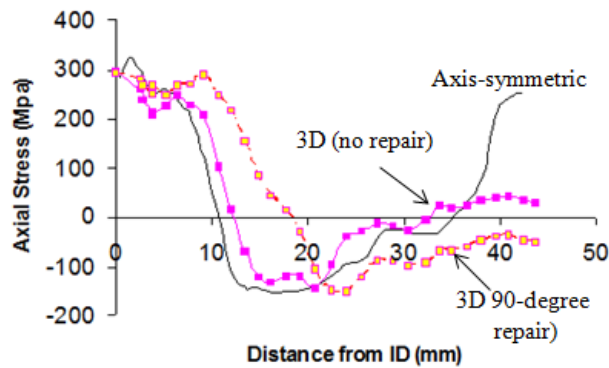


Figure A-6 Axial residual stresses plotted through the pipe wall thickness

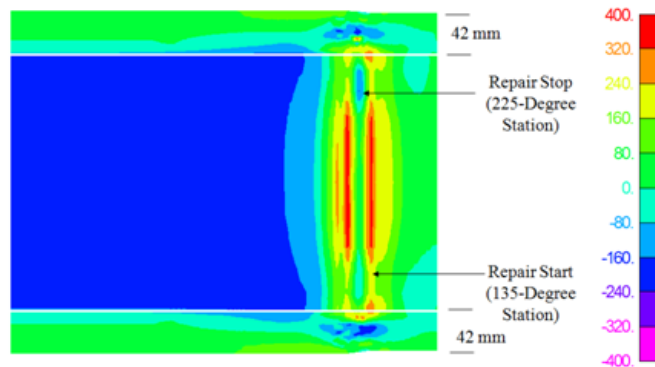


Figure A-7 Top view of axial weld residual stresses (MPa) for 3D repair case. This is a view of the pipe ID.

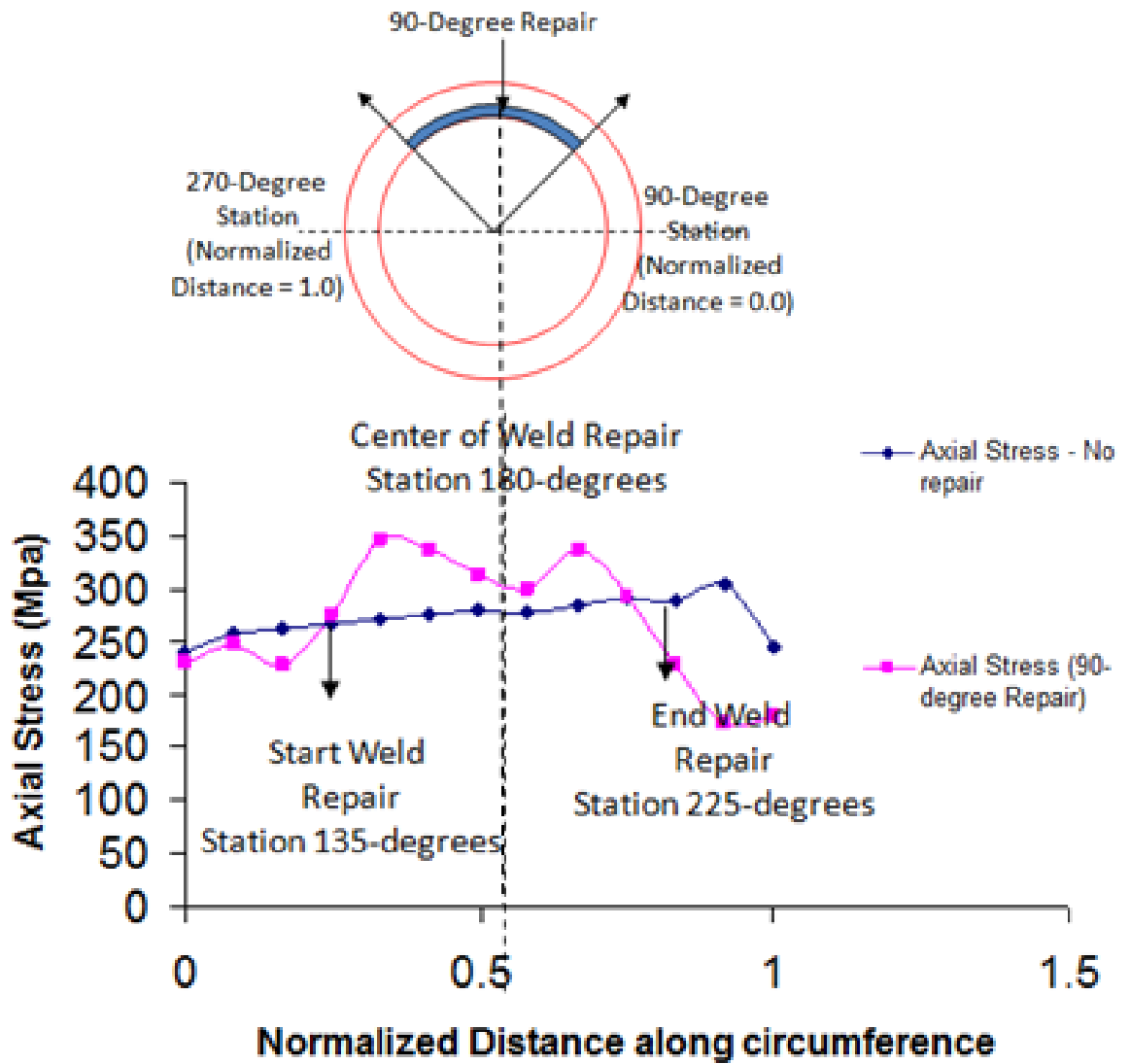


Figure A-8 Axial weld residual stresses in the center of the weld repair. The normalized circumferential distance starts at the 90-degree location and ends at the 270-degree location.

References

- 1 Brust, F. W., Chen, X. L., Yang, Z., “Modeling Distortion and Residual Stress During Welding,” Chapter 7 in *Processes and Mechanisms of Welding Residual Stress and Distortion*, Woodhead Publishing, July 2005, pp. 225 – 263.
- 2 Brust, F. W., and Kim, D., “Mitigating Welding Residual Stress and Distortion,” Chapter 8 in *Processes and Mechanisms of Welding Residual Stress and Distortion*, pp. 264 – 294, Woodhead Publishing, July 2005.
- 3 Brust, F. W., and Rudland, D., “Three Dimensional Aspects of Computational Weld Modeling,” *Proceedings of the ASME Pressure Vessels & Piping PVP 2008 Conference* July 27- 31, 2008, Chicago, IL USA.
- 4 F. W. Brust and R. B. Stonesifer, 1981, “Effects of Weld Parameters on Residual Stresses in BWR Piping Systems”, *EPRI Final Report, NP-1743*, March.
- 5 T. E. Barber, F. W. Brust, H. W. Mishler, and M. F. Kanninen, 1981, “Controlling Residual Stresses by Heat Sink Welding”, *EPRI Report NP-2159-LD*, December.
- 6 Scott, P. M., Brust, F. W., Wilkowski, G. M., and others, “BINP Final Report: Appendix G: Evaluation of Reactor Pressure Vessel (RPV) Nozzle to Hot-Leg Piping Bimetallic Weld Joint Integrity for the V. C. Summer Nuclear Power Plant,” NUREG/CR-6837, Vol. 2, June 2005.

Appendix B

Material Data Used for Analysis

The dissimilar metal welding process involves depositing molten weld material (Alloy 82/182) to join an A508 nozzle with a 316 (or 304) stainless steel safe-end. The 304 stainless steel cladding is also added to the ID of the nozzle prior to applying the dissimilar metal (DM) weld. During weld metal deposition, parts of the base materials (nozzle and stainless steel safe-end) near the weld can melt and solidify. As such, the temperature-dependent material properties are needed and were used for simulating weld residual stress, including the thermo-physical (i.e., thermal expansion, etc.) and mechanical properties of the materials involved in butt weld fabrication.

The material properties necessary for the butt weld stress analysis were collected from various sources in the open literature and through data exchanges with industry. These data were originally developed for earlier PWSCC efforts [1,2]. The temperature-dependent stress-strain curves for Alloy 82/182 solution-annealed weld metal, carbon steel, the SA-508, and stainless steel were experimentally determined at ORNL [3,4].

A508 Nozzle Material

The temperature-dependent material property data for A508 nozzle material came from test data developed by Oak Ridge National Laboratory (ORNL) [3,4]. The original stress-strain curve for the heat of A508 is shown in Figure B-1. Unfortunately, there are data at only five temperatures (the 1,500C data are set to very low values since the material is near melting). Note that for weld analyses, the stress at the first deviation from nonlinearity is used for yield rather than the 0.2% offset yield stress. Figure B-1 lists thermal conductivity, heat capacity, elastic modulus and Poisson's ratio, stress strain curves, and Norton creep properties (for PWHT analysis)

Finally, it is interesting to observe the stress-strain curves for other heats of A508. Materials with similar chemical content show quite similar behaviors, as seen in Figure B-2. Figure B-2 plots yield and ultimate stress from a number of different material databases along with the ORNL data. Several sets of data are from forgings with the test specimen cut in the axial and circumferential directions. There are also Japanese data (Hitachi) and French data (CEA) shown on this plot.

For the post weld heat treatment (PWHT), a power law defined as $\dot{\epsilon}^s = A_s \sigma^{n_s}$ was used and temperature dependent creep parameters [5] are listed in Figure B-1. Creep properties are only necessary up to the PWHT temperature of 607C. The room temperature creep properties are set to a small number for analysis to prevent creep from occurring at low temperatures. Figure B-1 also presents the thermo-physical data such as conductivity and specific heat. The annealing temperature was set 1200C.

Alloy 82/182 Weld Material and Alloy 52 Weld Material

The temperature-dependent material data for the Alloy 82/182 material were also obtained from ORNL data. The test data were obtained on annealed weld material since the weld modeling process assumes the weld metal is cooling from a molten state with no prior strain-hardening during the analysis. Using 'as welded' material property data will significantly overestimate the weld residual stresses since the weld process strain-hardens the weld metal about 10 percent.

Figure B-3 shows the stress-strain curve data used for all nozzle inlay weld analyses. These are the direct data used for the isotropic-hardening analysis cases. The annealing temperature is equal to 1300C. Figure B-4 shows material data for Alloy 52, which was tested at Emc² as part of Task 1 of this program [6]. The bottom plot shows the comparison between the Alloy 82/182 and Alloy 52 where the properties are seen to be almost identical, except at room temperature where the Alloy 52 curve is about 10% higher. Since Alloy 82/182 properties were used in the analyses presented here for inlay (since Alloy 52 properties were not available when the analyses were conducted) there should only be a slight difference at room temperature between weld residual stress results. At the operating temperature of 300C there should be essentially no difference in the stress results. Figure B-5 shows the thermo-physical data of conductivity and specific heat along with elastic modulus, coefficient of thermal expansion, and Poisson's ratio that were used. The creep properties for Alloy 82/182 were obtained from the Special Metals Corporation Bulletin [7].

316 Stainless Steel Base Metal

The temperature-dependent material property data for the TP316 stainless steel various temperatures in the range from RT to 1,400C are shown in Figure B-6. Figure B-7 presents the thermo-physical data and other necessary material data. The annealing temperature is set 1050C. Creep properties for stainless steel were obtained from Reference [8]. For the stainless steel closure weld these same properties were used for both base and weld metal.

Norton Creep

T (Degree C)	Conductivity (W/mm-C)	CTE, mm/mm-C	T (Degree C)	T (Degree C)	c_p (J/kg-C)	T (Degree C)	A_s (Mpa Units)	n
25	0.0384							
50	0.03941	1.170E-05	38	21.0	460.5	21.0	4.40E-30	4.00
100	0.04108	1.183E-05	66	175.0	519.0	175.0	4.40E-30	4.00
150	0.04121	1.201E-05	93	225.0	536.0	225.0	1.95E-17	6.05
200	0.04092	1.219E-05	121	275.0	553.0	275.0	2.11E-11	4.88
250	0.04043	1.237E-05	149	325.0	574.0	325.0	2.11E-11	4.88
300	0.03949	1.256E-05	177	375.0	595.0			
350	0.03907	1.273E-05	204	475.0	662.0			
400	0.0383	1.287E-05	232	575.0	754.0			
450	0.03735	1.305E-05	260	675.0	867.0			
500	0.03644	1.321E-05	288	725.0	1200.0			
550	0.03577	1.336E-05	316	775	875.0			
600	0.03481	1.354E-05	343	875	846.0			
650	0.03422	1.366E-05	371	912.0	605.0			
700	0.03415	1.382E-05	399	1327.0	735.0			
750	0.05899	1.397E-05	427	1527.0	835.0			
800	0.03668	1.470E-05	700					
850	0.02689	1.690E-05	800					
900	0.02835	1.690E-05	1000					
950	0.02775	1.700E-05	1005					
1000	0.02832	2.020E-05	2000					
1100	0.0295							
1200	0.03093							
1300	0.03235							
1400	0.03378							

T (Degree C)	E, GPa	Poisson's Ratio
21.1	201.33	0.3
93.3	196.51	0.3
148.9	193.06	0.3
204.4	188.92	0.3
260.0	186.17	0.3
315.6	182.03	0.3
371.1	174.44	0.3
426.7	164.79	0.3
482.2	153.07	0.3
760.0	100.25	0.3
800.0	20.00	0.3
1000.0	6.00	0.3
1440.6	-	0.3

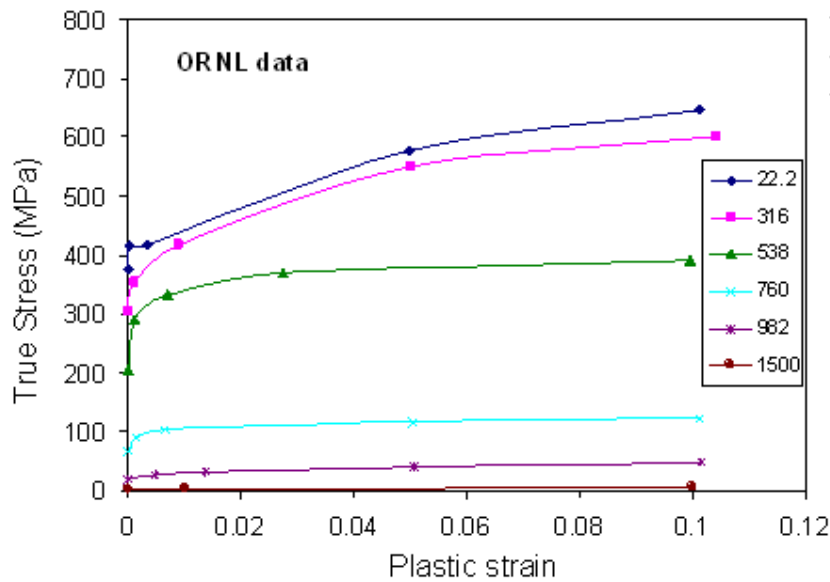


Figure B-1 A508 nozzle stress-strain curve data and thermal data.

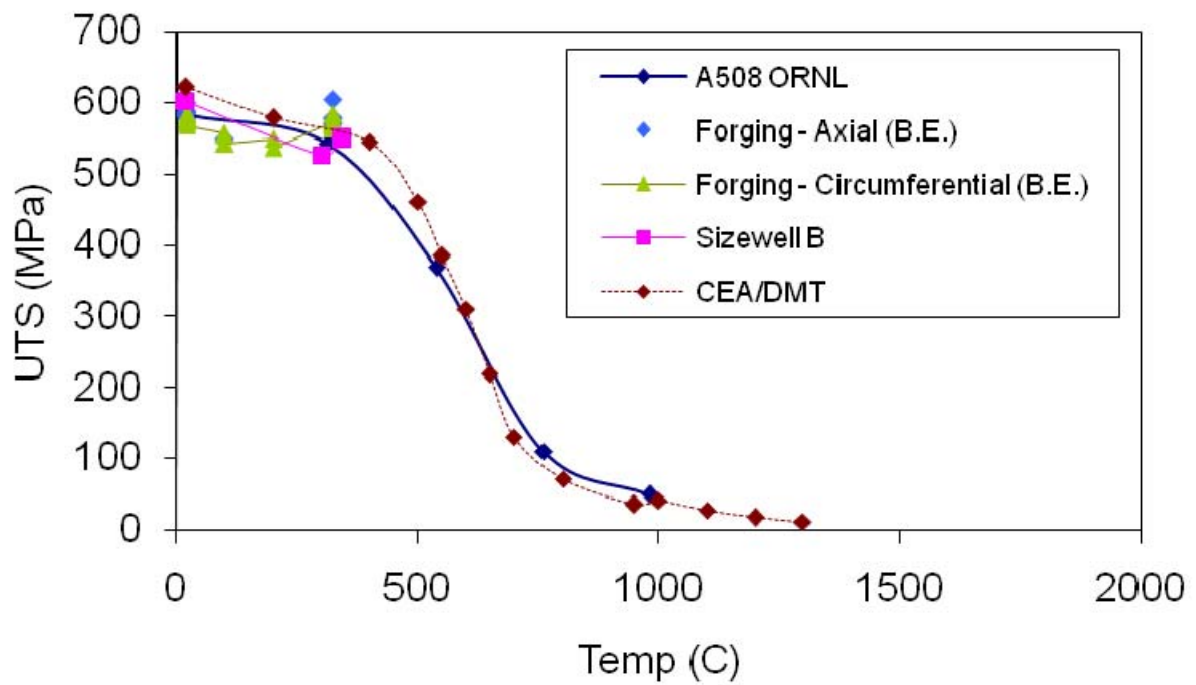
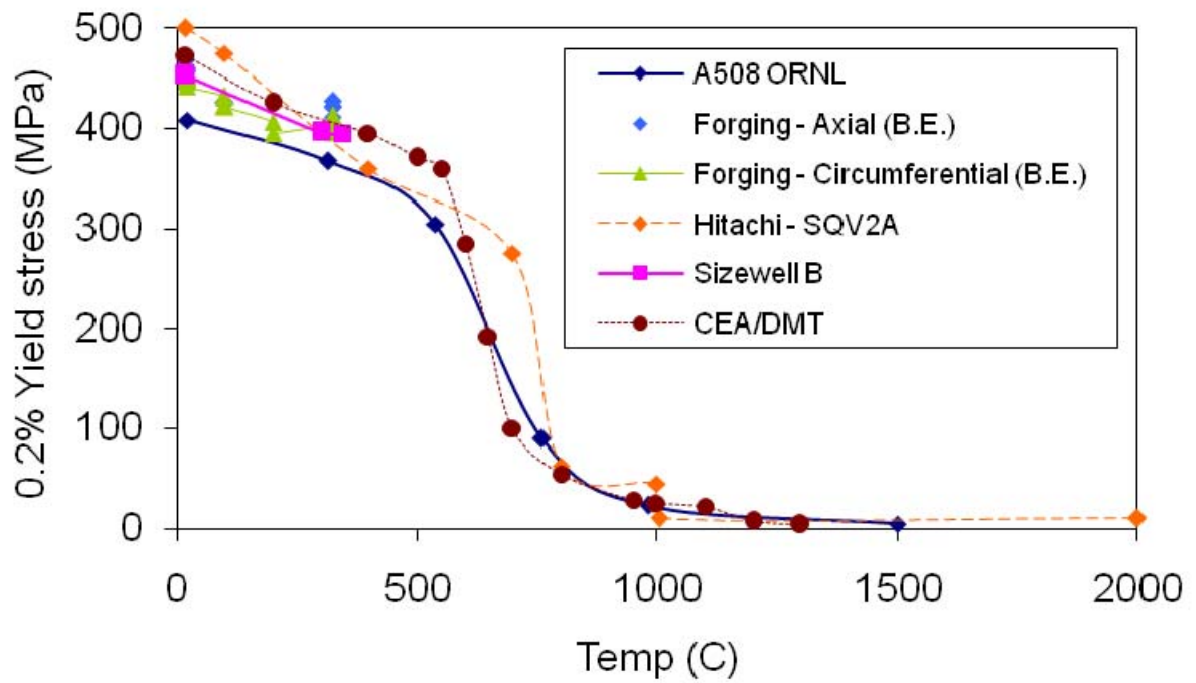


Figure B-2 Comparison of yield and ultimate stress for A508 material and similar grades of steel

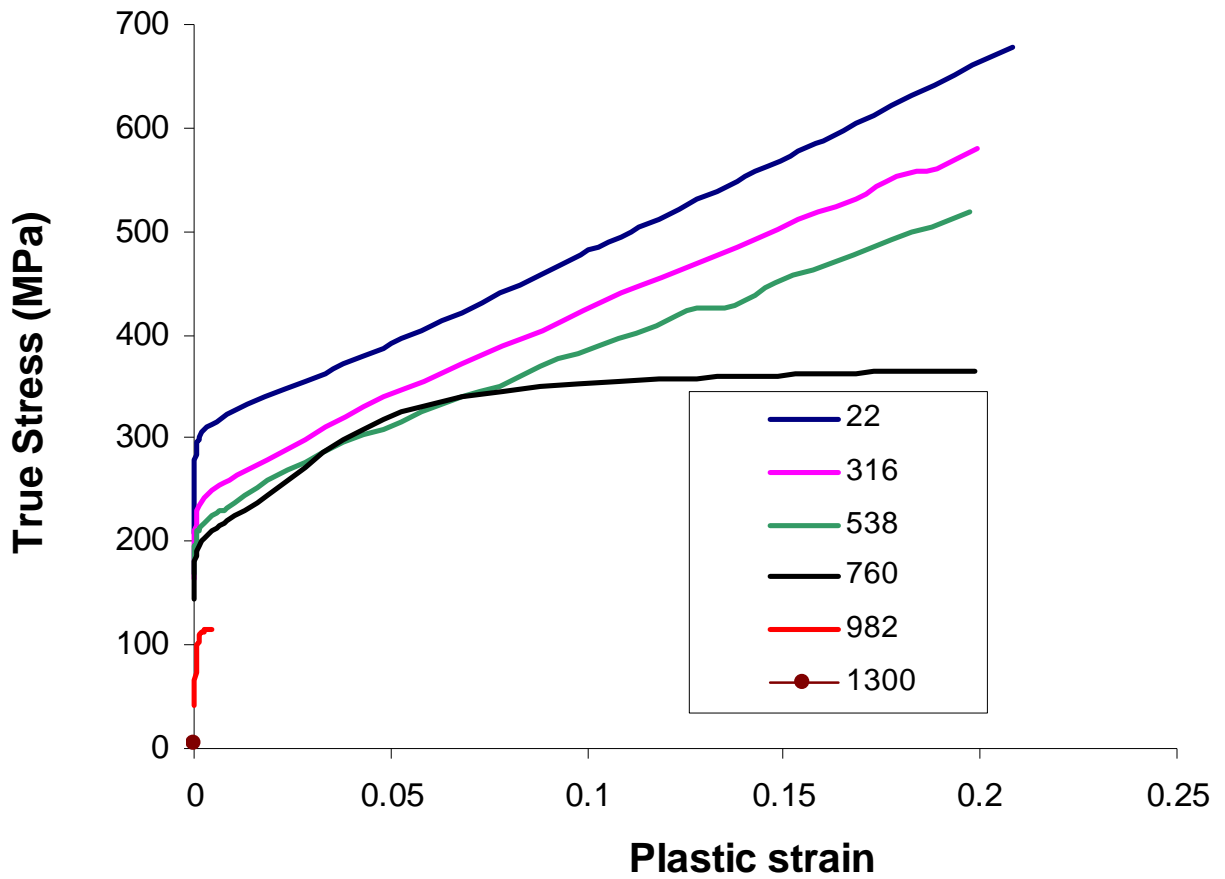


Figure B-3 Alloy 82/182 weld metal true stress-strain data as a function of temperature (22, 316, 538, 760, 962, and 1300C) used for all nozzles

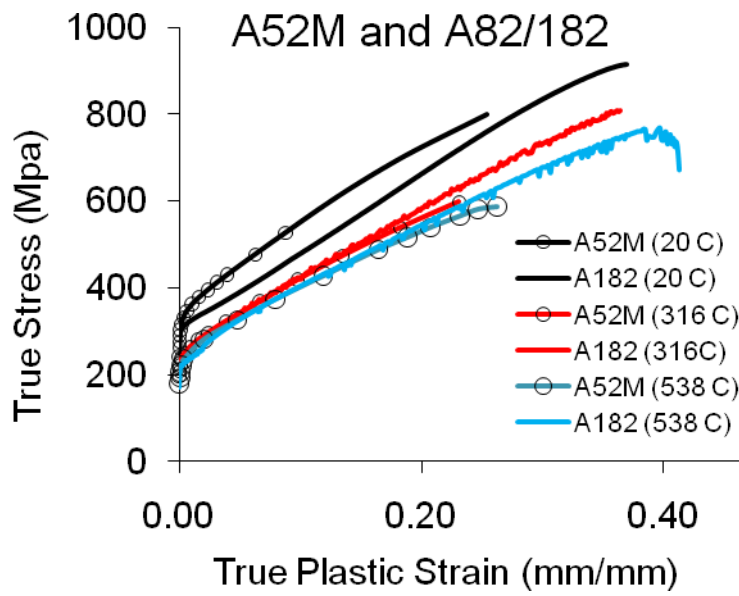
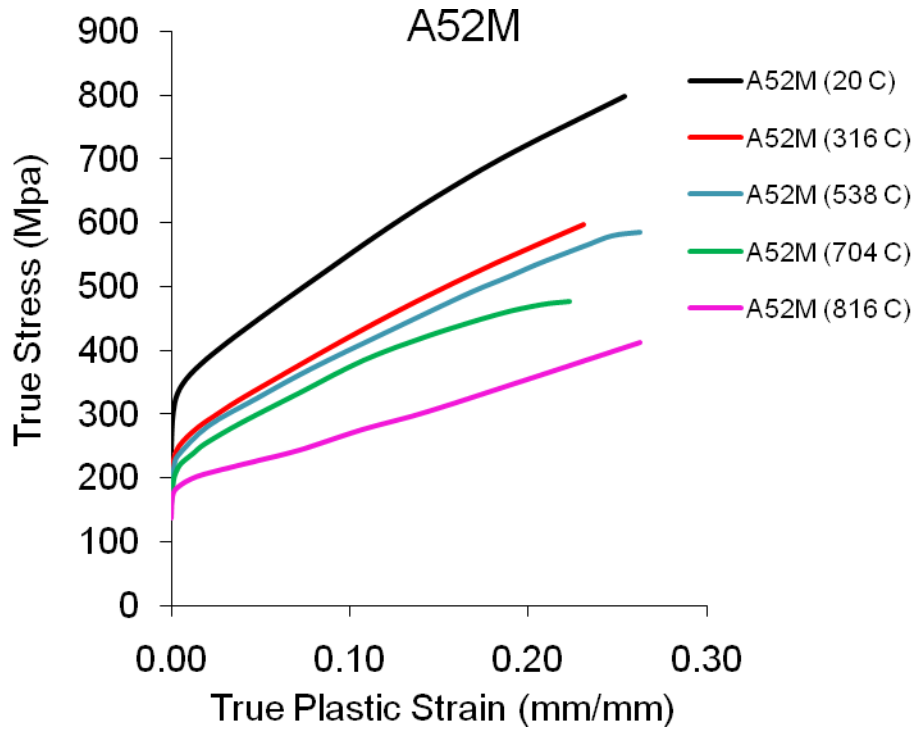


Figure B-4 True stress strain curve comparisons for Alloy 52 and Alloy 82/182

T (Degree C)	E, GPa	Poisson's Ratio
21.1	213.75	0.29
93.3	208.23	0.31
148.9	206.16	0.32
204.4	203.40	0.33
260.0	199.96	0.33
315.6	197.89	0.34
371.1	194.44	0.35
426.7	190.30	0.36
482.2	186.17	0.37
537.8	182.03	0.4
600.0	180.00	0.4
700.0	172.00	0.4
800.0	164.00	0.4
900.0	154.00	0.4
1000.0	143.00	0.4
1150.0	115.0	0.4
1260.0	78.3	0.4
1315.6	39.3	0.4

CTE, mm/mm-C	T (Degree C)
1.24E-05	38
1.27E-05	66
1.30E-05	93
1.32E-05	121
1.33E-05	149
1.35E-05	177
1.36E-05	204
1.38E-05	232
1.39E-05	260
1.40E-05	288
1.41E-05	316
1.42E-05	343
1.43E-05	371
1.44E-05	399
1.45E-05	427
1.49E-05	500
1.53E-05	600
1.58E-05	700
1.61E-05	800
1.64E-05	900
1.66E-05	1093
1.66E-05	1371

T (Degree C)	Conductivity (W/mm-C)
20.0	0.0142
77.0	0.0151
127.0	0.0160
177.0	0.0168
227.0	0.0177
327.0	0.0195
427.0	0.0213
527.0	0.0230
627.0	0.0248
727.0	0.0265
827.0	0.0283
927.0	0.0301
1027.0	0.0318
1127.0	0.0336
1227.0	0.0353
1327	0.0371
1500	0.0398

Norton Creep

T (Degree C)	A _c (Mpa Units)	n
20.0	4.40E-50	4.00
532.0	4.40E-40	4.00
538.0	1.44E-21	6.17
595.0	1.24E-20	6.64
1370.0	1.24E-20	6.64

T (Degree C)	c _p (J/kg-C)
20	444
100	465
200	486
300	502
400	519
500	536
600	578
700	595
800	611
900	628
1400	713

Figure B-5 Thermal and mechanical parameters for Alloy 82/182 weld metal.

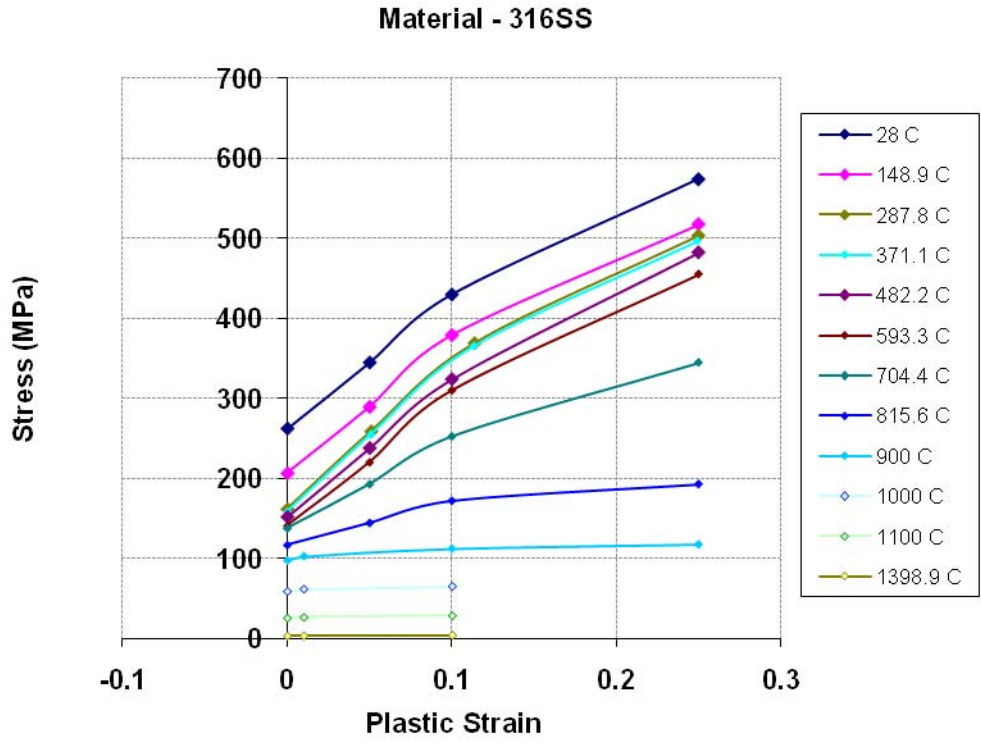


Figure B-6 Fitted stress-strain response for TP316.

CTE, mm/mm-C	T (Degree C)
1.54E-05	20
1.56E-05	66
1.58E-05	93
1.60E-05	121
1.61E-05	149
1.64E-05	177
1.66E-05	204
1.68E-05	232
1.70E-05	260
1.71E-05	288
1.73E-05	316
1.74E-05	343
1.76E-05	371
1.77E-05	399
1.78E-05	427
1.82E-05	600
1.85E-05	700
1.88E-05	800
1.91E-05	900
1.94E-05	1000
1.97E-05	1100
2.00E-05	1200
2.07E-05	1420
2.07E-05	1460

T (Degree C)	E, GPa	Poisson's Ratio
21	195	0.27
93	190	0.27
149	186	0.29
204	183	0.31
260	178	0.32
316	174	0.31
371	171	0.3
427	166	0.28
482	162	0.26
593	153	0.24
704	144	0.23
816	132	0.22
900	117	0.22
1000	100	0.22
1100	80	0.22
1200	57	0.22
1300	30	0.22
1400	2	0.22

T (Degree C)	Conductivity (W/mm-C)
21	0.0133
149	0.0156
260	0.0173
371	0.0190
482	0.0208
538	0.0215
704	0.0239
900	0.02666
1000	0.02808
1100	0.0295
1200	0.03093
1300	0.03235

Norton Creep

T (Degree C)	c_p (J/kg-C)
20	451.76
74	473.95
88	478.55
204	514.56
317	540.52
424	552.66
549	569.41
651	585.31
1000	599.0
1500	620.00

T (Degree C)	A_2 (Mpa Units)	n
20.0	4.43E-50	4.00
400.0	4.43E-40	4.00
475.0	5.84E-33	9.78
500.0	2.05E-32	9.97
525.0	4.15E-29	9.06
550.0	5.28E-26	8.20
575.0	3.67E-25	8.20
600.0	2.27E-24	8.20
625.0	1.62E-23	8.18
650.0	1.04E-22	8.16
675.0	2.05E-20	7.42
700.0	3.08E-18	6.72
725.0	1.20E-16	6.25
750.0	4.69E-15	5.77

Figure B-7 TP316 material data for weld analysis.

References

- 1 D. Rudland, G. Wilkowski Y.-Y. Wang, and W. Norris, "Analysis of Circumferential Through-Wall Crack K-solutions for CRDM Nozzles," International Journal of Pressure Vessels and Piping, Vol. 81, 2004, pp. 961-971.
- 2 Scott, P. M., Brust, F. W., Wilkowski, G. M., and others, "BINP Final Report: Appendix G: Evaluation of Reactor Pressure Vessel (RPV) Nozzle to Hot Leg Piping Bimetallic Weld Joint Integrity for the V. C. Summer Nuclear Power Plant," NUREG/CR-6837, Vol. 2, June 2005.
- 3 D. Rudland, G. Wilkowski Y.-Y. Wang, and W. Norris, "Analysis of Circumferential Through-Wall Crack K-solutions for CRDM Nozzles," International Journal of Pressure Vessels and Piping, Vol. 81, 2004, pp. 961-971.
- 4 Scott, P. M., Brust, F. W., Wilkowski, G. M., and others, "BINP Final Report: Appendix G: Evaluation of Reactor Pressure Vessel (RPV) Nozzle to Hot Leg Piping Bimetallic Weld Joint Integrity for the V. C. Summer Nuclear Power Plant," NUREG/CR-6837, Vol. 2, June 2005.
- 5 Aerospace Structural Metals Handbook, Code 1208, 8630 Steel, Metals and Ceramics Information Center, Battelle, 1990.
- 6 Brust, F. W., Zhang, T., Shim, DJ, and Wilkowski, G, "Evaluation of Flaws in Reactor Penetration Heads", Draft report to NRC, November, 2009, under review.
- 7 Special Metals Corporation Bulletin, www.specialmetals.com, for alloy 600, 2004.
- 8 Structural Alloys Handbook, 1990 Edition, Volume 2, Metals and Ceramics Information Center, Battelle.

Appendix C

Compendium of Welding Residual Stress Results

This appendix provides a compendium of weld residual stress solutions (without inlays) that can be used to perform PWSCC and fatigue evaluations for indications found in dissimilar metal welds. These solutions represent the welding residual stress states prior to the application of an inlay, as described in the main body of the report. The first section of this appendix (Section 1.0) provides solutions for Model 1 with a 50% repair (Cases 8 to 10 from Table C-1). This section also provides results for Model 2 with 12, 25, and 50% repairs (Cases 8 to 14 from Table C-2). Section 2 provides additional results for some of the other cases considered (Cases 11 and 12 from Table C-1 for Model 1) which dealt with an embedded flaw in the DM weld and a cast stainless steel safe-end. In all cases, the welding residual stress simulation process, the weld geometry, and the model inputs are discussed in Section 3 of the main report.

1. Compendium of Weld Residual Stresses for Hot Leg Nozzle Geometry Without Mitigation: With and Without Stainless Steel Safe-end Weld

Cases 8 and 9 From Table C-1(Model 1)

For completeness, this appendix presents welding residual stress plots for different cases from Table 1 (Model 1) and Table 2 (Model 2) from Section 3.2.3. Table C-1 reproduces Table 1 and Table C-2 reproduces Table 2 of Section 3.2.3. The results shown in this section can be used for PWSCC growth analyses for cases with and without the stainless steel safe-end weld. The stainless steel safe-end weld is known to improve (make more compressive) the WRS state on the ID of a DM weld. The dimensions for Model 1 are presented in Figure 5 of the main body of this report.

Centerline Location - Figure C-1 shows the axial (top) and hoop (bottom) weld residual stress distributions for Cases 8 and 9 from Table C-1 taken along the weld centerline. These cases represent a 50% repair performed prior to the application of the stainless steel safe-end weld, i.e., a pre-service repair. The stainless steel safe-end weld reduces both axial and hoop weld residual stresses in the DM weld. A polynomial 4th order fit to the calculated stress distributions is shown with the equation constants listed. These fits were made with Excel using a least squares fit. For an idealized crack growth analysis, these constants can be used directly. The 4th order fit was used since published stress intensity factor solutions for surface cracks in pipe are typically up to a 4th order fit. It is noted that a 6th order fit more accurately captures the distribution, especially at the ID and OD, but since the K-solutions are typically not developed for 6th order fits, these are not included. In all plots in this appendix, the polynomial fits for the cases without the stainless steel safe-end weld are in 'red' and the fit for the cases with the SS safe-end weld are in 'blue'. It is seen that the fit for the axial stresses is reasonable at the nozzle ID, and less accurate near the OD. Note that the simulation results and not the curve fit solutions, tabulated in Table C-3 for the case without a SS safe-end weld and Table C-4 for the case with the SS safe-end

weld, should be used in a natural crack growth analysis since the thermal fit algorithm used in the AFEA approach can capture the non-polynomial behavior more accurately. Note that the hoop weld residual stresses tend to ‘wiggle’ somewhat. Often, this is due to the plotting algorithm within ABAQUS viewer when paths are used to extract results. This local fluctuation in the stresses also occurs due to the heating and cooling of each weld pass. This behavior is amplified when isotropic hardening is assumed. Isotropic hardening tends to produce higher (in absolute magnitude) weld residual stress predictions.

DM Weld/SS, DM Weld/Butter, and DM Weld/Nozzle Locations - Figures C-2 to C-4 show similar plots and polynomial fits for the other locations through the nozzle wall for Cases 8 and 9 from Table C-1. Hoop stresses for the cases along the DM weld/SS line and DM weld/nozzle line sometimes fluctuate locally since these are along the material discontinuity (in material properties) line. Finally, Figure C-5 shows a comparison of axial WRS for the weld centerline location with no SS safe-end weld assumed (Case 8), with the SS safe-end weld assumed (Case 9), and after inlay weld (Case 1) for comparison. It is clear that the stainless steel weld has a strong stress benefit at the DM weld, while the inlay eliminates the residual stress benefits of the stainless steel safe-end weld.

The WRS using an isotropic hardening assumption may tend to be an upper bound (both in tension and compression). For many cases, the calculated crack growth rate may be higher than they would appear in service. However, there are cases where the compression may become large, reducing crack growth rates, so that the predictions of growth may not always be conservative from a time standpoint. Finally, it is noted that these stresses are all at 300C with no pressure applied. For crack growth predictions, the user must combine the service loads (pressure, bending, thermal expansion, etc.) with the welding residual stress. If the operating temperature is higher than 300C, it is conservative to use these values since WRS generally decrease as the temperature increases.

Case 10 From Table C-1(Model 1)

This section provides weld residual stresses for the special case where a repair is made after the stainless steel safe-end weld is made. Such a repair, which is called a PWSCC repair in this report, essentially eliminates the advantages of the stainless steel weld. Here these results are presented along with the Case 9 results (repair before the stainless steel safe-end weld) for comparison.

Centerline Location - Figure C-6 shows the results for Case 9 (repair before the stainless steel safe-end weld, i.e. pre-service repair) and Case 10 (PWSCC repair), without mitigation at the weld centerline location. The Case 9 results are shown for contrast (these are the same as presented in Figure C-1) illustrating the effect of the PWSCC repair and how such a repair eliminates the benefits produced from the SS safe-end weld. Axial stresses are presented in the top illustration and hoop stresses in the bottom illustration. The fourth order polynomial fit to the distribution is also presented for convenience. In Figure C-6 (top) a 6th order fit is also shown for comparison. The 6th order polynomial fit provides a better match with the finite element results, especially at the ID and OD regions. However, as mentioned above, the 4th order fit is provided for all the distributions since published stress intensity solutions typically use a 4th order fit to the stress. The actual WRS data are tabulated in Table C-5.

DM Weld/SS, DM Weld/Butter, and DM Weld/Nozzle Locations - Figures C-7 through C-9 provide the axial and hoop stresses, along with the 4th order polynomial fit, for stresses along the DM weld/SS line, the DM weld/butter line, and DM weld/nozzle line, respectively. Again, the results for a pre-service repair with the stainless steel safe-end weld (which are identical to the Case 9 results presented in Figures C-2 to C-4) are shown at each location for comparison. The ‘wiggles’ in some of the plots are caused in part by the multiple pass nature of the welds (which can lead to slight bead-to-bead stress variations) along with ABAQUS plotting anomalies, which are especially prevalent along the DM weld/SS and DM weld/nozzle interfaces. These local variations cause some difficulties in obtaining a reasonable 4th order fit. However, the resulting crack growth predictions should not be affected significantly. As discussed with relation to Figures C-1 to C-4, the actual weld residual stresses (Tables C-4 and C-5) should be used for the natural crack growth calculations for better accuracy.

Cases 8 to 11 From Table C-2 (Model 2) – No Stainless Steel Weld

This section compiles residual stress distributions for the Model 2 (Figure 9 in main body of report) hot leg for Cases 8 to 11 in Table C-2. These compilations represent the weld residual stresses for the case of no repair (Case 8), and 12, 25, and 50% repairs (Cases 9, 10, 11, respectively) without a stainless steel safe-end weld.

Centerline Location - Figure C-10 summarizes the axial (upper plot) and hoop (lower plot) weld residual stresses prior to application of the stainless steel safe-end weld. These WRS could be used for crack growth analysis in a DM weld where the stainless steel weld was long. For the case of no ID repair, the weld residual stresses are tensile at the nozzle ID. However, once the repairs are made, the tensile ID stresses rise sharply just inside the pipe ID. Model 2 wall thickness is quite thick (~81 mm at the stainless steel side and ~87 mm at the nozzle side, Figure 9). The WRS behavior observed is due to the thickness used in this model. For smaller diameter pipe (spray and surge size), where the thickness is smaller, the large increase in stress at the ID is not apparent. Essentially, for such a thick nozzle, the WRS crosses through zero stress three times, as seen in the top illustration in Figure C-10. As the repair depth increases from 12% to 50%, it is seen that the distance through the thickness where the stresses cross through zero becomes deeper (for instance, the 12% repair crosses zero at about $R/t = 0.27$, the 25% repair crosses at $R/t = 0.29$, and 50% repair at about $R/t = 0.32$ for the centerline location). The location of the maximum compression stress also increases as the repair depth increases. Interestingly, the maximum axial tensile stress for the 25% and 50% repairs are about the same while for the 12% repair the maximum axial stress is lower. The hoop stresses are shown in the bottom illustration of Figure C-10. The undulations in the curves are due to the pass-by-pass local heating and cooling and by the isotropic hardening assumption. The hoop WRS are strongly affected by the repair.

Figure C-11 provides 4th order polynomial fits for the no repair and 12% repair cases. In general, the 4th order fits do not capture the residual stress distributions perfectly, but can be used for idealized crack growth analysis. Figure C-12 provides the same information for the 25% and 50% repair cases, including the 4th order polynomial curve fits. Again, the fits tend to average the stresses of the actual calculations and can be used for idealized crack growth predictions. For

natural crack growth, the actual data should be used since the thermal fit to the WRS data can provide very good predictions. The actual WRS data is tabulated in Table C-6.

DM Weld/SS Line Location – Figure C-13 provides the WRS at the DM weld and stainless steel safe-end location. Note that the insert in Figure C-13 defines the actual path, which is longer than a path directly through the thickness. However, the data are plotted as a function of the radius divided by the thickness. The axial stresses are higher along the centerline compared with the DM weld/SS location. However, the distance at which the stress crosses through zero follows the same trends as discussed earlier. The hoop stresses from this location also have the same trends as the stresses from the centerline location. Figure C-14 summarizes the 4th order fits for the no repair and 12% repair cases while Figure C-15 does the same for the 25% and 50% fits. The WRS data for the DM weld/SS line for the case of no SS weld (Model 2) is listed in Table C-7.

DM Weld/Butter Line Location – Figure C-16 compares the WRS for the no repair and three repair cases along the DM weld/butter location. Again, even though the path where the stresses were extracted is angled, the plots are presented at radial locations through the nozzle wall. Similar trends are observed as compared to the centerline case. The WRS are maximum (and most severe for PWSCC growth concerns) for the centerline and this location. Figure C-17 shows the distribution and 4th order fit for the no repair and 12% repair, while Figure C-18 is for the 25% and 50% repair cases. Table C-8 tabulates the WRS for these cases.

DM Weld/Nozzle Line Location – Figure C-19 shows the results along the DM weld/nozzle line. The stresses at this location are lower than at the centerline or DM weld/butter location on average. However, the ID stresses are more tensile. The ‘hump’ and higher tensile stresses observed at the centerline and DM weld/butter locations are not seen at this location (compare to Figures C-10 and C-16). Figures C-20 and C-21 show the polynomial fits. These fits represent the analysis results more accurately than the centerline and DM weld/butter fits since the stresses only cross zero twice at this location as compared with three times at the other locations. Table C-9 tabulates the WRS for these cases.

Cases 12 to 14 From Table C-2 (Model 2) – With Stainless Steel Safe-End Weld

This section compiles residual stress distributions for Model 2 (Figure 9), Cases 12 to 14 in Table C-2. These compilations represent the weld residual stresses for the case with a stainless steel safe-end weld and a 12% repair (Case 12), and 25, and 50% pre-service repairs (Cases 13, 14, respectively).

Centerline Location - Figure C-22 summarizes the axial (upper plot) and hoop (lower plot) weld residual stresses after application of the stainless steel safe-end weld. The stainless steel safe-end weld improves (reduces) the weld residual stresses if the SS weld is in the proximity of the DM weld (within 75 to 100 mm). These WRS could be used for crack growth analysis in a DM weld with a short safe-end. If the safe-end is long, the distributions shown in Figures C-10 to C-21 should be used. The weld residual stresses become compressive at the ID. Note that Model 2 is quite thick (~81 mm at the stainless steel side and ~87 mm at the nozzle side, Figure 9). The axial stresses reach a maximum tensile level of about 200 MPa at a depth of $R/t \sim 0.15$ to 0.2 regardless of the repair depth. However, the deeper 50% repair does not cause a large

compression region as compared to the other repair depths. This suggests that for crack growth predictions, the 50% deep repair case will not cause the crack growth to slow down as much in the compressive zone, and through-wall crack growth will be more rapid. The hoop stresses for the 12% and 25% repairs are close to each other, while the 50% repair deviates somewhat.

Figure C-23 presents these same plots for the centerline location with 4th order polynomial (least squares) fit shown. These curve fits can be used in idealized crack growth predictions. The fit is good at the ID and OD, but deviations occur for all stress distributions in the interior of the wall thickness. A 4th order polynomial fit does not capture this distribution accurately because the stresses cross through zero three times (for axial stresses). Table C-10 tabulates the results for these cases.

DM Weld/SS Line Location – Figure C-24 provides the WRS at the DM weld and stainless steel safe-end location. Note from the insert in Figure C-24 the path where the stresses were extracted is angled. However, the data are plotted as a function of the radial location divided by the thickness. The axial stresses are higher along the centerline compared with the DM weld/SS location. The hoop stresses behave similarly to those at the centerline location. The undulations in the hoop stress plots exist due to the complicated repair depths and the pass-to-pass local fluctuations in the local stresses. Figure C-25 summarizes the 4th order fits for the all cases. Table C-11 tabulates the WRS results for these cases.

DM Weld/Butter Line Location – Figure C-26 compares the WRS for the three repair cases along the DM weld/butter location. Again, the path where the stresses are extracted is actually angled, but the plots are presented along a radial location through the nozzle wall. The trends in stress are similar to those shown earlier. The WRS are maximum (and most severe for PWSCC growth concerns) for the centerline and this location. The hoop stresses along this line fluctuate through the thickness. Figure C-27 shows the distribution and 4th order fits for the 12% repair, 25% and 50% repair cases. Table C-12 tabulates the WRS for the DM weld/butter line.

DM Weld/Nozzle Line Location – Figure C-28 shows the results along the DM weld/nozzle line. The axial stresses at this location are slightly tensile at the ID. However, the hoop stresses at the ID are more tensile. Figures C-29 shows the polynomial fits. These data are tabulated in Table C-13 for these cases.

Finally, Figure C-30 summarizes the differences between Model 1 and Model 2 for the centerline location. These are for Cases 8 and 9 for Model 1 and Cases 11 and 14 for Model 2. The differences between two hot leg geometries are seen here. The general trends are similar, but some of the magnitudes are different.

2. Summary of Additional Weld Residual Stresses for Hot Leg

For completeness, this part of the appendix presents welding residual stress plots for different cases from Table 1 (Model 1) and Table 2 (Model 2) from Section 3.2.3. Results not shown in the main body of the report are presented here and are labeled with a ‘*’ in the tables below.

Case 11, (75% PWSCC Flaw and 50% Pre-service Flaw). This example examines the axial weld residual stress for a case where the inlay is deposited in a hot leg nozzle where a pre-existing flaw exists. This might be the case where a flaw was not detected prior to depositing the inlay. There are two flaw examples considered here. Referring to Figure C-31, the deep embedded flaw case (lower left) considers an 11.4 mm flaw that is assumed to exist 5.1 mm under the OD of the DM weld. The weld and butter lines are shown in this illustration for reference. The second embedded flaw case, called the shallow embedded flaw case (lower right in Figure C-31), consists of a flaw that begins 9.52 mm above the ID of the machined inlay and is 24 mm in length. The flaws were modeled simply by removing elements and possible contact was ignored.

Figure C-32 shows the axial weld residual stresses before and after application of the 75% PWSCC repair. Recall that a 75% PWSCC repair is a repair occurring over 75% of the wall depth after deposition of the SS safe-end weld. The stresses on the ID reverse from compression to tension and the tension on the OD reverses to compression, a well known deleterious effect of weld repairs. Figure C-33 shows the axial WRS (at 300C) along two paths (see Figure C-31) compared to the case with no flaw. The presence of the deep flaw decreases the axial stress near the ID. Near the OD, the stress state depends on the path chosen. For Path 1 (which follows closely to the flaw where the stresses must approach zero at the free surface) the stresses oscillate more than for Path 2. Finally, Figure C-34 shows a comparison of WRS for Case 4 with and without an embedded flaw (Model 1). It is seen that only the stresses in the vicinity of the deep embedded flaw are altered by the presence of the flaw.

Figure C-35 shows the axial residual stress state for Case 1 with and without the presence of a flaw during the deposition of the inlay (Model 1). It is seen that the flaw reduces the WRS state in magnitude (both tensile and compression) compared to the case without the embedded flaw. Hence, from a WRS standpoint, the flaw has little effect. However, in practice if a flaw did exist and was not detected prior to application of the inlay, a PWSCC crack may link up and reduce the time to leakage.

Case 12, (Case 1 Assuming Cast Stainless Steel Properties). Figure C-36 compares the weld centerline axial weld residual stresses at 300C (no pressure applied) for a wrought and cast stainless steel safe-end. The material properties for the cast stainless are available at room temperature up to 320C and are about 15% higher than wrought stainless steel. The weld residual stresses do not change much at the weld centerline. In fact, the stresses vary about the same amount at all locations including the DM weld/SS line.

Table C- 1 Weld Residual Stress Analysis Cases for Model 1 (from Section 3.2.3)

WRS Case #	WRS case	Inlay depth	Comments
1	50% pre-service repair	3 mm	DMW-50% Repair-SS Weld- Inlay ⁺
2	50% PWSCC repair	3 mm	DMW-SS Weld-50% Repair-Inlay ⁺
3	75% (2-inch) pre-service repair	3 mm	DMW-75% Repair-SS Weld- Inlay ⁺
4	75% (2-inch) PWSCC repair	3 mm	DMW-SS Weld-75% Repair-Inlay
5	50% preservice-75%PWSCC repair	3 mm	DMW-50% Repair-SS Weld- 75% Repair- Inlay ⁺
6	50% pre-service repair	6 mm	DMW-50% Repair-SS Weld- Inlay ⁺
7	50% PWSCC repair	6 mm	DMW-SS Weld-50% Repair-Inlay ⁺
8	50% pre-service repair – No SS Weld	None	DMW-50% Repair [*]
9	50% pre-service repair –SS Weld	None	DMW-50% Repair-SS Weld [*]
10	50% PWSCC repair – No inlay	None	DMW-SS Weld-50% Repair [*]
11	Pre-existing flaw cases	3 mm	Deep embedded OD flaw and embedded flaw near ID
12	50% pre-service repair	3 mm	DMW-50% Repair-SS Weld- Inlay [*] Cast Stainless Steel Properties

⁺presented in section 3.2.3

^{*}presented here

Table C- 2 Weld Residual Stress Analysis Cases for Model 2 (from Section 3.2.3)

WRS Case #	WRS case	Inlay depth	Comments
1	12% pre-service repair	3 mm	DMW-12% Repair-SS Weld- Inlay ⁺
2	12% preservice-12%PWSCC repair	3 mm	DMW-12% Repair-SS Weld-12% Repair-Inlay ⁺
3	12% PWSCC repair	3 mm	DMW-SS-12% Repair-Inlay ⁺
4	50% pre-service repair	3 mm	DMW-50% Repair-SS-Inlay ⁺
5	50% PWSCC repair	3 mm	DMW-SS-50% Repair-Inlay ⁺
6	25% pre-service repair	3 mm	DMW-50% Repair-SS-Inlay ⁺
7	25% PWSCC repair	3 mm	DMW-SS-50% Repair-Inlay ⁺
8	DMW with No repair-No SS weld	None	DMW-No Repair-No SS Weld [*]
9	DMW with 12% repair-No SS weld	None	DMW-12% Repair-No SS Weld [*]
10	DMW with 25% repair-No SS weld	None	DMW-25% Repair-No SS Weld [*]
11	DMW with 50% repair-No SS weld	None	DMW-50% Repair-No SS Weld [*]
12	DMW with 12% repair- After SS weld	None	DMW-12% Repair- SS Weld [*]
13	DMW with 25% repair-After SS weld	None	DMW-25% Repair- SS Weld [*]
14	DMW with 50% repair-After SS weld	None	DMW-50% Repair- SS Weld [*]

⁺presented in section 3.2.3

^{*}presented here

Table C-3 Case 8 – Model 1 (No SS Weld) – 50% Repair

Weld Centerline			DMW/SS			DMW/Butter			DMW/Nozzle		
R/t	Axial MPa	Hoop MPa	R/t	Axial MPa	Hoop MPa	R/t	Axial MPa	Hoop MPa	R/t	Axial MPa	Hoop MPa
0.000	44.3	281.7	0.000	164.1	247.5	0.000	-68.6	251.2	0.000	63.5	310.1
0.024	80.3	271.0	0.024	161.0	282.9	0.021	-7.0	275.2	0.024	73.0	284.0
0.050	117.3	266.8	0.033	139.1	285.1	0.046	70.9	329.1	0.048	102.3	291.0
0.065	131.5	268.4	0.042	124.5	280.4	0.066	111.6	343.8	0.071	131.8	287.2
0.086	146.5	275.1	0.053	112.2	276.5	0.086	157.3	363.7	0.092	154.7	293.5
0.107	148.5	281.7	0.067	106.0	282.3	0.102	185.4	367.9	0.117	185.1	313.5
0.116	187.7	347.2	0.080	109.6	288.4	0.106	192.1	370.0	0.128	258.2	319.4
0.125	216.6	384.0	0.100	116.8	289.7	0.118	219.5	369.7	0.136	271.5	319.5
0.145	175.5	323.1	0.117	103.7	276.5	0.128	320.1	553.5	0.143	271.2	308.7
0.159	150.5	314.8	0.128	126.6	269.3	0.143	297.7	482.6	0.175	250.3	332.8
0.181	138.0	327.1	0.139	141.3	382.9	0.175	261.9	450.9	0.204	137.7	323.0
0.207	150.1	420.6	0.167	152.9	380.8	0.204	208.1	470.3	0.235	93.9	305.6
0.227	150.9	495.7	0.201	128.4	415.4	0.235	60.1	415.5	0.267	55.6	278.4
0.249	109.6	443.0	0.224	110.3	403.9	0.267	6.4	349.0	0.298	45.1	271.0
0.260	87.7	424.1	0.247	103.2	378.6	0.298	0.4	339.5	0.328	9.7	256.7
0.278	76.7	419.7	0.272	65.2	338.2	0.328	-19.5	328.1	0.358	-23.6	215.9
0.290	63.7	405.7	0.298	53.8	360.2	0.358	18.2	332.6	0.388	4.9	212.7
0.310	62.6	419.4	0.328	41.6	394.4	0.388	-12.0	322.9	0.423	8.5	235.9
0.332	42.0	420.2	0.358	-50.5	319.9	0.423	-47.1	313.3	0.457	-0.3	229.5
0.348	7.9	392.3	0.387	-99.7	302.8	0.457	15.0	340.7	0.492	-52.7	193.0
0.361	-32.5	364.7	0.413	-46.3	364.0	0.492	-4.4	367.7	0.527	-100.1	118.7
0.383	-59.1	353.2	0.439	-15.2	357.9	0.529	-74.6	360.4	0.562	-164.0	34.4
0.394	-56.6	347.8	0.465	-87.5	285.0	0.565	-108.1	309.3	0.597	-214.8	-29.1
0.417	-33.7	359.4	0.491	-68.1	320.5	0.602	-157.0	257.7	0.632	-254.0	-67.6
0.450	-20.8	354.8	0.526	-0.7	393.1	0.639	-242.7	180.6	0.667	-271.9	-65.9
0.471	-48.0	340.2	0.559	-70.4	314.3	0.677	-313.2	90.1	0.702	-290.5	-40.4
0.502	-72.5	331.0	0.592	-136.5	260.7	0.714	-344.8	56.8	0.735	-237.2	-0.4
0.522	-55.3	367.1	0.634	-142.6	274.9	0.748	-321.2	91.3	0.768	-190.2	50.0
0.553	-65.8	429.8	0.675	-200.2	222.6	0.782	-219.5	168.2	0.801	-119.8	106.4
0.577	-93.7	385.2	0.715	-258.5	159.5	0.815	-74.6	258.9	0.836	-19.3	157.7
0.608	-126.5	333.8	0.743	-241.8	146.4	0.849	55.0	312.8	0.871	92.9	202.2
0.625	-135.8	320.6	0.771	-214.8	180.5	0.884	148.6	319.8	0.906	141.1	240.5
0.644	-172.7	286.4	0.801	-138.1	292.2	0.918	216.8	326.5	0.937	250.5	259.0
0.662	-224.8	246.3	0.831	-29.8	329.7	0.945	242.8	309.7	0.969	263.1	245.8
0.674	-258.0	226.9	0.841	-2.2	334.4	0.973	253.2	268.8	1.000	267.5	233.2
0.709	-275.0	192.9	0.872	87.0	338.2	1.000	256.7	254.0			
0.718	-274.8	183.8	0.925	178.8	363.4						
0.740	-282.6	160.8	1.000	225.6	306.1						
0.746	-281.9	160.5									
0.777	-245.2	201.9									
0.792	-206.5	247.8									
0.812	-148.9	306.4									
0.829	-59.4	351.5									
0.834	-29.8	367.2									
0.856	50.0	408.2									
0.881	120.1	419.0									
0.909	175.5	422.2									
0.929	190.0	363.8									
0.961	204.6	318.9									
1.000	214.9	304.6									

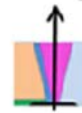
Table C-4 Case 9 – Model 1 (After SS Weld Only) – 50% Repair

Weld Centerline			DMW/SS			DMW/Butter			DMW/Nozzle		
R/t	Axial MPa	Hoop MPa	R/t	Axial MPa	Hoop MPa	R/t	Axial MPa	Hoop MPa	R/t	Axial MPa	Hoop MPa
0.000	116.6	385.8	0.000	225.2	362.1	0.000	-15.4	325.0	0.000	99.6	345.1
0.014	137.7	378.9	0.010	257.3	360.9	0.021	46.4	359.3	0.019	123.2	358.1
0.043	180.0	368.3	0.019	247.6	385.6	0.046	124.8	420.7	0.043	147.8	365.9
0.061	195.2	362.4	0.042	196.7	422.4	0.070	178.3	443.3	0.063	174.2	395.4
0.079	201.5	364.9	0.060	174.1	426.5	0.090	223.8	459.8	0.084	200.3	380.5
0.103	193.6	375.7	0.074	168.2	431.8	0.110	261.5	464.1	0.105	227.4	435.5
0.114	208.3	412.2	0.094	174.0	435.0	0.122	345.5	573.6	0.121	274.3	419.9
0.134	236.7	454.3	0.110	169.3	425.4	0.130	365.1	608.9	0.131	311.7	398.3
0.145	218.6	443.9	0.128	189.6	564.5	0.158	354.8	567.9	0.143	316.9	382.9
0.178	201.3	464.7	0.135	201.3	521.0	0.175	348.4	561.6	0.159	313.3	379.3
0.204	198.7	528.1	0.153	202.9	496.3	0.204	254.1	551.6	0.170	301.3	390.8
0.233	175.1	568.3	0.166	209.9	517.0	0.235	107.5	458.9	0.175	292.0	390.9
0.262	129.9	521.3	0.172	213.3	522.1	0.267	41.2	402.7	0.204	181.7	375.1
0.296	91.3	478.2	0.201	175.9	544.8	0.298	42.2	398.5	0.235	129.2	362.3
0.344	66.2	498.9	0.224	151.7	528.4	0.328	29.1	382.6	0.267	85.9	346.9
0.374	-18.9	430.3	0.247	141.8	497.7	0.358	66.7	408.3	0.298	64.6	346.7
0.406	-20.7	398.7	0.272	103.6	447.4	0.358	66.7	408.3	0.328	69.6	339.7
0.443	43.5	452.6	0.297	91.8	465.6	0.388	48.9	423.4	0.358	39.2	316.5
0.454	42.6	440.2	0.328	75.7	489.9	0.423	19.0	405.9	0.388	44.0	306.2
0.482	21.9	410.2	0.358	-19.8	391.1	0.457	74.2	419.4	0.423	85.3	319.1
0.497	11.7	416.1	0.387	-57.9	373.6	0.492	86.0	473.4	0.457	85.0	326.3
0.518	27.9	408.3	0.413	1.8	453.4	0.529	33.3	484.7	0.492	58.9	298.7
0.537	77.9	509.0	0.439	38.9	458.6	0.565	-12.1	426.6	0.527	12.9	220.9
0.542	77.9	526.4	0.465	-9.7	392.5	0.602	-64.4	372.9	0.562	-66.6	117.5
0.561	52.8	549.4	0.491	23.8	439.1	0.639	-182.4	267.9	0.597	-150.9	29.1
0.597	-12.6	476.6	0.526	84.9	521.5	0.677	-278.9	142.9	0.632	-222.4	-26.5
0.604	-13.8	475.0	0.559	32.6	455.4	0.714	-311.2	98.2	0.667	-267.4	-43.7
0.632	-19.6	458.9	0.592	-13.2	408.5	0.748	-294.9	122.1	0.702	-288.5	-39.9
0.666	-137.6	372.3	0.634	-9.1	422.8	0.782	-243.9	161.3	0.735	-284.5	-14.7
0.692	-193.6	294.7	0.675	-90.1	344.4	0.815	-184.0	212.5	0.768	-258.0	23.5
0.731	-268.4	202.1	0.715	-216.4	211.0	0.849	-123.4	263.0	0.801	-210.4	71.6
0.757	-293.8	167.9	0.743	-240.6	141.4	0.884	-69.8	295.3	0.836	-144.0	127.3
0.759	-294.8	167.4	0.771	-249.7	129.9	0.918	-10.8	338.1	0.871	-71.1	183.8
0.786	-278.6	203.9	0.801	-230.7	215.4	0.945	27.6	355.4	0.906	5.2	230.2
0.809	-232.6	251.5	0.831	-180.4	259.6	0.973	36.3	325.4	0.937	68.9	265.0
0.837	-153.0	303.8	0.841	-164.8	268.5	1.000	50.9	326.2	0.969	103.2	277.3
0.856	-121.6	331.6	0.872	-120.9	293.3				1.000	117.7	275.5
0.874	-85.3	365.7	0.925	-70.4	347.3						
0.877	-84.1	361.5	1.000	-56.6	296.4						
0.906	-88.1	311.7									
0.924	-81.8	304.6									
0.966	-85.5	289.0									
1.000	-89.5	279.4									

Table C-5 Case 10 – Model 1 (50% Repair After SS Weld) – 50% PWSCC Repair

Weld Centerline			DMW/SS			DMW/Butter			DMW/Nozzle		
R/t	Axial MPa	Hoop MPa	R/t	Axial MPa	Hoop MPa	R/t	Axial MPa	Hoop MPa	R/t	Axial MPa	Hoop MPa
0.000	116.6	385.8	0.000	225.2	362.1	0.000	-15.4	325.0	0.000	99.6	345.1
0.014	137.7	378.9	0.010	257.3	360.9	0.021	46.4	359.3	0.019	123.2	358.1
0.043	180.0	368.3	0.019	247.6	385.6	0.046	124.8	420.7	0.043	147.8	365.9
0.061	195.2	362.4	0.042	196.7	422.4	0.070	178.3	443.3	0.063	174.2	395.4
0.079	201.5	364.9	0.060	174.1	426.5	0.090	223.8	459.8	0.084	200.3	380.5
0.103	193.6	375.7	0.074	168.2	431.8	0.110	261.5	464.1	0.105	227.4	435.5
0.114	208.3	412.2	0.094	174.0	435.0	0.122	345.5	573.6	0.121	274.3	419.9
0.134	236.7	454.3	0.110	169.3	425.4	0.130	365.1	608.9	0.131	311.7	398.3
0.145	218.6	443.9	0.128	189.6	564.5	0.158	354.8	567.9	0.143	316.9	382.9
0.178	201.3	464.7	0.135	201.3	521.0	0.175	348.4	561.6	0.159	313.3	379.3
0.204	198.7	528.1	0.153	202.9	496.3	0.204	254.1	551.6	0.170	301.3	390.8
0.233	175.1	568.3	0.166	209.9	517.0	0.235	107.5	458.9	0.175	292.0	390.9
0.262	129.9	521.3	0.172	213.3	522.1	0.267	41.2	402.7	0.204	181.7	375.1
0.296	91.3	478.2	0.201	175.9	544.8	0.298	42.2	398.5	0.235	129.2	362.3
0.344	66.2	498.9	0.224	151.7	528.4	0.328	29.1	382.6	0.267	85.9	346.9
0.374	-18.9	430.3	0.247	141.8	497.7	0.358	66.7	408.3	0.298	64.6	346.7
0.406	-20.7	398.7	0.272	103.6	447.4	0.358	66.7	408.3	0.328	69.6	339.7
0.443	43.5	452.6	0.297	91.8	465.6	0.388	48.9	423.4	0.358	39.2	316.5
0.454	42.6	440.2	0.328	75.7	489.9	0.423	19.0	405.9	0.388	44.0	306.2
0.482	21.9	410.2	0.358	-19.8	391.1	0.457	74.2	419.4	0.423	85.3	319.1
0.497	11.7	416.1	0.387	-57.9	373.6	0.492	86.0	473.4	0.457	85.0	326.3
0.518	27.9	408.3	0.413	1.8	453.4	0.529	33.3	484.7	0.492	58.9	298.7
0.537	77.9	509.0	0.439	38.9	458.6	0.565	-12.1	426.6	0.527	12.9	220.9
0.542	77.9	526.4	0.465	-9.7	392.5	0.602	-64.4	372.9	0.562	-66.6	117.5
0.561	52.8	549.4	0.491	23.8	439.1	0.639	-182.4	267.9	0.597	-150.9	29.1
0.597	-12.6	476.6	0.526	84.9	521.5	0.677	-278.9	142.9	0.632	-222.4	-26.5
0.604	-13.8	475.0	0.559	32.6	455.4	0.714	-311.2	98.2	0.667	-267.4	-43.7
0.632	-19.6	458.9	0.592	-13.2	408.5	0.748	-294.9	122.1	0.702	-288.5	-39.9
0.666	-137.6	372.3	0.634	-9.1	422.8	0.782	-243.9	161.3	0.735	-284.5	-14.7
0.692	-193.6	294.7	0.675	-90.1	344.4	0.815	-184.0	212.5	0.768	-258.0	23.5
0.731	-268.4	202.1	0.715	-216.4	211.0	0.849	-123.4	263.0	0.801	-210.4	71.6
0.757	-293.8	167.9	0.743	-240.6	141.4	0.884	-69.8	295.3	0.836	-144.0	127.3
0.759	-294.8	167.4	0.771	-249.7	129.9	0.918	-10.8	338.1	0.871	-71.1	183.8
0.786	-278.6	203.9	0.801	-230.7	215.4	0.945	27.6	355.4	0.906	5.2	230.2
0.809	-232.6	251.5	0.831	-180.4	259.6	0.973	36.3	325.4	0.937	68.9	265.0
0.837	-153.0	303.8	0.841	-164.8	268.5	1.000	50.9	326.2	0.969	103.2	277.3
0.856	-121.6	331.6	0.872	-120.9	293.3				1.000	117.7	275.5
0.874	-85.3	365.7	0.925	-70.4	347.3						
0.877	-84.1	361.5	1.000	-56.6	296.4						
0.906	-88.1	311.7									
0.924	-81.8	304.6									
0.966	-85.5	289.0									
1.000	-89.5	279.4									

Table C-6 Model 2 Weld Centerline Line (No SS Weld)



No Repair			12% Repair			25% Repair			50% Repair		
R/t	Axial MPa	Hoop MPa	R/t	Axial MPa	Hoop MPa	R/t	Axial MPa	Hoop MPa	R/t	Axial MPa	Hoop MPa
0.000	232.5	25.6	0.000	-86.7	243.2	0.000	-91.7	239.0	0.000	-116.4	220.2
0.012	241.2	18.5	0.020	-11.5	299.5	0.027	46.5	335.2	0.024	3.1	313.2
0.024	231.9	15.4	0.050	91.7	344.6	0.054	150.1	393.7	0.050	117.5	381.1
0.035	244.7	11.9	0.091	169.4	380.4	0.076	209.9	427.6	0.080	202.1	428.9
0.043	247.9	14.5	0.131	273.0	485.4	0.091	241.3	447.0	0.099	242.8	451.9
0.064	183.0	43.7	0.179	296.7	553.3	0.109	301.4	502.2	0.113	334.9	563.5
0.084	132.2	59.1	0.205	272.0	550.4	0.127	357.4	567.3	0.127	347.3	566.0
0.099	92.5	57.1	0.229	206.2	543.1	0.156	368.8	561.7	0.156	360.7	561.3
0.113	76.3	84.0	0.256	83.2	493.7	0.205	188.6	541.9	0.179	345.4	561.2
0.131	96.5	143.2	0.263	46.6	471.4	0.229	34.0	482.2	0.205	185.5	533.8
0.142	73.1	116.7	0.273	-19.5	420.8	0.256	26.1	445.8	0.229	41.0	495.6
0.156	26.7	88.4	0.297	-155.0	289.6	0.263	35.1	449.8	0.256	32.7	422.1
0.179	-41.8	139.0	0.320	-252.4	207.2	0.273	24.2	461.4	0.263	37.1	400.9
0.205	-52.6	200.5	0.345	-306.9	133.9	0.297	-33.4	426.8	0.273	51.0	432.9
0.229	-55.6	185.2	0.378	-293.3	133.7	0.320	-153.8	325.2	0.297	49.0	441.1
0.256	-79.4	179.1	0.383	-292.3	139.3	0.345	-249.2	214.0	0.320	-6.0	389.1
0.263	-87.1	162.6	0.416	-279.8	157.1	0.378	-307.3	103.4	0.345	-69.8	334.4
0.273	-102.3	178.6	0.452	-246.9	202.2	0.383	-316.4	93.6	0.378	-117.8	330.6
0.297	-122.0	196.1	0.465	-236.9	215.4	0.416	-344.4	83.6	0.383	-115.2	334.5
0.320	-126.6	208.6	0.495	-210.6	233.2	0.452	-315.2	135.5	0.416	-51.3	361.4
0.345	-160.0	179.4	0.509	-183.6	259.5	0.465	-303.2	152.8	0.452	-60.8	365.0
0.346	-160.6	179.7	0.532	-147.3	306.0	0.495	-273.6	178.3	0.465	-82.3	366.9
0.378	-169.7	197.1	0.552	-145.8	277.2	0.509	-250.6	208.8	0.495	-103.6	397.1
0.383	-171.7	203.1	0.553	-144.7	276.1	0.532	-224.2	268.2	0.509	-87.4	429.0
0.416	-165.5	189.7	0.581	-143.8	276.8	0.552	-221.7	251.0	0.532	-92.0	422.4
0.452	-154.0	236.9	0.611	-91.7	317.1	0.581	-200.1	248.3	0.552	-165.9	360.8
0.465	-152.8	251.8	0.627	-46.3	362.7	0.611	-142.8	291.4	0.581	-205.8	269.5
0.495	-138.1	269.6	0.646	-4.8	371.8	0.646	-49.1	356.3	0.611	-246.4	201.3
0.532	-81.8	329.6	0.666	10.7	359.3	0.666	-29.5	345.9	0.627	-267.1	190.1
0.553	-87.2	297.9	0.683	3.4	353.3	0.683	-30.6	341.3	0.666	-307.0	152.2
0.581	-95.2	301.1	0.705	-27.6	349.0	0.705	-51.6	337.1	0.683	-325.4	144.1
0.611	-49.7	343.9	0.711	-34.8	356.2	0.711	-56.1	343.8	0.711	-310.8	143.3
0.627	-9.6	389.1	0.732	-36.3	376.0	0.732	-50.0	363.5	0.732	-278.6	160.6
0.646	26.5	394.2	0.748	-4.4	402.8	0.748	-14.0	394.3	0.748	-256.9	205.6
0.666	36.3	374.5	0.761	4.9	414.3	0.761	-1.4	408.8	0.761	-237.4	244.8
0.683	23.3	365.2	0.773	16.3	405.1	0.790	36.4	405.5	0.773	-213.5	264.7
0.705	-13.0	360.1	0.790	35.1	405.0	0.814	110.7	439.8	0.790	-171.3	297.7
0.732	-24.1	386.8	0.814	99.4	433.9	0.817	117.2	440.1	0.814	-53.1	378.2
0.748	5.7	413.2	0.817	104.9	433.6	0.835	157.7	431.6	0.835	33.0	406.3

0.761	12.5	424.3
0.790	35.5	412.0
0.814	98.2	445.0
0.835	137.9	438.0
0.866	169.3	420.4
0.937	159.5	444.5
0.956	77.6	389.1
0.976	-7.1	350.6
1.000	-53.1	325.8

0.835	138.2	420.2
0.866	172.6	401.3
0.901	220.4	440.6
0.937	181.8	435.9
0.956	107.0	393.9
0.976	31.5	371.3
1.000	-8.6	352.8

0.866	200.6	415.9
0.901	255.9	457.7
0.910	260.3	460.1
0.937	227.1	455.5
0.956	158.1	414.5
0.976	85.7	393.5
1.000	45.8	379.0

0.866	137.3	415.3
0.901	262.4	459.4
0.910	275.1	455.6
0.937	288.3	428.9
0.956	253.9	390.4
0.976	233.8	381.6
1.000	229.5	376.2

Table C-7 Model 2 DMW/SS Line (No SS Weld)



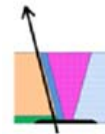
No Repair			12% Repair			25% Repair			50% Repair		
R/t	Axial MPa	Hoop MPa	R/t	Axial MPa	Hoop MPa	R/t	Axial MPa	Hoop MPa	R/t	Axial MPa	Hoop MPa
0.000	227.2	92.7	0.000	-55.5	272.3	0.000	-2.3	333.7	0.000	-29.4	318.5
0.004	244.3	98.1	0.012	17.3	302.3	0.020	78.0	376.3	0.020	54.3	365.8
0.016	274.9	103.0	0.024	47.9	312.9	0.043	131.3	423.7	0.043	110.5	412.9
0.028	269.4	98.7	0.050	104.5	336.1	0.062	173.5	453.3	0.062	154.3	441.7
0.043	256.3	58.1	0.065	129.6	347.1	0.076	206.8	470.5	0.076	189.0	459.5
0.062	208.2	78.6	0.087	159.2	362.5	0.098	260.9	485.2	0.098	245.2	476.3
0.087	170.9	146.3	0.101	168.0	396.9	0.105	271.4	485.1	0.112	259.9	475.8
0.101	145.4	170.0	0.116	219.3	490.7	0.118	300.0	480.0	0.131	291.4	474.2
0.118	115.6	182.0	0.118	228.6	499.6	0.131	302.3	478.9	0.145	312.9	563.5
0.131	79.8	165.0	0.131	225.5	339.6	0.155	321.3	555.7	0.155	315.8	553.7
0.160	6.6	104.9	0.160	256.4	462.5	0.179	295.0	569.6	0.179	290.9	575.8
0.179	-27.3	146.6	0.179	267.1	471.9	0.206	138.4	507.7	0.206	138.1	507.4
0.206	-22.4	232.4	0.206	250.6	474.6	0.231	82.6	433.4	0.231	63.0	418.9
0.231	-45.0	225.0	0.231	205.8	473.3	0.256	80.6	444.9	0.256	65.3	395.4
0.256	-101.7	191.6	0.256	107.2	423.0	0.283	24.6	452.9	0.283	57.9	389.5
0.283	-126.1	241.6	0.283	-47.1	356.2	0.310	-102.0	334.7	0.310	27.6	425.8
0.310	-122.7	269.8	0.310	-171.1	268.9	0.343	-223.6	167.0	0.343	-10.2	438.6
0.343	-164.2	183.5	0.343	-238.6	149.9	0.375	-292.6	108.0	0.375	-103.5	324.4
0.375	-189.4	212.9	0.375	-266.7	132.8	0.407	-287.4	141.7	0.407	-120.8	289.4
0.407	-163.2	261.8	0.407	-259.3	175.0	0.435	-271.2	117.7	0.435	-55.6	387.4
0.435	-172.9	221.9	0.435	-250.8	147.4	0.463	-257.4	130.2	0.463	-67.2	383.4
0.463	-165.2	247.8	0.463	-227.5	168.3	0.491	-223.2	215.9	0.491	-146.5	267.9
0.491	-113.0	326.5	0.491	-181.2	261.5	0.519	-214.3	214.3	0.519	-119.7	288.2
0.519	-108.7	311.8	0.519	-171.5	261.6	0.556	-228.6	178.4	0.556	-104.7	323.7
0.556	-135.2	266.0	0.556	-186.1	226.9	0.593	-173.9	267.1	0.593	-209.2	228.0
0.593	-87.4	339.5	0.593	-131.7	307.9	0.629	-94.7	331.9	0.629	-255.8	147.5
0.629	-13.7	380.8	0.629	-54.9	355.6	0.673	-65.8	318.5	0.673	-273.1	105.8
0.673	0.4	351.1	0.673	-31.1	331.7	0.717	-48.0	347.3	0.717	-263.2	163.6
0.717	-1.5	372.4	0.717	-24.4	356.6	0.761	-41.8	338.1	0.761	-211.2	213.2
0.761	-14.8	354.8	0.761	-29.1	329.3	0.792	-33.6	313.2	0.792	-165.0	227.9
0.792	-20.5	321.6	0.792	-25.2	285.7	0.823	4.6	322.2	0.823	-104.1	286.7
0.823	8.9	339.6	0.823	9.3	291.8	0.854	89.2	392.3	0.854	11.5	394.3
0.854	83.7	404.1	0.854	82.5	358.1	0.886	182.7	437.3	0.886	175.3	464.3
0.886	160.7	433.6	0.886	160.5	412.9	0.924	222.2	428.0	0.924	277.9	439.9
0.924	180.9	423.3	0.924	189.6	407.3	0.962	248.1	429.2	0.962	321.7	395.2
0.962	189.3	429.6	0.962	205.6	401.2	0.962	248.1	429.2	1.000	270.5	304.1
1.000	182.3	372.5	1.000	202.1	353.1	1.000	242.6	360.8			

Table C-8 Model 2 DMW/Butter Line (No SS Weld)



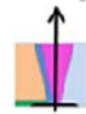
No Repair			12% Repair			25% Repair			50% Repair		
R/t	Axial	Hoop	R/t	Axial	Hoop	R/t	Axial	Hoop	R/t	Axial	Hoop
MPa	MPa		MPa	MPa	MPa	MPa	MPa	MPa	MPa	MPa	MPa
0.000	274.2	62.8	0.000	-13.1	297.2	0.000	20.9	399.9	0.000	-2.0	388.5
0.012	265.2	34.8	0.021	45.7	315.3	0.021	73.5	406.6	0.021	53.0	397.5
0.029	235.6	-13.8	0.042	91.9	334.1	0.042	139.1	429.8	0.046	130.0	423.1
0.046	171.9	-15.7	0.062	133.5	353.6	0.062	189.4	441.8	0.062	172.4	435.7
0.062	121.1	-7.9	0.079	163.0	369.6	0.083	235.8	445.2	0.083	220.8	441.1
0.083	61.7	-13.3	0.100	203.2	527.5	0.108	290.2	488.4	0.108	278.4	486.9
0.096	48.6	11.6	0.112	240.6	524.2	0.121	373.2	586.1	0.125	351.5	568.9
0.108	45.3	47.1	0.125	247.4	481.9	0.129	351.6	558.7	0.142	339.5	530.9
0.123	58.6	104.0	0.137	250.5	456.0	0.142	338.0	535.4	0.171	253.1	493.2
0.133	61.8	125.4	0.171	256.0	458.4	0.171	263.3	503.0	0.201	118.6	426.7
0.153	27.7	72.5	0.201	221.2	463.9	0.201	123.2	434.8	0.233	47.5	383.7
0.171	-27.9	80.9	0.233	134.4	443.5	0.233	48.4	398.3	0.266	54.0	402.2
0.201	-42.8	121.3	0.266	-67.6	304.7	0.266	24.9	411.5	0.298	15.7	403.8
0.233	-36.7	164.4	0.298	182.1	202.0	0.298	-31.3	381.2	0.329	2.0	408.3
0.266	-93.7	57.6	0.329	237.8	145.2	0.329	148.2	258.8	0.360	-66.6	352.4
0.298	111.5	131.9	0.360	294.4	48.3	0.360	301.4	84.2	0.391	-45.0	378.9
0.329	-74.9	200.9	0.391	301.1	55.3	0.391	336.2	37.1	0.427	16.7	421.0
0.360	128.5	100.1	0.427	273.4	129.6	0.427	358.8	49.1	0.463	-75.0	372.6
0.391	180.8	118.8	0.463	245.0	159.4	0.463	348.6	67.8	0.499	-80.9	393.7
0.427	173.1	190.1	0.499	162.6	225.4	0.499	275.1	143.9	0.536	-88.8	381.2
0.463	159.8	206.6	0.536	129.9	240.7	0.536	231.1	193.6	0.574	226.8	233.4
0.499	100.2	265.2	0.574	149.5	201.3	0.574	222.2	173.1	0.612	316.9	115.7
0.536	-76.6	268.5	0.612	-27.4	277.3	0.612	117.5	251.7	0.651	367.4	57.7
0.574	109.1	223.9	0.651	10.9	327.8	0.651	-20.4	308.1	0.690	394.4	19.1
0.612	-36.9	303.4	0.690	-33.2	232.5	0.690	-52.4	223.0	0.729	351.0	78.3
0.651	34.4	348.8	0.729	-21.3	279.9	0.729	-39.0	275.4	0.763	250.3	192.6
0.690	-19.8	240.8	0.763	12.1	350.5	0.763	23.9	350.2	0.798	115.3	267.9
0.729	-28.8	284.6	0.798	72.3	353.0	0.798	62.4	354.6	0.833	62.2	338.7
0.763	13.7	351.1	0.833	191.7	409.7	0.833	170.7	419.3	0.868	191.6	372.7
0.798	32.1	355.3	0.868	234.7	424.6	0.868	254.0	446.6	0.903	241.2	356.4
0.833	136.9	433.9	0.903	220.5	399.3	0.903	240.5	427.5	0.939	265.7	355.1
0.868	220.1	467.9	0.939	166.9	387.4	0.939	211.4	417.2	0.967	260.3	349.4
0.903	194.6	441.7	0.967	92.3	370.6	0.967	161.9	399.1	0.995	248.3	337.9
0.939	150.5	419.3	0.995	52.0	328.0	0.995	77.2	350.4	1.024	237.9	343.0
0.967	88.0	388.6	1.024	24.1	306.0	1.024	32.5	328.3			
1.0	-9.0	315.2									

Table C-9 Model 2 DMW/Nozzle Line (No SS Weld)



No Repair			12% Repair			25% Repair			50% Repair		
R/t	Axial	Hoop	R/t	Axial	Hoop	R/t	Axial	Hoop	R/t	Axial	Hoop
	MPa	MPa		MPa	MPa		MPa	MPa		MPa	MPa
0.000	182.1	-0.5	0.000	175.8	303.1	0.000	287.3	371.5	0.000	271.4	360.7
0.023	134.6	7.1	0.019	172.9	283.3	0.023	248.8	338.9	0.011	248.8	345.2
0.049	81.9	14.5	0.046	185.0	262.7	0.049	242.1	309.9	0.031	229.4	322.6
0.066	51.5	9.0	0.066	191.6	246.6	0.066	227.6	292.9	0.046	230.5	307.6
0.092	13.7	-16.1	0.092	192.0	229.4	0.088	203.0	266.4	0.058	224.1	296.0
0.108	-20.5	-65.2	0.112	197.8	248.2	0.116	179.8	226.4	0.075	203.0	276.9
0.131	-10.5	-39.7	0.116	228.5	261.1	0.135	154.3	241.4	0.099	172.7	245.5
0.167	-9.8	-2.1	0.124	230.8	273.1	0.167	164.9	281.6	0.116	156.4	218.0
0.196	-3.2	-14.6	0.128	226.2	268.7	0.196	111.7	231.4	0.135	141.1	229.7
0.228	-9.4	-44.3	0.139	183.2	216.5	0.228	55.4	166.7	0.167	157.5	278.3
0.260	-27.2	-80.3	0.151	155.3	198.3	0.260	-8.4	82.3	0.196	121.2	268.9
0.292	-60.3	-116.5	0.167	132.3	171.6	0.292	-108.1	-19.6	0.228	93.5	286.9
0.322	-91.1	-140.0	0.196	36.3	71.1	0.322	-209.3	-119.6	0.260	86.5	292.0
0.352	-83.6	-129.4	0.228	-51.1	-11.4	0.352	-271.3	-199.2	0.292	27.5	252.2
0.382	-92.2	-106.1	0.260	-127.4	-67.9	0.382	-304.5	-221.6	0.322	-7.1	247.7
0.417	-125.4	-89.8	0.292	-184.7	-125.9	0.417	-295.9	-188.8	0.352	17.0	268.5
0.452	-130.4	-88.4	0.322	-209.6	-186.7	0.452	-265.9	-162.0	0.417	-41.5	235.1
0.487	-127.4	-86.3	0.352	-191.5	-193.5	0.487	-248.3	-146.5	0.452	-43.7	224.2
0.522	-96.7	-37.4	0.382	-182.6	-162.3	0.522	-200.1	-86.2	0.487	-103.0	140.9
0.558	-52.8	29.5	0.417	-196.7	-135.1	0.558	-139.2	-9.3	0.522	-196.6	25.2
0.593	-45.0	54.1	0.487	-176.2	-116.4	0.593	-113.3	24.3	0.558	-266.6	-65.3
0.629	-48.7	48.8	0.522	-136.8	-61.9	0.629	-98.7	27.6	0.629	-344.1	-101.6
0.664	-16.5	60.1	0.558	-84.8	9.9	0.664	-50.0	46.7	0.664	-345.0	-65.4
0.700	23.1	95.1	0.629	-66.1	37.6	0.700	5.6	89.2	0.700	-291.0	-4.6
0.733	24.3	114.4	0.664	-27.1	52.7	0.733	21.8	115.7	0.733	-211.4	59.0
0.766	26.4	109.4	0.700	19.4	91.4	0.766	39.1	117.8	0.766	-121.6	111.3
0.799	38.2	96.2	0.766	36.2	113.2	0.799	65.1	111.4	0.799	-27.0	159.1
0.835	55.9	86.2	0.835	78.2	97.3	0.835	97.1	108.5	0.835	76.6	200.6
0.870	71.1	106.6	0.870	98.8	119.2	0.870	127.1	135.5	0.870	168.5	241.9
0.905	87.6	140.8	0.905	119.3	144.7	0.905	160.7	172.5	0.905	238.0	275.2
0.937	129.6	186.4	0.937	165.2	167.4	0.937	213.0	199.2	0.937	281.0	289.7
0.968	208.5	257.9	0.968	219.7	206.4	0.968	257.7	227.4	0.968	288.5	280.7
1.000	260.3	295.4	1.000	245.7	226.0	1.000	276.1	240.9	1.000	290.6	269.0

Table C-10 Model 2 Weld Centerline Line (After SS Weld) Mod



12% Repair

R/t	Axial MPa	Hoop MPa
0.000	-259.6	63.7
0.020	-214.8	131.7
0.039	-132.3	169.4
0.058	-68.6	196.3
0.076	-20.1	217.8
0.091	10.7	231.4
0.106	36.9	243.6
0.124	69.8	260.6
0.131	136.2	344.7
0.156	172.3	406.4
0.179	185.8	422.5
0.205	175.6	424.7
0.229	122.8	422.4
0.256	12.6	381.8
0.263	-20.4	361.4
0.273	-83.6	316.5
0.297	-211.6	197.8
0.320	-301.9	121.4
0.345	-346.0	51.7
0.346	-347.1	49.9
0.378	-328.2	52.8
0.383	-325.1	58.4
0.416	-292.1	60.8
0.452	-247.1	115.2
0.465	-232.0	131.3
0.495	-192.0	152.4
0.509	-158.6	179.1
0.532	-114.8	226.1
0.581	-100.8	201.6
0.611	-41.6	244.7
0.627	7.8	291.8
0.646	53.5	302.5
0.666	72.4	291.6
0.683	68.6	287.1
0.711	35.0	293.4
0.732	36.8	314.3
0.748	71.7	341.5
0.761	83.3	354.1
0.790	118.0	346.8
0.814	186.4	377.8
0.835	228.2	365.5
0.866	266.5	348.5
0.901	319.5	389.9
0.937	287.1	388.9
0.956	215.8	348.7
0.976	142.5	336.7
1.000	102.6	327.9

25% Repair

R/t	Axial MPa	Hoop MPa
0.000	-262.0	59.4
0.020	-196.6	155.9
0.043	-99.2	257.9
0.064	-11.3	311.9
0.084	54.5	341.2
0.095	86.8	355.8
0.109	152.2	409.5
0.113	202.1	474.1
0.124	219.4	481.5
0.131	224.2	474.9
0.156	251.2	472.2
0.179	251.3	478.4
0.205	90.9	448.7
0.229	-54.8	370.2
0.256	-43.3	344.1
0.273	-34.7	372.4
0.297	-84.2	362.4
0.320	-198.8	268.2
0.345	-283.3	158.9
0.346	-287.1	153.1
0.378	-332.5	50.7
0.383	-340.7	40.4
0.416	-365.7	28.1
0.452	-319.6	87.2
0.458	-315.8	93.9
0.495	-254.3	134.1
0.509	-221.8	161.0
0.532	-175.5	207.5
0.552	-162.4	182.7
0.581	-147.3	191.3
0.611	-77.7	241.4
0.646	30.8	301.9
0.666	56.1	287.2
0.683	58.2	283.0
0.705	35.6	292.7
0.732	37.6	345.9
0.748	79.8	377.1
0.773	116.3	365.9
0.814	215.0	403.5
0.817	219.7	402.2
0.835	247.5	381.0
0.866	274.0	341.2
0.901	322.1	361.0
0.937	284.0	356.3
0.956	223.4	333.6
0.976	165.1	345.3
1.000	136.0	348.2

50% Repair

R/t	Axial MPa	Hoop MPa
0.000	-299.6	-5.8
0.020	-250.4	89.5
0.043	-162.6	202.1
0.064	-65.2	258.4
0.084	9.5	290.8
0.091	34.2	302.2
0.095	45.6	306.1
0.099	57.2	310.6
0.113	166.0	426.3
0.127	189.8	432.0
0.137	199.6	427.4
0.156	223.5	428.0
0.179	220.8	436.4
0.205	56.6	406.9
0.229	-84.1	344.8
0.256	-66.6	250.1
0.263	-55.2	228.2
0.273	-35.7	266.7
0.297	-26.3	295.9
0.320	-67.1	248.1
0.345	-114.7	195.8
0.346	-117.5	196.2
0.378	-150.9	210.2
0.383	-144.5	215.0
0.416	-48.3	241.2
0.452	-43.4	255.6
0.458	-47.8	250.4
0.465	-61.0	266.9
0.509	-50.6	370.9
0.532	-42.3	375.0
0.552	-110.3	312.3
0.581	-144.6	219.3
0.611	-178.7	147.3
0.646	-207.7	103.6
0.683	-227.5	86.9
0.705	-209.3	79.0
0.761	-105.9	195.8
0.773	-78.2	217.5
0.790	-31.6	253.2
0.817	107.6	351.7
0.835	188.8	374.6
0.866	286.9	357.3
0.901	371.0	347.9
0.937	316.7	271.7
0.956	269.8	237.9
0.976	248.6	240.2
1.000	248.2	234.7

Table C-11 Model 2 DMW/SS Line (After SS Weld) Mc



12% Repair

R/t	Axial MPa	Hoop MPa
0.000	-259.6	63.7
0.020	-214.8	131.7
0.039	-132.3	169.4
0.058	-68.6	196.3
0.076	-20.1	217.8
0.091	10.7	231.4
0.106	36.9	243.6
0.124	69.8	260.6
0.131	136.2	344.7
0.156	172.3	406.4
0.179	185.8	422.5
0.205	175.6	424.7
0.229	122.8	422.4
0.256	12.6	381.8
0.263	-20.4	361.4
0.273	-83.6	316.5
0.297	-211.6	197.8
0.320	-301.9	121.4
0.345	-346.0	51.7
0.346	-347.1	49.9
0.378	-328.2	52.8
0.383	-325.1	58.4
0.416	-292.1	60.8
0.452	-247.1	115.2
0.465	-232.0	131.3
0.495	-192.0	152.4
0.509	-158.6	179.1
0.532	-114.8	226.1
0.581	-100.8	201.6
0.611	-41.6	244.7
0.627	7.8	291.8
0.646	53.5	302.5
0.666	72.4	291.6
0.683	68.6	287.1
0.711	35.0	293.4
0.732	36.8	314.3
0.748	71.7	341.5
0.761	83.3	354.1
0.790	118.0	346.8
0.814	186.4	377.8
0.835	228.2	365.5
0.866	266.5	348.5
0.901	319.5	389.9
0.937	287.1	388.9
0.956	215.8	348.7
0.976	142.5	336.7
1.000	102.6	327.9

25% Repair

R/t	Axial MPa	Hoop MPa
0.000	-262.0	59.4
0.020	-196.6	155.9
0.043	-99.2	257.9
0.064	-11.3	311.9
0.084	54.5	341.2
0.095	86.8	355.8
0.109	152.2	409.5
0.113	202.1	474.1
0.124	219.4	481.5
0.131	224.2	474.9
0.156	251.2	472.2
0.179	251.3	478.4
0.205	90.9	448.7
0.229	-54.8	370.2
0.256	-43.3	344.1
0.273	-34.7	372.4
0.297	-84.2	362.4
0.320	-198.8	268.2
0.345	-283.3	158.9
0.346	-287.1	153.1
0.378	-332.5	50.7
0.383	-340.7	40.4
0.416	-365.7	28.1
0.452	-319.6	87.2
0.458	-315.8	93.9
0.495	-254.3	134.1
0.509	-221.8	161.0
0.532	-175.5	207.5
0.552	-162.4	182.7
0.581	-147.3	191.3
0.611	-77.7	241.4
0.646	30.8	301.9
0.666	56.1	287.2
0.683	58.2	283.0
0.705	35.6	292.7
0.732	37.6	345.9
0.748	79.8	377.1
0.773	116.3	365.9
0.814	215.0	403.5
0.817	219.7	402.2
0.835	247.5	381.0
0.866	274.0	341.2
0.901	322.1	361.0
0.937	284.0	356.3
0.956	223.4	333.6
0.976	165.1	345.3
1.000	136.0	348.2

50% Repair

R/t	Axial MPa	Hoop MPa
0.000	-299.6	-5.8
0.020	-250.4	89.5
0.043	-162.6	202.1
0.064	-65.2	258.4
0.084	9.5	290.8
0.091	34.2	302.2
0.095	45.6	306.1
0.099	57.2	310.6
0.113	166.0	426.3
0.127	189.8	432.0
0.137	199.6	427.4
0.156	223.5	428.0
0.179	220.8	436.4
0.205	56.6	406.9
0.229	-84.1	344.8
0.256	-66.6	250.1
0.263	-55.2	228.2
0.273	-35.7	266.7
0.297	-26.3	295.9
0.320	-67.1	248.1
0.345	-114.7	195.8
0.346	-117.5	196.2
0.378	-150.9	210.2
0.383	-144.5	215.0
0.416	-48.3	241.2
0.452	-43.4	255.6
0.458	-47.8	250.4
0.465	-61.0	266.9
0.509	-50.6	370.9
0.532	-42.3	375.0
0.552	-110.3	312.3
0.581	-144.6	219.3
0.611	-178.7	147.3
0.646	-207.7	103.6
0.683	-227.5	86.9
0.705	-209.3	79.0
0.761	-105.9	195.8
0.773	-78.2	217.5
0.790	-31.6	253.2
0.817	107.6	351.7
0.835	188.8	374.6
0.866	286.9	357.3
0.901	371.0	347.9
0.937	316.7	271.7
0.956	269.8	237.9
0.976	248.6	240.2
1.000	248.2	234.7

Table C-12 Model 2 DMW/Butter Line (After SS Weld) Mod



12% Repair

R/t	Axial MPa	Hoop MPa
0.000	-198.6	148.4
0.021	-133.9	169.3
0.042	-79.4	191.4
0.062	-28.4	214.5
0.083	10.8	232.2
0.104	71.8	400.2
0.112	103.3	393.9
0.123	115.9	358.7
0.133	122.3	332.2
0.153	142.1	332.9
0.171	147.9	339.7
0.201	126.5	350.7
0.233	52.2	332.0
0.266	-140.4	200.4
0.298	-245.0	101.8
0.329	-290.6	49.0
0.360	-337.0	-44.0
0.391	-331.6	-32.2
0.427	-289.8	47.7
0.463	-248.8	82.6
0.499	-154.3	153.4
0.536	-109.3	173.7
0.574	-118.2	138.8
0.612	-24.5	219.1
0.651	68.4	273.9
0.690	33.7	182.7
0.729	42.9	233.6
0.763	104.4	307.3
0.798	140.9	312.2
0.833	242.6	370.1
0.868	315.1	385.9
0.903	292.3	361.7
0.939	259.3	352.1
0.967	210.5	337.9
1.000	79.4	284.2

25% Repair

R/t	Axial MPa	Hoop MPa
0.000	-169.9	273.9
0.021	-115.3	293.8
0.042	-44.9	332.0
0.062	17.1	354.7
0.083	79.0	371.1
0.104	132.9	386.9
0.112	182.1	468.7
0.123	245.2	522.1
0.133	231.5	494.0
0.153	222.8	491.6
0.171	157.2	451.7
0.201	19.6	347.2
0.233	-37.4	287.6
0.266	-48.8	319.3
0.298	-94.6	300.5
0.329	-203.1	178.9
0.360	-345.2	-2.2
0.391	-366.1	-47.3
0.427	-376.7	-21.4
0.463	-353.4	9.5
0.499	-266.3	93.0
0.536	-200.5	141.6
0.574	-174.7	118.1
0.612	-58.7	216.1
0.651	55.5	279.2
0.690	41.0	186.4
0.729	68.4	244.9
0.763	155.8	328.3
0.798	205.0	313.0
0.833	259.9	315.4
0.868	288.5	307.2
0.903	269.4	294.0
0.939	252.7	302.4
0.967	219.5	307.0
1.000	124.8	310.9

50% Repair

R/t	Axial MPa	Hoop MPa
0.000	-226.5	222.0
0.021	-171.5	257.5
0.042	-100.2	292.7
0.062	-34.3	311.1
0.083	31.9	323.8
0.104	91.3	342.4
0.112	142.5	424.0
0.123	208.7	479.4
0.133	196.4	451.1
0.153	187.4	445.6
0.171	116.2	405.4
0.201	-17.9	296.1
0.233	-68.7	214.7
0.266	-42.4	246.8
0.298	-61.2	268.3
0.329	-62.4	307.3
0.360	-115.2	245.3
0.391	-67.5	270.7
0.427	11.7	350.0
0.463	-73.3	311.4
0.499	-63.2	341.8
0.536	-54.4	334.0
0.574	-182.4	171.9
0.612	-253.8	48.6
0.651	-281.8	-4.1
0.690	-284.4	-33.0
0.729	-219.1	42.5
0.763	-84.1	185.9
0.798	94.7	259.3
0.833	242.8	256.9
0.868	290.9	217.6
0.903	287.5	180.4
0.939	289.7	184.3
0.967	279.6	197.0
1.000	270.8	213.4

Table C-13 Model 2 DMW/Nozzle Line (After SS Weld) Model 2



12% Repair

R/t	Axial MPa	Hoop MPa
0.000	13.5	178.0
0.023	18.3	157.6
0.042	33.8	145.5
0.062	47.7	132.0
0.079	55.9	121.8
0.100	54.6	111.4
0.120	114.6	161.6
0.135	96.0	149.9
0.151	46.9	111.5
0.167	28.3	88.1
0.196	-57.9	-8.7
0.228	-136.4	-92.7
0.260	-203.6	-152.9
0.292	-250.5	-212.0
0.322	-264.8	-269.8
0.352	-236.7	-272.4
0.382	-217.1	-237.0
0.417	-219.7	-205.3
0.452	-200.7	-190.9
0.487	-176.3	-177.6
0.522	-125.7	-118.6
0.558	-62.8	-42.3
0.593	-37.0	-9.0
0.629	-23.1	-5.7
0.664	26.0	13.8
0.700	82.5	57.1
0.733	100.4	84.9
0.766	120.9	89.1
0.799	152.6	85.5
0.835	185.7	83.7
0.870	207.1	103.0
0.905	225.5	125.9
0.937	262.1	147.9
0.968	293.9	176.0
1.000	306.2	187.3

25% Repair

R/t	Axial MPa	Hoop MPa
0.000	104.2	242.7
0.023	85.1	224.9
0.042	92.7	211.8
0.062	93.8	201.6
0.079	83.7	192.9
0.100	63.2	158.6
0.120	57.4	167.2
0.135	35.0	182.6
0.151	55.2	214.2
0.167	53.5	226.2
0.196	8.9	181.9
0.228	-35.7	116.0
0.260	-88.0	23.0
0.292	-176.0	-92.3
0.322	-266.0	-200.3
0.352	-316.9	-276.8
0.382	-339.9	-295.0
0.417	-320.0	-257.2
0.452	-277.2	-224.9
0.487	-245.5	-203.5
0.522	-182.4	-137.0
0.558	-106.9	-54.0
0.593	-67.5	-14.2
0.629	-39.7	-4.7
0.664	22.8	20.9
0.700	92.3	70.3
0.733	123.7	104.5
0.766	157.6	114.8
0.799	198.7	115.8
0.835	219.8	110.7
0.870	225.2	120.7
0.905	239.3	140.6
0.937	261.0	154.0
0.968	272.5	161.4
1.000	275.8	161.7

50% Repair

R/t	Axial MPa	Hoop MPa
0.000	52.1	197.1
0.023	33.3	181.7
0.042	43.7	169.5
0.062	46.1	159.1
0.079	26.5	147.2
0.100	-5.0	83.0
0.120	-2.5	91.8
0.135	-8.3	112.0
0.151	17.3	152.1
0.167	19.3	166.3
0.196	-6.4	169.1
0.228	-18.9	184.5
0.260	-8.6	183.6
0.292	-54.5	167.9
0.322	-76.0	161.4
0.352	-31.6	181.0
0.382	-48.6	179.1
0.417	-66.9	185.4
0.452	-53.0	170.5
0.487	-98.5	67.5
0.522	-177.5	-58.3
0.558	-229.8	-141.0
0.593	-256.8	-174.2
0.629	-268.6	-151.2
0.664	-252.9	-84.3
0.700	-181.8	7.9
0.733	-76.1	96.8
0.766	46.5	157.6
0.799	167.2	188.0
0.835	249.3	193.2
0.870	288.6	194.3
0.905	303.9	193.6
0.937	302.9	182.3
0.968	295.2	170.0
1.000	293.4	163.9

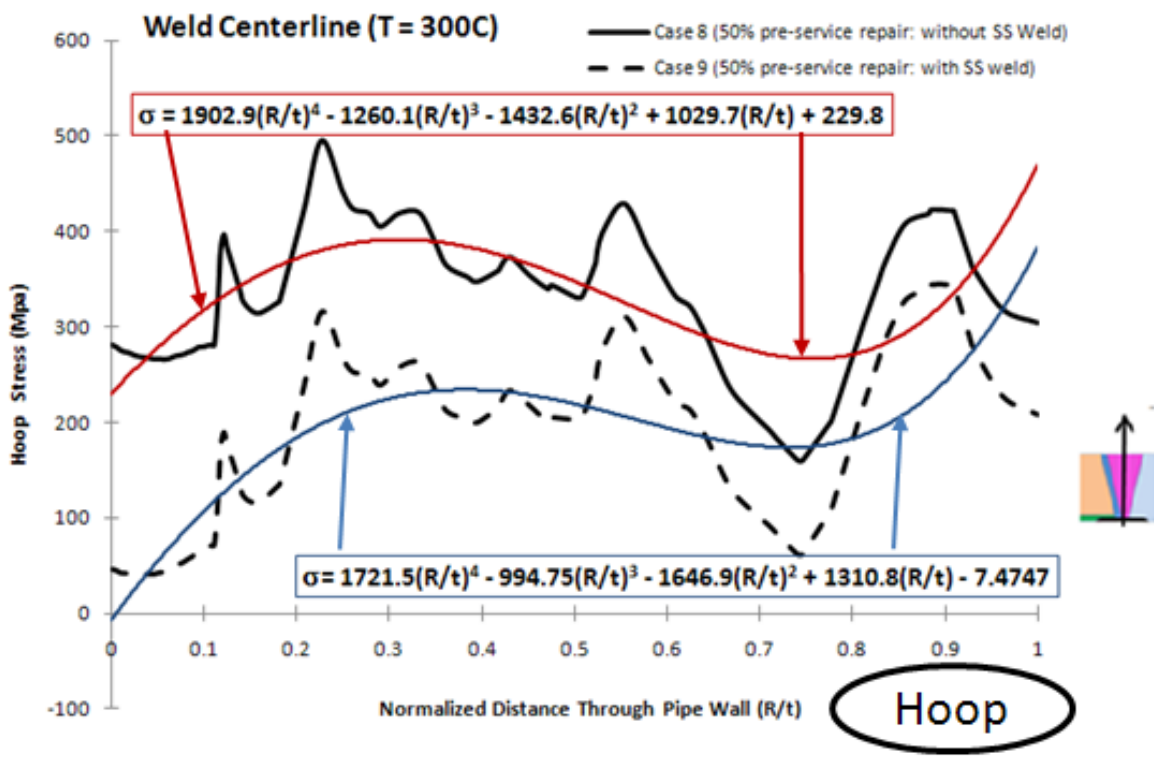
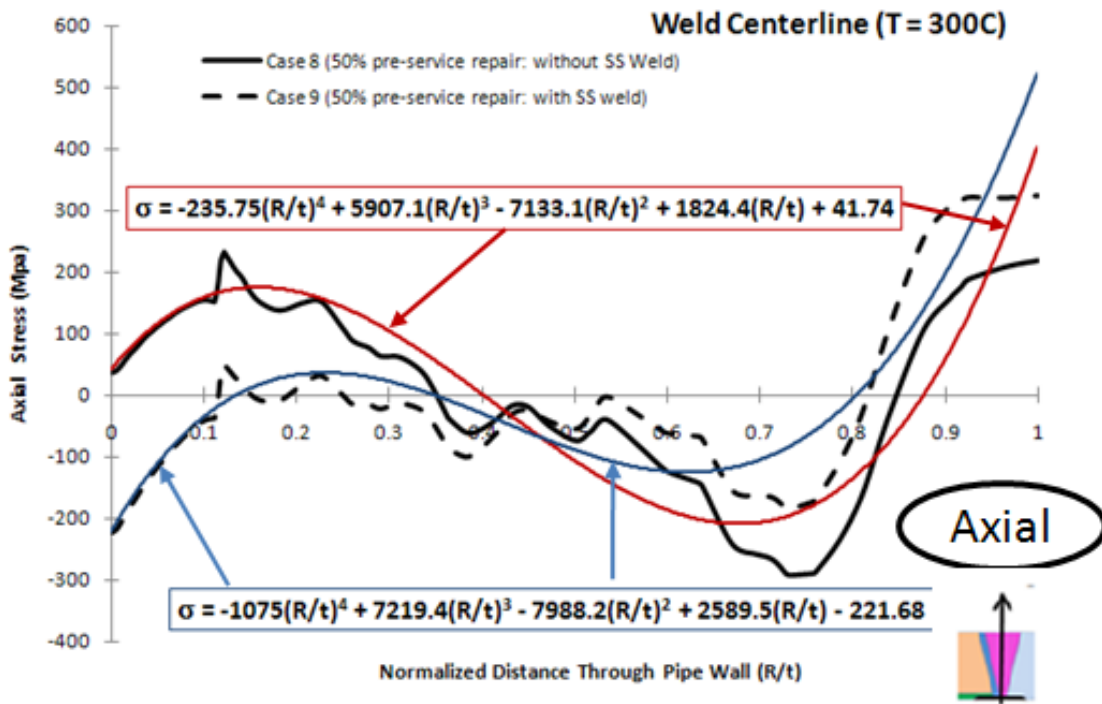


Figure C- 1 Axial and Hoop WRS (Model 1) for Cases 8 and 9 (50% repair: centerline).

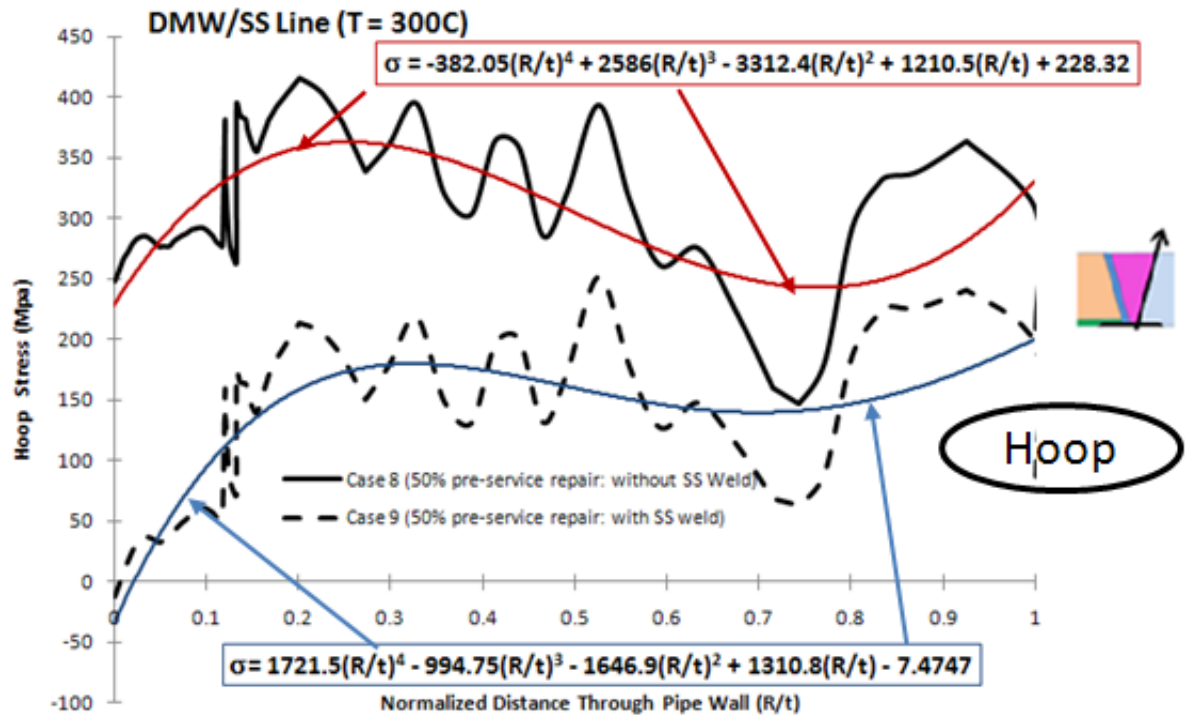
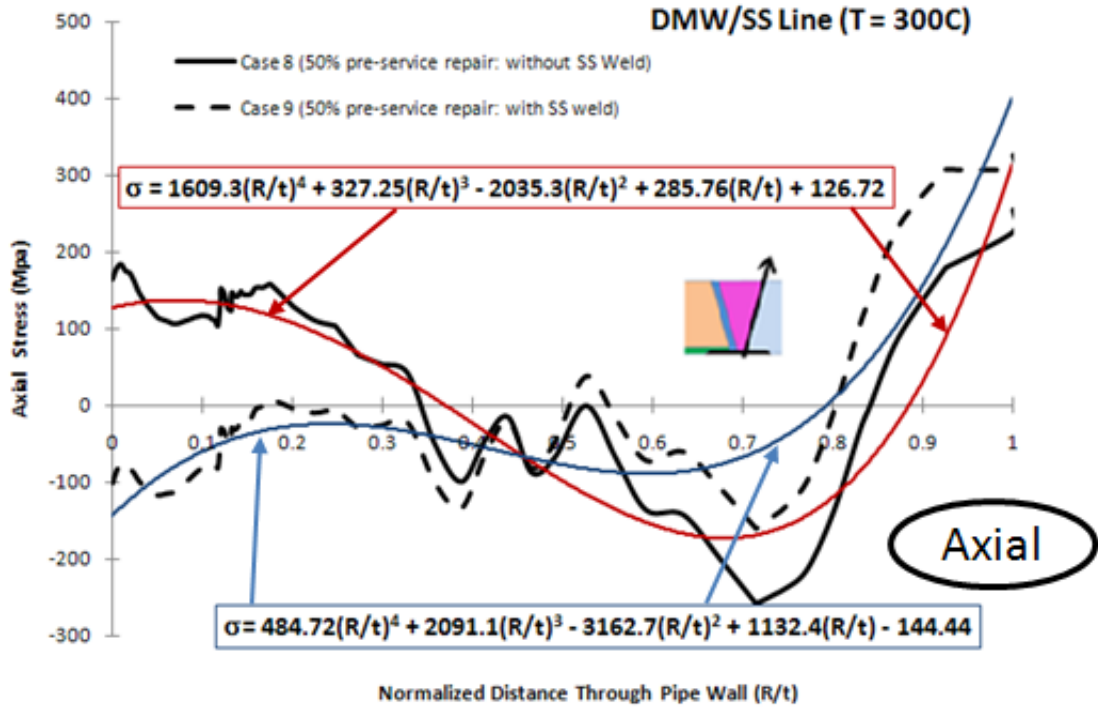


Figure C-2 Axial and Hoop WRS (Model 1) for Cases 8 and 9 (50% repair case: DM Weld/SS line).

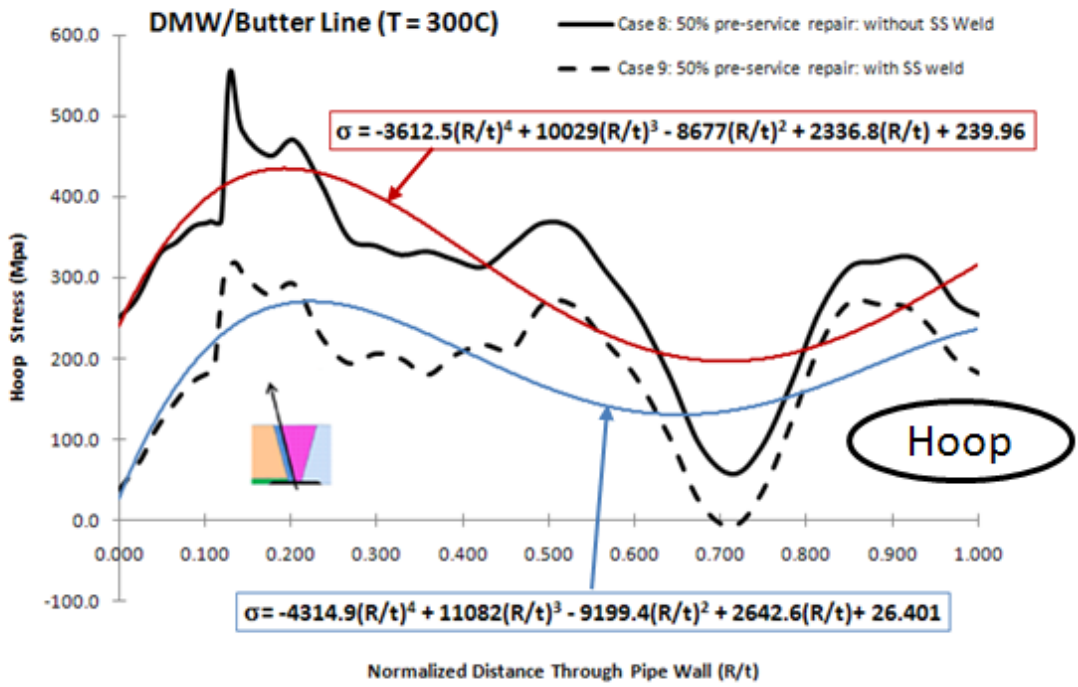
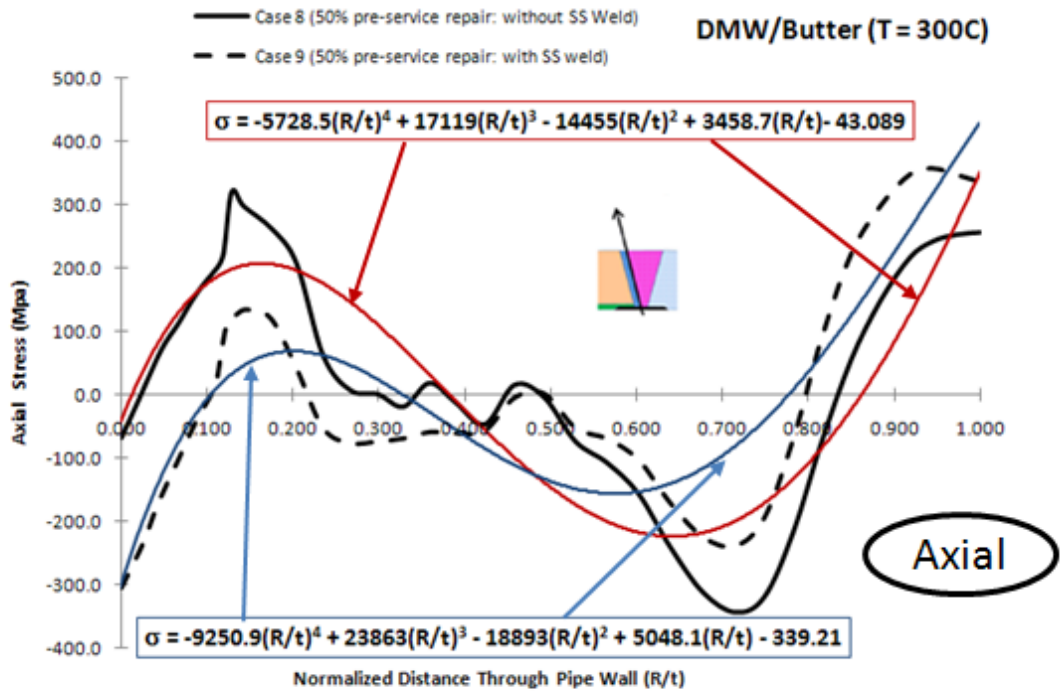


Figure C-3 Axial and Hoop WRS (Model 1) for Case 8 and 9 (50% repair case: DM Weld/Butter).

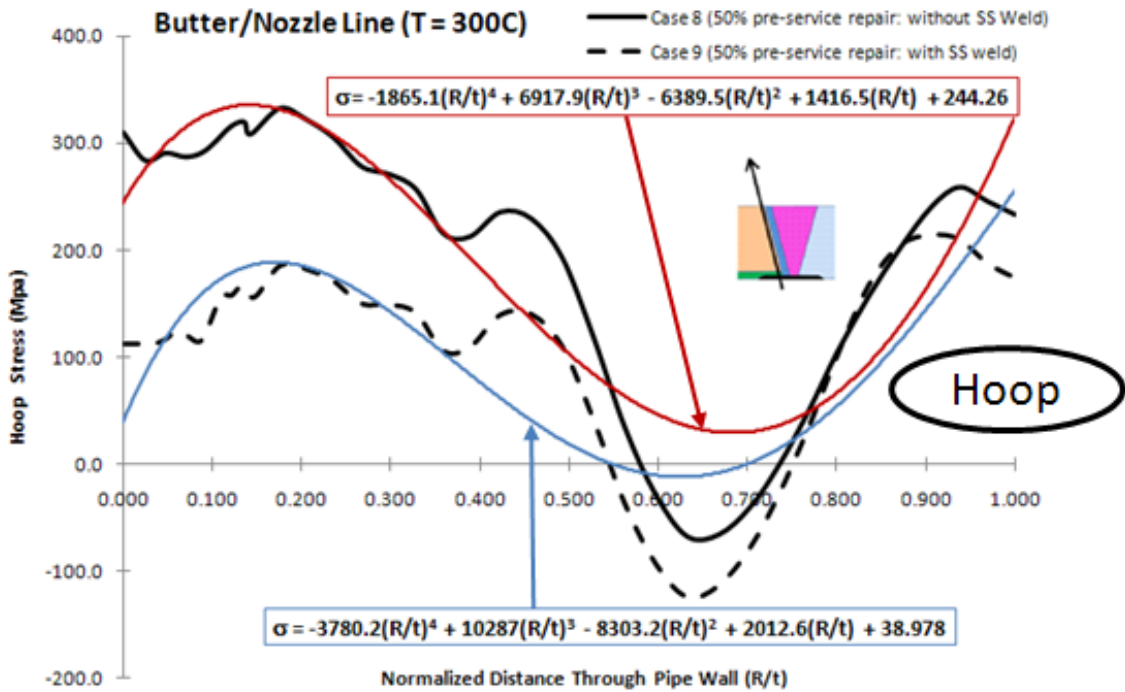
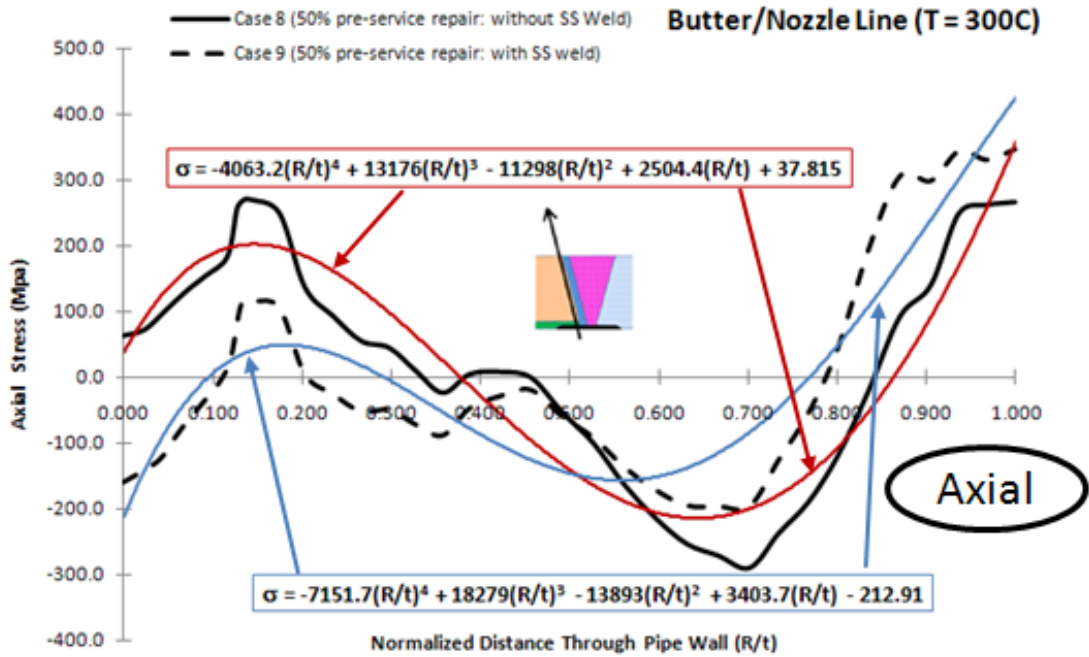


Figure C-4 Axial and Hoop WRS (Model 1) for Case 8 and 9 (50% repair case: DM Weld/Nozzle).

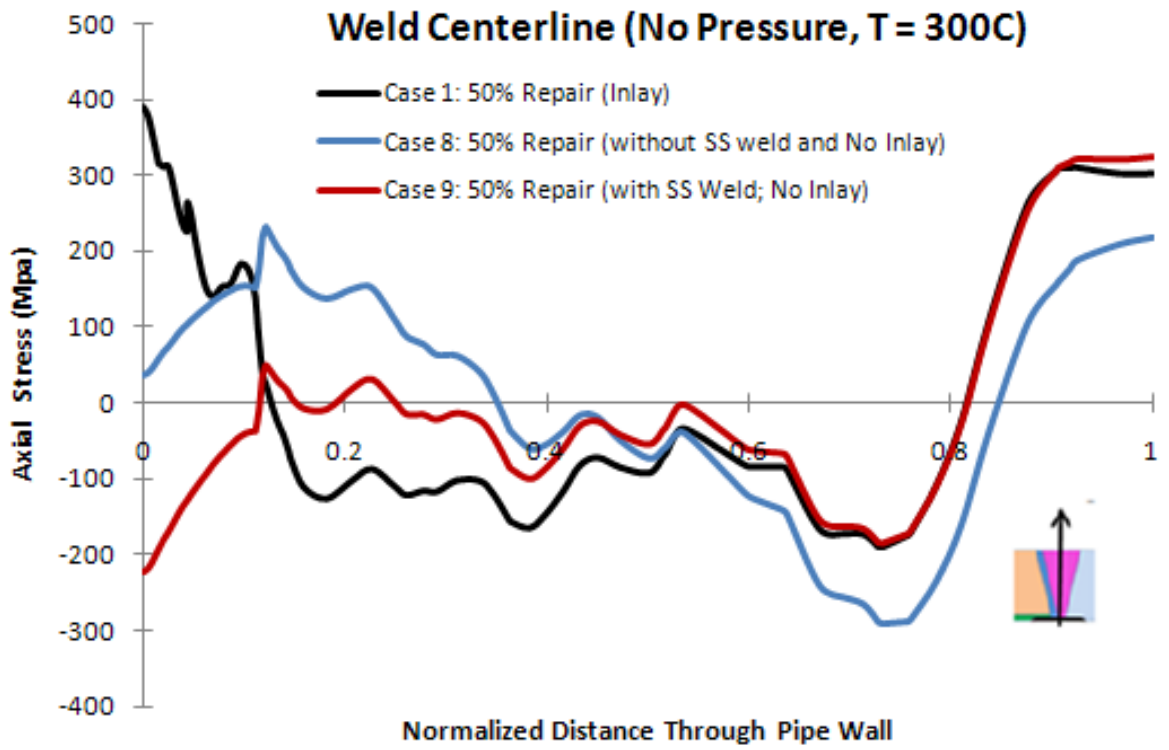


Figure C-5 WRS for Model 1 for 50% repair case.

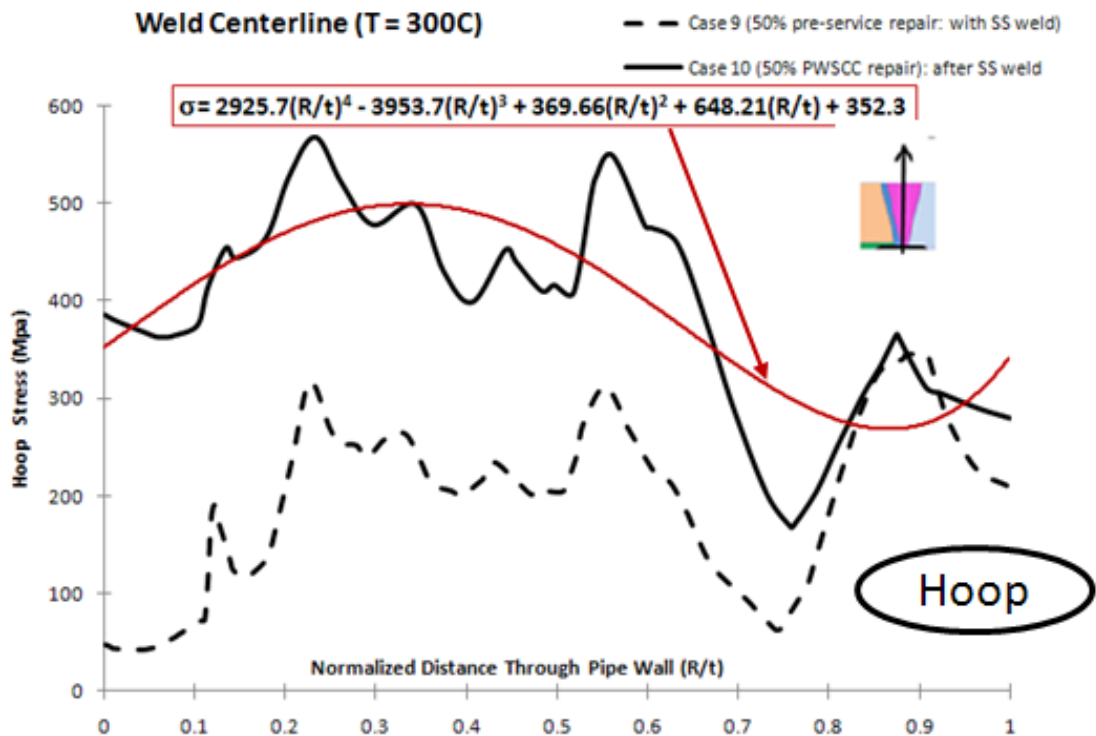
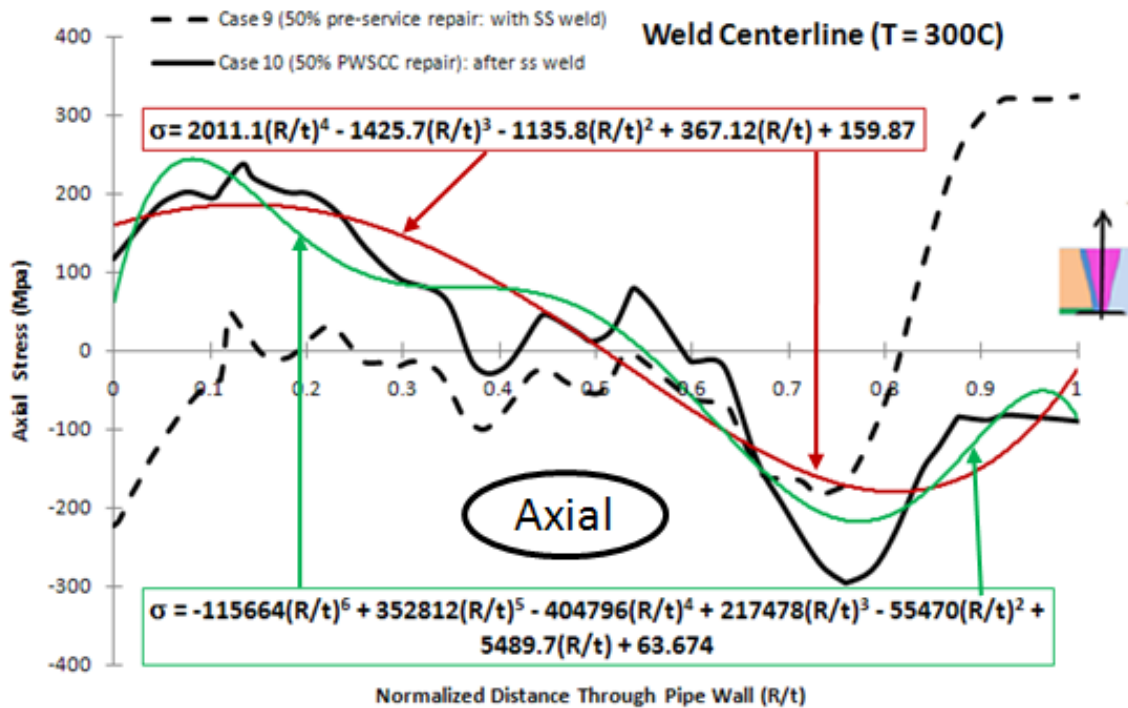


Figure C-6 Axial and Hoop WRS (Model 1) for Case 9 and 10 (50% repair case: Centerline).

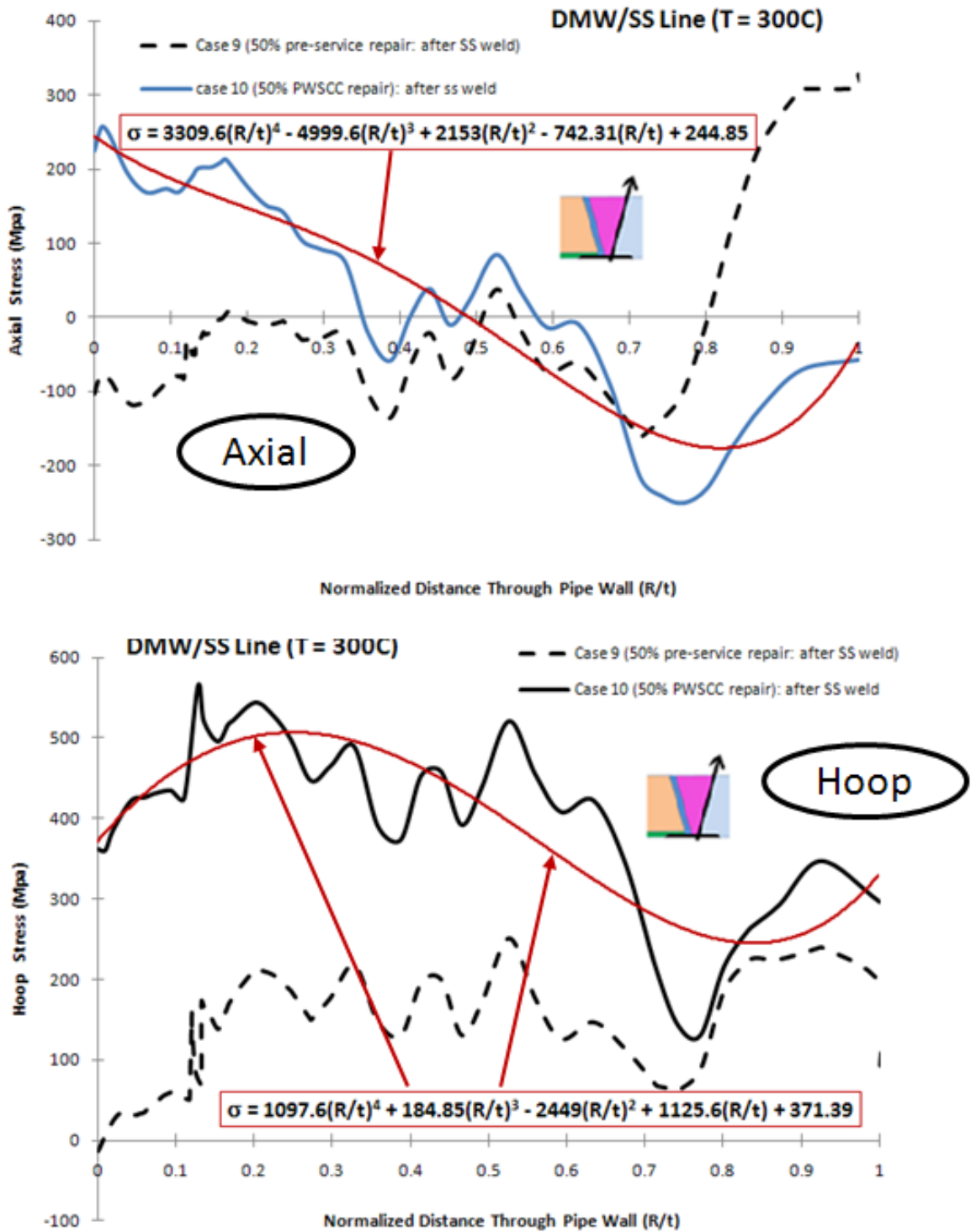


Figure C-7 Axial and Hoop WRS (Model 1) for Case 9 and 10 (50% repair case: DM Weld/SS Line).

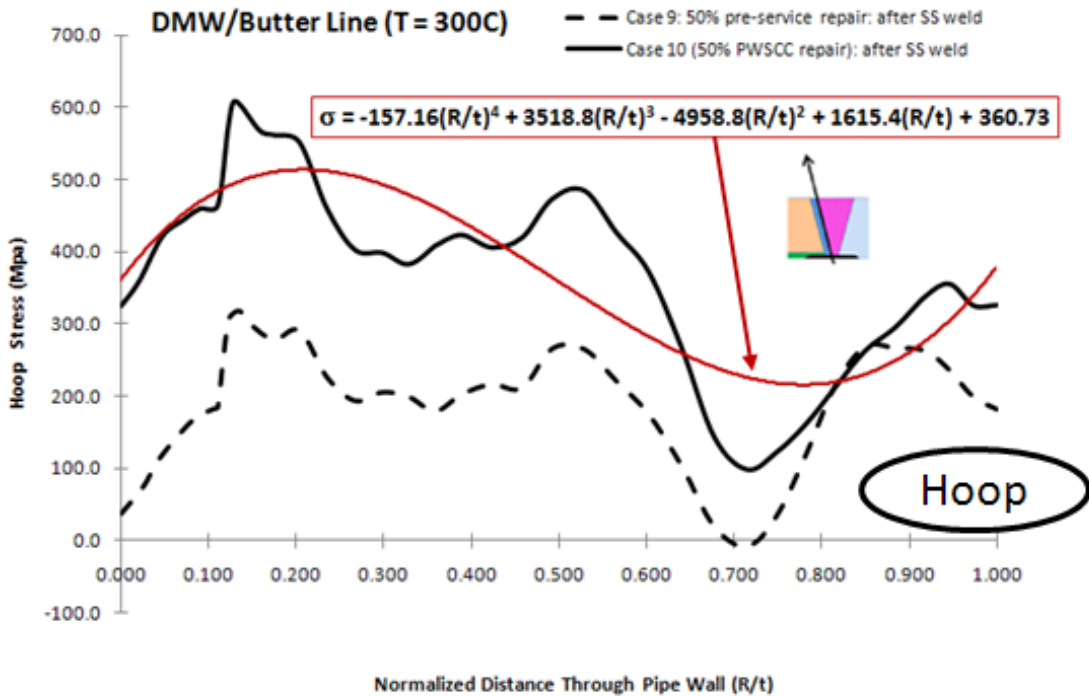
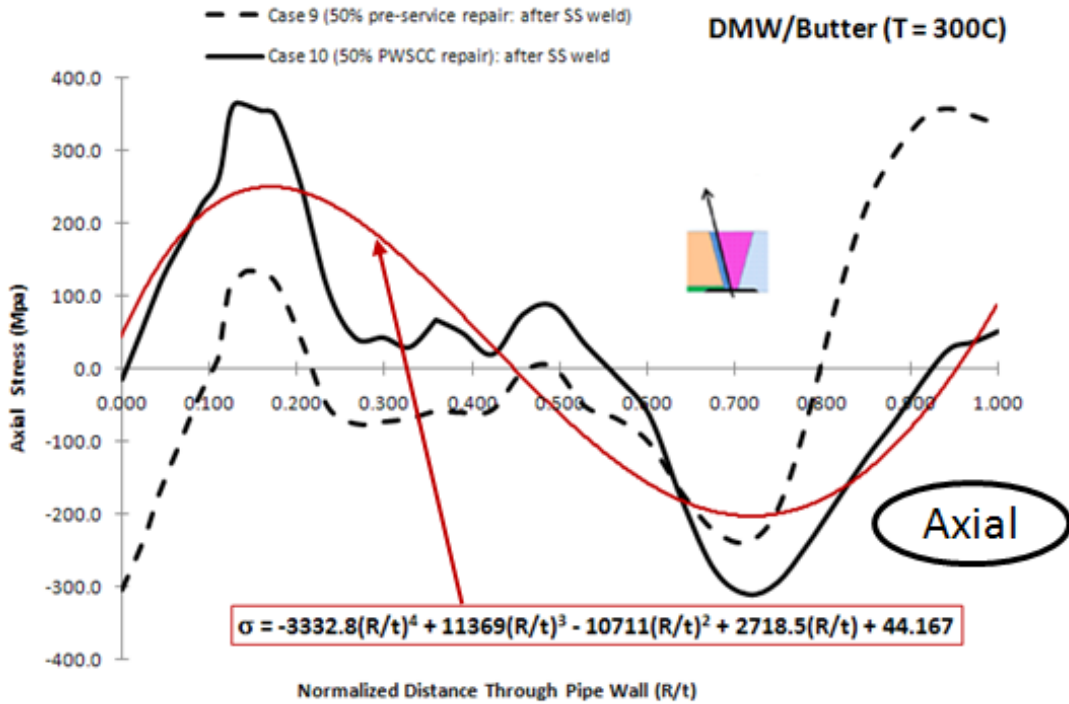


Figure C-8 Axial and Hoop WRS (Model 1) for Case 9 and 10 (50% repair case: DM Weld/Butter).

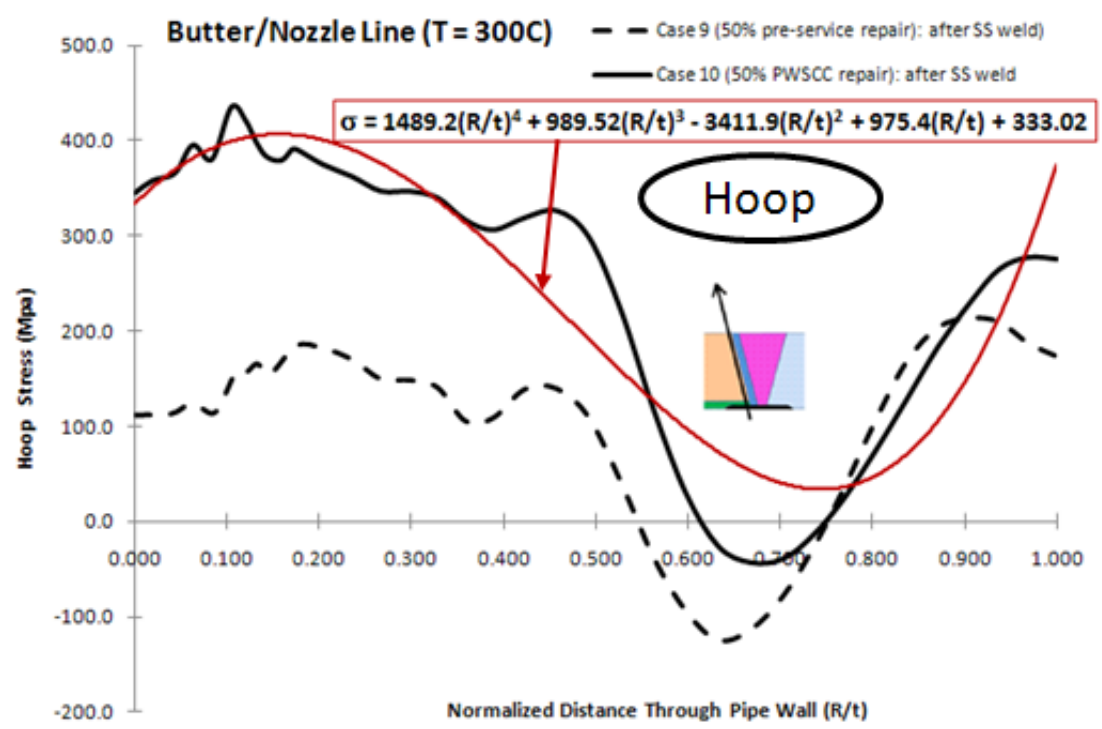
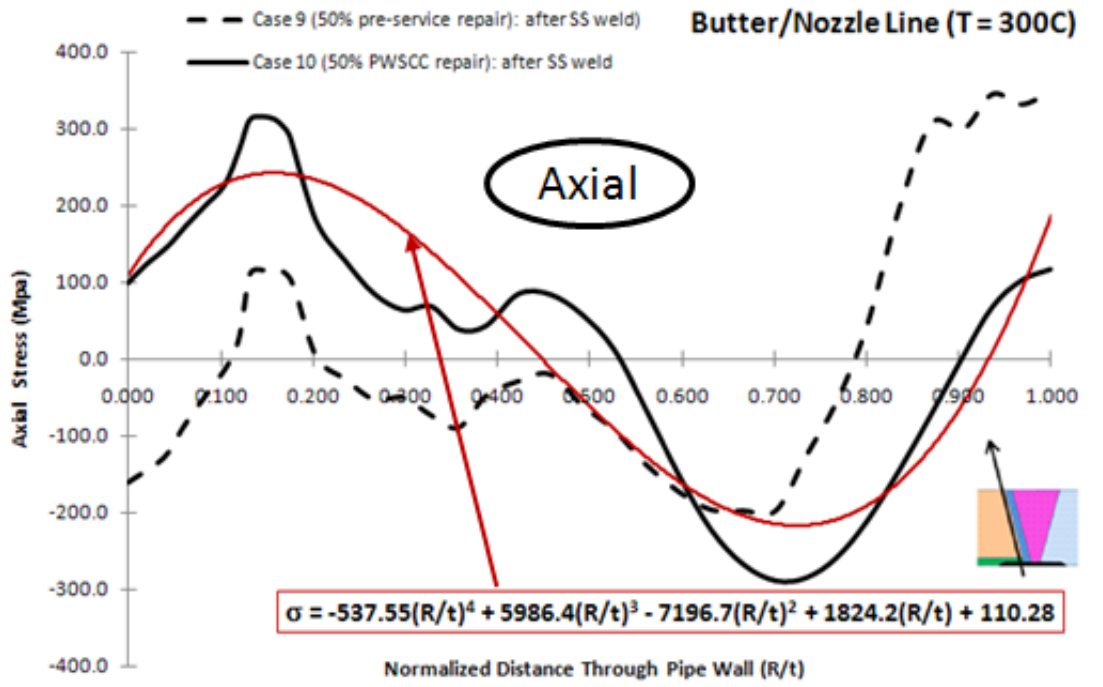


Figure C-9 Axial and Hoop WRS (Model 1) for Case 9 and 10 (50% repair case: DM Weld/Nozzle).

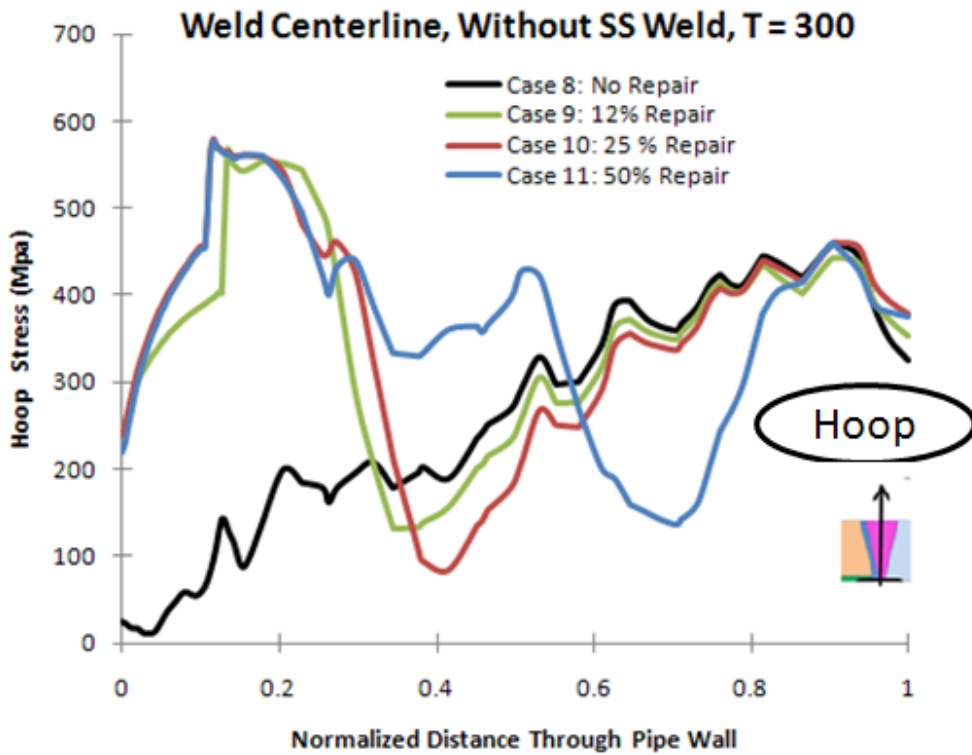
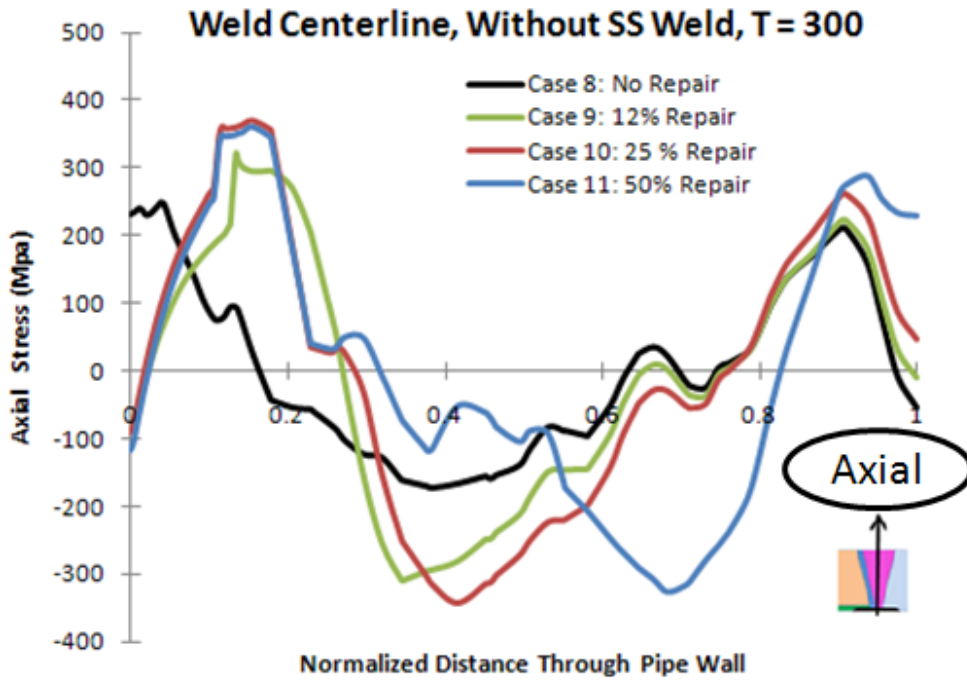


Figure C-10 Axial and Hoop WRS at weld centerline line for different depth repairs for the case without the stainless steel weld (Model 2).

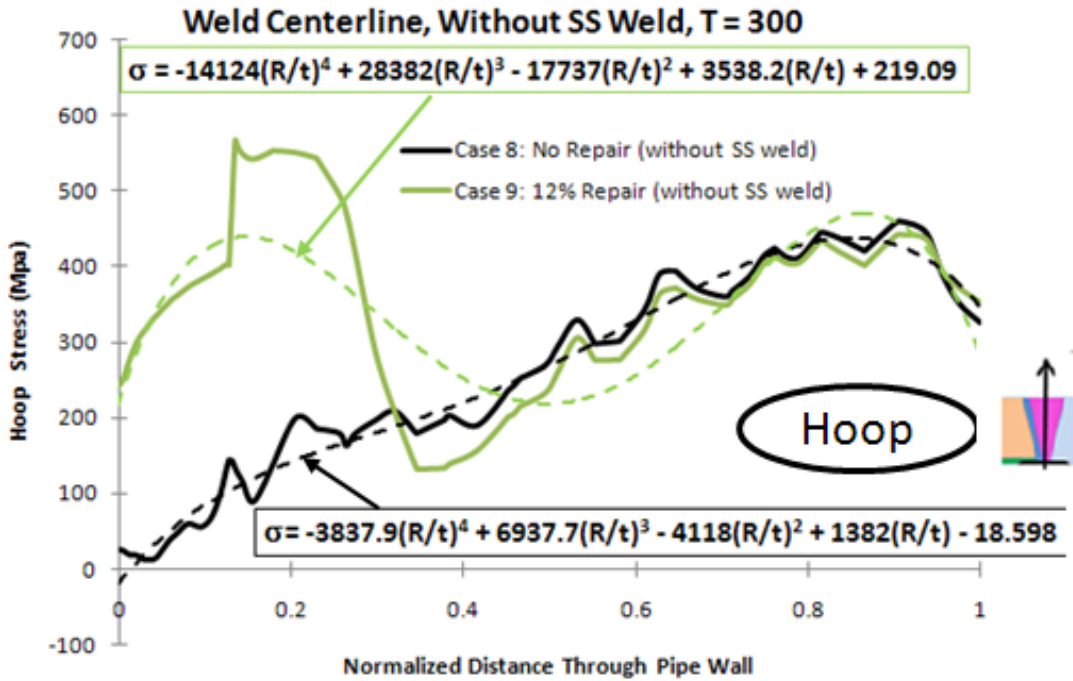
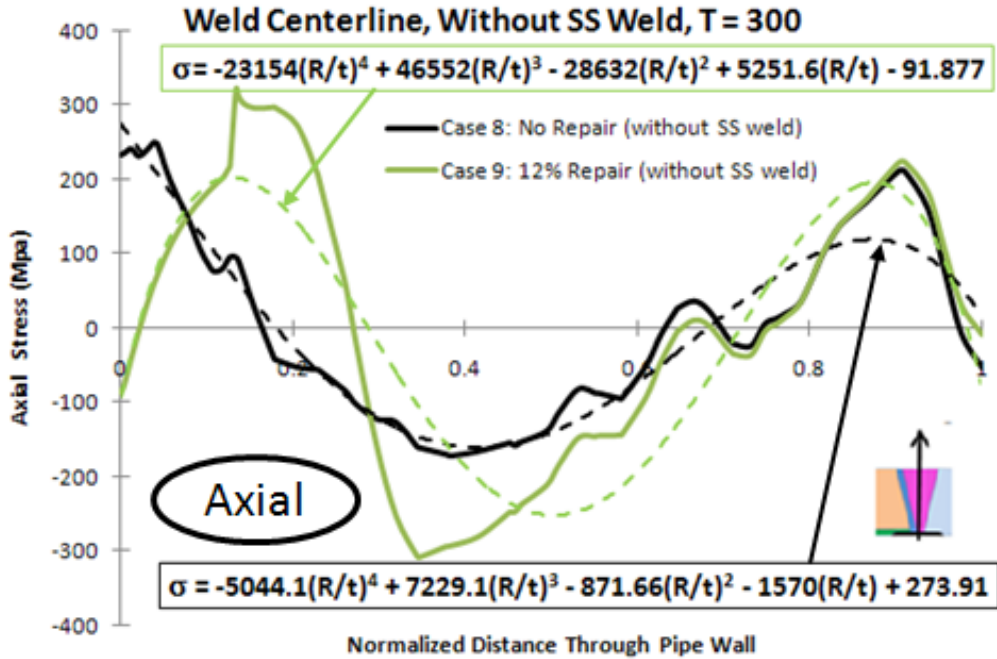


Figure C-11 Axial and hoop WRS at weld centerline line for different no repair and 12% deep repair for the case without the stainless steel weld (Model 2).

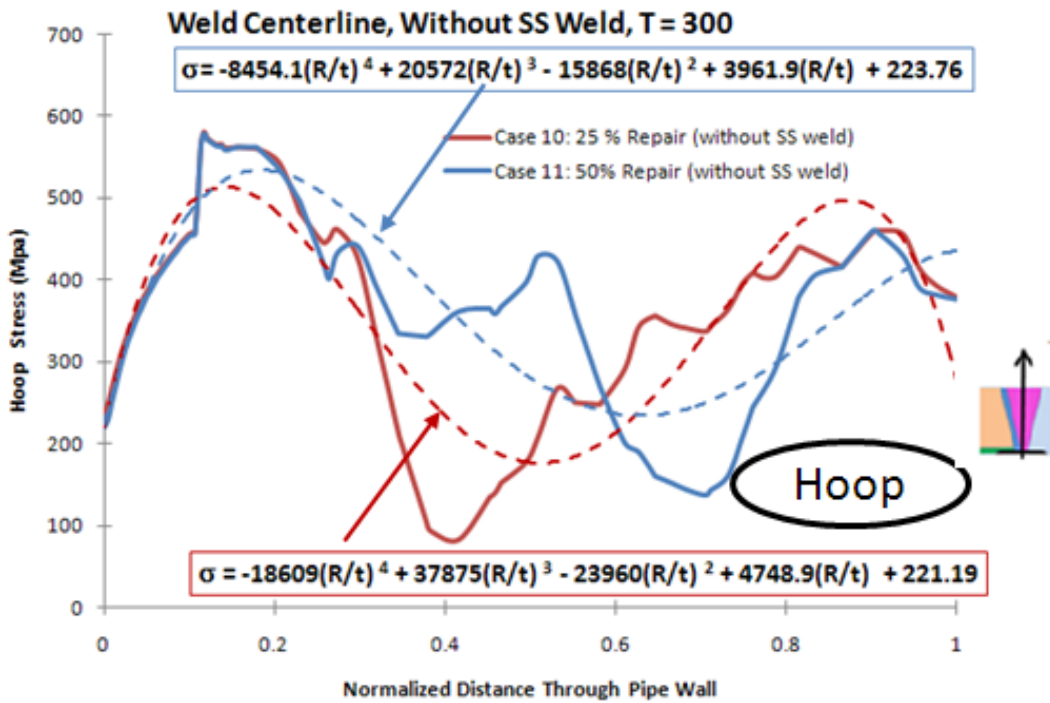
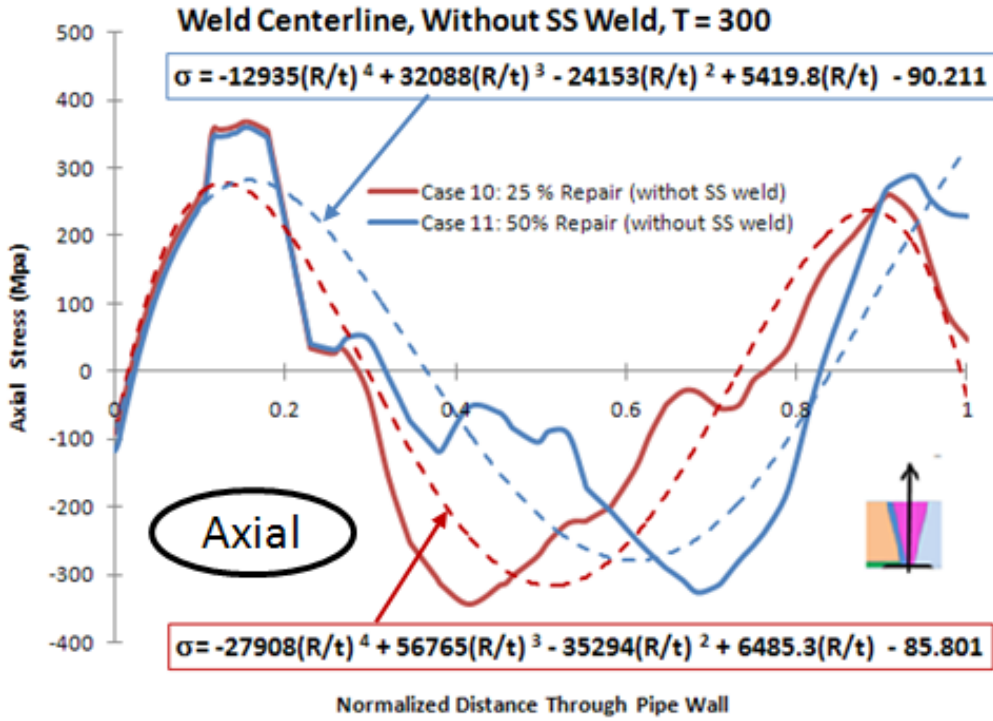


Figure C-12 Axial and hoop WRS at weld centerline line for different 25% repair and 50% deep repair for the case without the stainless steel weld (Model 2).

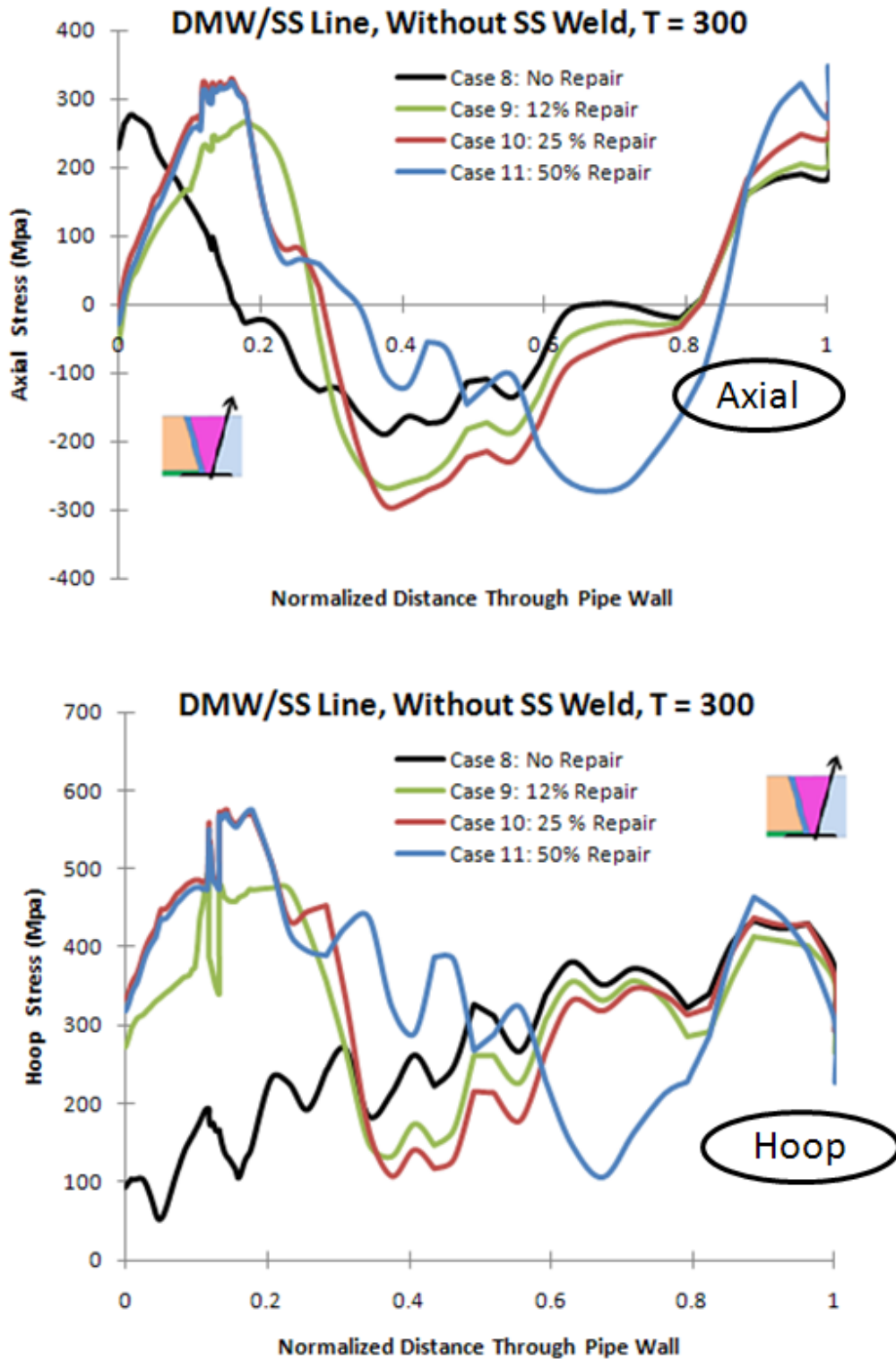


Figure C-13 Axial and Hoop WRS at DM Weld/SS line for different depth repairs for the case without the stainless steel weld (Model 2).

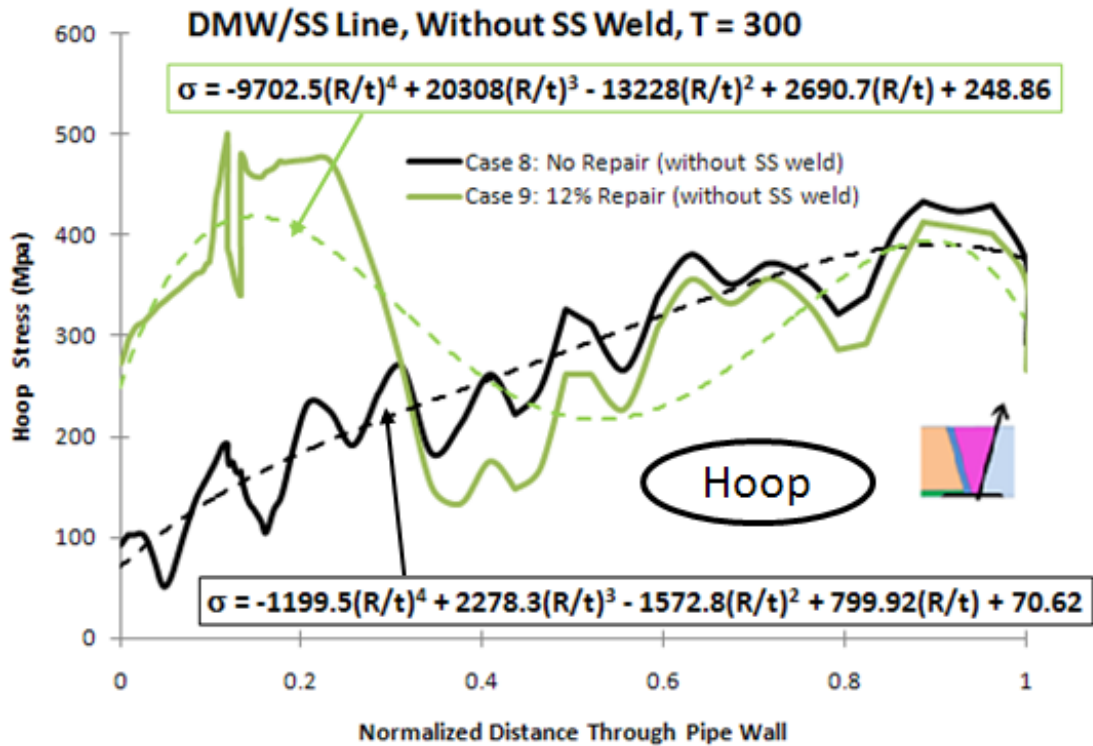
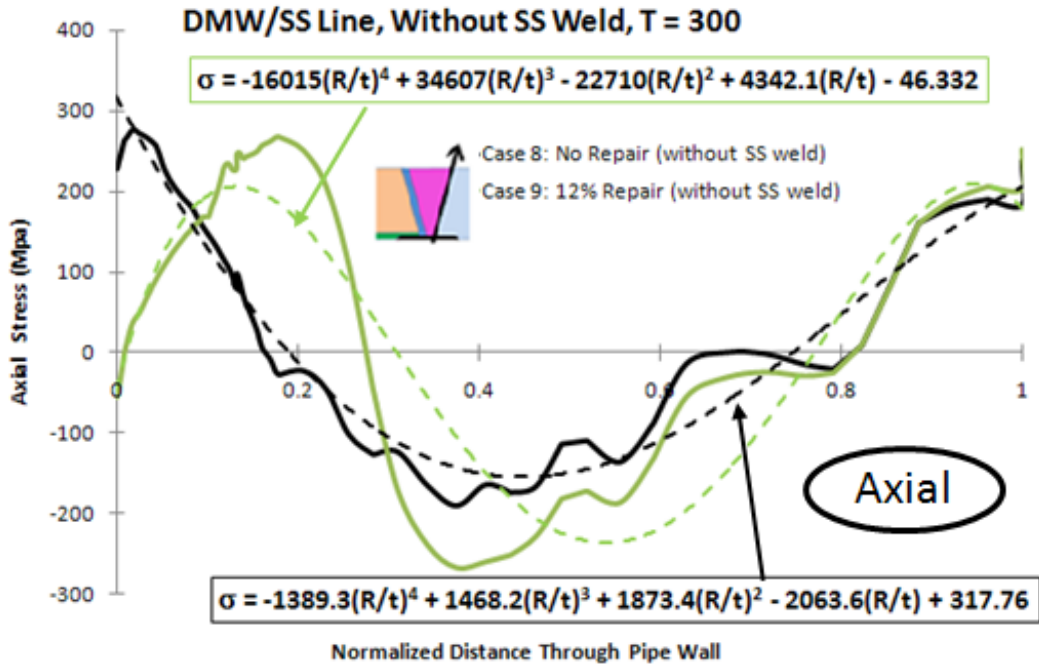


Figure C-14 Axial and hoop WRS at DM Weld/SS line for no repair and 12% deep repair for the case without the stainless steel weld (Model 2).

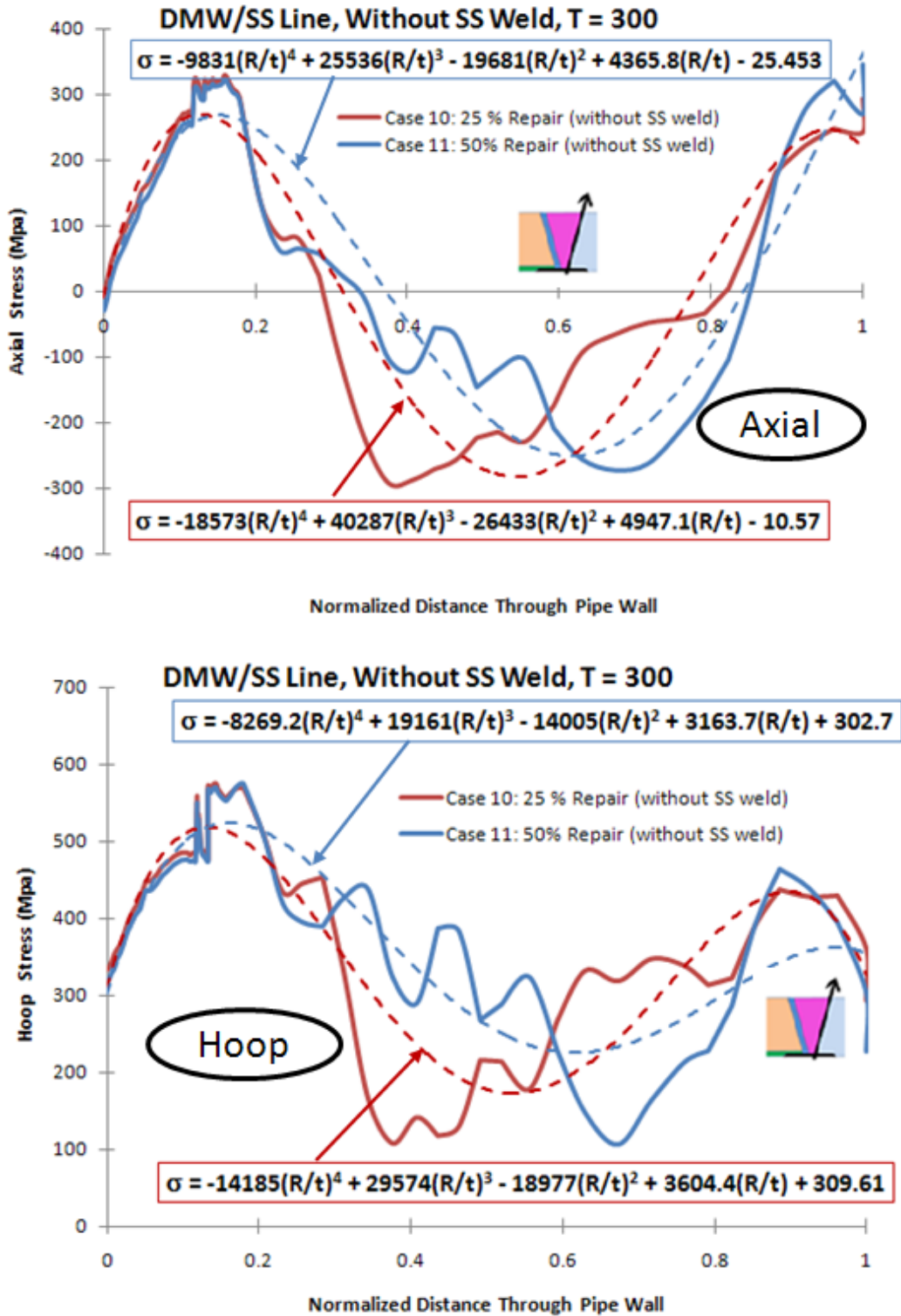


Figure C-15 Axial and hoop WRS at DM Weld/SS line for 25% repair and 50% deep repair for the case without the stainless steel weld (Model 2).

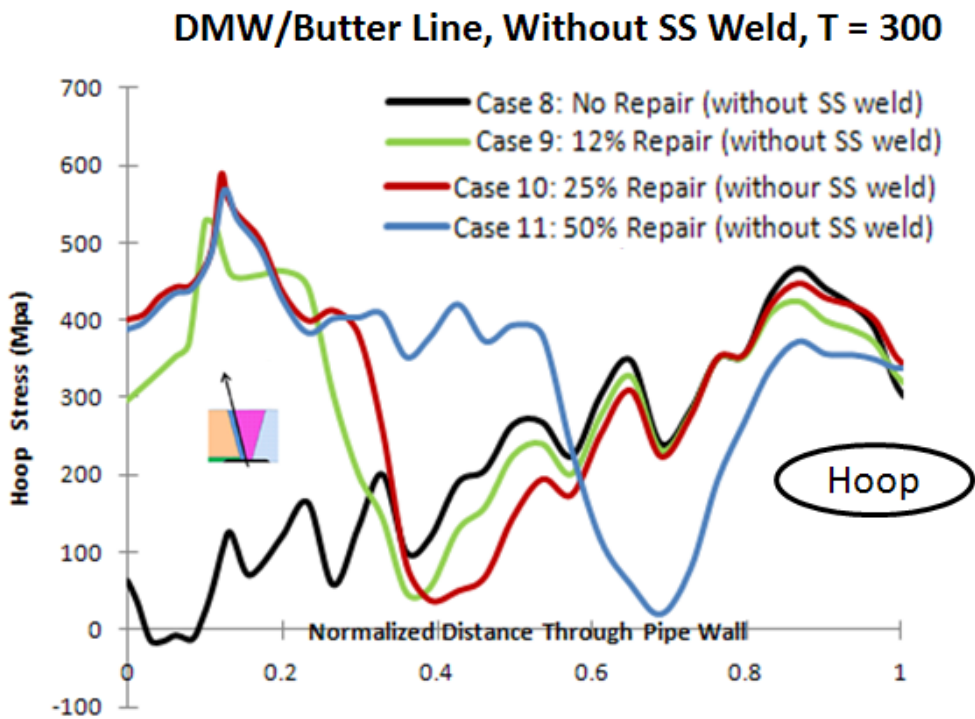
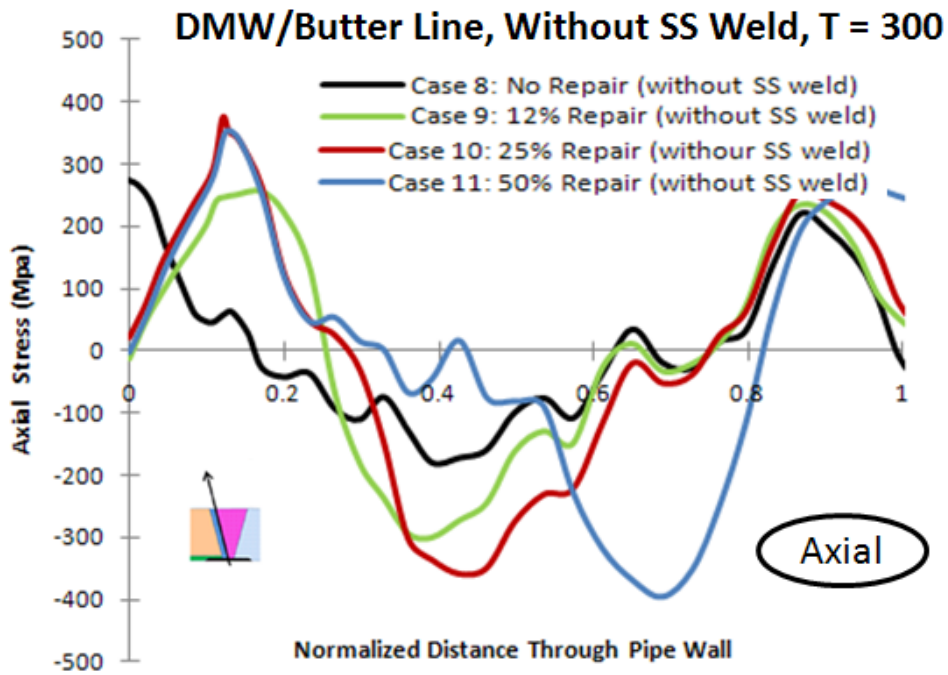


Figure C-16 Axial and Hoop WRS at DM Weld/Butter line for different depth repairs for the case without the stainless steel weld (Model 2).

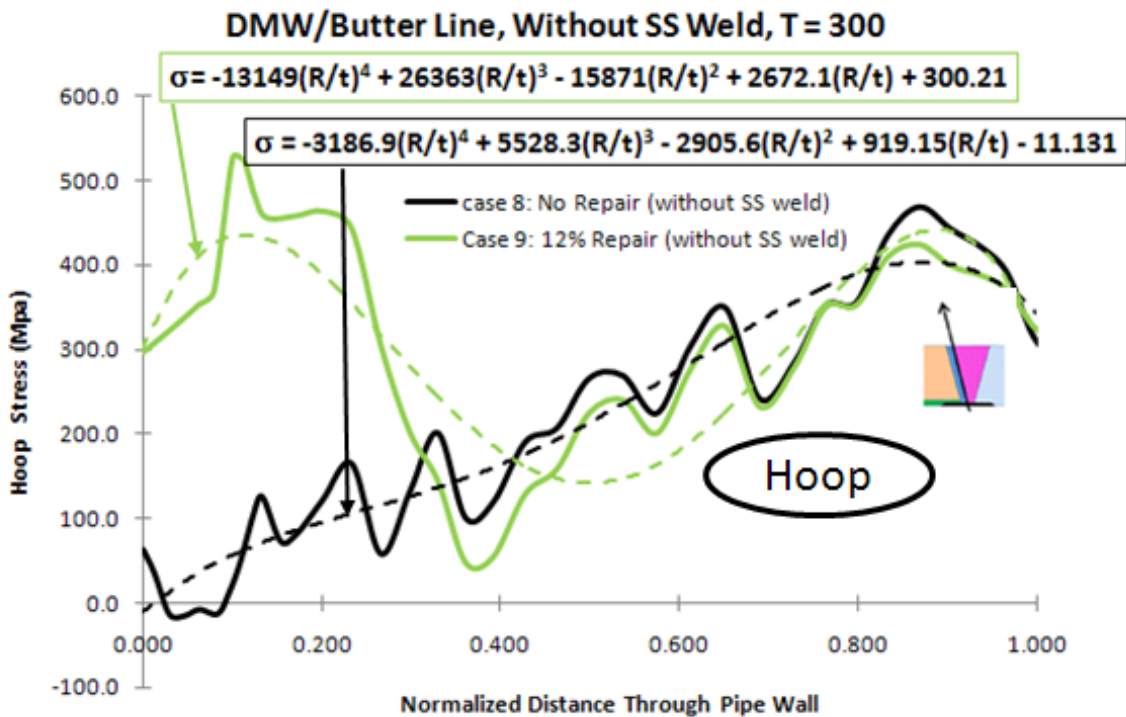
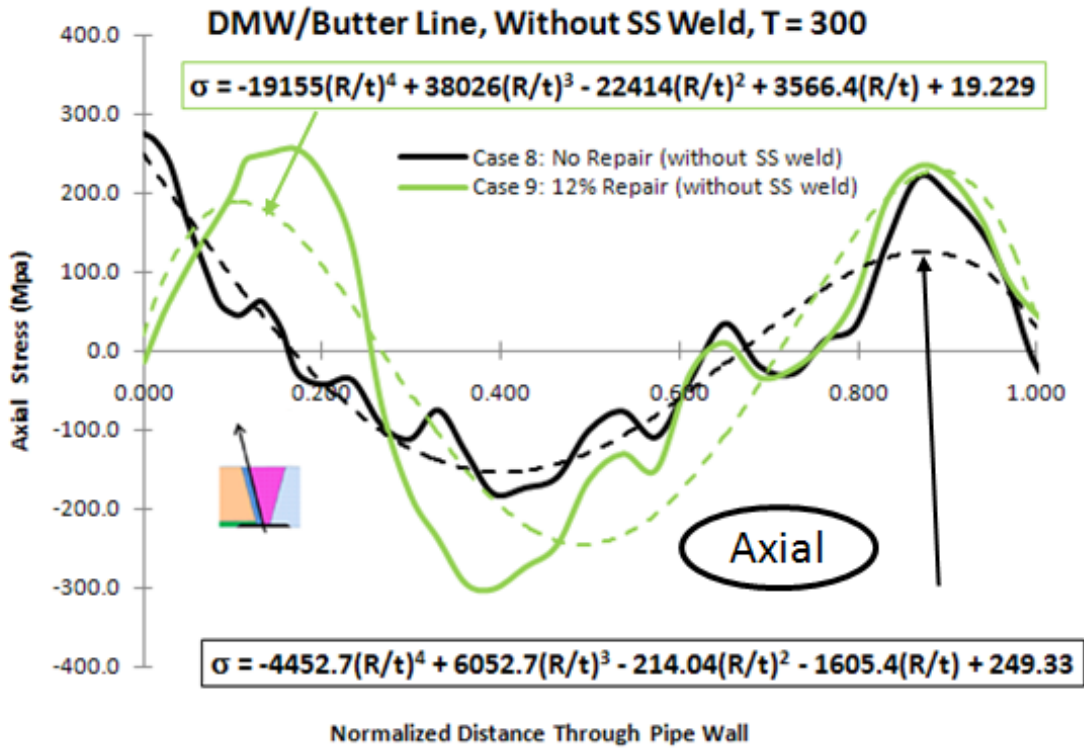


Figure C-17 Axial and hoop WRS at DM Weld/Butter line for no repair and 12% deep repair for the case without the stainless steel weld (Model 2).

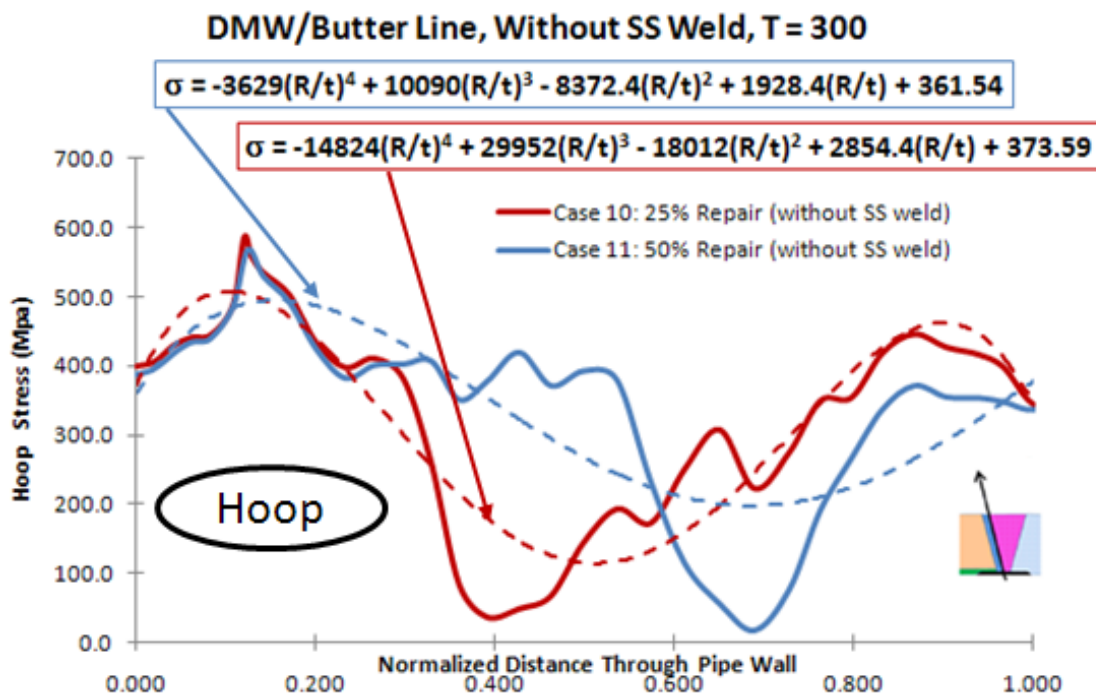
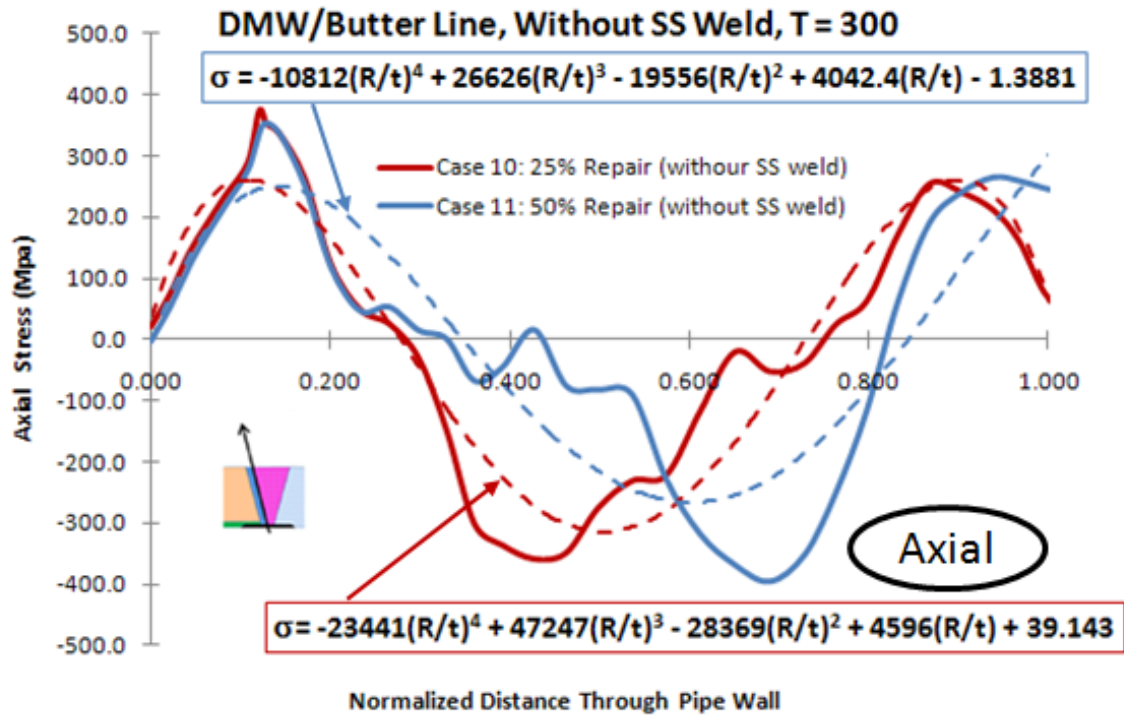


Figure C-18 Axial and hoop WRS at DM Weld/Butter line for 25% repair and 50% deep repair for the case without the stainless steel weld (Model 2).

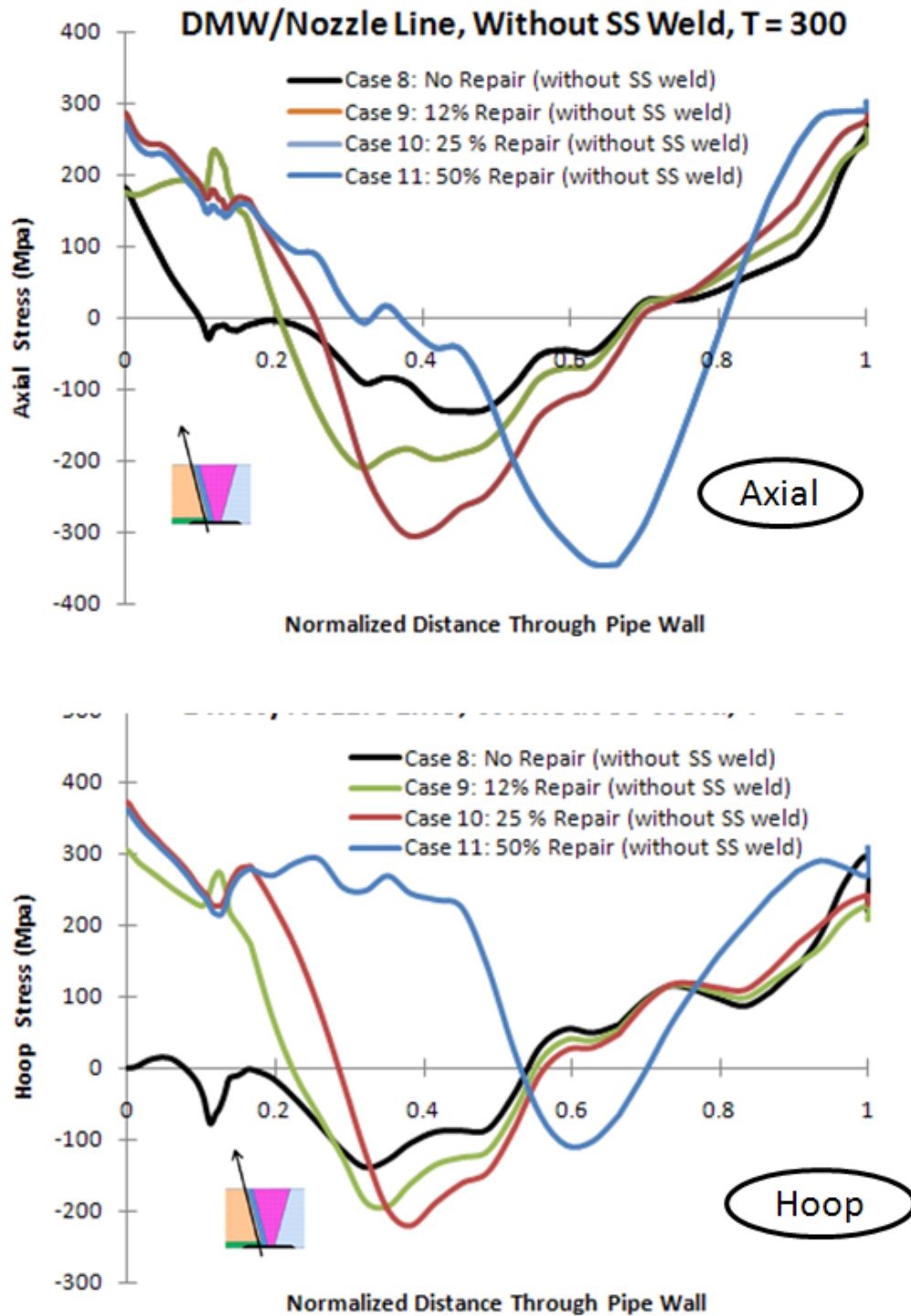


Figure C-19 Axial and Hoop WRS at DM Weld/Nozzle line for different depth repairs for the case without the stainless steel weld (Model 2).

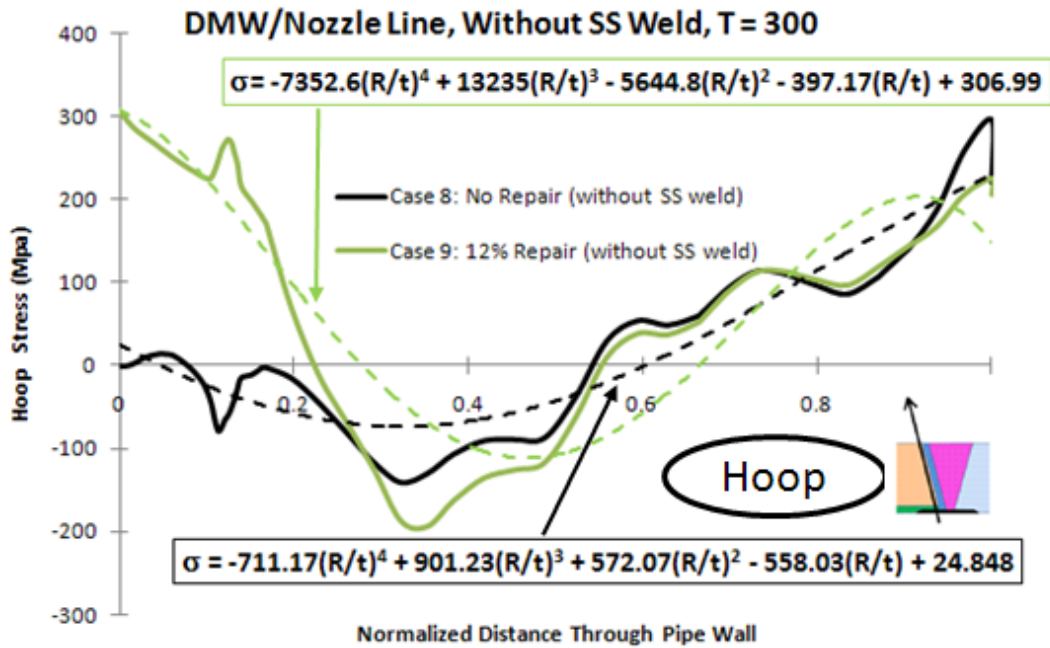
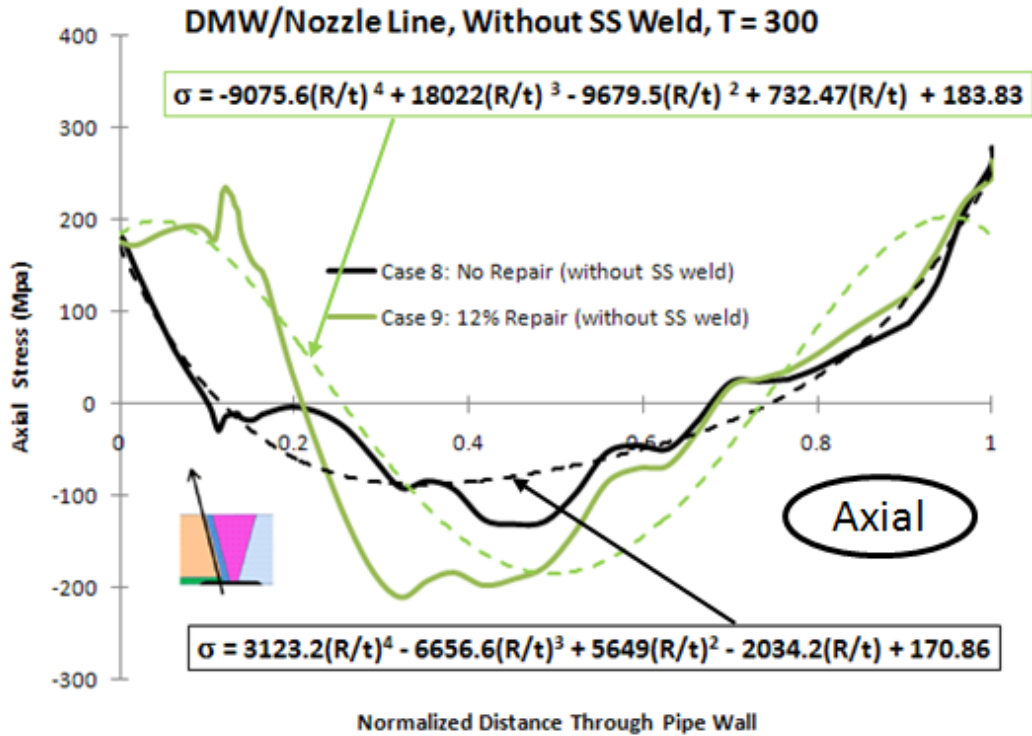


Figure C-20 Axial and hoop WRS at DM Weld/Nozzle line for no repair and 12% deep repair for the case without the stainless steel weld (Model 2).

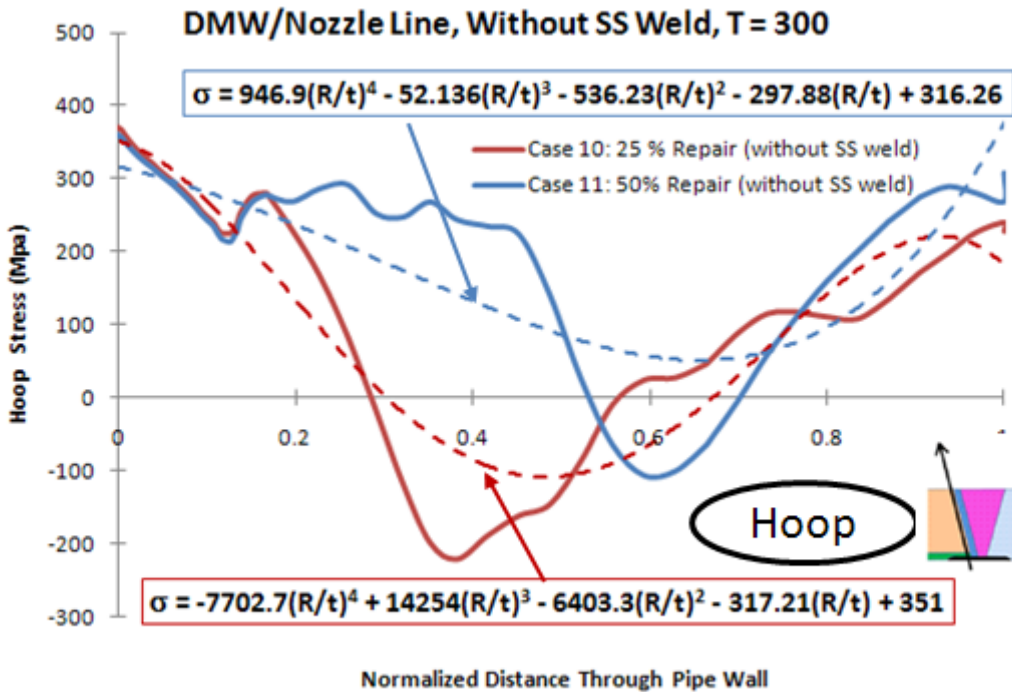
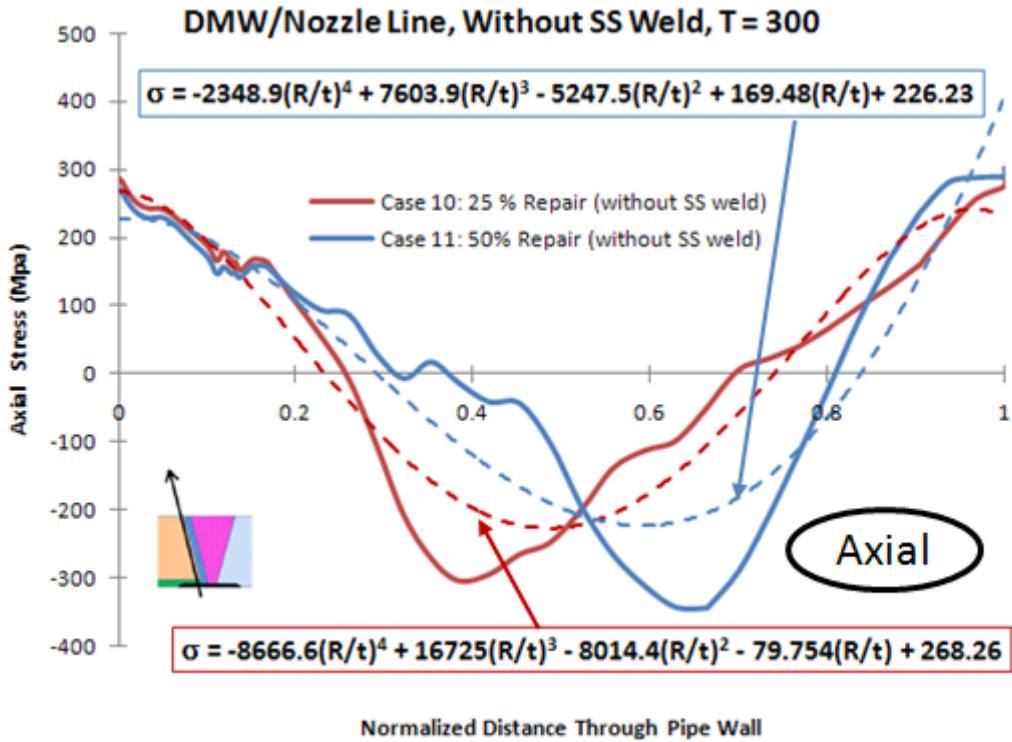


Figure C-21 Axial and hoop WRS at DM Weld/Nozzle line for 25% repair and 50% deep repair for the case without the stainless steel weld (Model 2).

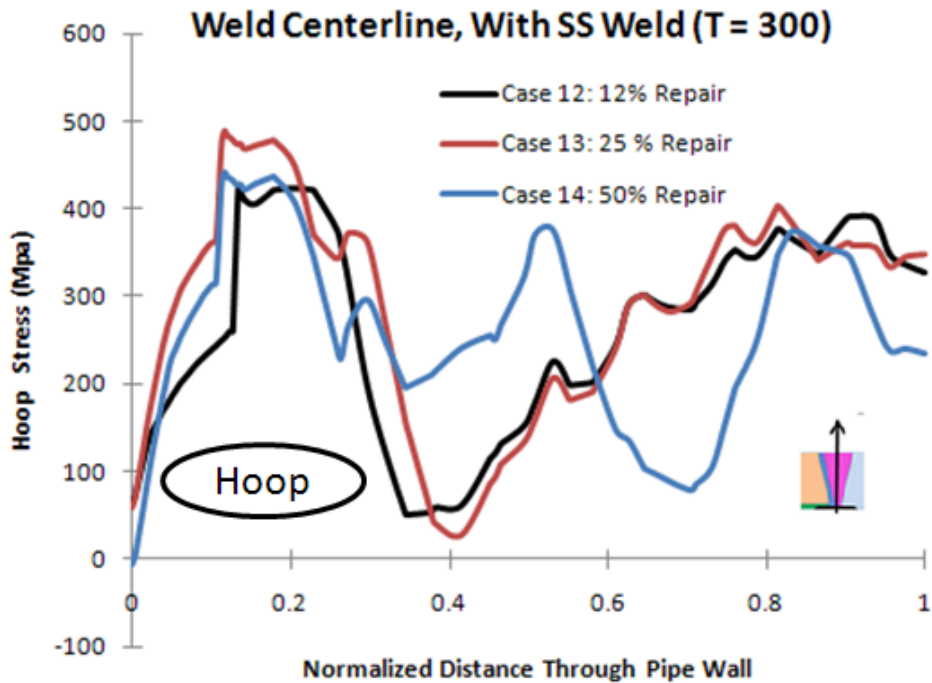
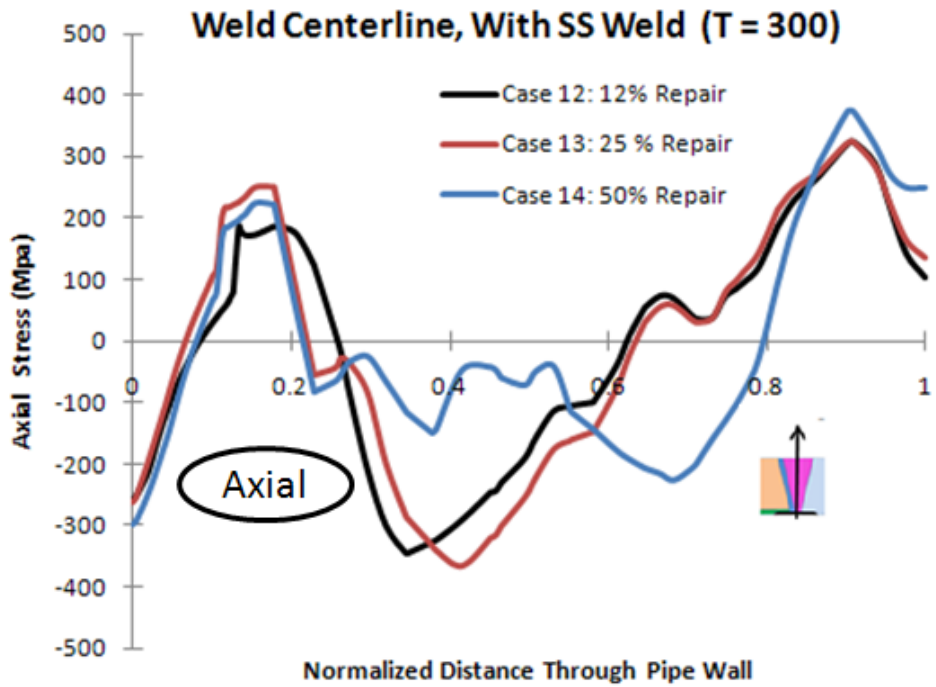


Figure C-22 Axial and Hoop WRS at weld centerline line for different depth repairs for the case with safe-end weld (Model 2).

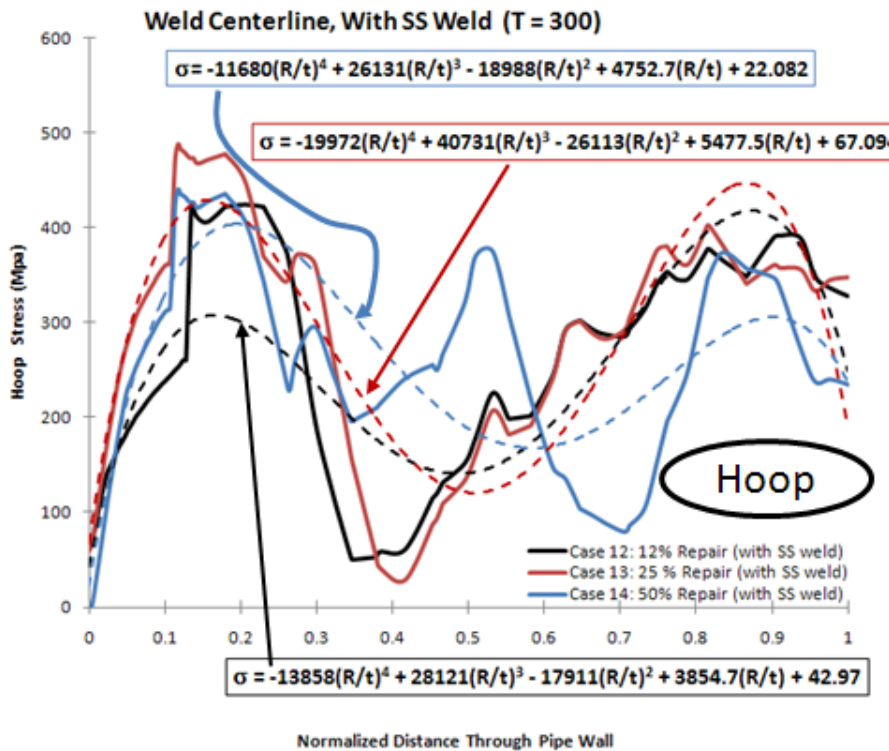
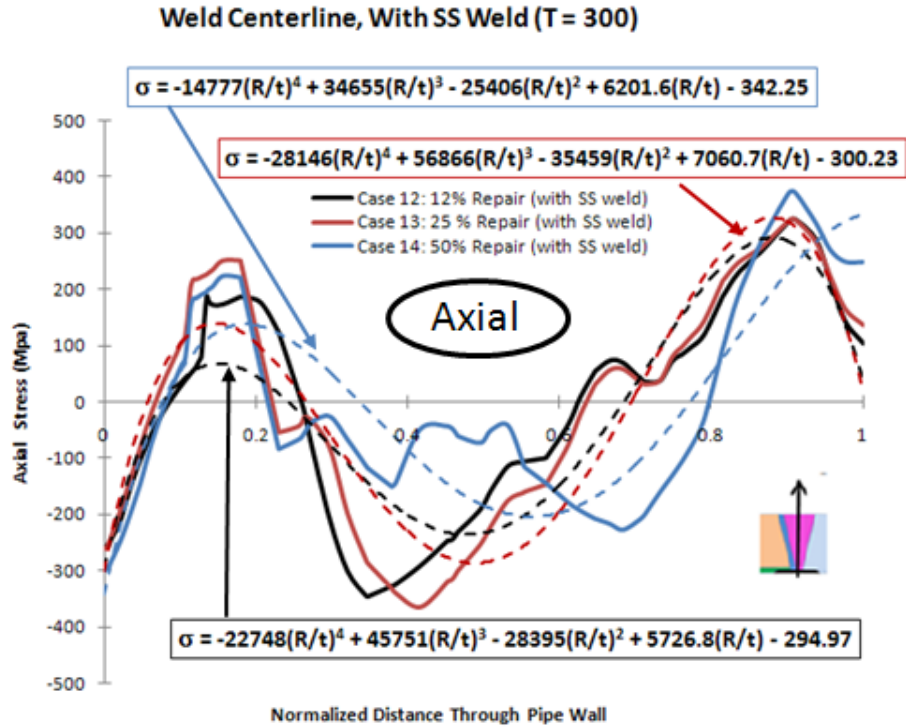


Figure C-23 Axial and Hoop WRS at weld centerline line for different depth repairs for the case with safe-end weld (Model 2).

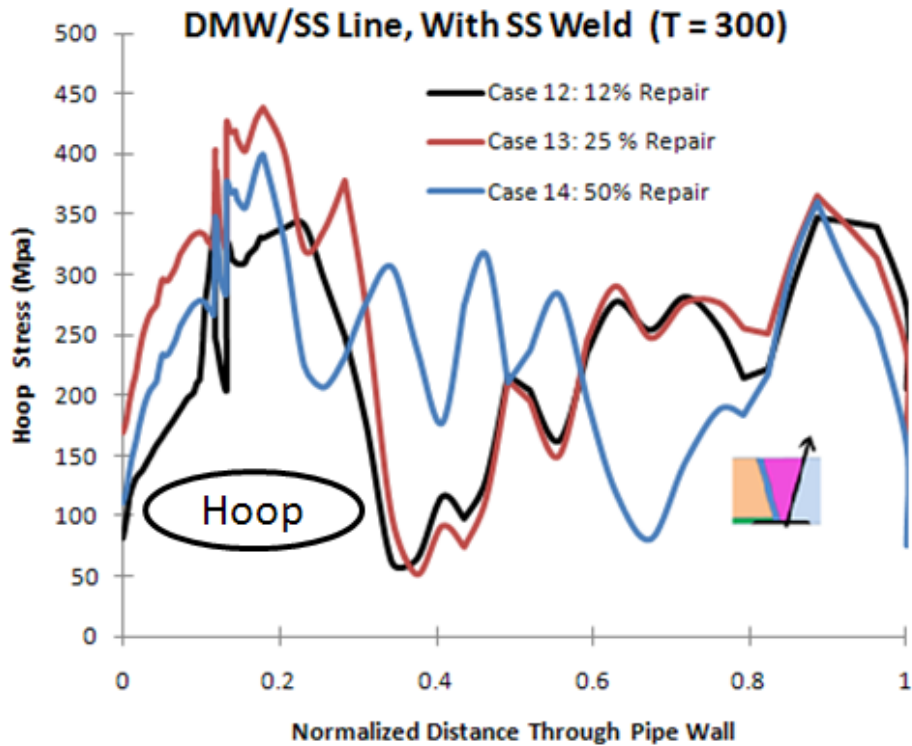
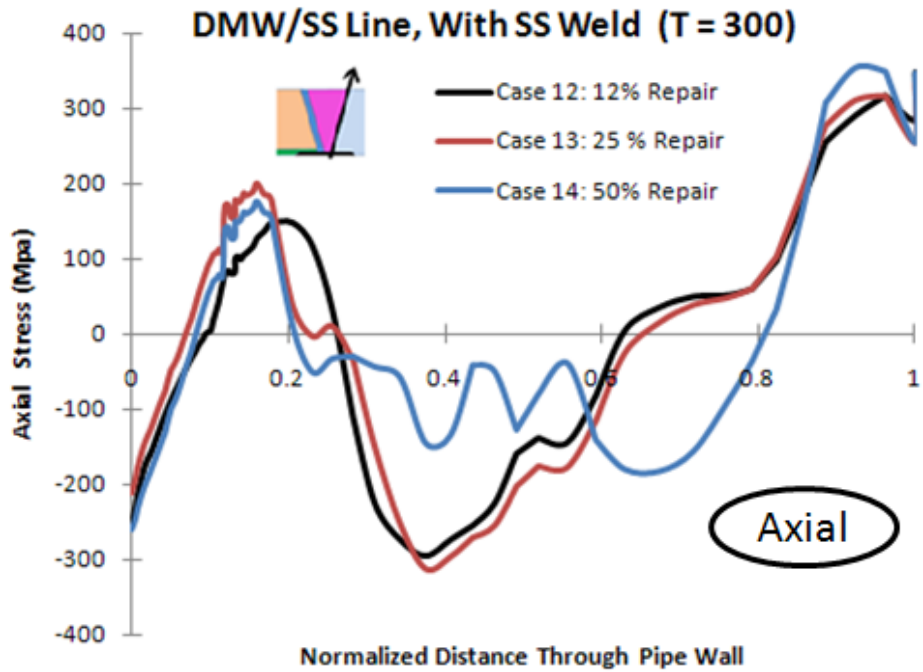


Figure C-24 Axial and Hoop WRS at DM Weld/SS line for different depth repairs for the case with safe-end weld (Model 2).

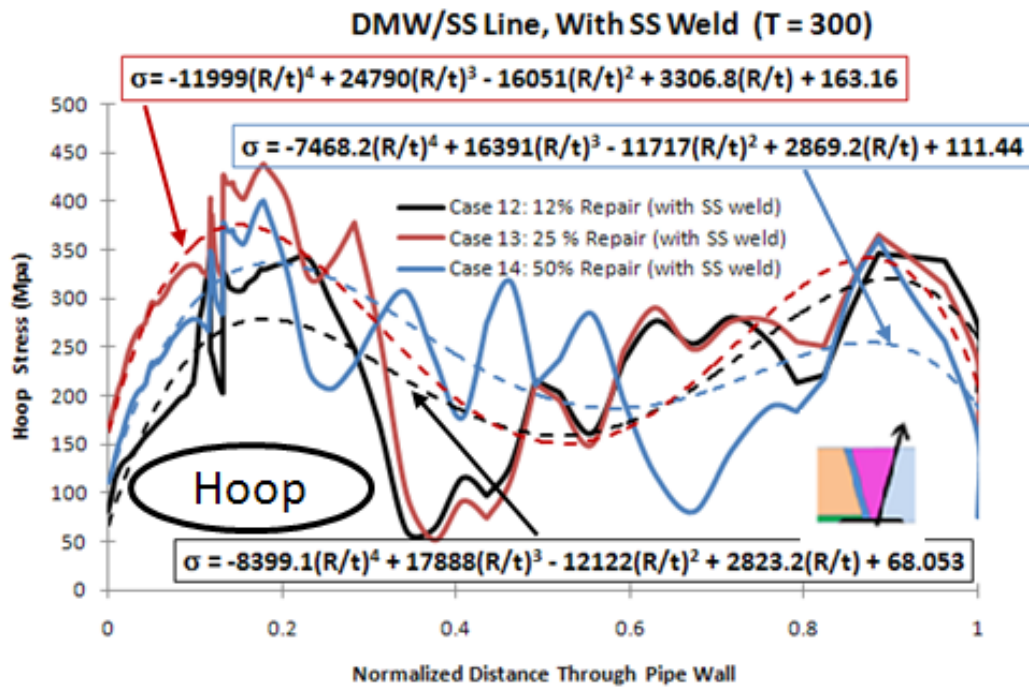
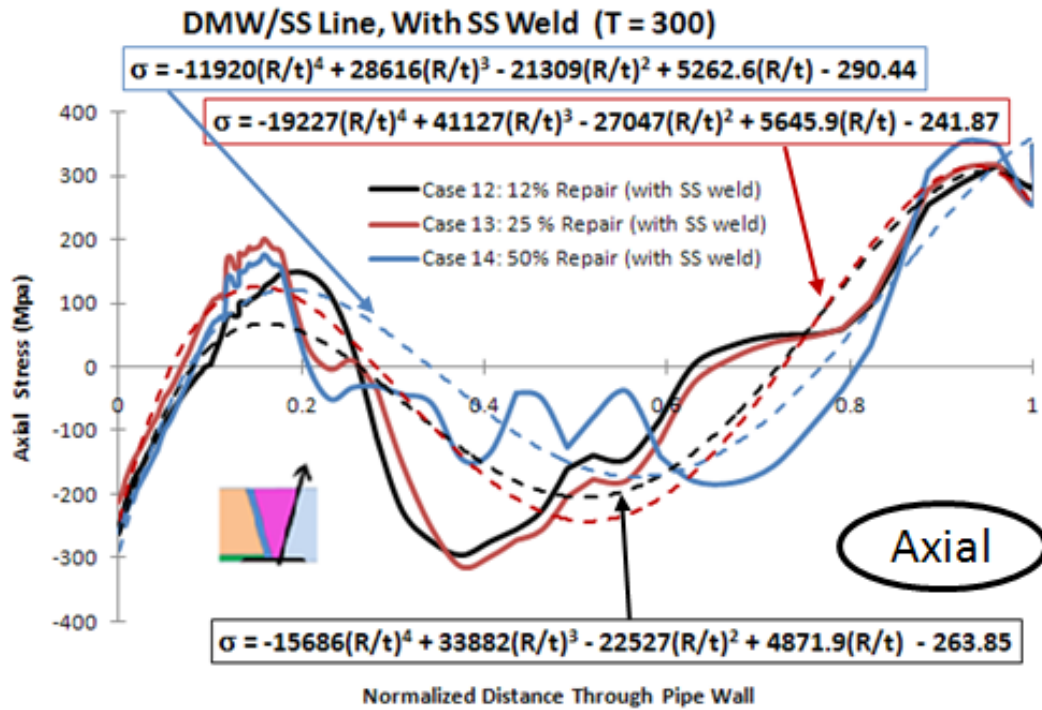


Figure C-25 Axial and Hoop WRS at DM Weld/SS line for different depth repairs for the case with safe-end weld (Model 2).

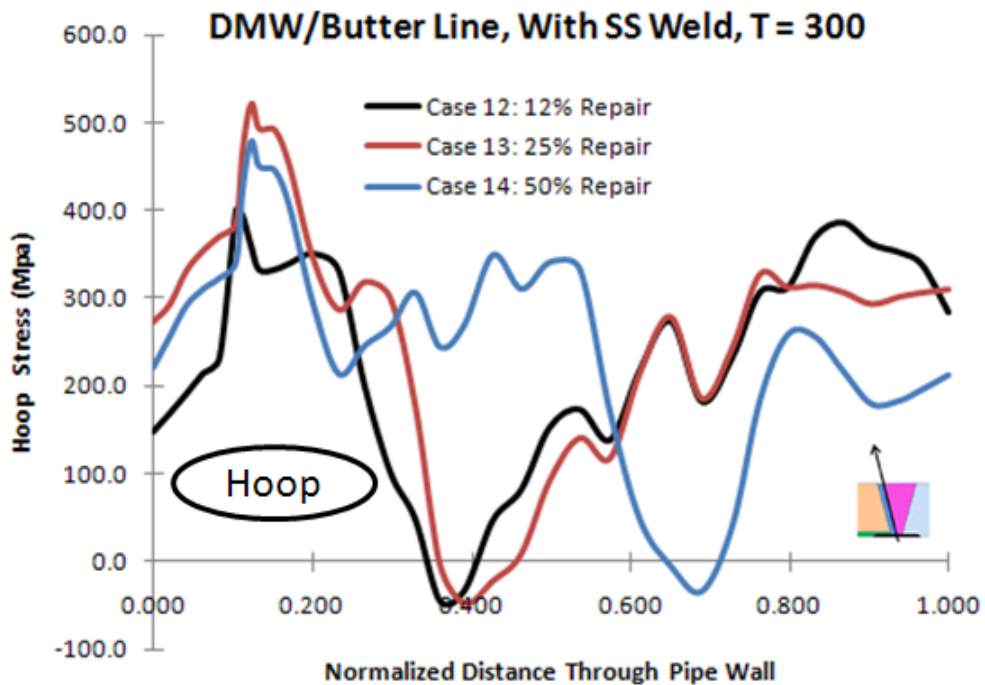
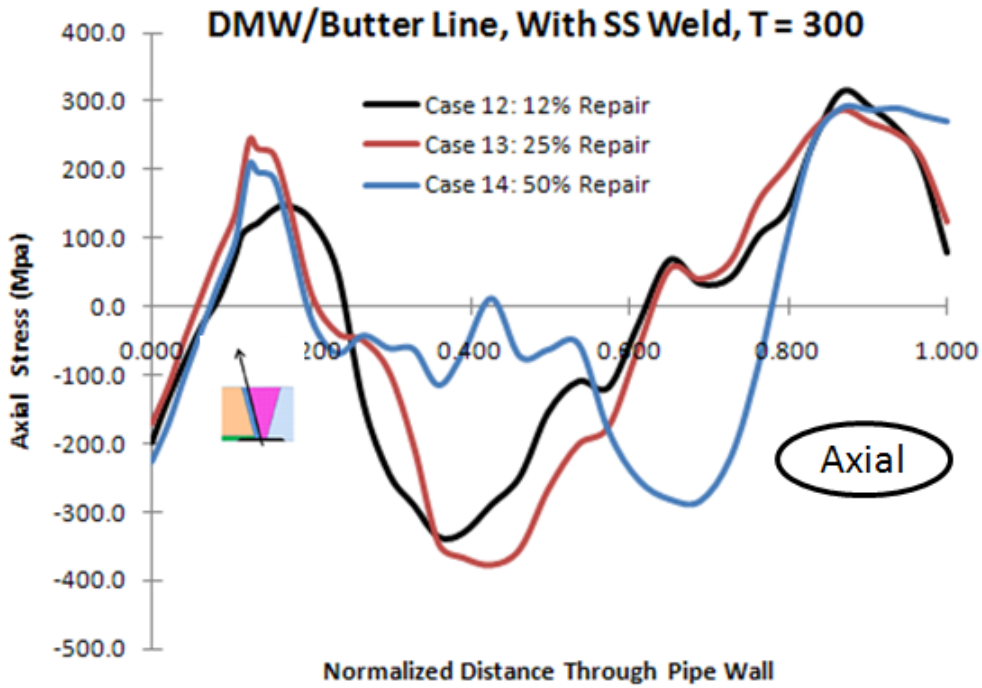


Figure C-26 Axial and Hoop WRS at DM Weld/Butter line for different depth repairs for the case with safe-end weld (Model 2).

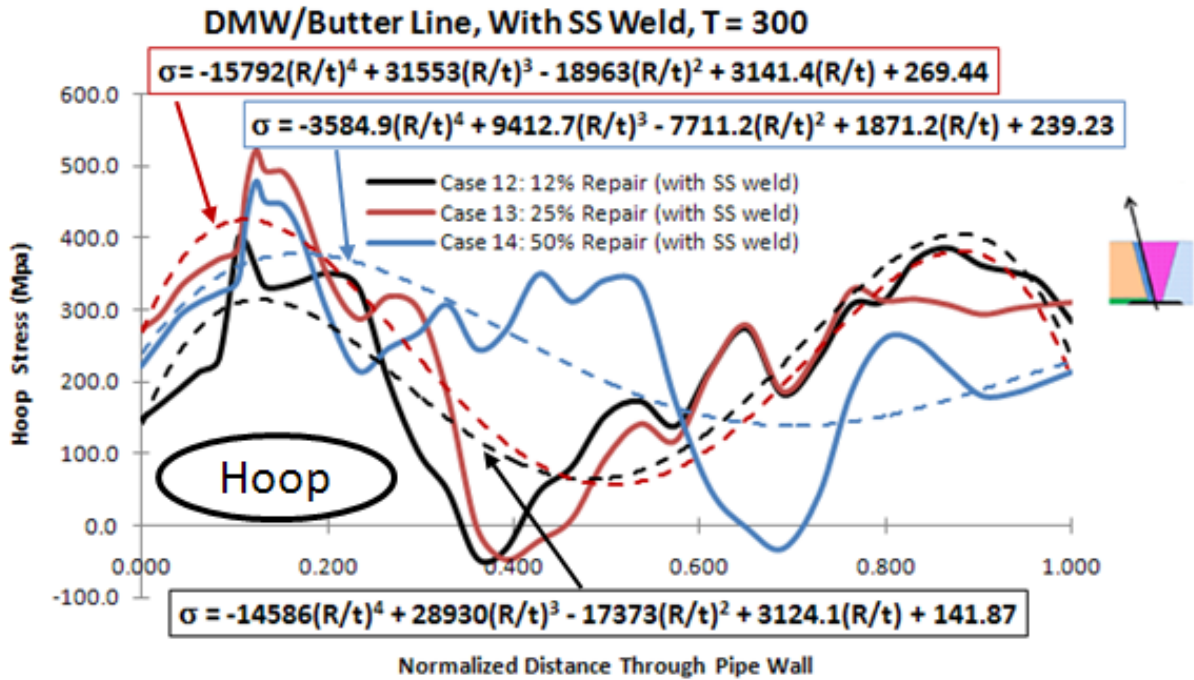
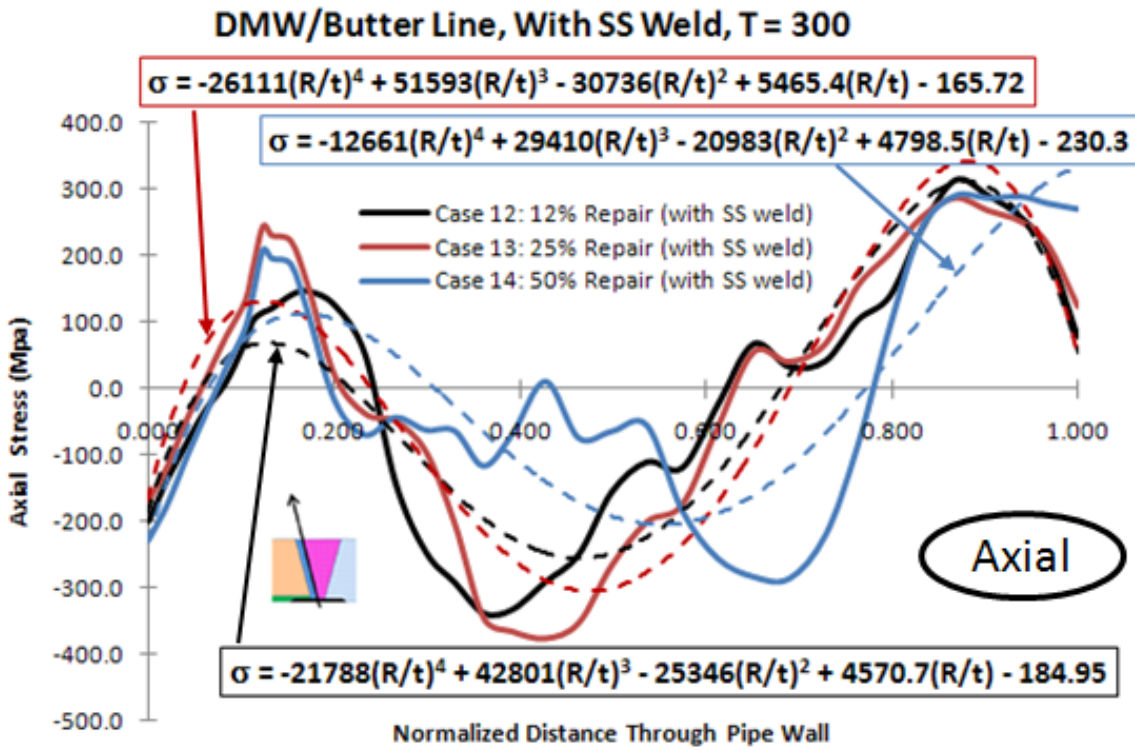
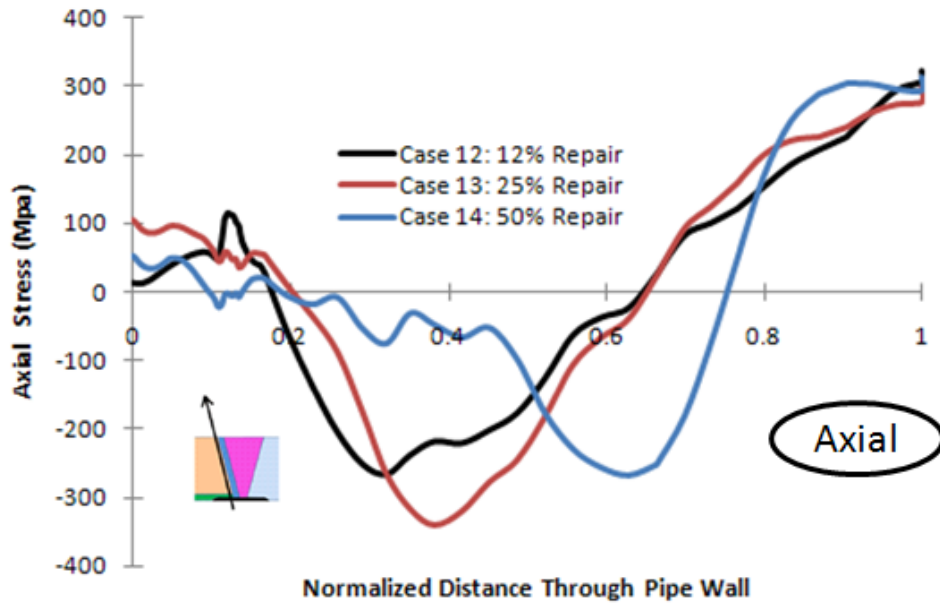


Figure C-27 Axial and Hoop WRS at DM Weld/Butter line for different depth repairs for the case with safe-end weld (Model 2).

DMW/Nozzle Line, With SS Weld, T = 300



DMW/Nozzle Line, With SS Weld, T = 300

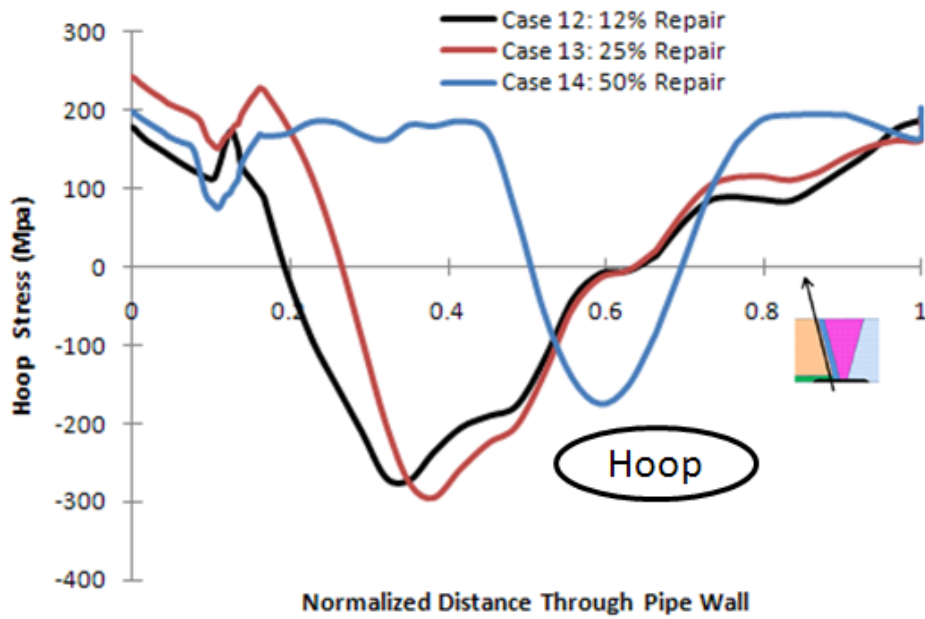


Figure C-28 Axial and Hoop WRS at DM Weld/Nozzle line for different depth repairs for the case with safe-end weld (Model 2).

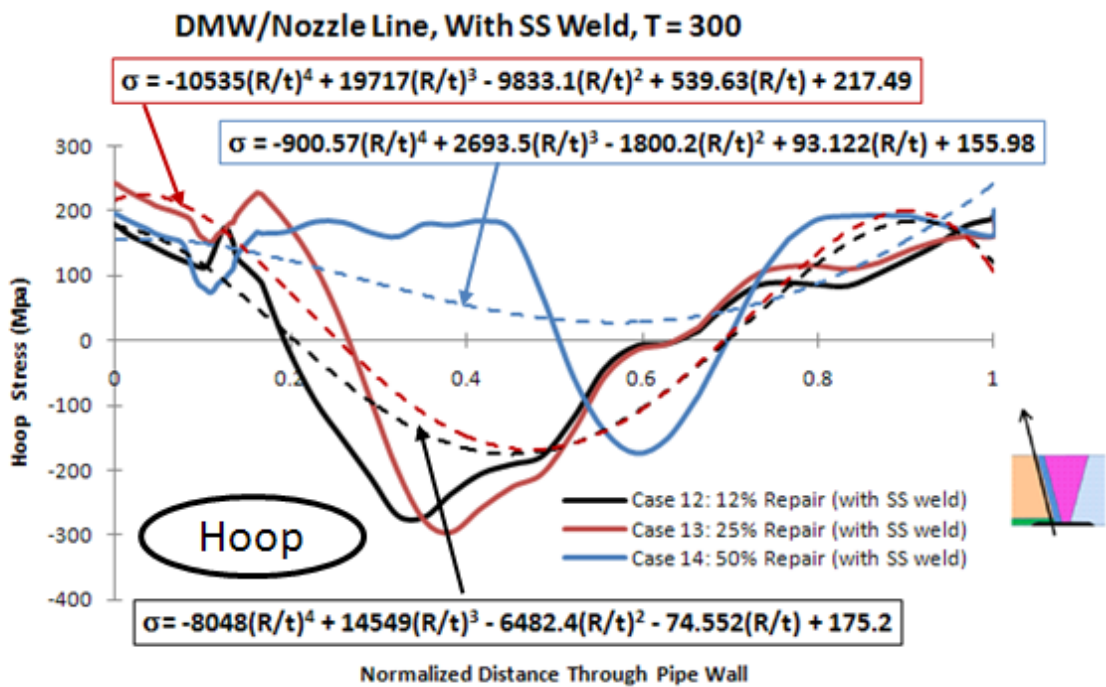
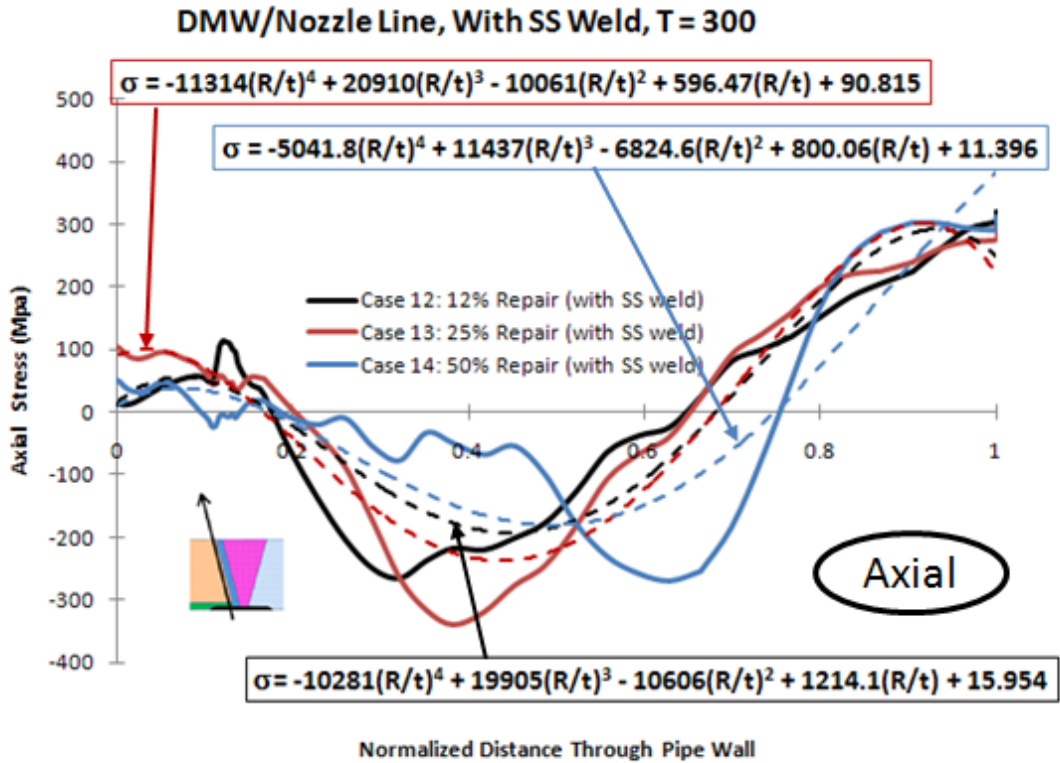


Figure C-29 Axial and Hoop WRS at DM Weld/Nozzle line for different depth repairs for the case with safe-end weld (Model 2).

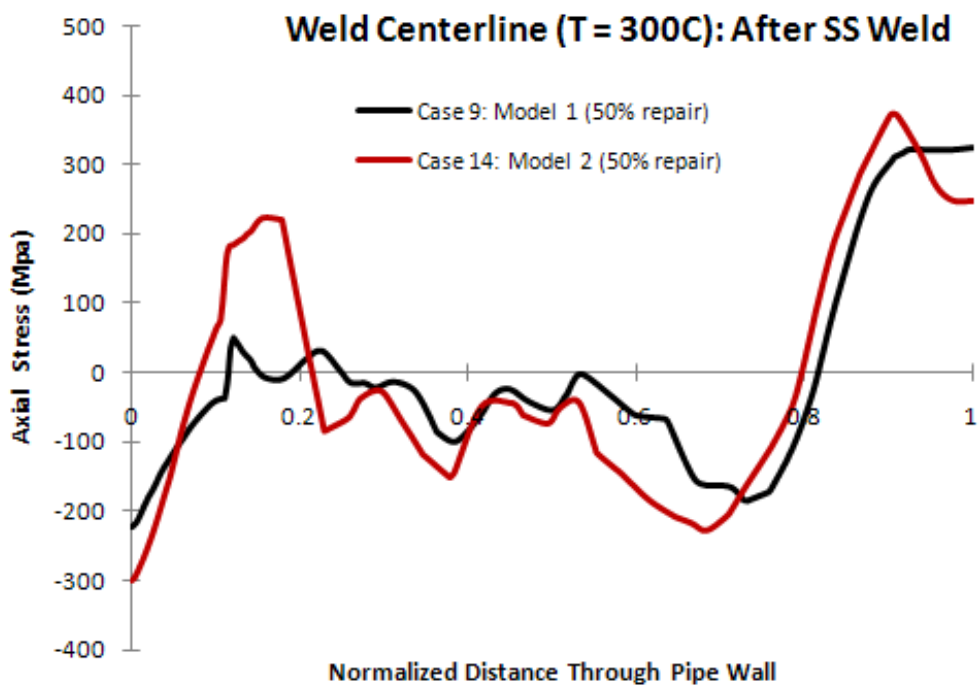
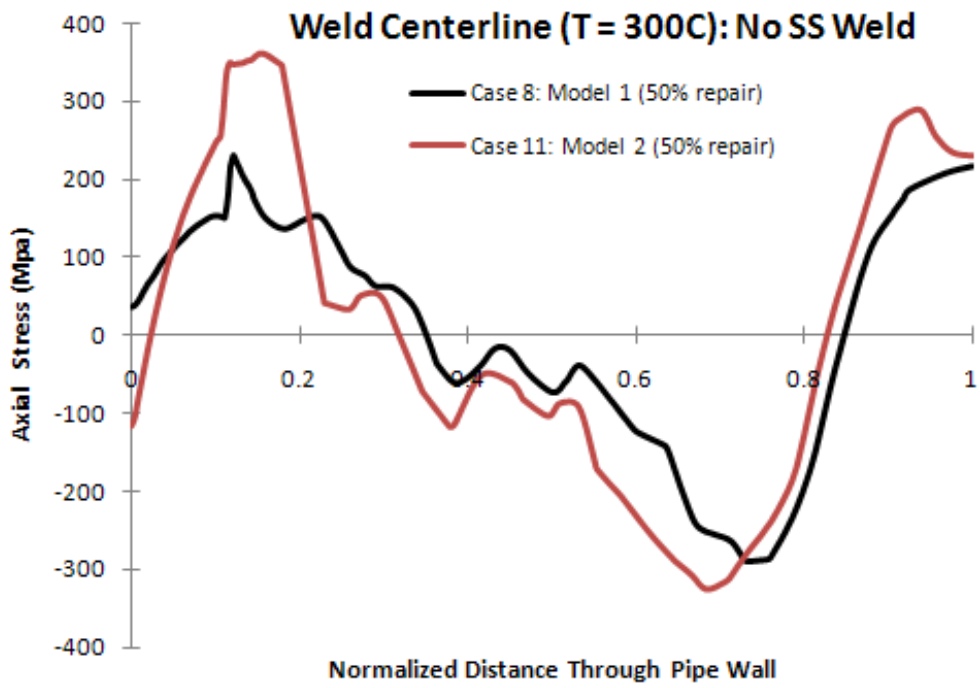


Figure C-30 Comparison of Model 1 and Model 2 WRS before and after SS weld.

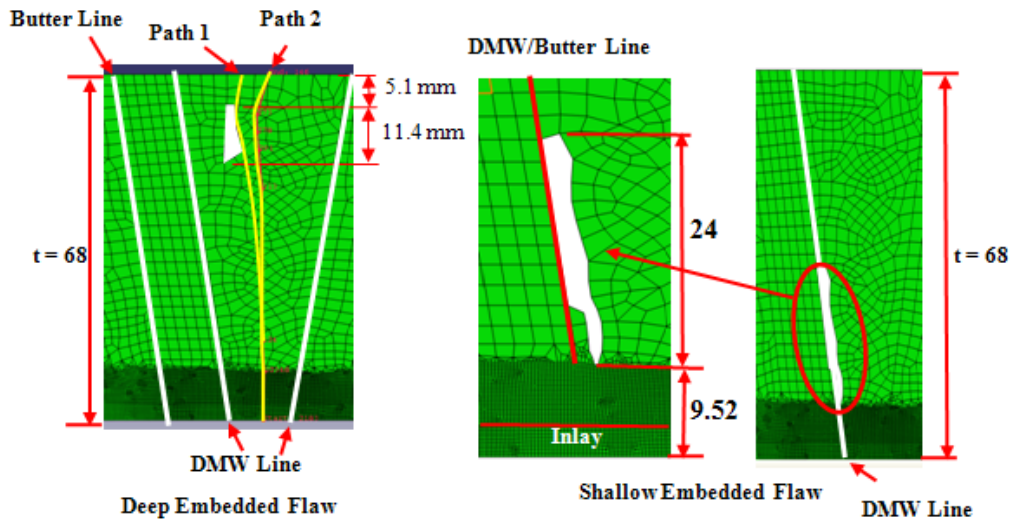


Figure C-31 Embedded Flaw WRS cases.

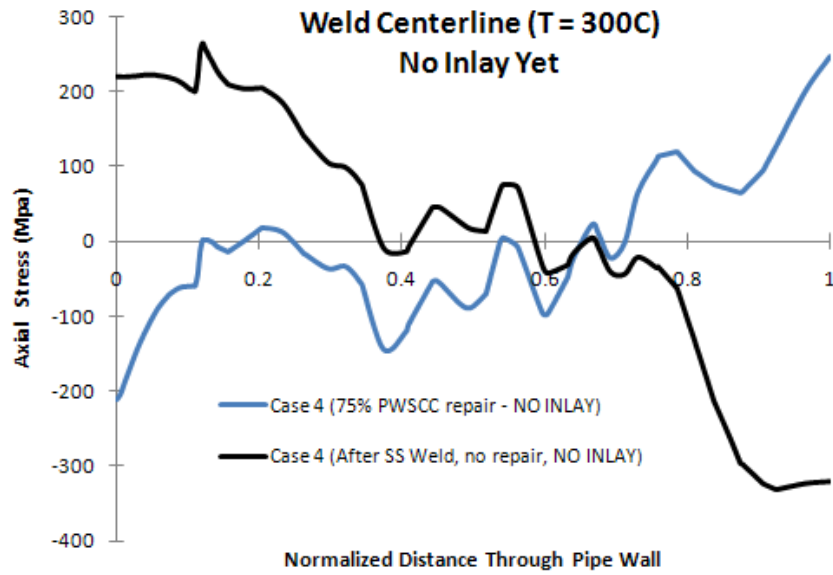


Figure C-32 Comparison of axial stresses after SS safe-end weld and after 75% repair.

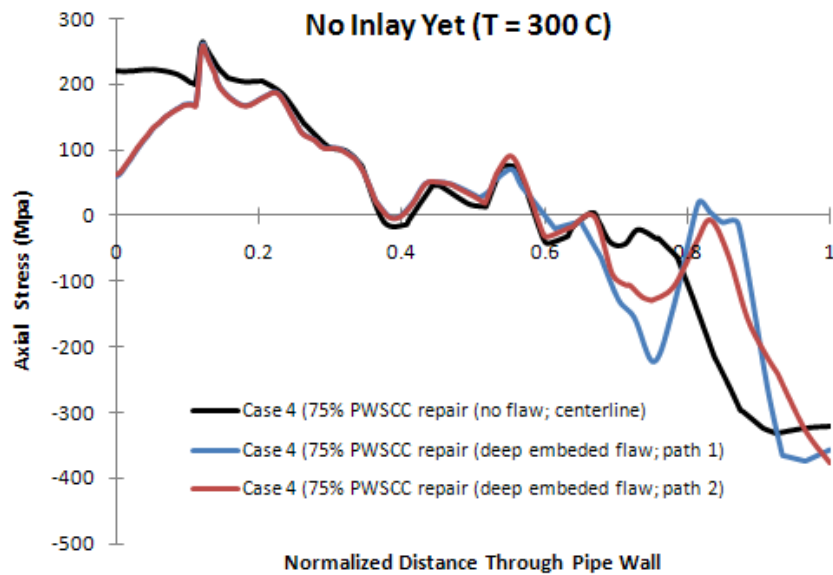


Figure C-33 Axial WRS comparison in DM Weld for Case 4 (75% PWSCC flaw) – before inlay.

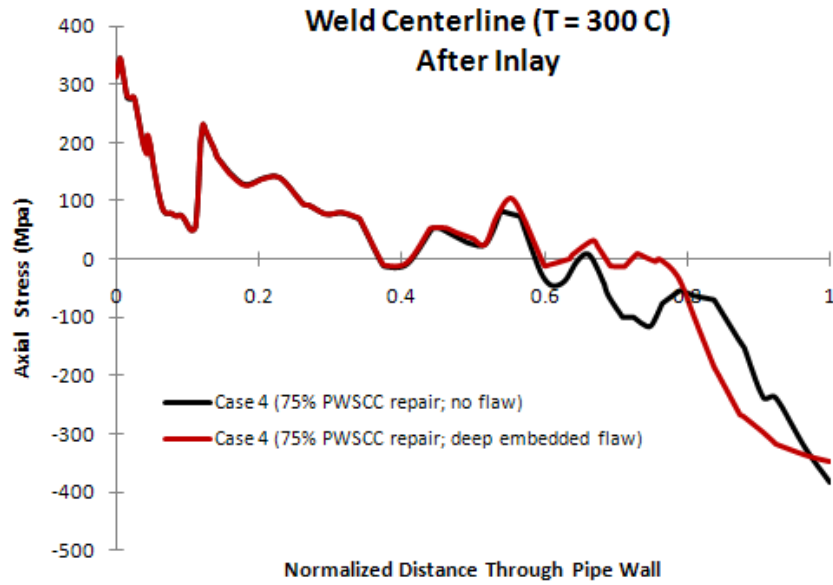


Figure C-34 Case 4 axial WRS at centerline for no flaw and deep embedded flaw.

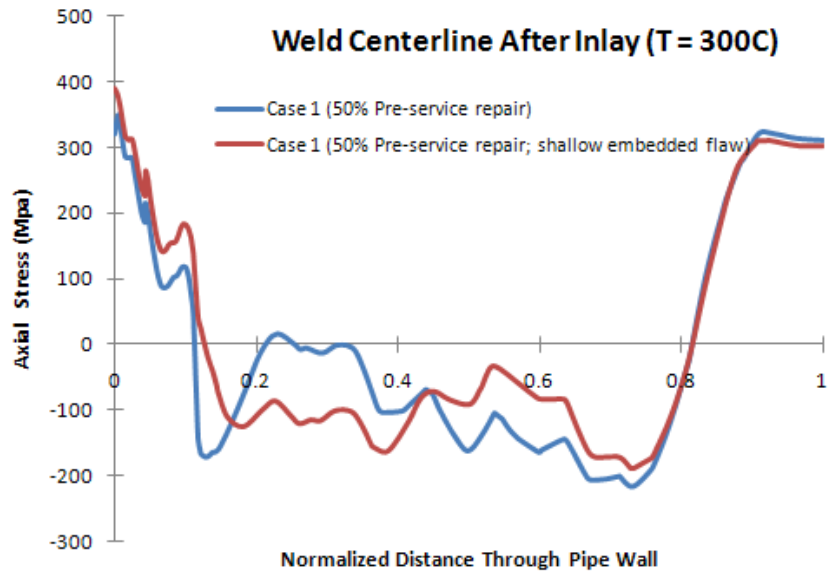


Figure C-35 50% Pre-service repair case; with and without flaw.

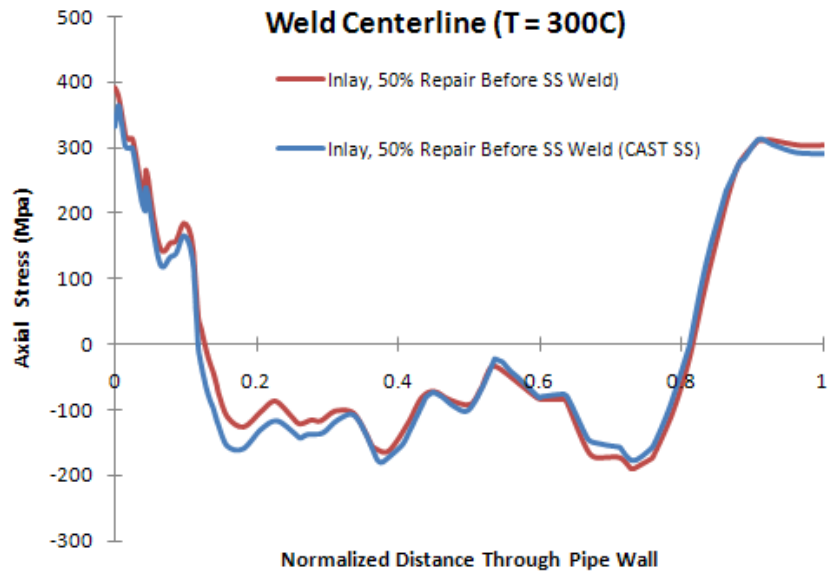


Figure C-36 Case 1 with cast stainless steel properties.